INTERNATIONAL REACTOR PHYSICS EXPERIMENTS EVALUATION PROJECT (IRPhEP) GUIDE TO THE EXPRESSION OF UNCERTAINTY

PRIMARY AUTHOR:

Adimir Dos Santos
Instituto de Pesquisas Energeticas e Nucleares

CONTRIBUTING AUTHORS:

Anatoli M. Tsiboulia
Institut of Physics and Power Engineering

Luka Snoj
Vladimir Radulović
Žiga Štancar
Jozef Stefan Institute

Zoltán Szatmáry
Institute of Nuclear Techniques of the Technical University of Budapest

Patrick D. Blaise
Centre d'Etudes de Cadarache

John D. Bess
Margaret Marshall
Idaho National Laboratory

J. Blair Briggs
Under Contract with the OECD NEA

INDEPENDENT REVIEWERS:

Evgeny Ivanov

Institut de Radioprotection et de Sûreté Nucléaire (IRSN)

Makoto Ishikawa
Shigeaki Okajima

Japan Atomic Energy Agency

Massimo Salvatores

CEA, Nuclear Energy Division, Cadarache, Saint-Paul-lez-Durance, France

Ivo Kodeli

Jozef Stefan Institute

Yevgeny Rozhikhin

Institut of Physics and Power Engineering

Ian Hill

Organization for Economic Co-Operation and Development – Nuclear Energy Agency

FORWARD

The methods used by the International Reactor Physics Experiment Evaluation Project (IRPhEP) to treat uncertainties encountered in experimental data and in the derivation of benchmark models have followed guidance provided by the International Criticality Safety Benchmark Evaluation Project (ICSBEP) since it was initiated as a pilot activity in 1999. Those methods have evolved significantly since the ICSBEP was initiated in 1992 and formal initiation of the IRPhEP in 2003. While the methods developed by the ICSBEP have been very helpful, the IRPhEP Technical Review Group has recognized the need for specific guidance on the treatment of uncertainties associated with reactor physics methods since its inception. An effort to develop such guidance was initiated by the OECD NEA in late 2016. Development of the IRPhEP Guide to the Expression of Uncertainty is expected to be an evolutionary process as is the ICSBEP Guide and may take several years to provide guidance for all types of reactor physics measurements.

Due to the evolutionary background of both efforts and the fact that criticality sections of many IRPhEP evaluations have been taken directly from the *International Handbook of Evaluated Criticality Safety Benchmark Experiments (ICSBEP Handbook)* and included in the *International Handbook of Evaluated Reactor Physics Measurements (IRPhEP Handbook),* the reader will often encounter similar inconsistencies in both Handbooks, as noted in the *ICSBEP Guide to the Expression of Uncertainties*.

Theoretical bases and derivations of methods that are included in the *ICSBEP Guide to the Expression of Uncertainties* are not repeated in this Guide. The information provided in this *IRPhEP Guide to the Expression of Uncertainty* is patterned more closely to the information provided in *Appendix C* of the ICSBEP Guide, but more specifically addresses uncertainties in reactor physics measurements other than criticality.

1.0 INTRODUCTION[1]

The technological uncertainties of a reactor are challenging both for reactor operation and analysis. When some neutronic characteristics of a reactor (e.g. neutron flux, buckling, reaction rates) are computed, the quantities specified as input data are usually nominal values of the reactor such as nominal geometry and composition, design temperature, etc. There are differences in the models used for the calculations and the real systems. In case of design calculations, this fact is taken into account by suitably chosen safety margins that are usually conservative estimates of the effects of the uncertainties on safety related reactor parameters (e.g. peaking factors, reactivity worths, etc.). For this reason, a sound estimate of these effects could help decrease excessive safety margins. The problem of estimating the effects of technological uncertainties is more complicated in the case of code validation since not only calculated but also measured quantities intervene.

A longer-term benefit is improvement of the state of the art of reactor physics analysis. Appropriate benchmarks can be used for this purpose only if their total uncertainties are well known. Realistic uncertainties from a diverse set of experiments provide the data needed to uncover weaknesses in neutron cross section data and calculational methods. Once these weaknesses have been characterized, it should be possible to reduce or eliminate them. This process holds the promise of more accurate reactor physics calculations in the future. This is important despite the fact that a large safety margin is usually added[2]. Firm knowledge of the uncertainty provides a foundation for setting appropriate safety margins. As the state of the art improves, smaller safety margins can be justified.

Best-estimate parameter values and uncertainties are needed to attain these goals. The evaluator should resist any tendency to either overestimate or underestimate uncertainty. It is a misconception that making large uncertainty estimates is always a conservative approach. If the total uncertainty is unrealistically large, some existing biases may be hidden in the uncertainty margins when comparing calculational results and benchmark (model) *values. In that case the computer code/nuclear data might be considered as validated in the domain of the benchmarks, while actually a bias may exist. On the other hand, if the total uncertainty is unrealistically low, calculation results may appear erratic or indicate a bias where none exists. This may lead, incorrectly, to modifications of cross sections or lack of confidence in codes or experiments, when the real deficiency was neglected uncertainty. Therefore the uncertainty reported in the benchmark evaluation must be as realistic and accurate as possible. This requires the evaluator to be rigorous, complete, and objective.*

In code validation, the calculated and experimental values are both burdened with random and systematic uncertainties. The former are random due to the statistical uncertainties of the nuclear data and the technological uncertainties of the input data while the latter are random due to the statistical errors of the measurements and the technological uncertainties of the reactor. Systematic uncertainties stemming from the nuclear data used in the calculations and from the measurement methods also play an important role in this process. It follows that the technological uncertainties affect both the calculated and the experimental values, but they do it in different ways and to different degrees. This makes accounting for uncertainties in code validation rather delicate. It is therefore essential to obtain the finest details of every experiment in order to determine which effects of the technological uncertainties are included in the empirically estimated standard deviations and which are not.

Examples of the technological uncertainties include:

---

[1] *The Effects of Technological Uncertainties on the Neutron Flux*, Zoltán Szatmáry, Technical University of Budapest.

[2] Safety margins are added for many reasons, not only as a result of qualification.

- *Uncontrolled biases of some reactor parameters (such as temperature),*
- *Insufficient reproducibility of some reactor parameters (such as boron concentration),*
- *Irregularities of the reactor lattice,*
- *Inhomogeneity of the fuel characteristics (i.e. pellet diameter, clad diameter, UO_2 density, air gaps between the pellets, heterogeneous MOX fuel, etc.),*
- *Deliberately introduced perturbations (such as detector* (activation) *foils or fission chambers).*

Uncertainties addressed by the IRPhEP can be divided into 3 categories: 1) Uncertainties in measurement methods; 2) Uncertainties in all physical and chemical parameters of the experiments; and 3) uncertainties in biases introduced by the use of parameters derived from calculations or from other experiments, desired simplification, or by modelling limitations. Guidance on how to address those uncertainties is provided in the following sections. The uncertainties in measurements methods and benchmark models are addressed and practical examples provided.

Provided herein are the means and examples to evaluate experimental data for which uncertainty data are available. This information can also be utilized to estimate the uncertainty in reactor physics measurements for which detailed experimental uncertainty data were not obtained and/or recorded.

2.0 UNCERTAINTY GUIDE

Uncertainties addressed by the IRPhEP can be divided into 3 categories: 1) Uncertainties in measurement methods, 2) Uncertainties in all physical and chemical parameters of the experiments (facility parameters – typically derived in Section 2 of an IRPhEP Evaluation), and 3) uncertainties in biases introduced by the use of parameters derived from calculations or from other experiments (e.g. delayed neutron fractions and corresponding decay constants, calculated factor such as gamma self-absorption factors, self-shielding factors, Diven factors, etc.), desired simplification (typically derived in Section 3 of an IRPhEP Evaluation), or by modelling limitations (typically derived in Section 4 of an IRPhEP Evaluation).

Uncertainty due to measurement methods for critical, subcritical, and certain types of reactivity measurements are often small compared to uncertainty in facility parameters. Uncertainty in most other reactor physics measurements are dominated by uncertainty in the measurement methods. The uncertainty in biases should always be minimized by the evaluator.

Uncertainty in nuclear data can sometimes impact the uncertainty in facility parameters and /or bias. Care must be taken when performing difference calculations that utilize different nuclear data components (with and without calculations).

Guidance on how to address each of the ten measurement types, X, included in the IRPhEP Handbook, is divided into the following five main subheadings.

2.X <u>Type of Measurement</u>

2.X.1 *Uncertainties in Measurement Methods*

Includes a description of each measurement method and the uncertainties associated with each method. Typical values as well as maximum and minimum values are included.

2.X.2 *Uncertainties in Experimental Configuration*

Uncertainties in all physical and chemical parameters of the experiments (facility parameters – typically derived in Section 2 of and IRPhEP Evaluation) are discussed and typical values as well as maximum and minimum values that are considered bounding are provided.

2.X.3 *Uncertainties in Biases and Benchmark Models*

Uncertainties in biases introduced by using parameters derived from calculations or from other experiments (e.g. delayed neutron fractions and corresponding decay constants, calculated factors such as the gamma self-absorption factors, self-shielding factors, Diven factors, etc.), desired simplification (typically derived in Section 3 of and IRPhEP Evaluation), or by modelling limitations (typically derived in Section 4 of and IRPhEP Evaluation) are provided. Typical uncertainty values as well as maximum and minimum values that are considered bounding are provided.

Uncertainties in Benchmark Models are obtained assuming no correlation among parameters and by quadratically combining the uncertainties in measurement methods, uncertainties in facility parameters (experimental configuration), and uncertainty in bias (generally not discussed in this Guide) to obtain the overall uncertainty in the benchmark model, σ_p^{Be}:

$$\sigma_p^{Be} = \sqrt{\sigma_{MM}^2 + \sigma_{EC}^2 + \sigma_{Bias}^2}$$

where σ_{MM} is the uncertainty in the measurement method, σ_{EC} is the uncertainty due to uncertainty in experimental configuration, σ_{Bias} is the uncertainty due to all biases (should be minimized).

2.X.4 *Practical Examples*

At least one practical example is provided for each measurement type. In some cases, examples are only briefly discussed and reference made to the actual example in the IRPhEP Handbook or a publication in a technical journal.

2.X.5 *References*

References that support the theory or provides additional information are given for each measurement type.

Experimental uncertainties of an integral parameter are usually given by the experimenters in the form of components. However, correlations between integral parameters are seldom found in the experiment reports; therefore, the NEA Nuclear Science Committee Working Party on International Nuclear Data Evaluation Co-operation has developed a three-step method to estimate them from the available experimental information. A description of the method and examples have been extracted directly from their report[3] and are provided in Appendix A. Furthermore, a methodology or rigorous approach to the evaluation of the covariance of reactor

[3] *Methods and Issues for the Combined Use of Integral Experiments and Covariance Data*, A report by the Working Party on International Nuclear Data Evaluation Co-operation of the NEA Nuclear Science Committee, NEA/NSC/WPEC/DOC(2013)445).

physics integral experiments was presented in a special ANS Reactor Physics Division (RPD) Session devoted to the Memory of Richard (Dick) McKnight and is publish in those transactions[4].

2.1 Critical and / or Subcritical Measurements

Comprehensive treatment of uncertainty in Critical and / or Subcritical Measurements may be found in the well-established *ICSBEP Guide to the Expression of Uncertainties*. Specific examples are provided in Appendix C of that document.

2.2 Buckling and Extrapolation Length Measurements

Guidance for the determination of uncertainties for Buckling and Extrapolation Measurements has not yet been formalized. However, a theoretical example for the determination of uncertainties in Buckling Measurements is provided in an unpublished paper entitled, *The Effects of Technological Uncertainties on the Neutron Flux*, Zoltán Szatmáry, Technical University of Budapest.

2.3 Spectral Characteristics Measurements

Spectral indices allow characterisation of an energetic distribution of neutrons in a core configuration. They are mainly measured in well characterised spectra such as regular lattices, though they can also be measured in mock-ups or simple configurations such as Godiva or Jezebel. Spectral characteristics often consist of spectral indices which are the ratios of two reaction rates; other spectral characteristics can refer to the measurement of the energy distribution of the neutron spectrum. Benchmark specifications of spectral characteristics in simplified geometry can have a high sensitivity to specific nuclear reactions, and so enable *qualification of nuclear data* associated with the calculation scheme in a given energetic range.

Standard measurements are carried out using:

- Miniature fission chambers (with standard diameters of few mm, inserted into the core)
- Activation foils,
- Fuel rod scanning (by particular gamma peak spectrometry),
- Proton Recoil.

Activation foil category also includes activations of wire and targets made with thin deposits of fissile or activation materials. Particularly to the targets made of thin deposits of fissile or activation material ZPR-TM-424 [2.3-1] provides a good description of calibration methods and their sources of uncertainties.

Detailed descriptions of these standard measurement methods are described in Section 2.7.

[4] G. Palmiotti and M Salvatores, *Role of Experiment Covariance in Cross Section Adjustments (Based on Seminal Work Performed by R.D. McKnight*, Transactions of the American Nuclear Society, Vol. 110, Reno, Nevada, June 15–19, 2014.

2.3.1 *Uncertainties in Measurement Methods*

2.3.1.1 Spectral Indices

The purpose of this section is to describe the measurement techniques of the spectral indices and their associated uncertainty analyses. The source of the uncertainties in the spectral indices will be described and discussed in a general sense. The maximum and minimum uncertainty bounds for the measurements and for the benchmark values are also provided.

The most comprehensive information on spectral indices and their uncertainties available earlier was presented in the CSEWG Handbook [2.3-2]. In the 1980s, much work has been done comparing the measurement methods of the basic reaction rate ratios (C8/F9, F9/F5, F8/F9) in fast critical assemblies at six laboratories of the world [2.3-3 and 2.3-4].

In the 2015 edition of the IRPhEP Handbook over 30 evaluations of the spectral indices performed at 13 different facilities are presented. The most widely-used method for measuring spectral indices is the activation method using different gamma-ray detectors (NaI, GeLi). In addition to activation methods, measurements are performed on fast critical mock-ups, (ZPPR-LMFR-EXP-001), with different fission chambers – regular, multi-isotopic, and absolute (BFS1-FUND-EXP-001), as well as with the solid-state track detectors (ZEBRA-LMFR-EXP-002).

Measurements of the neutron energy spectra are performed using two methods; proton-recoil (FFTF-LMFR-RESR-001) and time-of-flight (ZEBRA-FUND-RESR-001).

Experimental Methods used at different facilities for the spectral indexes measurements (presented in the 2015 Edition of the IRPhEP Handbook) are summarized in Table 2.3-1.

Table 2.3-1. Experimental methods used at different facilities for the spectral indices measurements (Presented in the 2015 Edition of the IRPhEP Handbook)

Facility[5]	Facility Type	Foils Activation	Fission Chambers	Solid-State Detectors	Spectra
DCA	HWR	GeLi			
DIMPLE	LWR	NaI			
IPEN	LWR	GeLi			
SCCA	SPACE	NaI			
SSCR	PWR	NaI			
ZR6	VVER	GeLi			
BFS-1	FUND	GeLi, NaI	MFC, TFC, AFC	SSD	
BFS-2	LMFR	GeLi, NaI	MFC,		
FFTF	LMFR	GeLi			PR
SNEAK	LMFR		FC		
ZEBRA	FUND	NaI	FC	SSD	PR, TOF
ZPPR	LMFR	GeLi			
ZPR	LMFR	NaI			

GeLi, NaI - type of gamma-detector
MFC - miniature fission chamber
TFC - triple-segment fission chamber
AFC - absolute fission chamber
PR – proton recoil
TOF - time-of-flight

Regarding thermal reactors, the most well-known spectral indices are the CSEWG benchmarks [2.3-2]. Common spectral indices include:

[5] See IRPhEP Handbook for facility descriptions.

- $^{28}\rho$ the epithermal to thermal neutron capture in ^{238}U,
- $^{25}\delta$ the epithermal to thermal neutron fission in ^{235}U,
- *C8/F* the neutron capture in ^{238}U to the total number of fissions,
- $^{28}\delta$ the fission rate in ^{238}U to fission rate in ^{235}U.

2.3.1.1a Spectral Index Definition

Consider the reaction rates of a specific nuclear reaction, such as capture or fission, occurring in two nuclides in a reactor environment. These reaction rates can also be of same nuclides and nuclear reaction in a different neutron spectrum (bare and cadmium covered for example).

By definition, the spectral index (*SI*) is defined as:

$$SI = \frac{R_1}{R_2} . F_{norm} . F_T, \qquad 2.3\text{-}1$$

where R_i is the reaction rate per target nuclide of isotope i (i=1 or 2), F_{norm} is a power normalization factor for distinct reactor power operations or the ratio of the monitor counts in the case of miniature fission chambers, and F_T is the temperature correction for different temperature operations.

The power normalization factor employed in the spectral index measurements is the ratio of the detector signals (either counts or current) that monitor the power in the reactor under consideration. The power normalization factor is given by:

$$F_{norm} = \frac{\bar{S}_2}{\bar{S}_1}, \qquad 2.3\text{-}2$$

where $\bar{S}_2$ and $\bar{S}_1$ are respectively the average detector signals for operation 2 and 1. Isotope 1 is irradiated in operation 1 and isotope 2 is irradiated in operation 2.

Spectral indices for thermal reactors are sensitive to temperature. In the case of different temperatures for each reaction rate measurement, a correction, F_T, must take place. F_T is determined by employing a sensitivity analysis of the spectral indices to the temperature and from these analyses the reaction rates can be transformed to the same temperature basis.

The temperature normalization factor can be expressed mathematically as:

$$F_T = (1 + \frac{S_{R1}^T \cdot \Delta T}{T_1}), \qquad 2.3\text{-}3$$

where Configuration 1 was taken as reference, $\Delta T = T_2 - T_1$; T_1 and T_2 are respectively the temperature for Configurations 2 and 1 giving in Kelvin unity, $S_{R_1}^T$ is the sensitivity coefficient of the reaction rate for Configuration 1 to the temperature and is given by:

$$S_{R_1}^T = \frac{T_1}{R_1} \cdot \frac{\partial R_1}{\partial T} \Big|_{T=T_1}, \qquad 2.3\text{-}4$$

and R_1, and R_2 in Equation 2.3-1 are related to the reaction rate (RR) (Section 2.7.1) given by Equation 2.7-2 for foil activation techniques, Equations 2.7-32 and 2.7-34 for fuel rod scanning techniques and Equation 2.7-39 for the case of the miniature fission chamber as:

$$R_i = \frac{RR_i}{N_i}, \qquad 2.3\text{-}5$$

where i refers to nuclide 1 or 2, RR_i is the reaction rate for nuclide i, and N_i the total number of atoms of nuclide i in the measurement device (either foil, fuel rod, or miniature fission chamber).

N_i is given by:

$$N_i = \frac{m_i N_{Av}}{M_i}, \qquad 2.3\text{-}6$$

where m_i, M_i, and N_{Av} are respectively, the mass, and the atomic mass of nuclide i, and Avogadro's Number.

The quantities measured in the spectral indices experiments employing foil activation or fuel rod scanning techniques are the reaction rates following the procedure extensively discussed in Section 2.7.1. In the case of the miniature fission chambers, the quantity measured is detector counts, which are proportional to the fission rates.

Some special kinds of spectral index such as $^{28}\rho$ and $^{25}\delta$ will require correction factors in order to achieve to their final values. These correction factors will transform the perturbed configuration (with foils, cadmium sleeves, etc.) into an unperturbed one (without the measurement devices). Example E2.3-4 shows how the correction factors are defined for the special cases of $^{28}\rho$ and $^{25}\delta$ and utilized to infer these spectral indices. Other spectral indices such as the ones employing miniature fission chambers might require other types of correction factors (see Example 2.3-3)

2.3.1.1b Uncertainty Types and Bounding Values for the Spectral Index Measurements

The uncertainties in the spectral indices can be classified into five categories:

1. Uncertainties in the measured reaction rates (described in Section 2.7.1),
2. Uncertainties in the power normalization (detector signals used to monitor power),
3. Uncertainties in temperature normalization,
4. Uncertainties in calculated correction factors (nuclear data, calculation model, transport equation solver), as in the case of $^{28}\rho$ and $^{25}\delta$ (see Example E2.3-4 for details),
5. Uncertainty in the mass of the device employed to get the reaction rates (mass or calibration of foil, fuel rod, or calibrated mass of miniature fission chamber).

In order to get the uncertainty in the spectral index consider the general equation for the propagation of the associated uncertainties [2.3-5 and 2.3-6]. Let x_i be an independent or correlated set of variables and w(x_i) a dependent function of this set of variables. Accordingly, the uncertainty of w(x_i) is:

$$\sigma_w^2 = \sum_{i=1}^{n} \left(\frac{\partial w}{\partial x_i}\right)^2 . \sigma_i^2 + 2. \sum_{i>j}^{n} \frac{\partial w}{\partial x_i} . \frac{\partial w}{\partial x_i} . cov(x_i, x_j), \qquad 2.3\text{-}7$$

where x_i is a generic independent variable, σ_i is the uncertainty of x_i and $\mathrm{cov}(x_i, x_j)$ is the covariance matrix of x_i and x_j.

In most of the uncertainty analyses all independent variables are assumed uncorrelated. However, it is left to the evaluator's judgement to perform additional analyses if necessary.

2.3.1.1c The Uncertainty Analysis for the Spectral Indices

Applying Equation 2.3-7 to Equation 2.3-1 and assuming all quantities uncorrelated, one gets:

$$\sigma_{SI} = SI.\sqrt{\left(\frac{\sigma_{R1}}{R_1}\right)^2 + \left(\frac{\sigma_{R2}}{R_2}\right)^2 + \left(\frac{\sigma_{F_{norm}}}{F_{norm}}\right)^2 + \left(\frac{\sigma_{F_T}}{F_T}\right)^2}. \qquad 2.3\text{-}8$$

σ_{R_1} and σ_{R_2} are obtained applying Equation 2.3-7 to Equation 2.3-5:

$$\sigma_{R_i} = RR_i.\sqrt{\left(\frac{\sigma_{RR_i}}{RR_i}\right)^2 + \left(\frac{\sigma_{N_i}}{N_i}\right)^2}, \qquad 2.3\text{-}9$$

where i is equal to 1 or 2, and σ_{RR_i} is the uncertainty in the reaction rate of nuclide i extensively discussed in Section 2.7.1.

σ_{N_i} is obtained applying Equation 2.3-7 to Equation 2.3-6. The final result is:

$$\sigma_{N_i} = N_i.\sqrt{\left(\frac{\sigma_{m_i}}{m_i}\right)^2 + \left(\frac{\sigma_{M_i}}{M_i}\right)^2}, \qquad 2.3\text{-}10$$

where σ_{m_i} and σ_{M_i} are respectively the uncertainty in the mass (foil mass, ^{235}U or ^{238}U mass in the scanning technique, or the calibrated mass of the miniature fission chamber) and the uncertainty in the atomic mass of nuclide i.

Equations 2.3-8 through 2.3-10 form a complete set of equations to calculate the uncertainty in the spectral index SI.

2.3.1.1d Other Uncertainty Considerations

Uncertainty of Power Normalization Factor

The uncertainty in the power normalization factor is mainly statistical or the spread of the signals of the detectors around the mean value. A possible systematic uncertainty would occur if this detector loses its linearity between the two reactor operations; this source of uncertainty is left to the evaluator's judgment.

Applying Equation 2.3-7 to Equation 2.3-2 yields:

$$\sigma_{SI}^{F_{norm}} = F_{norm} \cdot \sqrt{\left(\frac{\sigma_{\bar{S}_2}}{\bar{S}_2}\right)^2 + \left(\frac{\sigma_{\bar{S}_1}}{\bar{S}_1}\right)^2}, \qquad 2.3\text{-}11$$

where $\sigma_{\bar{S}_1}$ and $\sigma_{\bar{S}_2}$ are, respectively, the uncertainties of the detector signals for operation 1 and 2.

Uncertainty of Temperature Normalization

The uncertainty in the temperature normalization factor can be obtained applying Equation 2.3-7 to Equation 2.3-3:

$$\sigma_{SI}^{F_T} = \frac{S_{R_1}^{T} \cdot (\sigma_{T_2} - \sigma_{T_1})}{T_1} \quad , \qquad \text{2.3-12}$$

where $\sigma_{SI}^{F_T}$ is the uncertainty in the temperature normalization factor, σ_{T_2} and σ_{T_1} are respectively the temperature uncertainties for operation 1 and 2.

Systematic Uncertainties

The sources of the systematic uncertainties arise mainly from the reaction rates measurements. However the masses (the foil or fuel rod masses or the calibrated masses in the case of miniature fission chambers), and nonlinearity of the detectors that monitor the power and determine the power normalization both employed in the determination of the spectral indices can play an important role. The experiment report should provide enough information so that the evaluator can judge the possible sources of systematic uncertainties.

2.3.1.1e Final Spectral Index Measurement Uncertainty

The final spectral index uncertainty is obtained combining quadratically all uncertainty types and assuming no correlation among them. Let this uncertainty be denoted by $\sigma_{SI_{MM}}$; i.e., the measured method spectral index uncertainty for a generic reaction type and a generic measurement method. The final benchmark uncertainty for the spectral index experiment is given by:

$$\sigma_{SI_{MM}} = \sqrt{\sigma_{SI}^2 + \left(\sigma_{SI}^{F_{norm}}\right)^2 + \left(\sigma_{SI}^{F_T}\right)^2 + \left(\sigma_{SI}^{sys}\right)^2}, \qquad \text{2.3-13}$$

where the subscript SI represents the spectral index uncertainty of any of the measurement techniques described in this Guide or any other technique employed for the same purpose and σ_{SI}^{sys} is the systematic uncertainty.

2.3.1.1f Sources of Uncertainty and Bounding Values for the Spectral Index Measurements

Table 2.3-2a shows a summary of uncertainty sources and bounding values for spectral index measurements for thermal reactors. The list is not exhaustive, but it addresses most of the uncertainties employed in the uncertainty analysis described in subsequent subsections. The major contributor to the overall uncertainties of the spectral index measurement is the reaction rate measurements. Some of the main components of the reaction rate uncertainties are repeated in Table 2.3-2a in order to illustrate and make more understandable the sources of the uncertainties in the spectral indices. The definitions and sources of uncertainties are given in detail in Section 2.7.

Table 2.3-2a. Summary of uncertainties and bounding values for thermal reactors

Source of Uncertainty	Typical Value	Minimum Value	Maximum Value	Type of Uncertainty (A or B) [(a)]
Reaction Rate (RR)	3.0 %	1.0 %	5.0 %	B
Global Detector Efficiency (η_{RRP})	0.7 %	0.1 %	3 %	B
End of Irradiation Activity (A_0)	1.5 %	0.1 %	5 %	B
Detector Count; including A_0 (C)	0.5 %	0.1 %	30 %	B
Ramp Factor (F_{ramp})	1.0 %	0.1 %	5 %	B
Gamma Self-Absorption Factor (F_{abs})	2.0 %	0.1 %	5 %	B
Depression Flux Correction factor (F_{corr})	1.0 %	0.1 %	5 %	B
Fission Yield (Y_{RRP})	2.0 %	0.1 %	5 %	B
Reactor Power	2.0 %	1.0 %	5.0 %	B
Power detector signal	0.5 %	0.1 %	1.0 %	B
Calibrated Mass (MFC)	2.5 %	1.0 %	4.0 %	A
Power Normalization (F_{norm})	0.4 %	0.01 %	3.0 %	B
Temperature Normalization (F_T)	0.1 %	0.01 %	1 %	B
Calculated Factor (F_{corr})	2.5 %	0.1 %	3.0 %	B
Device mass	0.05 %	0.01 %	3.0 %	B
Spectral Index	3 %	0.5 %	5.0 %	Variable

(a) The Uncertainty Type (A or B) has the same meaning as in ICSBEP Uncertainty Guide.

For the measurements of spectral indices (see Eq. 2.3-1) with fission chambers in fast spectra the uncertainties in the power normalization factor (F_{norm}) and temperature normalization factor (F_T) are negligible. The major contributions to the uncertainties of the reaction rates RR come from the detector count and calibrated mass (typical values are given in Table 2.7-2). The uncertainty for the F8 (Fission Rates in ^{238}U) counting rate is larger than those for F5 (Fission Rates in ^{235}U) and F9 (Fission Rates in ^{239}Pu), rapidly increasing with increasing distance from the core center. Tables 2.3.2b and 2.3.2c show the summary for the uncertainty types and bounding values for the spectral indices F9/F5 and F8/F5, respectively.

Table 2.3-2b. Summary of uncertainties and bounding values F9/F5 in the core

Source of Uncertainty	Typical Value	Minimum Value	Maximum Value	Type of Uncertainty (A or B) [(a)]
Reaction Rate (RR_1)	1.5 %	0.5 %	2.5 %	B
Reaction Rate (RR_2)	1.5 %	0.5 %	2.5 %	B
Spectral Index	2.0 %	1.0 %	3.0 %	Variable

(a) The Uncertainty Type (A or B) has the same meaning as in ICSBEP Uncertainty Guide.

Table 2.3-2c. Summary of uncertainties and bounding values F8/F5 in the core

Source of Uncertainty	Typical Value	Minimum Value	Maximum Value	Type of Uncertainty (A or B) [(a)]
Reaction Rate (RR_1)	2.0 %	1.0 %	4.0 %	B
Reaction Rate (RR_2)	1.5 %	0.5 %	2.5 %	B
Spectral Index	2.5 %	1.0 %	4.0 %	Variable

(a) The Uncertainty Type (A or B) has the same meaning as in ICSBEP Uncertainty Guide.

2.3.1.2 Neutron Spectra

Time-of-Flight Method

A relation between neutron energy, E, and time of flight, t, for path length, l, is as follows:

$$E=5.23\times10^{3}\ l^{2}/t^{2} \qquad 2.3\text{-}14$$

where energy is expressed in electron-volts, path length in meters, and time of flight in microseconds.

In the ideal case (infinitely small duration of the neutron pulse and registration time interval, no background etc.) it is easy to obtain a relation between the pulse time distribution, $N(t)$, and their energy distribution, $N(E)$:

$$N(E) \sim N(t)\ t^{3} / l^{2} \qquad 2.3\text{-}15$$

In case of a known detector efficiency, $\varepsilon(E)$, the desired neutron spectrum, $\varphi(E)$, can be determined as:

$$\varphi(E) = N(E)/\varepsilon(E).$$

The accuracy of a neutron energy measurement by the Time-of-Flight method is determined by the accuracy of the time-of-flight measurement since the value of l, in most cases, can be obtained with any necessary uncertainty. A dispersion of time of flight for most facilities is determined mainly by two factors: 1) finite duration of the neutron pulse, Δt_n, and 2) the spread of time intervals between neutron entry into the detector and the appearance of an electrical pulse, Δt_d. Other components of the time-of-flight dispersion such as time analyzer channel width, resolution time of electronics, and dispersion of start signal appearance time are usually much less.

When all components are independent, the overall uncertainty in the time measurement is:

$$\Delta t = \left(\sum_i \Delta t_i^2 \right)^{1/2} \qquad 2.3\text{-}16$$

The Resolution Function will be a convolution of partial resolution functions corresponding to each source of uncertainty. These partial resolution functions, as a rule, are approximately rectangular or triangular in shape. However convoluting a large quantity of functions of arbitrary shape, according to central limit theorem of probability theory, a function close to Gaussian with a dispersion equal to the sum of partial dispersions is obtained.

From Equation (2.3-14) it is easy to obtain:

$$\Delta E/E=2\Delta t/t = 2.78\times10^{-2}\ E^{\frac{1}{2}}\Delta t/l. \qquad 2.3\text{-}17$$

In order to transform the time distribution of measured pulses into neutron energy spectrum, it is necessary to account for background and make corrections for inaccuracies of registration equipment, and corrections connected with neutron pulse shape. The accuracy of the spectrum being recovered depends strongly on the accuracy of the detector efficiency, $\varepsilon(E)$ [at best, the relative dependence, $\varepsilon(E)$, is known with uncertainty of about 5%].

The main components of uncertainty are [2.3-7]:

1. Detector efficiency,
2. Background,
3. Neutron pulse duration,
4. Perturbation of the neutron spectrum by the beam hole,
5. Dependence of the neutron spectrum on the degree of sub-criticality.

Typical uncertainties in neutron spectrum measurements by the Time-of-Flight method are given in Table 2.3-3.

Table 2.3-3. Summary of Uncertainties and Bounding Values

Source of Uncertainty	Typical Value (%)	Minimum Value (%)	Maximum Value (%)	Type of Uncertainty (A or B)
Detector efficiency	6	3	15	
Background	2	1	5	
Neutron pulse duration	3	0	10	
Flight path	3	2	4	
Total Uncertainty of Measurements	10	5	20	

2.3.2 *Uncertainties in Experimental Configuration*

The uncertainties in the spectral indices benchmark model are composed of three major parts:

1) Uncertainties in measurements,
2) Uncertainties from the facility and from the device parameters, and
3) Uncertainties from the experimental configuration.

The temperature uncertainty must also be propagated to the spectral index uncertainty through a sensitivity calculation as described in Section 2.7.2. These three components shall be combined quadratically in order to get the whole benchmark uncertainty.

Uncertainties in the experimental configuration are the uncertainties that arise from the fact that the experiment setup is not in perfect agreement with its design, i.e., there is an uncertainty connected to the position of the activation foils, detectors and auxiliary instrumentation, uncertainty of the experiment equipment composition etc. The category also includes uncertainties in the environmental conditions, namely the uncertainties in basic parameters of the experiment system which might not be of direct interest, but nevertheless affect the measured. This includes uncertainties such as those in the geometry, composition or integral physical parameters of the criticality system.

The Effect of Uncertainty in the Experimental Configuration

This kind of uncertainty follows closely the procedure of the *ICSBEP Uncertainty Guide* [2.3-6]. Here uncertainties are divided primarily into two categories: a) uncertainty in geometry, and b) uncertainty in physics, chemistry, and isotopic content of materials.

As an illustration, Tables 2.3-4a and 2.3-4b show, respectively the uncertainties in the geometry and materials. The empty columns should be filled by the evaluator as an aid to clarify the uncertainties. This list is not exhaustive. Different parameters will be listed for other types of configurations. Besides the uncertainties commonly derived from the *ICSBEP Uncertainty Guide* for the facility parameters, the geometric and material uncertainties of the device (foil, fuel rod or miniature fission chamber) employed to infer the spectral indices should be taken into consideration. The geometry and material details of the device have to be known in order to assign their specific uncertainties. Example uncertainties are shown in Tables 2.3-4a and 2.3-4b. A sensitivity analysis is performed in order to propagate the geometric and material uncertainties of the facility and of the measurement and auxiliary devices utilized to infer the spectral indices. The final total uncertainty arising from the parameters of the experimental configuration is the square root of the sum of the squares of each component. This type of uncertainty is denoted by σ_{PF}.

Table 2.3-4a. Uncertainties in geometry

Parameter Identification	Mean Measured Value	Reported Uncertainty in Parameter	Type of Uncertainty (A or B)[(a)]	Number of Degrees of Freedom	Standard Uncertainty
Active Fuel Height					
Fuel Pellet Diameter					
Clad Outer Diameter					
Clad Inner Diameter					
Fuel Rod Pitch					
Bottom Alumina Height					
Measurement Device location					
Absorber Position					
Structural Material Geometry					
Foil Position					
Foil Geometry					
Other Relevant Parameters					

(a) The Uncertainty Type (A or B) has the same meaning as in ICSBEP Uncertainty Guide.

Table 2.3-4b. Uncertainties in Materials

Parameter Identification	Mean Measured Value	Reported Uncertainty in Parameter	Type of Uncertainty (A or B) [(a)]	Number of Degrees of Freedom	Standard Uncertainty
^{235}U Enrichment (%)					
UO_2 Density (g/cm^3)					
UO_2 stoichiometric factor (%)					
^{234}U (wt.%)					
^{236}U (wt.%)					
Fuel impurities (ppm)					
Cladding Density (g/cm^3)					
^{55}Mn in Cladding SS (wt.%)					
Cladding composition					
Device Impurities (ppm)					
Moderator Poison (ppm)					
Measured Device Mass					
Other Relevant Parameters					

(a) The Uncertainty Type (A or B) has the same meaning as in ICSBEP Uncertainty Guide.

2.3.3 *Uncertainties in Biases and Benchmark Models*

Biases in Benchmark Models

Biases are introduced in Benchmark Models in three distinct ways:

1) By spectral index measurement methods whenever parameters derived from calculations or from other experiments are employed to infer the measured spectral indices;
2) By desired simplifications (typically derived in Section 3 of and IRPhEP Evaluation);
3) By modelling limitations (typically derived in Section 4 of IRPhEP Evaluation).

Biases in the spectral indices measurement methods shown in this section arise from the calculated factors; i.e., from the calculated correction factors. Examples 2.3-3 and 2.3-4 show how these correction factors are applied. The determination of the biases arising from the spectral index measurement methods is a very complicated problem and some of them may never be found. The bias determination for the calculated quantities requires the availability of well-defined experiments for these quantities to serve as benchmarks; here referred to as Reference Values. Examples of the measurements of the correction factor for the determination of $^{28}\rho$ and $^{25}\rho$ may be found in Ref. [2.3-8]. Examples of measurements of these spectral indices without correction factors are found in Ref. [2.3-9].

The bias induced by these calculated factors can be understood calculating the ratio, C/R, where C is the calculated correction factor and R is the reference value provided by the specific available benchmarks. If the C/R ratio is greater than 1, the calculated factor overestimates the measured spectral index. If the ratio is less than 1, the calculated factor underestimates the measured spectral index.

The bias in the spectral index measurement for a particular correction factor is given as:

$$B_{CF} = \frac{(R-C)}{C} \cdot SI_{MM} \,, \qquad 2.3\text{-}18$$

where B_{CF} is the bias for the specific calculated factor and its uncertainty arises from a standard error propagation. SI_{MM} is the measured spectral index given by Equation 2.3-1.

The benchmark model value for the spectral index experiment, after applying all possible biases and correction factors is given by:

$$SI_{Be} = SI_{MM} + B_{SL} + \frac{(R-C)}{C} \cdot SI_{MM}, \qquad 2.3\text{-}19$$

where $SI_{\boldsymbol{Be}}$ is the benchmark model spectral index value, the subscript MM represents a generic measurement method, and B_{SL} is the bias from the benchmark model simplification (typically derived in Section 3 of and IRPhEP Evaluation), or by modelling limitations (typically derived in Section 4 of IRPhEP Evaluation).

Equation 2.3-19 reduces to:

$$SI_{Be} = SI_{MM} \cdot \frac{R}{C} + B_{SL}, \qquad 2.3\text{-}20$$

The ratio $\frac{R}{C}$ is defined as the bias-factor. Equation 2.3-20 can be generalized for a specific number of measurement bias as:

$$SI_{Be} = SI_{MM} \cdot B_{MM} + B_{SL}, \quad 2.3\text{-}21$$

$B_{MM} = \prod_{i=1}^{N_B} B_i$ is the total measurement method bias-factors , N_B is the total number of bias-factors applied to the measurement method, and B_i is the specific measurement method bias-factors. Bias in simplifications also includes the exclusion of the auxiliary devices to fix the device (foil, miniature fission chamber, etc.) in the reactor system if not modelled in the benchmark model.

Uncertainties in Biases

Bias-factors in the measurement methods is always the inverse of the ratio of two quantities. The numerator is the reference value while the denominator is the calculated quantity. Its uncertainty can be found by applying Equation 2.3-7 to its definition and assuming no correlations. The final result is given by:

$$\sigma_{B_{MM}} = \sqrt{((1/C) \cdot \sigma_R)^2 + ((R/C^2) \cdot \sigma_C)^2}, \quad 2.3\text{-}22$$

where σ_R and σ_C are respectively the uncertainties in the specific reference experiment and in the calculated correction factor.

The total uncertainty in benchmark simplification and computational limitations is given by:

$$\sigma_{B_{SL}} = \sqrt{\sigma_{B_S}^2 + \sigma_{B_L}^2}, \quad 2.3\text{-}23$$

where σ_{B_S} is the uncertainty in the bias from simplifications and σ_{B_L} is the uncertainty in the bias from computational limitations.

As a starting point, the following paragraph was taken from the *ICSBEP Uncertainty Guide* [2.3-6] and adapted for spectral index measurements:

The evaluator should strive for a reasonable balance between making the benchmark model amenable to calculation and keeping the total spectral index **uncertainty of the model as small as practical.** Obviously, simplifications that make the benchmark model easier to use tend to make it more attractive to reactor physicist analysts. However, each simplification introduces an additional benchmark-model bias and a correlated uncertainty contribution. The use of benchmark models to validate a reactor physics analysis or to identify weaknesses in cross section data and calculational methods is more effective and reliable if the uncertainties are small. The only stage in the evaluation process where the evaluator legitimately can influence the magnitude of the total uncertainty is in deciding what simplifications to make to create the benchmark model. The **benchmark-model** is the best estimate of the value of spectral index that would be observed for an isolated experiment having exactly the geometry and materials described in the benchmark model. Thus one should aim at developing a benchmark model of the experiment which is simultaneously pragmatic for further evaluator's use, computationally not too demanding and free of major computational biases. This means that constructing a model with a great level of detail, which has a negligible contribution to the total benchmark-model uncertainty but significantly increases the complexity of the model and associated computational time, is not advisable. Additionally the evaluator should construct a benchmark-model including all parts of experiment that could potentially lead to the introduction of major spectral index biases, if not modelled. In the opposite case a rigorous study of the effect of the benchmark-model simplification on the computed spectral index should be performed.

Uncertainties in Benchmark Models

The uncertainties in the spectral index reaction rate benchmark model values are composed of three major parts:

a) Uncertainties in measurement method,
b) Uncertainties in biases,
c) Uncertainty from the facility and device parameters.

These three components are combined quadratically in order to get the whole benchmark uncertainty. The final benchmark uncertainty for the spectral index measurement method is given by:

$$\sigma_{SI_{MM}}^{Be} = \sqrt{\left(\sigma_{SI_{MM}} \cdot B_{MM}\right)^2 + \left(SI_{MM} \cdot \sigma_{B_{MM}}\right)^2 + \left(\sigma_{B_{SL}}\right)^2 + (\sigma_{PF})^2}\ , \qquad 2.3\text{-}24$$

where $\sigma_{SI_{MM}}^{Be}$ is the spectral index benchmark uncertainty for the measurement method MM, $\sigma_{B_{SL}} = \sqrt{\sigma_{B_S}^2 + \sigma_{B_L}^2}$, σ_{B_S} is the uncertainty in the bias from simplifications, σ_{B_L} is the uncertainty in the bias from limitations and σ_{PF} is the total uncertainty of the geometry and materials.

Table 2.3-5a shows a summary table listing the uncertainties, typical values, and minimum – maximum range of values that are considered bounding.

Table 2.3-5a. Summary of uncertainties and bounding values for benchmark models of thermal reactors

Source of Uncertainty	Typical Value (%)	Minimum Value (%)	Maximum Value (%)
Spectral Indices Measurement (SI)	3.0	0.5	5.0
Facility and Device Parameters	0.5	0.1	3.0
Benchmark model	4.0	1.2	7.0

Tables 2.3-5b and 2.3-5c show, respectively summary tables for F9/F5 and C8/F5 measured with the activation method and the fission chambers in fast spectra. Here C8 stands for capture rates in ^{238}U. Table 2.3-5c shows a summary table for C8/F9 measured with the activation method and the fission chambers in fast spectra. Uncertainties of Spectral Indices Measurement (SI) are taken from Tables 2.3-2b and 2.3-2c. The major contribution to the uncertainty of the Facility and Device Parameters come from uncertainty in the placement of fission chamber in the assembly.

Table 2.3-5.b. Summary of uncertainties and bounding values for benchmark models of fast reactors (F9/F5)

Sources of Uncertainty	Typical Value (%)	Minimum Value (%)	Maximum Value (%)
Spectral Indices Measurement (SI)	2.0	1.0	3.0
Facility and Device Parameters	0.5	Negligible	1.5
Benchmark model	2.0	1.0	3.5

Table 2.3-5.c. Summary of uncertainties and bounding values for benchmark models of fast reactors (C8/F5)

Source of Uncertainty	Typical Value (%)	Minimum Value (%)	Maximum Value (%)
Spectral Indices Measurement (*SI*)	2.5	1.0	4.0
Facility and Device Parameters	2.0	Negligible	4.0
Benchmark model	3.0	1.0	5.0

For non-basic nuclides the uncertainties of the measurements with absolute fission chambers are higher because of uncertainty in the mass of fissile deposits.

Uncertainties in Benchmark Model for Time-of-Flight

Table 2.3-6 shows summary table listing the uncertainties, typical values, and minimum – maximum range of values that are considered bounding for the neutron spectrum employing the Time-of-Flight (TOF) technique.

Table 2.3-6. Summary of uncertainties and bounding values for benchmark models for neutron spectrum

Sources of Uncertainty	Typical Value (%)	Minimum Value (%)	Maximum Value (%)
Perturbation of the neutron spectrum by the beam hole	5	5	10
Dependence of the neutron spectrum on the degree of sub-criticality	2	1	3
Total Uncertainty of the Benchmark Model	10	7	20

2.3.4 Practical Examples

This section considers some examples of the determination of the spectral indices: miniature fission chambers and the foil activation methods. Detailed examples of the determination of the spectral indices employing fuel rod scanning can be found in References 2.3-7 and 2.3-9.

Example 2.3-1: Determination of Spectral Indices Using Miniature Fission Chambers

The equations and the notations in this example are those used by CEA and do not exactly correspond to those of Section 2.3. CEA notations are kept to maintain consistency with the original documentation.

Roughly one hundred fission chambers of various types (fissile or fertile, with a diameter of ∅1.5, 4, 8 or 10mm) are available at EOLE, which can be used to characterise the spectrum at an area in the core. By taking ^{235}U, ^{238}U, ^{239}Pu, ^{242}Pu, and ^{237}Np as examples, the following spectral indices, among others, can be deduced:

- ^{238}U(n,f)/^{235}U(n,f)
- ^{239}Pu(n,f)/^{235}U(n,f)
- ^{237}Np(n,f)/^{239}Pu(n,f)
- ^{242}Pu(n,f)/^{239}Pu(n,f)

and all the other possible variants.

Basic Principle

The general expression of a spectral index employing miniature fission chamber of an isotope '*a*' relative to an isotope '*r*' is:

$$SI_r^a = \frac{{}^{Cont_a}/_{Cont_r}}{\left({}^{Cont_a}/_{Cont_r}\right)_c} B_{c,r} - B_{i,r} \qquad \text{(E2.3-1.1)}$$

where:

- SI_r^a is the spectral index,
- $B_{c,r} = \left(\frac{N_a^c}{N_a}\frac{\sigma_a^c}{\sigma_r^c} + \sum_{i\neq a}\frac{N_i^c}{N_a}\frac{\sigma_i^c}{\sigma_r^c}\right)$,
- $B_{i,r} = \sum_{i\neq a}\frac{N_i}{N_a}\frac{\overline{\sigma}_i}{\overline{\sigma}_r}$,
- $Cont_a/Cont_r$ is the ratio of count rates of the chamber 'a' to that of chamber 'r',
- $(Cont_a/Cont_r)_c$ is the same ratio in a reference spectrum (for example in a thermal column),
- N_a^c/Na represents the decay correction since the measurement in the reference spectrum (particularly the change due to decay, ^{238}Pu and ^{241}Pu),
- σ_a^c/σ_r^c is the relationship of cross-sections averaged in the reference spectrum,
- $\sum_{i\neq a}\frac{N_i^c}{N_a}\frac{\sigma_i^c}{\sigma_r^c}$ represents the contributions of impurities in the reference spectrum,
- $\sum_{i\neq a}\frac{N_i}{N_a}\frac{\overline{\sigma}_i}{\overline{\sigma}_r}$ represents the contributions of impurities during measurement.

The associated uncertainties depend greatly on the type of chamber used. They vary from 2% to nearly 10% for fertile fission chambers (^{238}Pu or ^{242}Pu lined).

Some examples

1. ^{239}Pu/ ^{235}U Spectral Index

^{239}Pu/ ^{235}U becomes the simplest case with both chambers assumed to be isotopically pure. In this case, the general expression reduces to:

$$SI_{235}^{239} = \frac{Cont_9/Cont_5}{(Cont_9/Cont_5)_c}\cdot\frac{\sigma_9^c}{\sigma_5^c}, \qquad \text{(E2.3-1.2)}$$

where SI_{235}^{239} is the ^{239}Pu/ ^{235}U spectral index. Defining $C = \frac{C_9/C_5}{(C_9/C_5)_c}$ and $R_\sigma = \frac{\sigma_9^c}{\sigma_5^c}$, the uncertainties in this case are expressed as:

$$\left(\frac{\sigma_{SI_{235}^{239}}}{SI_{235}^{239}}\right)^2 = \left(\frac{\sigma_C}{C}\right)^2 + \left(\frac{\sigma_{R_\sigma}}{R_\sigma}\right)^2 \quad \text{(E2.3-1.3)}$$

2. $^{237}Np/^{239}Pu$

In the ^{237}Np chamber, there can be no thermal column calibration, so the spectral index must be derived from calibrations in a fast spectrum. In this case, the count-rate ratio in the spectrum of interest is:

$$SI_{a,r} = \frac{k_{a(N_a\bar{\sigma}_a + \sum_{i\neq a} N_i\bar{\sigma}_i)}}{k_{rN_r\bar{\sigma}_r}} \quad \text{(E2.3-1.4)}$$

where k is the efficiency of the chambers.

Replacing the kN products by the effective masses yields the following relationship for the general spectral index

$$SI_{a,r} = \frac{m_r}{m_a}\frac{A_a}{A_r}(Cont_a/Cont_a) - \sum_{i\neq a}\frac{N_i}{N_a}\frac{\bar{\sigma}_i}{\bar{\sigma}_r} \quad \text{(E2.3-1.5)}$$

For the ^{237}Np chamber, $N_i = 0$, therefore:

$$SI_{a,r} = \frac{m_r}{m_a}\frac{A_a}{A_r}\frac{Cont_a}{Cont_r} \quad \text{(E2.3-1.6)}$$

where m_r, m_a are the effective masses and M_r, M_a are the atomic masses (239 and 237 respectively).

The uncertainty is simply calculated from the following:

$$\left(\frac{\sigma_{SI_{a,r}}}{SI_{a,r}}\right)^2 = \left(\frac{\sigma_{Cont_a}}{Cont_a}\right)^2 + \left(\frac{\sigma_{Cont_r}}{Cont_r}\right)^2 + \left(\frac{\sigma_{M_r}}{M_r}\right)^2 + \left(\frac{\sigma_{M_a}}{M_a}\right)^2 + \left(\frac{\sigma_{A_r}}{A_r}\right)^2 + \left(\frac{\sigma_{A_a}}{A_a}\right)^2 \quad \text{(E2.3-1.7)}$$

As a first example, consider the utilization of the calibrated miniature fission chambers to measure the ^{239}Pu/^{235}U and ^{237}Np/^{239}Pu spectrum indices in the IPEN/MB-01 research reactor facility. These experiments were carried out by IPEN and CEA teams in October 2007. The analyses of the results are performed subsequently. The details of the miniature fission chambers employed in the experiments to measure the spectral indices are shown in Table E2.3-1.1. The effective masses and uncertainties are given for the 0.4R channel.

Table E2.3-1.1. Description of the experimental miniature fission chambers

	^{235}U n°888	**^{239}Pu n°809**	**^{239}Pu n°811**	**^{237}Np n°812**
CM[(a)] (µg)	140.965	161.73	152.981	367.73
σ_{CM} (%)	2.40 %	2.20 %	2.20 %	2.70 %
Atomic Mass	235.0392	239.05216		237.048167

(a) CM stands for Calibrated Mass

The monitor fission chambers employed in the experiments were ^{235}U FC n°1104 and n°954. They are usually utilized respectively for the doubling time measurement and power calibration. They were positioned in an asymptotic position, at the core periphery.

Figure E2.3-1.1 shows the reactor configuration employed in the experiment. The miniature fission chambers were placed in the grid core positions B04 (Monitor FC) and G15 (Experimental FC). The fuel rods at these positions were removed and in their place two aluminum tube, sealed at the bottom, with the miniature fission chambers inside were positioned. The aluminum tubes were utilized to avoid the contact between miniature chamber and the moderator water. The miniature fission chambers were positioned at the central axial position of the active core.

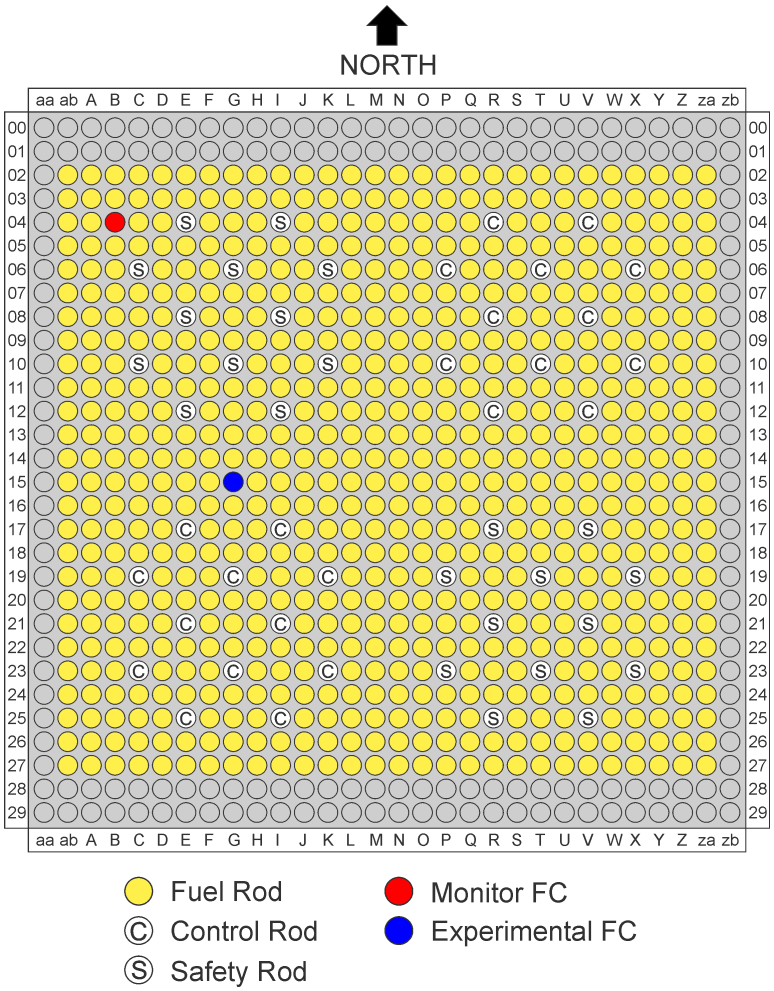

Figure E2.3-1.1. Experimental IPEN/MB-01 core configuration

The IPEN/MB-01 reactor operated at 10 W for the ^{239}Pu/^{235}U fission spectrum index experiments and at 30 W for the ^{237}Np /^{239}Pu case. Six distinct operations were performed since the monitors, the ^{235}U, and the ^{239}Pu fission chambers had to be changed. Table E2.3-1.2 synthesizes the results of all operations. The integral spectrum given by the miniature fission chambers is at 0.4R threshold.

Table E2.3-1.2. Experimental results for all core configurations

	10W			**30W**		
	^{235}U n°888	**^{239}Pu n°809**	**^{239}Pu n°811**	**^{237}Np n°812**	**^{239}Pu n°809**	**^{239}Pu n°811**
Acquisition Time (s)	600	600	600	1000	200	200
Integral (cps/s)	4441	9822	9301	367	29671	28772
Monitor ^{235}U n°1104 (cps/s)	1718	1713	1723	5175	5189	5180
Monitor ^{235}U n°954 (cps/s)	3487	3477	3487	10239	10272	10275

The spectral index is given by Equations 2.3-1 through 2.3-3 (Section 2.3.1). These equations were rewritten in a single equation for the case of the miniature fission chambers as:

$$SI_{235}^{239} = \frac{m_{235}}{m_{239}} \cdot \frac{M_{239}}{M_{235}} \cdot \frac{Cont_{239}}{Cont_{235}} \cdot \frac{Mon_{235}}{Mon_{239}}, \qquad \text{E2.3-1.8}$$

where the subscripts 239 and 235 stand, respectively, for ^{239}Pu and ^{235}U fission chambers, $Cont_i$ (i stands for either 239 or 235) is the miniature fission chamber i counts, and Mon_i stands for monitor i counts. The monitors were always ^{235}U. The notation Mon_{239} means the counts of the ^{235}U monitor in the ^{239}Pu fission chamber experiment.

In Equation E2.3-1.8, the normalization factor F_{norm} was taken care by the ratio of the monitor counts. F_T was essentially 1.0 due to the very good temperature homogenization control of the IPEN/MB-01 reactor. The experiment temperature was set at 20.0 ℃.

The uncertainty analysis can be carried out employing Equation 2.3-8 through 2.3-10 (Section 2.3.1). These equations were also combined into a single equation. Employing the same notation as in Equation E2.3-1.8, one has:

$$\sigma_{SI_{235}^{239}} = SI_{235}^{239} \cdot \sqrt{\left(\frac{\sigma_{m_{235}}}{m_{235}}\right)^2 + \left(\frac{\sigma_{m_{239}}}{m_{239}}\right)^2 + \left(\frac{\sigma_{Cont_{239}}}{Cont_{239}}\right)^2 + \left(\frac{\sigma_{Cont_{235}}}{Cont_{235}}\right)^2 + \left(\frac{\sigma_{Mon_{239}}}{Mon_{239}}\right)^2 + \left(\frac{\sigma_{Mon_{235}}}{Mon_{235}}\right)^2}, \qquad \text{E2.3-1.9}$$

where the uncertainty in the atomic mass has been neglected and the uncertainty in the detector counts was taken equal to their square root of their counts.

The final results for the spectral indices $\frac{^{239}Pu}{^{235}U}$ are shown in Table E2.3-1.3.

Table E2.3-1.3. Experimental results for the $\frac{^{239}Pu}{^{235}U}$ spectral index

Monitor	^{239}Pu/^{235}U		
	Pu9 N°809	**Pu9 N°811**	**Average**
U5-1104	1.966 ± 0.065	1.967 ± 0.065	1.967 ± 0.065
U-954	1.966 ± 0.065	1.963 ± 0.065	1.965 ± 0.065
		Total	1.966 ± 0.065

Similarly for the case of $\frac{^{237}Np}{^{239}Pu}$, this spectral index can be written as:

$$SI\left(\frac{^{237}Np}{^{239}Pu}\right) = \frac{m_{239}}{m_{237}} \cdot \frac{M_{237}}{M_{239}} \cdot \frac{Cont_{237}}{Cont_{239}} \cdot \frac{Mon_{239}}{Mon_{237}}, \qquad \text{E2.3-1.10}$$

and its uncertainty is given by:

$$\sigma_{SI_{239}^{237}} = SI_{239}^{237} \cdot \sqrt{\left(\frac{\sigma_{m_{239}}}{m_{239}}\right)^2 + \left(\frac{\sigma_{m_{237}}}{m_{237}}\right)^2 + \left(\frac{\sigma_{Cont_{239}}}{Cont_{239}}\right)^2 + \left(\frac{\sigma_{Cont_{237}}}{Cont_{237}}\right)^2 + \left(\frac{\sigma_{Mon_{239}}}{Mon_{239}}\right)^2 + \left(\frac{\sigma_{Mon_{237}}}{Mon_{237}}\right)^2}, \qquad \text{E2.3-1.11}$$

The final results for this spectral index are shown in Table E2.3-1.4.

Table E2.3-1.4. Experimental results for the $\frac{^{237}Np}{^{239}Pu}$ spectral index

Monitor	^{237}Np/^{239}Pu		
	Pu9 N°809	**Pu9 N°811**	**Average**
U5-1104	5.41E-03 ± 0.18E-03	5.55E-03 ± 0.18E-03	5.48E-03 ± 0.18E-03
U5-954	5.41E-03 ± 0.18E-03	5.58E-03 ± 0.18E-03	5.50E-03 ± 0.18E-03
		Total	5.49E-03 ± 0.18E-03

The results shown in Tables E2.3-1.3 and E2.3-1.4 do not contain the uncertainty contributions of the experimental configuration and, in this case, the benchmark value and its corresponding uncertainties are given in the line labelled Total.

Example 2.3-2: Determination of Spectral Indices Using Foil Activation Techniques

Consider as a second example the determination of the spectral indices: ^{45}Sc(n,γ)/^{115}In(n.n´) and ^{24}Mg(n,p)/^{115}In(n.n´) employing the foil activation technique. These experiments were performed in the IPEN/MB-01 research reactor facility. All foils were irradiated in its central core region at 100W. The details of the foils employed in the experiments are shown in Table E2.3-2.1.

Table E2.3-2.1. Foil description for the determination of the spectral indices

Foil	Mass (g)	Radius (cm)	Thickness (cm)	Nuclear Reaction	Abundances (Target Nuclide)
In	0.2134 ± 0.0001	0.4245 ± 0.0001	0.0516 ± 0.0001	^{115}In(n,n')^{115m}In	0.9571 ± 0.0005
Sc	0.0173 ± 0.0001	0.4245 ± 0.001	0.0127 ± 0.0001	^{45}Sc(n,γ)^{46}Sc	1.0
Mg	0.0483 ± 0.0001	0.4000 ± 0.0001	0.0553 ± 0.0001	^{24}Mg(n,p)^{24}Na	0.7899 ± 0.0004

The reaction rates were obtained similarly to the example of ^{115}In(n,n')^{115m}In shown in Section 2.7.3. The results are shown in Table E2.3-2.2.

Table E2.3-2.2. Experimental reaction rates

Foil	Reaction Rate (RR) (Reactions/second)	N0 (number of Target Nuclei)	Reaction Rate per atom (RR/N0)	Power Monitor (cps[(a)])	Nuclear Reaction
In	1.762E+05 ± 2.5E+03	1.070E+21	1.646E-16 ± 2.3E-18	37687	$^{115}In(n,n')^{115m}In$
Sc	3.579E+08 ± 4.2E+06	1.340E+22	2.672E-14 ± 3.1E-16	37306	$^{45}Sc(n,\gamma)^{46}Sc$
Mg	1.150E+03 ± 37	9.569E+20	1.202E-18 ± 3.9E-20	37335	$^{24}Mg(n,p)^{24}Na$

(a) Counts per second

The power normalization factors as well as the benchmark spectral indices are given in Table E2.3-2.3. The uncertainty in the power detector monitor counts was taken equal to their square root. F_T was essentially 1.0 due to the very good temperature homogenization control of the IPEN/MB-01 reactor. The experiment temperature was set at 20.0 °C.

Table E2.3-2.3. The experimental spectral indices

	Power normalization F_{norm}	Spectral Indices
$^{45}Sc(n,\gamma)/^{115}In(n,n')$	1.01 ± 0.01	1.64E+02 ± 3.0
$^{24}Mg(n,p)/^{115}In(n,n')$	1.01 ± 0.01	7.37E-03 ± 2.6E-04

The results shown in Table E2.3-2.3 do not contain the uncertainty contributions of the facility parameters and in this case the benchmark value and its corresponding uncertainties are the experimental spectral indices shown in this table.

Example 2.3-3: Correction Factors due to FC Structure and Connectors

MFCs are usually made of titanium parts and a connector allows plugging them on organic coaxial cables. As they are not watertight, they can only be used in air channels. They come in two outer diameters depending on the amount of fissile material required for the measurement: Ø4 mm (CF4) for less than 200 µg of fissile coating or Ø8 mm (CF8R or CF8Rgr) for coatings up to a few mg. Detectors active length are respectively 10 mm and 24 mm. CF8Rgr is a new detector design that allows putting two fissile deposits, one on each electrode. The gap between electrodes is also reduced in order to improve charge collection. Their cross section is given on Figure E2.3-3.1.[2.3-10]

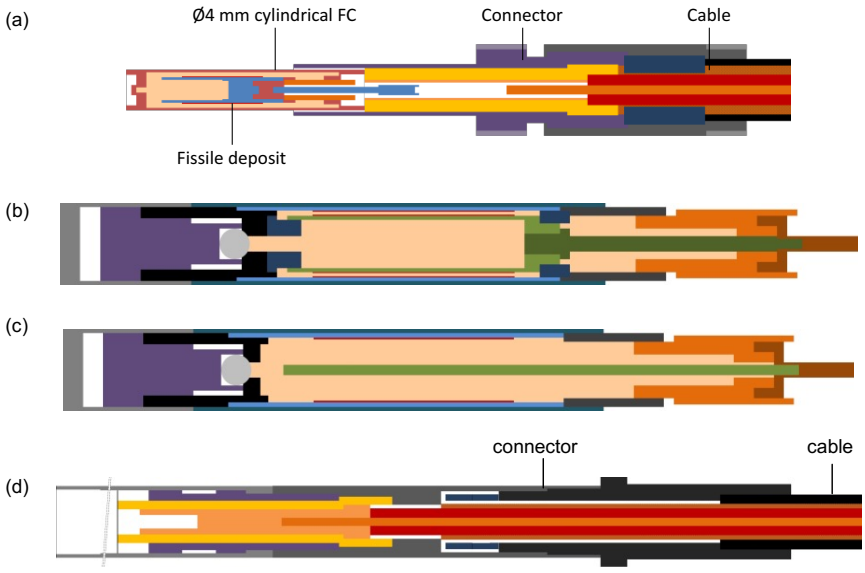

Figure E2.3-3.1. Drawings used for the MC modeling of the CF4 with connector and cable (a), CF8Rgr (b), CF8R (c) and their connector and organic cable (d). Signal cables are shielded cables with copper core, polyethylene insulator, copper shield and plastic jacket.

Although MFCs are small and made of materials that slightly interact with neutrons, it is known that the transmission cable conveying the signal to the electronic module (detector, connector and signal cable) has a local effect on the neutron flux as well as a global effect on the core reactivity. The impact on the measured fission rate is negative (i.e. the observed fission rate is lower than the unperturbed fission rate).

Our main objective is to quantify this effect on the observed fission rate in order to correct it as efficiently as possible. A parameter study is required because the effect is expected to vary greatly depending on several parameters: detector design (geometry, materials), neutrons energy spectrum and fissile isotopes in the fissile coating.

In order to quantify and correct any effect on fission rates, it is possible to make use of Monte Carlo calculations using a precise modeling of the detector and its close environment. Correction factors for various fissile isotopes and neutron spectra can then be determined with high fidelity.

To assess the method, a simplified calculation route is compared to a whole core calculation in the case of the MINERVE reactor in the MAESTRO configuration [2.3-11], representative of a light water reactor (LWR) UO_2 spectrum.

A complete Monte Carlo modeling of MFCs is performed, associated to JEFF3.1 library to model the detectors based on the schematics shown in Figure E2.3-3.1. 3D Models were constructed very precisely and include as few approximations as possible in order to allow sensitivity studies. However, some simplifications were introduced for complex parts such as threads and feed-through, but materials masses were conserved. Actual materials were modeled but only by introducing the most significant alloy grades (for instance only stainless steel grade is used for all stainless steel components). It is to be noted that the fissile deposit is not included in the model because its mass and thickness are very small (typically 1 mg and 1 µm). It has been shown that there is no neutron self-shielding inside the fissile deposit

Three neutron fission spectra are considered in the study (see Figure E2.3-3.2). The so-called thermal spectrum corresponds to the spectrum obtained in the thermal cavity of the BR1 reactor. It is very

close to a purely Boltzmann spectrum at 300 K (maximum at 26 meV). MARK3 spectrum is the reference spectrum used for fission chambers calibration [2.3-12].

Finally, MAESTRO spectrum is obtained at the center of the MINERVE reactor in the MAESTRO configuration. This mixed energy spectrum is very close to the one of a PWR at nominal power. The proportion of thermal neutron flux (below 1 eV) is 15 %, epithermal neutron flux represent 39 % and fast neutron fluxes (energy above 0.1 MeV) is 45 % of the total neutron flux.

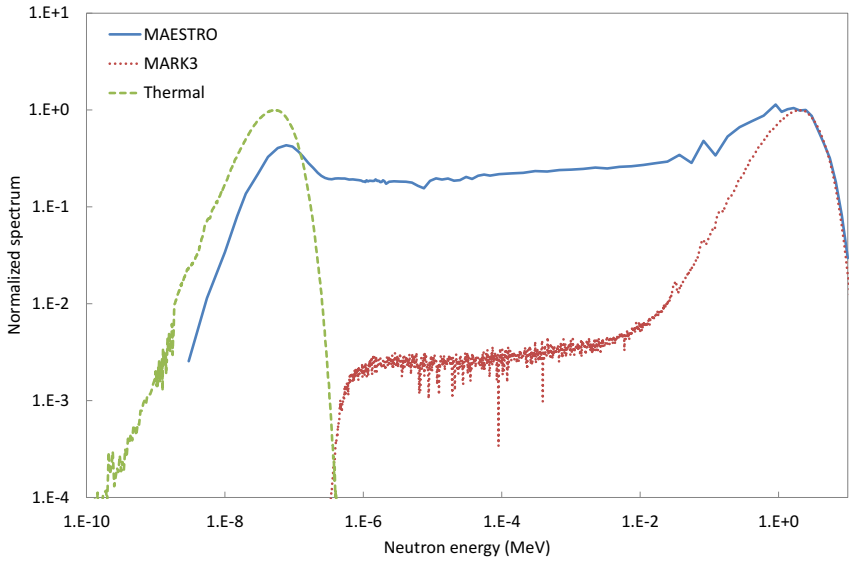

Figure E2.3-3.2. Neutron flux spectra (normalized to 1) used in the case study: thermal (BR1 cavity, green dashed line), mixed spectrum (MINERVE experimental zone, blue solid line) and reference spectrum for MFCs calibration (MARK3, red dots*)*

Correction Factors

Correction factors are computed based on two calculation results. The first one, without the detector, is basically a calculation of the infinite dilution integral fission rate. The second one is obtained with the entire detector geometry. Let R be the fission rate, S the neutron spectrum, x the fissile isotope and D refer to the detector geometry. A correction factor is expressed as:

$$f(x,S,D) = \frac{R_D(x,S)}{R(x,S)} - 1 \qquad \text{(E2.3-3.1)}$$

The factor uncertainty is given by the calculation standard deviation. As the standard deviation CV (in %) is the same for the two calculations, the final uncertainty is CV*√2.

Tables E2.3-3.1 to E2.3-3.3 give the corrections factors for thermal, MARK3 and MAESTRO fission rates respectively. Among the fissile isotopes tested, two are widely used to measure thermal neutron flux: ^{235}U and ^{239}Pu. The others are fertile isotopes sensitive to fast neutrons: ^{238}U, ^{237}Np, ^{238}Pu, ^{240}Pu, and ^{242}Pu. Although in practice, one has to take into account impurities in the fissile deposit, only pure isotopes are considered here. In the following tables, standard deviation uncertainties are given at 1 standard deviation.

Table E2.3-3.1. Correction factors (in percent) for fission rates and for various fissile isotopes in the case of a thermal neutron spectrum

Isotope	CF4		CF8R		CF8Rgr	
	Factor	CV	Factor	CV	Factor	CV
U-235	-3.7 %	0.2 %	-6.4 %	0.1 %	-8.3 %	0.1 %
U-238	-3.7 %	0.2 %	-6.4 %	0.1 %	-8.1 %	0.1 %
Np-237	-3.8 %	0.2 %	-6.3 %	0.1 %	-8.3 %	0.1 %
Pu-238	-3.9 %	0.2 %	-6.4 %	0.1 %	-8.5 %	0.1 %
Pu-239	-3.6 %	0.2 %	-6.6 %	0.1 %	-7.8 %	0.1 %
Pu-240	-3.6 %	0.2 %	-6.0 %	0.1 %	-7.9 %	0.1 %
Pu-242	-3.7 %	0.2 %	-6.1 %	0.1 %	-8.1 %	0.1 %

Table E2.3-3.2. Correction factors (in percent) for various fissile isotopes in the case of a fast neutron spectrum (MARK3)

Isotope	CF4		CF8R		CF8Rgr	
	Factor	CV	Factor	CV	Factor	CV
U-235	0.0 %	0.4 %	0.2 %	0.4 %	0.1 %	0.4 %
U-238	-0.7 %	0.2 %	-1.1 %	0.2 %	-1.1 %	0.2 %
Np-237	-0.3 %	0.1 %	-0.4 %	0.2 %	-0.4 %	0.1 %
Pu-238	-0.2 %	0.2 %	-0.3 %	0.2 %	-0.2 %	0.2 %
Pu-239	-0.1 %	0.7 %	0.1 %	0.7 %	-0.1 %	0.7 %
Pu-240	-0.3 %	0.1 %	-0.4 %	0.2 %	-0.4 %	0.1 %
Pu-242	-0.3 %	0.1 %	-0.3 %	0.2 %	-0.4 %	0.1 %

Table E2.3-3.3. Correction factors for various fissile isotopes in the case of a mixed neutron spectrum
(MAESTRO configuration in MINERVE reactor)

Isotope	CF4		CF8R		CF8Rgr	
	Factor	CV	Factor	CV	Factor	CV
U-235	-2.5 %	0.2 %	-3.9 %	0.3 %	-6.1 %	0.3 %
U-238	-0.5 %	0.2 %	-0.9 %	0.3 %	-1.1 %	0.3 %
Np-237	-0.2 %	0.1 %	-0.3 %	0.2 %	-0.4 %	0.2 %
Pu-238	-1.4 %	0.2 %	-2.3 %	0.4 %	-3.4 %	0.4 %
Pu-239	-1.9 %	0.2 %	-3.1 %	0.4 %	-4.9 %	0.4 %
Pu-240	-0.3 %	0.2 %	-0.4 %	0.3 %	-0.5 %	0.3 %
Pu-242	-0.2 %	0.1 %	-0.3 %	0.2 %	-0.4 %	0.2 %

As expected, our results show huge differences depending on the isotope and the neutron spectrum. First, correction factors are all negative, which indicates that the observed fission rate is smaller than the real one without the detector perturbation.

As shown in the last three tables, corrections factors tend to be much larger when calculated in the thermal spectrum case. For all MFC types, it is observed that the factors are constant whatever the

fissile isotope. This is due to the fission cross sections that all exhibit a 1/v behavior in the thermal energy range. Note that it is not possible to observe experimentally this effect in the case of fertile isotopes because of the very low cross section in the thermal part. The decrease in fission rates comes obviously from the absorption of neutrons by radiative capture in the detector itself and other parts of the measurement line. The effect is worth -3.8 % for the CF4 geometry, -6.4 % for the CF8R geometry and down to -8.3 % for the CF8Rgr geometry on an average.

Results are completely different in the case of a fast neutron spectrum (MARK3). Indeed, correction factor are below 1% in most cases, and very often the effect is negligible (see Table E2.3-3.2. Nonetheless the ^{238}U fission rate should be corrected, as the estimated correction factor is the highest (down to -1.1% in the CF8Rgr case). The effect in this case is related to the neutron scattering in the detector parts and because ^{238}U has the highest energy cutoff, it is the most affected by scattering. This is shown on Table E2.3-3.2. All fertile isotopes are affected to a lesser extent. It is to be noted that these corrections factors have been taken into account in the calibration method to provide unbiased results.

Results obtained in the case of a mixed neutron spectrum (MAESTRO configuration in MINERVE) are given in Table E2.3-3.3. One can see that correction factors are very different from one isotope to the other. On the one hand, fertile isotopes are not affected in the MAESTRO case. The sole exception is again ^{238}U, which correction factor ranges from -0.5 % to -1 %, i.e. similar to the correction obtained for the MARK3. On the other hand, thermal isotopes behave like in the thermal spectrum case. Differences in the correction factors (around -2.5 % for ^{235}U CF4 detectors) are likely to come from the fact that the thermal component in the MAESTRO spectrum is less thermal than the Boltzmann spectrum due to neutron absorption by the water.

In order to better understand which part of the measurement line causes the effect on the fission rate, several calculations were performed by adding step by step the detector, the connector and the signal cable. Calculations were performed in the simplified geometry and with the MAESTRO neutron spectrum.

Results are given in Table E2.3-3.4. **Error! Reference source not found.** One can observe that the chamber itself is responsible for the whole neutron effect on the fission rate. Even though the connector is very large in the case of CF8R and CF8Rgr geometries, it does not affect the fission rate on the fissile deposit that is located a few cm below.

This is also true for the signal cable: no direct effect can be seen on the fission rate measurement. So, one important conclusion is that the connector and cable can be removed from the experiment modeling as it does not impact the fission rate calculations at the location of the fissile deposit. Indirect neutron effect could still occur because of the local reactivity effect of the whole measurement line. In particular, absorption in the cable could decrease the fission rate of close fuel elements. This would lead to an indirect decrease of the measured fission rate.

Table E2.3-3.4. Correction factors (in percent) in different measurement configurations (Standard deviation is around 0.3%.)

Isotope	Geometry	All	Chamber + Connector	Chamber alone	Connector alone	Cable alone
U235	CF4	-2.6 %	-2.6 %	-2.5%	-0.1%	0.0%
	CF8R	-4.1 %	-4.2 %	-4.1%	-0.1%	0.0%
	CF8Rgr	-6.5 %	-6.5 %	-6.2%	-0.1%	0.0%
U238	CF4	-0.6 %	-0.6 %	-0.5%	-0.1%	-0.1%
	CF8R	-0.9 %	-0.9 %	-0.9%	-0.0%	0.0%
	CF8Rgr	-1.1 %	-1.0 %	-0.9%	-0.1%	0.0%
Np237	CF4	-0.3 %	-0.2 %	-0.1%	-0.1%	0.0%
	CF8R	-0.3 %	-0.3 %	-0.3%	0.0%	0.0%
	CF8Rgr	-0.4 %	-0.3 %	-0.3%	0.0%	0.0%

So, structure correction to particular spectral indices measured in thermalized spectra can lead to non-negligible modification of the raw signal processing, even if impurity corrections have already been taken into account.

Example 2.3-4: The Special Case of $^{28}\rho$ and $^{25}\delta$

The spectral indices $^{28}\rho$ and $^{25}\delta$ constitute a special case. They are normally measured employing the foil activation technique. These spectral indices are defined as:

$$SI = \frac{\int_{0.625eV}^{20MeV} \int_V \int_{4\pi} \sigma(E).\Phi(r,E,\Omega) dV dE d\Omega}{\int_0^{0.625eV} \int_V \int_{4\pi} \sigma(E).\Phi(r,E,\Omega) dV dE d\Omega} \qquad \text{E2.3-4.1}$$

where SI represents either $^{28}\rho$ or $^{25}\delta$, $\sigma(E)$ is either the ^{238}U capture cross section for the $^{28}\rho$ case or the ^{235}U fission cross section for the $^{25}\delta$ case, $\Phi(r,E,\Omega)$ represents the neutron angular flux at position, $\vec{r}$ energy E, and direction $\vec{\Omega}$, and V is the foil volume. The volume integral is performed in the foil space domain. In the definition of $^{28}\rho$ or $^{25}\delta$, the thermal energy cut-off is 0.625 eV.

The measurements of $^{28}\rho$ or $^{25}\delta$ are performed employing dismountable fuel rods containing uranium foils in its interior. The uranium foils are sandwiched with aluminium foils in order to prevent contamination of fission product or ^{239}Np from the fuel pellet. Usually, two distinct irradiations are performed; one without the cadmium sleeve and the other with the cadmium sleeve. The fuel rod at the foil position is wrapped with a cadmium sleeve. After irradiation the dismountable fuel rod is dismounted and the uranium foil is removed and taken to the HPGe detector to get the gamma counts as a function of decay time. The determination of the ^{238}U(n,γ) or ^{235}U(n,f) reaction rates follow the procedure extensively discussed in Section 2.7.1. The measurements are performed in the asymptotic region of the reactor. In the majority of cases highly enriched uranium foil is used for the $^{25}\delta$ case and depleted uranium foil is used for $^{28}\rho$. Some works [2.3-8, 2.3-9, and 2.3-14] considered the fuel rod scanning technique to get these special spectral indices.

The measured spectral indices $^{28}\rho$ or $^{25}\delta$ are given by:

$$SI = SI^*.F_{corr}, \quad \text{E2.3-4.2}$$

where SI represents either $^{28}\rho$ or $^{25}\delta$, SI^* is the perturbed spectral index and is given by:

$$SI^* = \frac{1}{R_{cd}-1}, \quad \text{E2.3-4.3}$$

R_{Cd} is either the cadmium ratio for the ^{238}U captures or for the ^{235}U fissions and it is given by:

$$R_{cd} = \frac{RR_{bare}}{RR_{cd}} \cdot F_{norm} \cdot F_T, \quad \text{E2.3-4.4}$$

RR_{bare} is the ^{238}U capture reaction rates or the ^{235}U fission reaction rates for the bare condition, i.e., the irradiation without the cadmium sleeve, RR_{Cd} is the ^{238}U capture or the ^{235}U fission reaction rates for the cadmium covered condition, i.e., the irradiation with the cadmium sleeve, F_{corr} [2.3-13] is the correction factor that has a twofold function. First, it transforms the perturbed spectral index into an unperturbed value. The perturbation in the reactor is due to the insertion of the uranium and aluminum foils inside of the dismountable fuel rod and due to introduction of the cadmium sleeve. Second, it transforms the cadmium cut-off energy to 0.625 eV.

The correction factor F_{corr} is calculated by employing a simplified model of the reactor. Usually an infinite array of fuel rods is considered [2.3-8 and 2.3-13].

The correction factor F_{corr} is defined as the ratio of the unperturbed spectral index to the perturbed value as:

$$F_{corr} = \frac{RR_{ep}/RR_{th}}{RR_{cd}/(RR_{bare}-RR_{cd})}, \quad \text{E2.3-4.5}$$

where:

$$RR_{ep} = \int_{0.625eV}^{20MeV} \int_V \int_{4\pi} \sigma(E).\Phi(r,E,\Omega) dV dE d\Omega \quad \text{E2.3-4.6}$$

is the epithermal reaction rate,

$$RR_{th} = \int_0^{0.625eV} \int_V \int_{4\pi} \sigma(E).\Phi(r,E,\Omega) dV dE d\Omega \quad \text{E2.3-4.7}$$

is the thermal reaction rate;

$$RR_{cd} = \int_0^{20MeV} \int_V \int_{4\pi} \sigma(E).\Phi^*(r,E,\Omega) dV dE d\Omega \quad , \quad \text{E2.3-4.8}$$

is the reaction rate in the uranium foils considering the presence of the uranium and aluminum foils and the cadmium sleeve,

$$RR_{bare} = \int_0^{20MeV} \int_V \int_{4\pi} \sigma(E).\Phi(r,E,\Omega) dV dE d\Omega, \qquad \text{E2.3-4.9}$$

is the reaction rate in the uranium foils considering the presence of uranium and aluminum foils only and $\Phi(r,E,\Omega)$ and $\Phi^*(r,E,\Omega)$ are, respectively, the neutron angular fluxes for the bare and for the cadmium covered cases.

The measured quantities for the determination of $^{28}\rho$ or $^{25}\delta$ are either the reaction rates in the highly enriched uranium foil in the case of $^{25}\delta$ or in the depleted uranium foil in the case of $^{28}\rho$.

Uncertainty Analysis for the Special Case of $^{28}\rho$ and $^{25}\delta$

The uncertainty analyses for $^{28}\rho$ and $^{25}\delta$ starts applying Equation 2.3-7 subsequently to Equations 2.3-4.2, 2.3-4.3, and 2.3-4.4 assuming that all variables are uncorrelated:

$$\sigma_{SI} = SI.\sqrt{\left(\frac{\sigma_{SI^*}}{SI^*}\right)^2 + \left(\frac{\sigma_{F_{corr}}}{F_{corr}}\right)^2} \qquad \text{E2.3-4.10}$$

where

$$\sigma_{SI^*} = \sqrt{\left(\frac{1}{(R_{cd}-1)}\right)^2 . \sigma_{R_{cd}}^{2\,2}}, \qquad \text{E2.3-4.11}$$

and

$$\sigma_{R_{cd}} = R_{cd}.\sqrt{\left(\frac{\sigma_{RR_{bare}}}{RR_{bare}}\right)^2 + \left(\frac{\sigma_{RR_{cd}}}{RR_{cd}}\right)^2 + \left(\frac{\sigma_{F_{norm}}}{F_{norm}}\right)^2 + \left(\frac{\sigma_{F_T}}{F_T}\right)^2}. \qquad \text{E2.3-4.12}$$

The uncertainty analyses described by Equations 2.3-4.10 through 2.3-4.12 apply to both $^{28}\rho$ and $^{25}\delta$ cases.

Example 2.3-5: Modified Conversion Factor

The modified conversion factor is a spectral index, but is particular in the sense that it does not use fission chambers but relies on the particular peak spectrometry technique. The modified conversion factor is defined as the ratio of ^{238}U radiative captures to the total fission rate in the fuel rod. It is mainly used in the MOX fuel rods.

$$Modified\ Conversion\ Factor = \frac{238\text{U Captures}}{Total\ Fissions} = \frac{C8}{F} \qquad \text{E2.3-5.1}$$

This definition is broader than that found in an all UO_2 core where the denominator is mainly the ^{235}U fission rate. This measurement is a post-irradiation measurement directly on the fuel rods.

The measurement is based on the detection of gamma peaks of two fission products: ^{143}Ce at 293.27 keV and ^{140}Ba at 537.31 keV, as well as ^{239}Np at 277.60 keV which characterises the capture rate of the ^{238}U through the reaction

$(^{238}U+n \rightarrow ^{239}U \xrightarrow{\beta^- 2.35min} ^{239}Np \xrightarrow{\beta^- 2.35days} ^{239}Pu)$.

This measurement requires the detection of low energy gamma rays, which requires the use of a high efficiency detector. The ^{140}La peak at 1,596 keV is used as power normalisation. It is shown in Section 2.7.1b that the ^{238}U capture rates and the total fission rates are given by the following expressions:

$$C8 = \frac{(\lambda_{U9}-\lambda_{Np}).N_{Np}}{g_{Np}.\eta_{Np}.f_{Np}.\frac{\lambda_{U9}}{\lambda_{Np}}.\left(1-e^{-\lambda_{Np}t_e}\right).e^{-\lambda_{Np}t_c}.\left(1-e^{-\lambda_{Np}t_m}\right)}, \text{ and} \quad \text{E2.3-5.2}$$

$$F = \frac{\lambda_p.C_{FP}}{Y_{FP}.I_{FP}.\eta_{FP}.f_{FP}.\left(1-e^{-\lambda_p t_e}\right).e^{-\lambda_p t_c}.\left(1-e^{-\lambda_p t_m}\right)}, \quad \text{E2.3-5.3}$$

which gives the final relationship for the modified conversion rate:

$$\frac{C8}{F} = \frac{\lambda_{U9}-\lambda_{Np}}{\lambda_P}.\frac{\lambda_{Np}}{\lambda_{U9}}.\frac{C_{Np}}{C_{FP}}.Y_{FP}.\frac{I_{FP}}{I_{Np}}.\frac{\eta_{FP}}{\eta_{Np}}.\frac{f_{FP}}{f_{Np}}.\frac{\left(1-e^{-\lambda_P.t_e}\right).e^{-\lambda_P.t_c}.\left(1-e^{-\lambda_P.t_m}\right)}{\left(1-e^{-\lambda_{Np}.t_e}\right).e^{-\lambda_{Np}.t_c}.\left(1-e^{-\lambda_{Np}.t_m}\right)} \quad \text{E2.3-5.4}$$

$$SI_{MCF} = \frac{C8}{F} \quad \text{E2.3-5.5}$$

The saturated count rates and the detection efficiencies are obtained from the procedures extensively discussed in Section 2.7. Fission yields, radioactive periods and gamma-ray emission probabilities can be extracted from the JEFF or ENDF/B nuclear data libraries. Finally, relative reaction rate calculations must be performed to estimate average fission yields and gamma self-shielding correction factor.

The Uncertainty Analysis for the Modified Conversion Factor

The uncertainty analyses for the Modified Conversion Ratio is obtained applying Equation 2.3-7 to Equation 2.3-5.5, assuming that all variables are uncorrelated:

$$\sigma_{\frac{C8}{F}} = \frac{C8}{F}\sqrt{\left(\frac{\sigma_{C8}}{C8}\right)^2 + \left(\frac{\sigma_F}{F}\right)^2} \quad \text{E2.3-5.6}$$

where the uncertainties in C8 and F are given in Section 2.7.1.

2.3.5 *References*

2.3-1 Brumbach, S.B. and D.W. Maddison, D.W. "Reaction Rate Calibration Techniques at ZPPR for 239pu Fission, 235U Fission, 238U Fission, and 238U Capture," ZPR-TM-424, June 10, 1982.

2.3-2 "Cross Section Evaluation Working Group Benchmark Specification," ENDF-202, BNL-19302, 1974.

2.3-3 Scholtyssek, W., et. al.: "IRMA: Interlaboratory Comparison of Fission and Capture Rate Measurement Techniques at MASURCA," Proc. of International Reactor Physics Conference, Jackson Hole, Wyoming, USA (Sept.1988).

2.3-4 Doulin, V.A., et. al.: "SFINX: Soviet-French Integral Experiment on Measuring the Capture and Fission at MASURCA and BFS," Proc. of International Reactor Physics Conference, Marseille, France (April 1990).

2.3-5 U.S. Guide to the Expression of Uncertainty in Measurement, ANSI/NCSL Z540-2-1997, p11.

2.3-6 V. F. Dean, "ICSBEP Guide to the Expression of Uncertainties," Rev. 5, September 30, 2008.

2.3-7 Kazanskij Yu. A., Vankov A.A., Inyutin E.I., "Neutron Spectrometry in Fast Reactor Physics," Atomic Energy Review, Vol. 13, No 4., International Atomic Energy Agency, Vienna 1975.

2.3-8 Bitelli, U.D. and Dos SANTOS, A. "The Spectral Indices of the IPEN/MB-01 Reactor: Measurements and Calculation," PHYSOR 2002, Seoul, Korea, October 7-10, 2002.

2.3-9 Dos Santos, A., Fanaro, L.C.C.B., Jerez, R., "The Experimental Determination and Evaluation of the Spectral Indices of the IPEN/MB-01 Reactor for the IRPhEP Project," Annals of Nuclear Energy 59. 126–138, 2013.

2.3-10 Geslot, B., et al., "Development and Manufacturing of Special Fission Chambers for In-core Measurement Requirements in Nuclear Reactors," ANIMMA 2009 (Proc. 1st International Conference on Advancements in Nuclear Instrumentation, Measurement Methods and their Applications, Marseille, France, 2009).

2.3-11 Leconte, P., et al., "MAESTRO: An Ambitious Experimental Programme for the Improvement of Nuclear Data of Structural, Detection, Moderating and Absorbing Materials - First Results for ^{nat}V, ^{55}Mn, ^{59}Co and ^{103}Rh," ANIMMA 2013 (3rd International Conference on Advancements in Nuclear Instrumentation, Measurement Methods and their Applications, Ghent, Belgium, 2013.

2.3-12 Lamirand, V., et al., "Miniature Fission Chambers Calibration in Pulse Mode: Interlaboratory Comparison at the SCKCEN BR1 and CEA CALIBAN Reactors," *IEEE Trans. Nucl. Sci.*, vol. 61, no. 4, pp. 2306–2311, Aug. 2014.

2.3-13 R. Sher and S. Fiarman, "Studies of Thermal Reactor Benchmark Data Interpretation: Experimental Corrections," EPRI NP-209, October 1976.

2.3-14 Dos Santos, A. et al., IPEN(MB01)-LWR- CRIT-COEF-KIN-RRATE-SPECT-POWDIS-RESR-001: Reactor Physics experiments in the IPEN/MB-01 Research Reactor Facility. International Handbook of Evaluated Reactor Physics Benchmark Experiments. NEA/NSC, 2012.

2.4 Reactivity Effects Measurements

2.4.1 *Uncertainties in Measurements*

Reactivity Considerations

Reactivity measurement in a nuclear reactor is by far the most common measurement performed in the Reactor Physics. By definition reactivity is the deviation from criticality. Although there are many mathematical definitions of reactivity (see for example the books of Henry [2.4-1] or Keepin [2.4-2]), the most commonly employed definition is given in terms of the effective multiplication factor (k_{eff}).

The reactivity (ρ or $\frac{\Delta k_{eff}}{k_{eff}}$) is defined in terms of this quantity by the following equation, although this is an approximation[2.4-3]:

$$\rho = \frac{k_{eff}-1}{k_{eff}} \qquad 2.4\text{-}1$$

From this equation, it may be seen that ρ may be positive, zero, or negative. The reactivity describes the deviation of an effective multiplication factor from unity**.**

Reactivity can further be classified as dynamic and static. The dynamic reactivity yields the correct flux transient, while the static reactivity increments add up to the correct critical state. In this way, these two reactivity concepts will affect their measurability and the analysis of measurements. The dynamic reactivity contains pronounced dynamic effects caused by delayed neutrons and continuous rod movements, for example. These two concepts of reactivity (static and dynamic) are required because in general, they give different results for a given measurement. The exception is for an initial stationary state, where static and dynamic reactivities are equal. Thus, neither one can be replaced by the other concept since they serve different purposes. The static reactivity describes the off-criticality of systems in steady, auxiliary states. Actual physical transitions between these auxiliary states are not contemplated because their consideration is conceptually unnecessary. In contrast, the dynamic reactivity is introduced to describe physical transitions between actual states of the reactor. The description of these actual transitions requires consideration of additional physical phenomena such as delayed neutrons and feedback effects, which are disregarded in static reactivity problems. More complete details about dynamic and static reactivity can be found in References [2.4-4] and [2.4-5].

Reactivity is not a quantity that is measured directly. Instead it is inferred from the detector signals together with a set of effective delayed neutron parameters and a kinetic model. Reactivity measurements can be split into two major categories:

1) Reactivity measurements close to the critical state
    a. IKM – Inverse Kinetic Method
    b. DTM – Doubling Time Method or PM – Period Method
2) Subcritical Measurements
    a. Static or Qasi-Static Methods such as SM – Source Multiplication Method and MSM – Modified Source multiplication Method
    b. Dynamic Methods
    c. Neutron Noise Methods

The 2015 Edition of the IRPhEP handbook contains over 500 evaluated experiments on reactivity measurements performed at 15 facilities. The most important characteristic from the point of view of the reactor safety is the control rod worth (CRW). The CRW measurements represent approximately half of the total number of reactivity measurements presented in the Handbook.

The important characteristic of the sodium-cooled fast reactors is Sodium Void Reactivity Effect (SVRE). There are approximately 50 such measurements at three facilities presented in the Handbook. Experimental methods used at different facilities for the CRW and SVRE measurements are given in Table 2.4.1-1.

Table 2.4.1-1. Experimental methods used at different facilities for the CRW and SVRE measurements

Facility	IKM	DTM or PM	SM, MSM
IPEN	CRW	IKM	
PROTEUS	CRW		CRW
NRAD	CRW	CRW	
HTTR	CRW		
BFS-2	SVRE		
FFTF	CRW		CRW
JOYO		CRW	
ZEBRA	SVRE		
ZPPR	SVRE		CRW, SVRE
ZPR		CRW	

Reactivity Uncertainty Analysis

The uncertainties in the reactivity can be classified into three categories:

1) Uncertainties in the measured parameters,
2) Uncertainties in the calculated correction factors,
3) Uncertainties in the effective delayed neutron parameters. The prompt neutron generation time is included in this category.

The uncertainties in the measured parameters arise from the uncertainties in detector currents (or count rates), temperature, time, or doubling time (DT). The uncertainties in the effective delayed neutron parameters arise from their measurements. However, this is not the common case. These parameters are rarely measured and most of the time the reactivity is inferred employing calculated effective delayed neutron parameters. The uncertainties of the detector currents, temperature, and time/doubling-time are a property of the data acquisition system of the facility under consideration (as well as the fitting process used for DT determination).

In order to get the uncertainty in the reactivity consider the general equation for the propagation of the associated uncertainties [2.4-6 and 2.4-7]. Let x_i be an independent or correlated set of variables and w(x_i) a dependent function of this set of variables. Accordingly, the uncertainty of w(x_i) is:

$$\sigma_w^2 = \sum_{i=1}^{n} \left(\frac{\partial w}{\partial x_i}\right)^2 . \sigma_i^2 + 2. \sum_{i>j}^{n} \frac{\partial w}{\partial x_i} . \frac{\partial w}{\partial x_j} . cov(x_i, x_j), \qquad 2.4\text{-}2$$

where x_i is a generic independent variable, σ_i is the uncertainty of x_i, and $\mathrm{cov}(x_i, x_j)$ is the covariance matrix of x_i and x_j.

Given the effective delayed neutron parameters (either measured or calculated) and their corresponding uncertainties Equation 2.4-2 can be applied directly in any reactivity measurement type in order to get its uncertainty in the reactivity. However, correlations may be found for the effective delayed neutron fractions (β_{eff_i}) and their corresponding decay constant (λ_i); both for family *i* and also for the detector currents or counts, doubling times, and temperature. In the following subsections these independent variables will all be considered uncorrelated.

2.4.1.1 Reactivity Measurements Close to the Critical State

Regarding category (a), to date there are two major techniques for the measurement of reactivity: inverse kinetics and the doubling time methods. Sample Oscillation Method is also a very important category of reactivity measurement technique but is not available in most facilities. Short descriptions of these experimental techniques are provided in the coming paragraphs.

2.4.1.1a Inverse Kinetic Method

In the inverse kinetic method, the reactivity is inferred assuming the validity of a point kinetic model. It can be shown from the point kinetic equations that the reactivity is given by [2.4-8]:

$$\rho(t) = \frac{\Lambda}{I(t)}\frac{dI(t)}{dt} + \beta_{eff} - \frac{\Lambda}{I(t)}\sum_{i=1}^{N_F}\lambda_i C_i(0)e^{-\lambda_i t} - \frac{1}{I(t)}\sum_{i=1}^{N_F}\lambda_i\beta_{effi}e^{-\lambda_i t}\int_0^t I(t')e^{\lambda_i t'}dt' \qquad 2.4\text{-}3$$

where:

$\rho(t)$ Represents the reactivity as a function of time,

$I(t)$ Represents the neutron flux or the detector signal,

β_{eff_i} Represents the effective delayed neutron fraction for family i,

β_{eff} Represents the total effective delayed neutron fraction,

λ_i Represents the decay constants for the delayed neutron of family i,

$C_i(0)$ represents the concentration of the i[th] delayed neutron precursor at the initial time,

N_F represents the total number of delayed neutron families,

and Λ represents the prompt neutron generation time.

Assuming that the reactor is critical at $t = 0$, it can be shown, for each family, i, that:

$$C_i(0) = \frac{\beta_{effi}}{\lambda_i\Lambda}I(0) \qquad 2.4\text{-}4$$

Equation 2.4-4 is the starting point to solve Equation 2.4-3. The reactivity measurement employing the inverse kinetic model is usually performed on line and the software that executes this function is called a reactimeter. The quantities measured in this model are the neutron detector signals, which generally operate in current mode and time. The detector signals must be linearly dependent on the neutron population. Temperature of the system has to be measured as well, in order to make corrections due to temperature reactivity feedback. The detector currents are then fed into electrometers where there is a conversion from current to voltage. The output of the electrometers are the quantity of interest, *I(t),* for the reactimeter's algorithm. The effective delayed neutron parameters and the prompt neutron generation time are calculated or arise from specific experiments.

A very significant correction is the change in the efficiency of the detector with a change in reactivity. The method of accounting of this effect was first proposed by Carpenter [2.4-9], and a comparison of the results of its implementation was carried out at the MASURCA facility by the laboratories of the three countries - the USA, the Former USSR, and France [2.4-10].

Uncertainty Analysis of the Inverse Kinetic Method

The uncertainty analysis for the Inverse Kinetic Method can be accomplished applying Equation 2.4-2 to Equation 2.4-3. The final result is:

$$\sigma_\rho = \sqrt{\left(\frac{\partial\rho}{\partial\Lambda}\right)^2 \cdot (\sigma_\Lambda)^2 + \sum_{i=1}^{NF}\left(\frac{\partial\rho}{\partial\beta_{effi}}\right)^2 \cdot \left(\sigma_{\beta_{effi}}\right)^2 + \sum_{i=1}^{NF}\left(\frac{\partial\rho}{\partial\lambda_i}\right)^2 \cdot \left(\sigma_{\lambda_i}\right)^2 + \left(\frac{\partial\rho}{\partial I}\right)^2 \cdot (\sigma_I)^2}, \quad 2.4\text{-}5$$

where

$$\frac{\partial\rho}{\partial\Lambda} = \frac{1}{I(t)} \cdot \frac{dI(t)}{dt}, \quad 2.4\text{-}6$$

$$\frac{\partial\rho}{\partial\beta_i} = 1 - \frac{\lambda_i \cdot e^{\lambda_i \cdot t}}{I(t)} \cdot \int_0^t I(t') \cdot e^{\lambda_i \cdot t'} \cdot dt' - \frac{I(0)}{I(t)} \cdot e^{-\lambda_i \cdot t}, \quad 2.4\text{-}7$$

$$\frac{\partial\rho}{\partial\lambda_i} = \frac{1}{I(t)}\left[-\beta_{effi} \cdot e^{-\lambda_i \cdot t} \cdot \int_0^t I(t') \cdot e^{\lambda_i \cdot t'} \cdot dt' + \beta_{effi} \cdot \lambda_i \cdot e^{-\lambda_i \cdot t} \cdot \int_0^t I(t') \cdot (t - t') e^{\lambda_i \cdot t'} \cdot dt'\right] \quad 2.4\text{-}8$$

$$\frac{\partial\rho(t)}{\partial I(t)} = -\frac{\rho(t)}{I(t)}, \quad 2.4\text{-}9$$

and all independent variables were assumed uncorrelated.

2.4.1.1b Doubling Time Method

The reactivity inferred from the doubling time method is given by the Inhour equation [2.4-1] as:

$$\rho = \frac{\Lambda}{T} + \sum_{i=1}^{ND} \frac{\beta_{effi}/T}{(1/T)+\lambda_i}, \quad 2.4\text{-}10$$

where T is the asymptotic period and ND represents the number of delayed neutron families. The symbols ρ, β_{eff}, Λ, and λ_i, have the same meaning as before. The doubling time ($T_{1/2}$) is equal to $T\ln(2)$. In most of the times ($T_{1/2}$) is the quantity measured but some experiments measure the first root ($\boldsymbol{\omega_\alpha}$) of the Inhour equation and from that the period T is inferred as T=1/ $\boldsymbol{\omega_\alpha}$.

Uncertainty Analysis of the Doubling Time Method

Uncertainty analysis of the Doubling Time Method can be performed by taking into consideration the uncertainties in the delayed neutron parameters and in the period as:

$$\sigma_\rho = \sqrt{\left(\frac{\partial\rho}{\partial\Lambda}\right)^2 \cdot \sigma_\Lambda^2 + \left(\frac{\partial\rho}{\partial T}\right)^2 \cdot \sigma_T^2 + \sum_{i=1}^{6}\left(\frac{\partial\rho}{\partial\beta_{effi}}\right)^2 \cdot \sigma_{\beta_{effi}}^2 + \sum_{i=1}^{6}\left(\frac{\partial\rho}{\partial\lambda_i}\right)^2 \cdot \sigma_{\lambda_i}^2}, \quad 2.4\text{-}11$$

where all independent variables were assumed uncorrelated,

$$\frac{\partial\rho}{\partial\Lambda} = \frac{1}{T}, \quad 2.4\text{-}12$$

$$\frac{\partial\rho}{\partial T} = -\frac{\Lambda}{T^2} - \sum_{i=1}^{6} \frac{\beta_{effi} \cdot \lambda_i}{(1+\lambda_i \cdot T)^2}, \quad 2.4\text{-}13$$

$$\frac{\partial\rho}{\partial\beta_{effi}} = \frac{1}{(1+\lambda_i \cdot T)}, \text{ and} \quad 2.4\text{-}14$$

$$\frac{\partial\rho}{\partial\lambda_i} = -\frac{\beta_{effi} \cdot T}{(1+\lambda_i \cdot T)}. \quad 2.4\text{-}15$$

Correlations can be taken into account in a straightforward fashion if the covariance matrix of the independent parameters is available.

2.4.1.2 Subcritical Methods

Subcritical measurement techniques in deeply subcritical systems (negative reactivities less than 10,000 pcm) constitute one of the last frontiers in Reactor Physics. Many techniques have been proposed, but none of them has been successfully considered acceptable to fulfil the requirements of benchmarks. The subcritical reactivity is closely related to the kinetic model applicable to the system. Several models [2.4-11, 2.4-12] were proposed to characterize the kinetics of subcritical reactors especially in regard to the reactivity of the system. Theoretical models suggest the unfolding of the system reactivity into two components: first, the reactivity of a system as normally obtained through the generalized perturbation theory [2.4-13] and second, the reactivity due to the source present in the system. This last component is extremely complex to obtain experimentally since the detector's efficiency is altered when the subcriticality level of the system changes. An experimental procedure based on these recent subcritical kinetic models proved successful up to -5,000 pcm was developed by dos Santos et. al. [2.4-14].

Regarding fast systems, the BERP ball experiments were recently approved for inclusion in the ICSBEP Handbook.

Methods used to determine subcritical reactivity are classified in three categories:

1) Static or quasi-static methods,
2) Dynamic methods,
3) Neutron noise methods.

2.4.1.2a Static or Quasi-Static Methods

The static or quasi-static methods rely mostly on the detector signals placed strategically around or inside of the reactor core. The reactor system is considered at steady state and the detector responses mainly counts, are collected for further analyses. The main assumption is that detector count rates are linked to sub-critical levels, and, consequently, count rate variations are linked to reactivity variation between two configurations. This is the main hypotheses for the development of the Source Multiplication Method [2.4-15]. This is simplest method to measure subcriticality from the three categories mentioned above.

As an illustration of this technique, consider the Modified Source Multiplication (MSM) method [2.4-16]. The Amplified Source Multiplication (ASM) method and its improved Modified Source Multiplication (MSM) method are based on the assumption that, in any fissioning system, detector count rates are linked to sub-critical levels, and, consequently, count rate variations are linked to reactivity variation between two configurations. They have been successfully applied to absorber (single or clusters) worth measurements in both thermal and fast spectra, or for void reactivity worths. These techniques give *relative* reactivity variations since they are based on the use of a calibration reactivity sample such as a pilot rod worth measured by the rod drop technique.

The ASM methodology, which is the basic technique to estimate a reactivity worth, uses relatively simple relationships between count rates of efficient fission chambers located in slightly subcritical reference and perturbed configurations. While this method works quite well for small reactivity variations, its raw results need to be corrected to take into account the flux perturbation in the fission chamber. This is performed by applying to the measurement a correction called the MSM factor. The MSM factor takes into account the local space and energy variation of the spectrum at the fission chamber location, through standard perturbation theory applied to neutron transport calculations in the perturbed configuration. This factor, applied to the fission chamber count rates obtained by ASM,

enables the direct interpretation of high reactivity perturbations through the response function of the fission chamber.

The MSM method can be applied to the following class of problems:

1. Knowing the reactivity of a reference « 0 » state (obtained by another method), one can deduce the reactivity of a perturbed state « 1 », or the reactivity variation between « 0 » and « 1 ».
2. Knowing the reactivity variation between two states « 0 » and « 1 », obtained by another method, one can deduce reactivity of state « 0 » or « 1 ».

The main interest of sub-critical measurements is to obtain the reactivity effect or reactivity coefficient, without using the exact characterization of two different states. In other words, the measured reactivity effect is directly the result we are looking for, with no need for another parameter.

The derivation of the equations for the MSM method is shown in Reference 2.4-25 (see Example E2.4-3). The final expression to infer the subcritical reactivity from this method is:

$$\frac{\rho_{m,1}(\vec{r})}{\rho_{m,0}(\vec{r})} = f_{MSM}(\vec{r}).\frac{R_{m,0}(\vec{r})}{R_{m,1}(\vec{r})} \qquad 2.4\text{-}16$$

where

$$f_{MSM}(\vec{r}) \equiv \frac{\rho_{c,1}}{\rho_{c,0}}.\frac{R_{c,1}(\vec{r})}{R_{c,0}(\vec{r})}, \qquad 2.4\text{-}17$$

$$\rho_{c,i} = \frac{S_{eff,i}}{<\varphi_i^*, F\Phi_i>}, \qquad 2.4\text{-}18$$

$$S_{eff,i} = <\varphi_i^*, S>, \qquad 2.4\text{-}19$$

S is the intrinsic source or the external source,
φ_i^* and Φ_i are the adjoint and the real neutron fluxes, respectively,
$R(\vec{r})$ is the detector reaction rate,
Subscript, *i*, represents state « 0 » or « 1 »,
Subscripts, c and m, represent, respectively, calculated and measured quantities, and
the notation $<,>$ represents integral over the space phase of the problem

The MSM correction factor ($f_{MSM}(\vec{r})$) is a correlation coefficient between the detector position and the inferred value of reactivity, knowing the standard of reactivity in the reference state.

The MSM technique usually employs several detectors, located in various core positions. When the MSM factor is equal to unity, the determination of reactivity is independent of the detector position. The flux form factor remains constant between the two configurations (with a small perturbation, the asymptotic flux is rapidly attained), as does the effective source, so the point-kinetics model applies.

The MSM requires a calculated correction factor ($f_{MSM}(\vec{r})$) and measured quantities $R_{m,0}(\vec{r})$and $R_{m,1}(\vec{r})$.

2.4.1.2b Dynamic Methods

The dynamic method is based on the analysis of the time response of detectors placed in the reactor after a source neutron pulse. The evolution of the detector count rates strongly reflects that of the neutron population over time. The technique assumes that the neutron point kinetics can represent the neutron population evolution over time after a pulse (considered as a Dirac peak). The Area method (also referred as the Sjöstrand method) [2.4-17] allows one to determine in a straightforward way the reactivity (in units of dollar) of a subcritical nuclear reactor with no input from theoretical calculations, as long as the assumptions of the neutron point kinetics hold in the reactor. Examples of utilization of this technique may be found in Ref. [2.4-18].

The Sjöstrand method is an experimental technique for subcritical reactivity measurement by means of Pulsed Neutron Source (PNS). Assuming point kinetics as representative of neutron population after the Dirac pulse, and assuming one averaged delayed neutron group, one has:

$$N(t) = N_0\left[\exp\left(\frac{\rho-\beta_{eff}}{\Lambda_{eff}}t\right)+\frac{\bar{\lambda}\Lambda_{eff}\beta_{eff}}{(\rho-\beta_{eff})^2}\exp\left(-\frac{\bar{\lambda}\rho}{\rho-\beta_{eff}}t\right)\right] \qquad 2.4\text{-}20$$

where $\bar{\lambda}$ is the average delayed neutron decay constant. The inclusion of six or more delayed neutron groups is straightforward.

From Eq. 2.4-20 one can see a fast component due to prompt neutrons and a slow component due to delayed neutrons. The integration of the prompt component gives the prompt area:

$$A_p = N_0\frac{\Lambda_{eff}}{-\rho+\beta_{eff}} \qquad 2.4\text{-}21$$

whereas the integration of the delayed component gives the delayed area:

$$A_d = N_0\frac{\beta_{eff}\Lambda_{eff}}{\rho(\rho-\beta_{eff})} \qquad 2.4\text{-}22$$

Then, the ratio of these two areas gives directly the value of the subcritical reactivity in units of dollar:

$$-\rho_{\$} = \frac{A_p}{A_d} = -\frac{\rho}{\beta_{eff}} \qquad 2.4\text{-}23$$

Experimentally, for a set of pulses repeated with a fixed frequency, a single Pulse Neutron Source histogram is constructed by summing the detector responses as a function of the time elapsed after the neutron pulse. The analysis consists in obtaining the prompt area, A*p*, and the delayed area, A*d*, from this histogram and the reactivity is calculated from Eq. 2.4-23. Figure 2.4-1 shows the expected response of a neutron detector for a single pulse of the source.

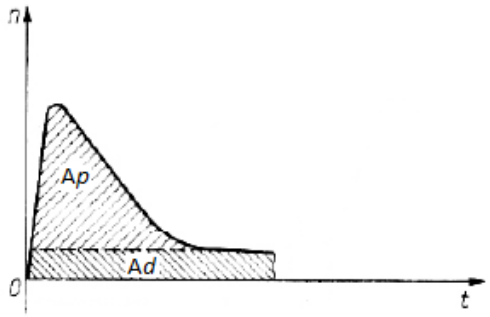

Figure 2.4-1. Detector response expected for a single pulse indicating the prompt and delayed areas

Although the area method is an old and well known technique, giving good results for subcritical reactivities measurements, spatial effects concerning detector and source positions should be taken into account in some cases, mainly for detectors in the reflector regions. Depending on the subcritical level, the point kinetics is not valid anymore, and Eq. 2.4-23 should be corrected for this. Finally the higher harmonics can also play an important role in this sort of experiments and they should be taken into consideration. A good example of such situation is given by W. Uytennhove et. al. [2.4-19].

2.4.1.2c Neutron Noise Methods

The neutron noise method is based on the macroscopic and microscopic noise acquisitions in the reactor system. The macroscopic noise relies on the measurements of the CPSD (Cross Power Spectral Density) while the microscopic noise relies on the measurements of Feynman-Ycurve. The validity of the point kinetic model is the basic principle to infer the subcritical reactivity. Examples of the applications of this method can be found in References [2.4-20] and [2.4-21]. The following paragraphs describe the Feynman-Ycurve method as an illustration

The Feynman-α method relies on the inverse ratio of measured counts and their variances (variance to mean ratio) in several time intervals (gate length). When the time scales of prompt and delayed neutrons are very different, as is the case for light water reactors, the variance to mean ratio (V/m) can be written as

$$\frac{V}{m} = 1 + \varepsilon \frac{\overline{\nu(\nu-1)}}{(\bar{\nu})^2(\beta-\rho)^2}(1-\beta)^2\left(1 - \frac{1-e^{-\propto t}}{\propto t}\right) \qquad 2.4\text{-}24$$

where ε is the detector efficiency, ν is the multiplicity of fission event, t is the counting time interval and α is the prompt decay constant given by $\alpha = (\beta-\rho)/\Lambda$.
The experimental procedure is as follow:

Being Z_i the counts for a given set of equal time intervals, the variance to mean ratio is given by:

$$\frac{V}{m} = \frac{\frac{1}{N}\sum_{i=1}^{N} Z_i^2 - \left(\frac{1}{N}\sum_{i=1}^{N} Z_i\right)^2}{\frac{1}{N}\sum_{i=1}^{N} Z_i} \qquad 2.4\text{-}25$$

The process is repeated for different gate lengths in order to get a curve like that in Fig. 2.4-2. The fitting of the experimental data of Figure 2.4-2 to Equation 2.4-25 gives the reactivity if β and Λ are known.

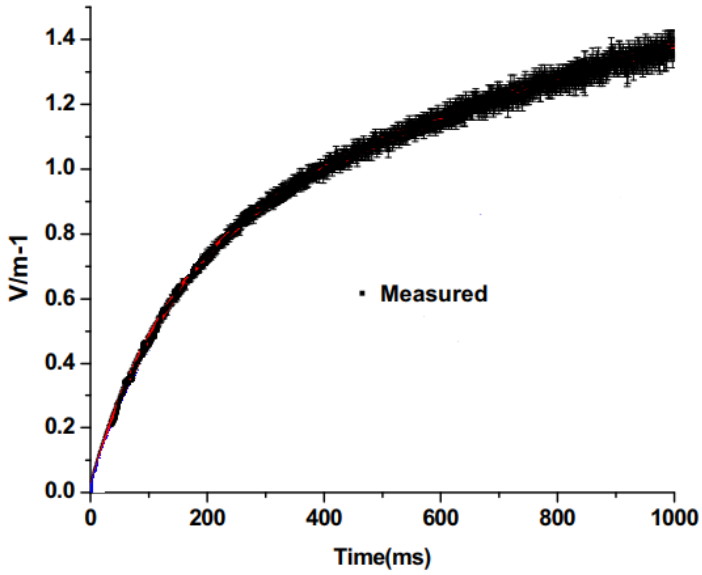

Figure 2.4-2. Variance to mean ratio minus one distribution for several time gates

For the case when the time scales of prompt and delayed neutrons are not very different, it is necessary to include in Equation 2.4-25 the contribution of the delayed neutron groups. See Ref. 2.4-17 for details.

2.4.1.2d Other Uncertainty Considerations

Uncertainty in Dates

Uncertainties of dates must be considered in the case of experiments carried out with decaying isotopes. ^{241}Pu is a good example of this category of uncertainty. This fissile plutonium isotope contributes to the effective delayed neutron parameter determination. All important dates should be reported in order to better determine the isotopes' concentrations when the experiment was performed.This uncertainty has to be propagated to the reactivity uncertainty through a sensitivity calculation and can be expressed as:

$$\sigma_\rho^D = S_\rho^D \cdot \sigma_D, \qquad 2.4\text{-}26$$

where σ_ρ^D is the uncertainty of the reactivity due to the uncertainty in date, S_ρ^D is the reactivity sensitivity coefficient to the date, and σ_D is the date uncertainty. The subscript ρ represents a generic reactivity from a generic measurement method.

Uncertainty of Temperature

The temperature uncertainty has to be propagated to the reactivity uncertainty through a sensitivity calculation. This uncertainty can be expressed as:

$$\sigma_\rho^T = S_\rho^T \cdot \frac{\sigma_T}{T}, \qquad 2.4\text{-}27$$

where σ_ρ^T is the uncertainty of the reactivity due to the uncertainty in the temperature, S_ρ^D is the reactivity sensitivity coefficient to the temperature, and σ_T is the temperature uncertainty.

Systematic Uncertainties

The systematic uncertainties from the experimental factors shall be evaluated. The experiment report should provide enough information so that the evaluator can judge the possible sources of systematic uncertainties.

Systematic uncertainties can arise from the nonlinearity of the detector employed for the reactivity measurements, instrumentation of detectors, neutron source characteristics as in PNS method, and several others. The kinetic model employed in the determination of this quantity can also play an important role. The great majority of the reactivity measurement methods rely on the validity of point kinetic model. The failure of this model can give rise to a systematic uncertainty in the determination of the reactivity.

2.4.1.2e Final Reactivity Effects Measurement Uncertainty

The final uncertainty in reactivity effects measurements is obtained combining all uncertainty types quadratically and assuming no correlation among them. Let this uncertainty be denoted by σ_{MM}; i.e., the measured method reactivity uncertainty for a generic measurement method. The final reactivity for the measurement method MM is given by:

$$\sigma_{\rho_{MM}} = \sqrt{\sigma_{\rho}^{2} + \left(\sigma_{\rho}^{D}\right)^{2} + \left(\sigma_{\rho}^{T}\right)^{2} + \left(\sigma_{\rho}^{sys}\right)^{2}}, \qquad 2.4\text{-}28$$

Where $\sigma_{\rho_{MM}}$ is the reactivity experimental uncertainty for the measurement method MM, the subscript ρ represents the reactivity uncertainty of any of the measurement techniques described in this Guide or any other technique employed for the same purpose and σ_{ρ}^{sys} is the systematic uncertainty.

2.4.1.2f Sources of Uncertainty and Bounding Values for Reactivity Effects Measurements

Tables 2.4-1a and 2.4-1b shows a summary for the uncertainties and bounding values for the reactivity measurements for thermal reactors. The reactivity bounding values are given in three intervals due to the difficulty in measuring small values of this quantity. Assigned uncertainty bounds reflect this difficulty. Also, the bounding values are given in units of pcm (Table 2.4-1a) or \$ (1\$ = 1 β_{eff}) (Table 2.4-1b).

Table 2.4-1a. Summary of uncertainties and bounding values for thermal reactors for the reactivity given in pcm units

Sources of Uncertainty	Typical Value	Minimum Value	Maximum Value	Type of Uncertainty (A or B) [(a)]
Detector Signal	0.5 %	0.1 %	3 %	A
Doubling time	0.5 %	0.1 %	2 %	B
Delayed Neutron Parameters	3.0 %	1.0 %	10.0 %	B
Measured Reactivity (ρ < 100 pcm)	3.0 %	0.5 %	10.0 %	B
Measured Reactivity (100<ρ<500 pcm)	2.0 %	0.5 %	8 %	B
Measured Reactivity (ρ>500 pcm)	2.0 %	0.5 %	6%	B

(a) The Uncertainty Type (A or B) has the same meaning as in ICSBEP Uncertainty Guide.

Table 2.4-1b. Summary of uncertainties and bounding values for thermal reactors for the reactivity given in dollar ($) units

Sources of Uncertainty	Typical Value	Minimum Value	Maximum Value	Type of Uncertainty (A or B) [a]
Detector Signal	0.5 %	0.1 %	3 %	A
Doubling time	0.5 %	0.1 %	2 %	B
Delayed Neutron Relative Abundances	2.0 %	0.5 %	6.0 %	B
Measured Reactivity ($\rho < 0.15\$$)	2.0 %	0.5 %	6.0 %	B
Measured Reactivity ($0.15\$<\rho<0.7\$$)	2.0 %	0.5 %	4.0 %	B
Measured Reactivity ($\rho>0.7\ \$$)	2.0 %	0.5 %	3.0%	B

(a) The Uncertainty Type (A or B) has the same meaning as in ICSBEP Uncertainty Guide.

Table 2.4-1c shows a summary for the uncertainties and bounding values for the reactivity measurements for fast reactors.

Table 2.4-1c. Summary of uncertainties and bounding values for fast reactors (in units of β_{eff})

Sources of Uncertainty	Typical Value	Minimum Value	Maximum Value	Type of Uncertainty (A or B) [a]
Detector Signal	0.5 %	0.1 %	3 %	A
Doubling time	0.5 %	0.1 %	2 %	B
Delayed Neutron Parameters	2.0 %	1.0 %	10.0 %	B
Measured Reactivity	2.0 %	1.0 %	10.0 % - ∞ [b]	B

(a) The Uncertainty Type (A or B) has the same meaning as in ICSBEP Uncertainty Guide.
(b) If the measured reactivity tends to zero.

2.4.2 *Uncertainties in Experimental Configuration*

Uncertainties in the experimental configuration are the uncertainties that arise from the fact that the experiment setup is not in perfect agreement with its design, i.e. there is an uncertainty connected to the position of the detectors and auxiliary instrumentation, uncertainty of the experiment equipment composition etc., which is discussed in Section 2.7.2 and in a practical examples in Section 2.7.4 (Example 2.7-1). The category also includes uncertainties in the environmental conditions, namely the uncertainties in basic parameters of the experiment system which might not be of direct interest, but nevertheless affect the measured. This includes uncertainties such as those in the geometry, composition or integral physical parameters of the criticality system. An example of the evaluation of an experiment configuration uncertainty is given in Section 2.7.4 (Example 2.7-1).

The Effect of the Parameter Uncertainty of the Facility

This kind of uncertainty follows closely the procedure of the *ICSBEP Uncertainty Guide* [2.3-6]. Here the uncertainties are divided primarily into two categories: a) uncertainty in geometry, and b) uncertainty in physics, chemistry, and isotopic content of materials.

As an illustration, Tables 2.4-2 and 2.4-3 show, respectively the uncertainties on geometry and the uncertainties on materials. The empty columns may be filled as an aid to clarify the uncertainties. This list is not exhaustive. Different parameters will be listed for other types of configurations. A

sensitivity analysis is performed in order to propagate the geometric and material uncertainties of the facility and of the measurement device utilized to infer the reactivity. The final total uncertainty arising from the parameters of the facility is the square root of the sum of the squares of each component. Let this type of uncertainty be represented by σ_{PF}.

Table 2.4-2. Uncertainties on geometry

Parameter Identification	Mean Measured Value	Reported Uncertainty in Parameter	Type of Uncertainty (A or B) [(a)]	Number of Degrees of Freedom	Standard Uncertainty
Active Fuel Height					
Fuel Pellet Diameter					
Clad Outer Diameter					
Clad Inner Diameter					
Fuel Rod Pitch					
Bottom Alumina Height					
Control Rod Position					
Control Rod Diameter					
Other Relevant Parameters					

(a) The Uncertainty Type (A or B) has the same meaning as in ICSBEP Uncertainty Guide.

Table 2.4-3. Uncertainties on materials

Parameter Identification	Mean Measured Value	Reported Uncertainty in Parameter	Type of Uncertainty (A or B) [(a)]	Number of Degrees of Freedom	Standard Uncertainty
^{235}U Enrichment (%)					
^{234}U (wt.%)					
UO_2 Density (g/cm^3)					
UO_2 stoichiometric factor (%)					
Cladding Density (g/cm^3)					
^{55}Mn in Cladding SS (wt.%)					
Cladding composition					
Control rod composition					
Other Relevant Parameters					

(a) The Uncertainty Type (A or B) has the same meaning as in ICSBEP Uncertainty Guide.

2.4.3 *Uncertainties in Biases and Benchmark Models*

Biases in Benchmark Model

Biases are introduced in the Benchmark Model in three distinct forms. By reactivity measurement methods employing parameters derived from calculations; by the desired simplification (typically derived in Section 3 of the IRPhEP Evaluation), or by modelling limitations (typically derived in Section 4 of the IRPhEP Evaluation). Biases in the reactivity measurement methods shown in this section arise from the calculated factors e.g., the effective delayed neutron parameters including the prompt neutron generation time and from the factor f_{MSM} of MSM method. Section 2.4.1 shows how these factors were applied.

The determination of the biases arising from the reactivity measurement methods is a very complicated problem and some of them may never be found. The bias determination for the calculated quantities requires the availability of well-defined experiments for these quantities to serve as benchmarks; here referred to as Reference Values. The bias induced by these calculated factors can be understood by calculating the ratio C/R, where C is the calculated quantity and R is the reference value provided by the specific available benchmarks. If C/R is higher than 1, the calculated factor overestimates the measured reactivity. On the other way around, the calculated factor underestimates the measured reactivity.

The bias in the reactivity measurements for a particular correction factor is given as:

$$B_{CF} = \frac{(R-C)}{C} \cdot SI_{MM} \,, \qquad 2.4\text{-}29$$

where B_{CF} is the bias for the specific calculated factor and its uncertainty arises from a standard error propagation.

The benchmark model for the reactivity experiment after applying all possible biases and correction factors is given by:

$$SI_{Be} = SI_{MM} + B_{SL} + \frac{(R-C)}{C} \cdot SI_{MM}, \qquad 2.4\text{-}30$$

where SI_{Be} is the benchmark reactivity model, the subscript MM represents a generic measurement method, SI_{MM} is the measured reactivity, and B_{SL} is the bias from the benchmark model simplification (typically derived in Section 3 of and IRPhEP Evaluation), or by modelling limitations (typically derived in Section 4 of IRPhEP Evaluation).

Equation 2.4-30 reduces to:

$$SI_{Be} = SI_{MM} \cdot \frac{R}{C} + B_{SL}, \qquad 2.4\text{-}31$$

The ratio $\frac{R}{C}$ is defined as the bias-factor. Equation 2.4-31 can be generalized for a specific number of measurement bias as:

$$SI_{Be} = SI_{MM} \cdot B_{MM} + B_{SL}, \qquad 2.4\text{-}32$$

where $B_{MM} = \prod_{i=1}^{N_B} B_i$ is the total measurement method bias-factors , N_B is the total number of bias-factors applied to the measurement method, and B_i is the specific measurement method bias-factor. Bias in simplifications also includes the exclusion of the auxiliary devices to fix the detectors in the reactor system if not modelled in the benchmark model.

The bias in the reactivity measurements originates whenever calculated parameters are employed in their inference. These are cases of the calculated effective delayed neutron parameters and the factor f_{MSM} employed in the MSM method.

The bias induced by the calculated effective delayed neutron parameters can be estimated following the approach proposed here. This approach is applicable to thermal reactor of uranium slightly enriched, but it may be applied to other cases if measurements of the effective delayed neutron parameters are available. Specific experiments performed at the IPEN/MB-01 research reactor facility were successfully performed and they were able to measure the relative abundances, the corresponding decay constants of delayed neutron parameters in a six group families and the prompt neutron generation time as well. The experiment was approved to be an international benchmark for

the IRPhEP [2.4-22]. The final benchmark values are shown in Table 2.4-4. The uncertainties in Table 2.4-4 were obtained from the experimental least-square fitting procedure and are 1-σ values.

Table 2.4-4. Totally experimental delayed neutron parameters of the IPEN/MB-01 reactor

$\beta_{eff,i}$	λ_i (s^{-1})
(2.679 ± 0.023)E-4	0.012456 ± 0.000031
(1.463 ± 0.069)E-3	0.0319 ± 0.0032
(1.34 ± 0.13)E-3	0.1085 ± 0.0054
(3.10 ± 0.10)E-3	0.3054 ± 0.0055
(8.31 ± 0.62)E-4	1.085 ± 0.044
(4.99 ± 0.27)E-4	3.14 ± 0.11
β_{eff} = (7.50 ± 0.19)E-3, Λ=(31.96 ± 1.06) μs	

The proposal here is to calculate two sets of reactivities employing the Inhour equation as given by Equation 2.4-10. The first set is called experimental and the delayed neutron parameters to be used in Equation 2.4-10 are given in Table 2.4.-4. The second set is called calculated and the effective delayed neutron parameters to be used in Equation 2.4-10 arise from the user specific library weighted in the IPEN/MB-01 benchmark geometric and material specifications as given in Section 3.6.5 of IPEN(MB01)-LWR-RESR-001 [2.4-22]. The periods to be used in Equation 2.4-10 can be chosen so that the inferred reactivities cover the interval of interest of the user application. The bias-factor induced by the calculated effective delayed neutron parameters can be determined calculating the ratio R/C, where C is the calculated and R is the reference value, in the reactivity interval specified by the user. In most cases, the value of R/C is nearly constant and is independent of the reactivity interval. The user can infer the quality of the effective delayed neutron data performing these analyses and from that infer a possible bias in his measurements.

One example of the inference of the reactivity bias due to the calculated effective delayed neutron parameters will be shown in the Practical Examples, Section 2.4.4.

The final value for the measured reactivity is given by:

$$\rho = \rho_{cal} \cdot \frac{R}{C}, \qquad 2.4\text{-}33$$

where ρ is the final value of the measured reactivity and ρ_{cal} is the reactivity calculated employing the calculated effective delayed neutron parameters. R/C is the bias-factor as described in the previous paragraph.

Uncertainties in Biases

Bias in measurement methods is always the inverse of the ratio of two quantities. The numerator is the calculated quantity while the denominator is the reference value. Its uncertainty can be found applying a standard propagation of the associated uncertainties assuming no correlations. The final result is given by:

$$\sigma_{B_{CF}} = \sqrt{((1/C) \cdot \sigma_R)^2 + ((R/C^2) \cdot \sigma_C)^2}, \qquad 2.4\text{-}34$$

where R and C represents the reference and the calculated values, respectively, and σ_R and σ_C are respectively the uncertainties in the specific experiment and in the calculations.

The total uncertainty in the benchmark simplification and in the benchmark limitation is given by:

$$\sigma_{B_{SL}} = \sqrt{\sigma_{B_S}^2 + \sigma_{B_L}^2}, \qquad 2.4\text{-}35$$

where σ_{B_S} is the uncertainty in the bias from simplifications and σ_{B_L} is the uncertainty in the bias from limitations.

As a starting point, the following paragraph was taken from the *ICSBEP Uncertainty Guide* [2.4-6] and adapted for reactivity measurements.

The evaluator should strive for a reasonable balance between making the benchmark model amenable to calculation and keeping the total reactivity **uncertainty of the model as small as practical.** Obviously, simplifications that make the benchmark model easier to use tend to make it more attractive to reactor physicist analysts. However, each simplification introduces an additional benchmark-model bias and a correlated uncertainty contribution. The use of benchmark models to validate a reactor physics analysis or to identify weaknesses in cross section data and calculational methods is more effective and reliable if the uncertainties are small. The only stage in the evaluation process where the evaluator legitimately can influence the magnitude of the total uncertainty is in deciding what simplifications to make to create the benchmark model. The **benchmark-model** is the best estimate of the value of reactivity that would be observed for an isolated experiment having exactly the geometry and materials described in the benchmark model. Thus one should aim at developing a benchmark model of the experiment which is simultaneously pragmatic for further evaluator's use, computationally not too demanding and free of major computational biases. This means that constructing a model with a great level of detail, which has a negligible contribution to the total benchmark-model uncertainty but significantly increases the complexity of the model and associated computational time, is not advisable. Additionally the evaluator should construct a benchmark-model including all parts of experiment that could potentially lead to the introduction of major reactivity biases, if not modelled. In the opposite case a rigorous study of the effect of the benchmark-model simplification on the computed reactivity should be performed.

Uncertainties in Benchmark Model

The uncertainties in the reactivity benchmark model are composed of three major parts:

1) Uncertainties in measurement method,
2) Uncertainties in biases,
3) Uncertainty from the facility and device parameters.

These three components shall be combined quadratically in order to get the whole benchmark uncertainty. The final benchmark uncertainty for the reactivity measurement method is given by:

$$\sigma_{\rho_{MM}}^{Be} = \sqrt{\left(\sigma_{\rho_{MM}} \cdot B_{MM}\right)^2 + \left(\rho_{MM} \cdot \sigma_{B_{MM}}\right)^2 + \left(\sigma_{B_{SL}}\right)^2 + {\sigma_{PF}}^2}, \qquad 2.4\text{-}36$$

where $\sigma_{\rho_{MM}}^{Be}$ is the reactivity benchmark uncertainty for the measurement method MM, $\sigma_{B_{SL}} = \sqrt{\sigma_{B_S}^2 + \sigma_{B_L}^2}$, σ_{B_S} is the uncertainty in the bias from simplifications and σ_{B_L} is the uncertainty in the bias from limitations.

Tables 2.4-5a and 2.4-5b show summary tables listing the uncertainties, typical values, and minimum – maximum range of values that are considered bounding for thermal reactors. Also, the reactivity values are given in units of pcm (Table 2.4-5a) or \$ (1\$ = 1 β_{eff}) (Table 2.4-5b).

Table 2.4-5a. Summary of uncertainties and bounding values for the benchmark model for thermal reactors

Source of Uncertainty	Typical Value (%)	Minimum Value (%)	Maximum Value (%)
Measured Reactivity (ρ < 100 pcm)	3.0	0.5	10.0
Measured Reactivity (100<ρ<500 pcm)	2.0	0.5	8
Measured Reactivity (ρ>500 pcm)	2.0	0.5	6
Facility and Device Parameters	0.5	0.1	2.0
Benchmark model (ρ<100 pcm)	4.0	1.0	12.0
Benchmark model (100<ρ<500 pcm)	3.0	1.0	9.0
Benchmark model (ρ>500 pcm)	3.0	1.0	7.0

Table 2.4-5b. Summary of uncertainties and bounding values for the benchmark model for thermal reactors

Source of Uncertainty	Typical Value (%)	Minimum Value (%)	Maximum Value (%)
Measured Reactivity (ρ < 0.15$)	2.0	0.5	6.0
Measured Reactivity (0.15$<$\rho$<0.7$)	2.0	0.5	4.0
Measured Reactivity (ρ>0.7 $)	2.0	0.5	3.0
Facility and Device Parameters	0.5	0.1	2.0
Measured Reactivity (ρ < 0.15$)	4.0	1.0	8.0
Measured Reactivity (0.15$<$\rho$<0.7$)	3.0	1.0	5.0
Measured Reactivity (ρ>0.7 $)	3.0	1.0	4.0

Table 2.4-5c shows a summary table listing the uncertainties, typical values, and minimum – maximum range of values that are considered bounding for fast reactors.

Table 2.4-5c. Summary of uncertainties and bounding values for the benchmark model for fast reactors

Source of Uncertainty	Typical Value (%)	Minimum Value (%)	Maximum Value (%)
Measured Reactivity	2.0	1.0	10.0 - ∞
Facility and Device Parameters	1.0	0.1	2.0
Benchmark model (in units β_{eff})	2.0	1.0	10.0 - ∞
Uncertainty of β_{eff}	5.0	3.0	6.0
Benchmark model (in units $\Delta k/k$)	5.0	3.0	6.0

2.4.4 *Practical Examples*

Example 2.4-1: Determination of Reactivity in the IPEN/MB-01 Reactor

The following example is part of the experiments performed in the IPEN/MB-01 reactor aiming to measure the relative abundance of the delayed neutrons [2.4-23] based on the Spriggs method [2.4-24]. The experiment considers the reactivity measurement of a small sample of Ag-In-Cd (80 wt. % Ag, 15 wt. % In, and 5 wt. % Cd) placed at the IPEN/MB-01 core center. The standard configuration of the IPEN/MB-01 reactor core (28×26 fuel rod positions) was employed for this goal. The sample was placed inside of an empty tube of SS-304 of the same diameter and thickness of the fuel rods but its height was much longer than the fuel rods in the core. A stopper was placed inside of this tube to accommodate the small sample. The stopper was designed such that it could have its height adjusted in order to change the sample reactivity. The sample was placed very close to the central radial position of the active core in order to optimize its reactivity. The sample was rapidly removed from the active core and as a consequence a transient was produced. The IPEN/MB-01 removal system consists of a high speed electric motor coupled with a beam catcher. The measured removal time is of the order of 6 ms (10^{-3} seconds). The intention here was to simulate a step of reactivity as closely as possible.

The experiment has several features that must be addressed by the acquisition system. Initially, when the sample is removed from the core there is a very fast change in the relative power due to the rapid decay of the largest (negative) root of the Inhour equation. After that the relative power changes due to the decay of the other negative roots. This change is less pronounced but still very important for the dynamic of the transient. The experimental acquisition system has to be fast enough to describe all the physics details of the transient. The experimental set up for the data collection of this experiment is composed of two compensated ionization chambers working in a current mode strategically located in the reactor core. Strategically means that the positioning of the detector is set up so that any spatial effect could be detected and taking into consideration in the measurements. IPEN/MB-01 core is described very well by the point kinetic model and no spatial effect in the reactivity measurement has been detected to date.

The signals from these chambers are fed into electrometers where there is a conversion from current to voltage (0-2 V). After that, the data are input into a Daq Card 16XE-50 set to 1kHz that guarantees a very high acquisition rate. At every 1 ms one experimental datum is collected. This last aspect is very important to describe the initial points of the transient mainly for the determination of the starting point (t=0) of the transient. The initial point is a kind of artificial because the transient is not truly a step. Of importance for this example is the measurement of the positive root of the Inhour equation. The sample reactivity can be inferred employing this root and the Inhour equation. Also, here the experiment performed at the IPEN/MB-01 reactor addressed this aspect adequately by collecting the data over a long run time to allow the terms of all negative roots to decay to nearly zero.

The experiment basically can be described as follows. Initially the reactor is brought to a critical state at 1 W with the sample inside of the core. The automatic control system is turned off and the reactor is run in the manual mode. The IPEN/MB-01 reactor possesses a very accurate mechanism for the relative control rod positioning [2.4-25]. Hence, an experienced operator positions the control rod such that the reactivity is a few cents from the true critical condition. This aspect is very important for the experiment and will guarantee that in the initial condition the reactor is really close to the criticality. The whole system is stabilized. The data collection system is activated and the detector currents which are proportional to the reactor power are written in a computer file for the subsequent power normalization. These data are collected for at least 5 minutes before the removal of the sample from the core. This aspect will guarantee a proper power normalization before the transient starts. The sample is then removed from the reactor core and the transient starts. The data are acquired during a time large enough that all events necessary for the analyses are captured. Later on, the experimental data are normalized taking into consideration the power before the transient and the final result is kept

in a computer file. Figure E2.4-1.1 shows the experimental data collected when the sample was removed from the core. Figure E2.4-1.1 shows clearly the fast change of the relative power density at the beginning of the transient as well as the region where the behaviour becomes asymptotic, thus allowing the determination of the first root of the Inhour equation (ω_α).

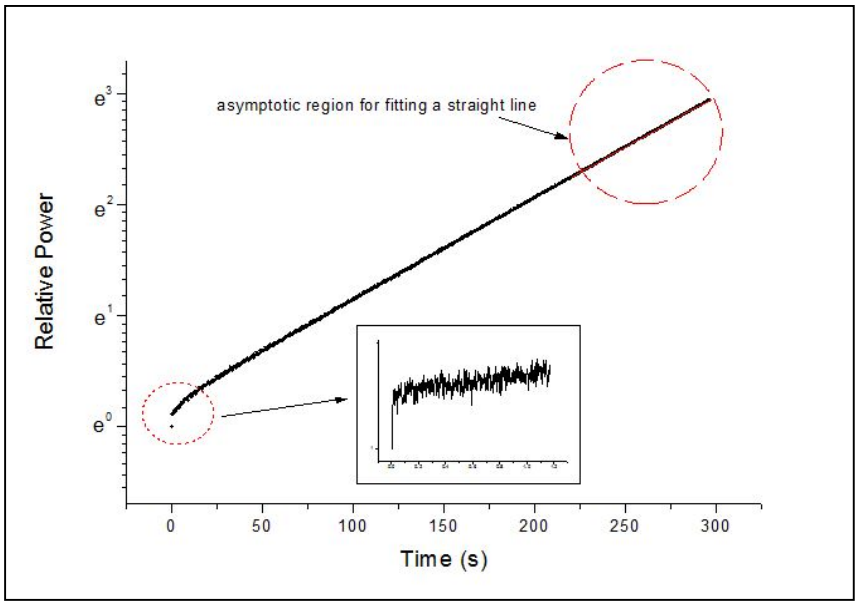

Figure E2.4-1.1. The relative power as a function of time

The first root of the Inhour Equation was measured fitting the region shown in Figure E2.4-1.1 in a straight line considering error bars of 1 % (statistical mainly) in the relative power. The ω_α parameter as well as its uncertainty obtained from the least square fit was:

$$\boldsymbol{\omega_\alpha = 0.00912294 \pm 0.00000048\ s^{-1}}$$

From this root the period could be determined as:

$$T = \frac{1}{\omega_\alpha} = 109.62\ s.$$ (The uncertainty on T is negligible.)

The reactivity of the sample was subsequently determined employing Equation 2.4-10 and it was equal to: **64.1** pcm. The effective delayed neutron parameters employed here are given in Table 2.4-4.

The uncertainty analysis was performed taking into consideration the uncertainties in the delayed neutron parameters and in the period as:

$$\sigma_\rho = \sqrt{\left(\frac{\partial\rho}{\partial\Lambda}\right)^2 \sigma_\Lambda^2 + \left(\frac{\partial\rho}{\partial T}\right)^2 \sigma_T^2 + \sum_{i=1}^{6}\left(\frac{\partial\rho}{\partial\beta_i}\right)^2 \sigma_{\beta_i}^2 + \sum_{i=1}^{6}\left(\frac{\partial\rho}{\partial\lambda_i}\right)^2 \sigma_{\lambda_i}^2}\ , \qquad \text{E2.4-1.1}$$

where:

$$\frac{\partial\rho}{\partial\Lambda} = \frac{1}{T}, \qquad \text{E2.4-1.2}$$

$$\frac{\partial\rho}{\partial T} = -\frac{\Lambda}{T^2} - \sum_{i=1}^{6}\frac{\beta_i\lambda_i}{(1+\lambda_i T)^2}, \qquad \text{E2.4-1.3}$$

$$\frac{\partial\rho}{\partial\beta_i} = \frac{1}{(1+\lambda_i T)}\ , \text{and} \qquad \text{E2.4-1.4}$$

$$\frac{\partial \rho}{\partial \lambda_i} = -\frac{\beta_i T}{(1+\lambda_i T)^2} \qquad \text{E2.4-1.5}$$

The parameters β_i, λ_i and Λ as well their uncertainties are given in Table 2.4-4. The uncertainty in the period (T) is negligible, since the uncertainty in ω_α is very small (only 0.005 %). The final result was 3.2 pcm. Consequently, the final value of the reactivity was 64.1 ± 3.2 pcm.

The experiment temperature was set at 20.0 °C due to the very good temperature homogenization and control of the IPEN/MB-01 reactor. The final result does not contain the uncertainty contributions of the facility parameters and in this case the benchmark value and its corresponding uncertainties are the experimental reactivity.

Example 2.4-2: Determination of the Bias-Factor due to the Calculated Effective Delayed Neutron Parameters

The second example considers the determination of the bias-factor due to the calculated effective delayed neutron parameters in the reactivity. This is applicable when the facility does not have the measured value of the effective delayed neutron parameters. The procedure here is applicable to thermal reactors fuelled with slightly enriched uranium, but it can be applied to any other situation as long as the measured effective delayed neutron parameters are available.

As a first step, the user of the Uncertainty Guide should access Section 3.6 of IPEN(MB01)-LWR-RESR-001 available in the IRPhEP Handbook. The benchmark model giving in this section has all the necessary data to model the IPEN/MB-01 reactor and from that to calculate the effective delayed neutron parameters. Having done this step, the user should select a set of periods (T) that give rise to the reactivity range that is object of the analysis. After that, the reactivity inferred from Equation 2.4-10 should be calculated employing both the calculated effective delayed neutron parameters and the benchmark ones given in Table 2.4-4. The bias induced by the calculated delayed neutron parameters can be inferred calculating the ratio C/E as described before.

A practical example of the proposed approach is described. Suppose that the user has an application that has a reactivity range from 100 through 200 pcm and the computer code MCNP®6 [2.4-26], and the nuclear data libraries ENDF/B-VII.0 [2.4-27] and JENDL-4.0 [2.4-28] are available for his analysis. The IPEN/MB-01 effective delayed neutron parameters calculated by MCNP6 are the same as those employed in Reference [2.4-29] and are given in Table E2.4-2.1.

Table E2.4-2.1. ENDF/B-VII.0 and JENDL-4.0 effective delayed neutron parameters of the IPEN/MB-01 reactor

ENDF/B-VII.0		**JENDL-4.0**	
β_i	λ_i (s^{-1})	β_i	λ_i (s^{-1})
2.20E-04 ± 1.0E-05	0.01249 ± 0.0	2.10E-04 ± 1.0E-05	0.01248 ± 0.0
1.21E-03 ± 3.0E-05	0.03172 ± 0.0	1.55E-03 ± 3.0E-05	0.03063 ± 0.0
1.20E-03 ± 3.0E-05	0.10985 ± 0.0	1.50E-03 ± 3.0E-05	0.11366 ± 3.0E-05
3.44E-03 ± 5.0E-05	0.31916 ± 2.0E-05	2.96E-03 ± 5.0E-05	0.30673 ± 5.0E-05
1.06E-03 ± 3.0E-05	1.34874 ± 8.0E-05	9.30E-04 ± 3.0E-05	1.18406 ± 5.1E-04
3.70E-04 ± 2.0E-05	8.79099 ± 4.3E-04	3.10E-04 ± 1.0E-05	3.16983 ± 3.0E-03
β_{eff} = 7.50E-3 ± 7.0E-05, Λ=(30.72 ± 0.03) μs		β_{eff} = 7.46E-3 ± 7.0E-05, Λ=(30.82 ± 0.03) μs	

The calculated and experimental reactivities in the range 100 through 200 pcm are shown in Tables E2.4.-2.2 and E2.4-2.3. The reactivities were calculated employing Equation 2.4-10 with the calculated effective delayed neutron parameters from Table E2.4-2.1 and with the experimental values from Table 2.4-4. The uncertainty in C/E was calculated employing Equation 2.4-34.

Table E2.4-2.2. Calculated and benchmark model reactivities

T (s)	ρ (pcm) ENDF/B-VII.0	ρ (pcm) Benchmark Model	C/E
50	100.8 ± 1.4	114.7 ± 5.0	0.88 ± 0.04
40	117.3 ± 1.6	133.1 ± 5.5	0.88 ± 0.04
30	141.3 ± 1.9	159.4 ± 6.2	0.89 ± 0.04
25	157.9 ± 2.1	177.5 ± 6.6	0.89 ± 0.04
15	210.8 ± 2.6	234.1 ± 8.0	0.90 ± 0.03

Table E2.4-2.3. Calculated and benchmark model reactivities

T (s)	ρ (pcm) JENDL-4.0	ρ (pcm) Benchmark Model	C/E
50	116.5 ± 1.4	114.7 ± 5.0	1.02 ± 0.04
40	135.3 ± 1.6	133.1 ± 5.5	1.02 ± 0.04
30	162.1 ± 1.9	159.4 ± 6.2	1.02 ± 0.04
25	180.5 ± 2.1	177.5 ± 6.6	1.02 ± 0.04
15	238.0 ± 2.6	234.1 ± 8.0	1.02 ± 0.04

Table E2.4-2.2 shows that the calculated reactivities are underestimated by around 12 % ± 4 %. This discrepancy should be considered as a bias-factor in the user application. The effect of the utilization of the effective delayed neutron parameters from ENDF/B-VII.0 reduces the reactivity by nearly 12 % ± 4 % in the reactivity range under consideration.

Table E2.4-2.3 shows that the calculated reactivities are overestimated by around 2 % ± 4 %. This discrepancy should be considered as a bias-factor in the user application. The effect of the utilization of the effective delayed neutron parameters from JENDL-4.0 increases the reactivity by nearly 2 % ± 4 % in the reactivity range under consideration. The bias-factor induced by JENDL-4.0 is smaller than that of ENDF/B-VII.0. JENDL-4.0 has better evaluations for the delayed neutron data for ^{235}U and ^{238}U.

Example 2.4-3: Amplified Source Multiplication (ASM) Method

The Amplified Source Multiplication (ASM) method and its improved Modified Source Multiplication (MSM) method have been widely used in the CEA's EOLE and MASURCA critical facilities over the past decades for the determination of reactivity worths by using fission chambers in subcritical configurations. The ASM methodology uses relatively simple relationships between count rates of efficient miniature fission chambers located in slightly subcritical reference and perturbed configurations. While this method works quite well for small reactivity variations, the raw results need to be corrected to take into account the flux perturbation at the fission chamber location. This is performed by applying to the measurement a correction factor called MSM. Reference 2.4-30 provides detailed descriptions of both methodologies, with their associated uncertainties.

Applications on absorber cluster worth in the MISTRAL-4 full MOX mock-up core and the last core loaded in MASURCA show the importance of the MSM correction on raw ASM data.

Example 2.4-4: Determination of Control Rod Worths in HTR-PROTEUS

The PROTEUS zero-power research reactor from the Paul Scherrer Institute (PSI) was configured as a pebble-bed reactor (PBR) critical facility from 1992 to 1996 and designated as HTR-PROTEUS. These High Temperature Reactor (HTR) experiments were assembled and conducted to investigate measurements of criticality, differential and integral control rod and safety rod worths, kinetics, reaction rates, water ingress effects, and small sample reactivity effects. This program was specifically conducted to develop benchmark calculations for the validation of reactor physics computer codes [2.4-31]. Of the four IRPhEP benchmark evaluations devoted to the evaluation of HTR-PROTEUS benchmark data only the latter three currently contain evaluated control rod worth measurement data; control rod worth experiments, however, were performed for all HTR-PROTEUS core loadings:

- PROTEUS-GCR-EXP-001
  - Cores 1, 1A, 2, and 3
  - Hexagonal Close Packing
  - 1:2 Moderator-to-Fuel Pebble Ratio
- PROTEUS-GCR-EXP-002
  - Core 4
  - Random Packing
  - 1:1 Moderator-to-Fuel Pebble Ratio
- PROTEUS-GCR-EXP-003
  - Cores 5, 6, 7, and 8
  - Columnar Hexagonal Point-On-Point Packing
  - 1:2 Moderator-to-Fuel Pebble Ratio
- PROTEUS-GCR-EXP-004
  - Cores 9 and 10
  - Columnar Hexagonal Point-On-Point Packing
  - 1:1 Moderator-to-Fuel Pebble Ratio

An important aspect of the HTR-PROTEUS experimental program was to maintain accuracy when measuring absorber rod reactivity worth across the various core configurations and moderation properties. Requirements included utilization of a methodology that was compatible with small highly reflected thermal systems; applicable to highly subcritical core loadings; have a limited dependence upon calculations; be complimentary to other techniques with characterizable uncertainties; and be economically feasible. Ultimately pulsed neutron source (PNS) and inverse kinetics (IK) techniques were selected. For small positive reactivities, such as differential control rod calibration, the stable period (SP) technique was utilized exclusively.

Perturbation analyses in geometric and material properties of HTR-PROTEUS were not performed to evaluate the uncertainty in these reactivity effects measurements as the experimental measurement uncertainties were typically greater in magnitude. For example, the slight vertical movement of a control rod position was worth < 1 ¢ for one of the withdrawable control rods. Limited measured data were available regarding typical measurement uncertainties in the HTR-PROTEUS facility; however, as indicated previously, the desire was to implement techniques and methodologies complimentary with other methods and systems.

Typical uncertainties in rod drop method measurements have been reported on the order of 5 % to 6 % for TRIGA [2.4-32] and MASURCA [2.4-33] reactors with the dominant systematic uncertainty in the kinetic constants and neutron flux perturbations and the statistical component of the uncertainty

usually < 1 %. Reported uncertainties for the SP method in a TRIGA reactor are < 10 % and account for control rod positions, rod shadowing effects, and statistical uncertainties [2.4-34]. Reported PNS measurement uncertainties applicable to rod worth measurements in HTR-PROTEUS are between 3 % and 4 % [2.4-31].

Common uncertainties include delayed neutron data that is systematic and common across all measurement methods, and flux redistribution within a subcritical core. Changes in the flux are dominated by long-lived delayed neutron precursors, whose distribution closely resembles that of the critical reactor shortly after core perturbation. Rod shadowing, or anti-shadowing, effects can also significantly impact the measured worth of a given control rod. Without detailed information regarding detectors and their positions during the HTR-PROTEUS measurements, calculations of flux form factors to account for flux redistribution and shadowing effects could not be performed [2.4-35]. Measurement values for rod bank worth measurements compared against the summation of individual rod worth measurements yielded differences between 1 % and 4 % for the withdrawable control rods and 11 % to 13 % for the safety/shutdown rods. These differences were utilized to assess a bounding uncertainty to apply as the uncertainty due to rod shadowing effects.

A total uncertainty of 6 % was selected to adequately represent the uncertainty in the IK and SP techniques implemented in HTR-PROTEUS rod worth measurements for the withdrawable controls rods and autorod. A total uncertainty of 8 % was selected for the IK and PNS techniques utilized for safety/shutdown rod worth measurements. The uncertainty in the measured worth of the safety/shutdown rods is greater than that of the control rods due to the greater impact of rod shadowing.

The impact of random pebble arrangements in Core 4 (PROTEUS-GCR-EXP-002) added an additional element of uncertainty assessment not found within the other hand-stacked pebble loadings. The uncertainty in pebble placement for the randomly packed core was experimentally investigated via three independent loadings of Core 4; a maximum uncertainty of up to 6 % in an individual control worth and ~ 1 % in the control rod bank worth was obtained [2.4-30]. Simulations of the computational models with varied pebble arrangements were found to agree with the measured data. The total uncertainty in the control rod bank worth for Core 4 remains 6 %; however, the total uncertainty in individual control rod worth measurements was increased to 9 %.

Benchmark values for absorber rod worths in Cores 4, 9, and 10 are summarized in Table E2.4-4.1. Calculated worths were obtained using MCNP5 and ENDF/B-VII.0. All calculations are within 3σ of the benchmark experiment values; the statistical uncertainty in the calculations was limited to a minimum value of ~ 1 ¢. More comprehensive details regarding the experimental data, methods, uncertainty evaluation, and benchmark model development can be found in the individual benchmark evaluation reports and a summary paper [2.4-36].

It should be noted that historic values for reactivity worths in HTR-PROTEUS were reported in dollars or cents using β_{eff} values between 720 and 730 pcm calculated using TWODANT [2.4-37]. More recent calculations were performed using the adjoint-weighted point kinetics capabilities of MCNP 5 [2.4-38 and 2.4-39] with ENDF/B-VII.0 nuclear data to determine β_{eff} values between 685 and 715 pcm for the various core configurations of HTR-PROTEUS; an uncertainty of 5 % is applied to account for the uncertainty in β_{eff} due to nuclear data parameters.

Table E2.4-4.1. Calculations of HTR-PROTEUS rod worth measurements with MCNP5 and ENDF/B-VII.0[(a)]

Core #	Measured Parameter	Method[(b)]	Benchmark Worth			Calculated Worth			$\frac{\rho_C - \rho_B}{\rho_B}$ (%)
			ρ_B	±	1σ	ρ_C	±	1σ	
4	Control Rod 1	SP	-0.40	±	0.04	-0.35	±	0.02	-13
	Control Rod 2	SP	-0.38	±	0.03	-0.34	±	0.02	-11
	Control Rod 3	SP	-0.37	±	0.03	-0.35	±	0.02	-5
	Control Rod 4	SP	-0.39	±	0.04	-0.37	±	0.02	-5
	Control Rod Bank	SP	-1.54	±	0.09	-1.44	±	0.07	-6
9	Control Rod 1	IK	-0.41	±	0.02	-0.38	±	0.02	-7
	Control Rod 2	IK	-0.41	±	0.02	-0.37	±	0.02	-10
	Control Rod 3	IK	-0.41	±	0.02	-0.38	±	0.02	-7
	Control Rod 4	IK	-0.41	±	0.02	-0.38	±	0.02	-7
	Control Rod Bank	SP	-1.58	±	0.09	-1.55	±	0.08	-2
	Partial Bank Insertion	SP	-0.73	±	0.04	-0.70	±	0.04	-4
	Autorod	IK	-0.10	±	0.01	-0.12	±	0.02	20
	Safety/Shutdown Rod 5	IK	-3.74	±	0.17	-3.78	±	0.19	1
	Safety/Shutdown Rod 6	IK & PNS	-3.82	±	0.10	-3.82	±	0.19	< 1
	Safety/Shutdown Rod 7	IK	-3.70	±	0.30	-3.82	±	0.19	3
	Safety/Shutdown Rod 8	IK	-3.60	±	0.29	-3.70	±	0.19	3
	Safety/Shutdown Rods 5+6	IK & PNS	-8.02	±	0.20	-8.03	±	0.40	< 1
	Safety/Shutdown Rods 5+7	IK	-7.44	±	0.60	-7.76	±	0.39	4
	Safety/Shutdown Rods 5+8	IK	-7.40	±	0.59	-7.69	±	0.38	4
	Safety/Shutdown Rods 5+6+7	IK & PNS	-12.11	±	0.28	-12.30	±	0.61	2
	Safety/Shutdown Rods 5+6+7+8	IK & PNS	-16.52	±	0.42	-16.98	±	0.85	3
10	Control Rod 1	IK	-0.30	±	0.02	-0.29	±	0.02	-3
	Control Rod 2	IK	-0.29	±	0.02	-0.28	±	0.02	-3
	Control Rod 3	IK	-0.29	±	0.02	-0.25	±	0.02	-14
	Control Rod 4	IK	-0.30	±	0.02	-0.28	±	0.02	-7
	Control Rod Bank	SP	-1.15	±	0.07	-1.11	±	0.06	-3
	Partial Bank Insertion	SP	-0.39	±	0.02	-0.37	±	0.02	-5
	Autorod	IK	-0.073	±	0.004	-0.08	±	0.01	10
	Safety/Shutdown Rod 5	IK	-2.82	±	0.11	-2.73	±	0.14	-3
	Safety/Shutdown Rod 6	IK & PNS	-2.82	±	0.09	-2.75	±	0.14	-2
	Safety/Shutdown Rod 7	IK	-2.80	±	0.16	-2.73	±	0.14	-2
	Safety/Shutdown Rod 8	IK	-2.72	±	0.15	-2.66	±	0.13	-2
	Safety/Shutdown Rods 5+6	IK & PNS	-5.95	±	0.17	-5.70	±	0.29	-4
	Safety/Shutdown Rods 5+7	IK	-5.73	±	0.32	-5.54	±	0.28	-3
	Safety/Shutdown Rods 5+8	IK	-5.75	±	0.33	-5.49	±	0.27	-5
	Safety/Shutdown Rods 5+6+7	IK & PNS	-9.29	±	0.21	-8.65	±	0.43	-7
	Safety/Shutdown Rods 5+6+7+8	IK & PNS	-12.67	±	0.31	-11.81	±	0.59	-7

(a) For Cores 4, 9, and 10, the calculated β_{eff} values are 694, 693, and 685 pcm, respectively.
(b) Worth measurements in the HTR-PROTEUS were performed using inverse kinetics (IK), stable period (SP), and/or pulsed neutron source (PNS) methods.

2.4.5 *References*

2.4-1 Henry, A. F. *Nuclear Reactor Theory*, Cambridge, MA, MIT Press, 1975. , G. R.

2.4-2 Keepin G. R. *Physics of Nuclear Kinetics*, Massachusetts, Addison-Wesley Publishing Company, 1965.

2.4-3 G. I. Bell and S. Glasstone, "Nuclear Reactor Theory," Van Nostrand Reinhold, New York (1970).

2.4-4 Karl O. Ott and Robert J. Neuhold, "Introductory Nuclear Reactor Dynamics," American Nuclear Society, La Grange Park, Illinois, USA, 1985.

2.4-5 Weston M. Stacey, John Wiley, "Nuclear Reactor Physics," 2001.

2.4-6 U.S. Guide to the Expression of Uncertainty in Measurement, ANSI/NCSL Z540-2-1997, p11.

2.4-7 V. F. Dean, "ICSBEP Guide to the Expression of Uncertainties," Rev. 5, September 30, 2008.

2.4-8 J. R. Harries, "Inverse Kinetics Reactivity Measurements on the Materials Testing Reactor HIFAR," Australian Atomic Energy Commission, AAEC/E456, 1978.

2.4-9 S. Carpenter, "Measurements of Control Rod Worth using ZPPR," Proc. of Spec. Meet. on Control Rod Measurement Techniques, Reactivity Worth and Power Distribution, Cadarache, April 1976.

2.4-10 J. Gauthier et al., "Comparison of Control Rod Worth of Fast Reactors," Atomnaya Energiya, vol. 66, iss. 5, May 1989.

2.4-11 Gandini, A., "ADS Subcriticality Evaluation Based on the Generalized Reactivity Concept," Annals of Nuclear Energy. Vol. 31, pp. 813-821, 2004.

2.4-12 Dulla, S., et al., "Kinetic Parameters for Source Driven Systems," PHYSOR-2006. ANS Topical Meeting on Reactor Physics Organized and hosted by the Canadian Nuclear Society. Vancouver, BC, Canada, September, 2006.

2.4-13 Gandini, A., 2001. HGPT Based Sensitivity Time-Dependent Method for the Analysis of Subcritical Systems. Annals of Nuclear Energy. Vol. 28, pp. 1193-1217, 2001.

2.4-14 A. dos Santos et. al.," A New Experimental Approach for Subcritical Reactivity Determination of Multiplying Systems," Annals of Nuclear Energy. Vol. 59, pp. 243-254, 2013.

2.4-15 M. Tsuji, "Subcriticality Measurement by Neutron Source Multiplication Method with a Fundamental Mode Extraction," Journal of Nuclear Science and Technology, Vol. 40, No. 3, p. 158–169 (March 2003).

2.4-16 Blaise, F. Mellier And P. Fougeras, Application of the Modified Source Multiplication (MSM) Technique to Subcritical Reactivity Worth Measurements in Thermal and Fast Reactor Systems, IEEE Transactions on Nuclear Science, 58(3), 1166-1176, 2011.

2.4-17 Sjöstrand, N. G., "Measurement on a Subcritical Reactor using a Pulsed Neutron Source," Arkivför Fysik, 11, 13 (1956).

2.4-18 P. Gajda et. al., "Correction Methods for Pulsed Neutron Source Reactivity Measurement in Accelerator Driven Systems," NUKLEONIKA 58(2):287−293, 2013.

2.4-19 W. Uyttenhove et. al., "Detector Positioning for the Initial Subcriticality Level Determination in Accelerator-Driven Systems," Proceedings of PHYSOR 2012 Advances in Reactor Physics Linking Research, Industry, and Education, Knoxville, Tennessee, USA, April 15-20, 2012, on CD-ROM, American Nuclear Society, LaGrange Park, IL (2012).

2.4-20 K. Kumar, "Measurement of Sub-critical Reactivity in a Heavy Water Reactor by Neutron Noise Methods using a Time Stamping Data Acquisition System," Annals of Nuclear Energy, Volume 87, Part 2, January 2016, Pages 720–727.

2.4-21 C. Dubi et. al., "Experimental Validation of Analytic Formulas for the Statistical Uncertainty in the Feynman-**α** Method," Annals of Nuclear Energy, Volume 106, August 2017, Pages 84–90.

2.4-22 Dos Santos, A., Silva, Graciete Simões de Andrade e, Fanaro, L.C.C.B., Yamaguchi, Mitsuo, Jerez, Rogério, Diniz, Ricardo, Kuramoto, Renato Yoichi Ribeiro IPEN(MB01)-LWR-RESR-001: Reactor Physics Experiments in the IPEN/MB-01 Research Reactor Facility In: International Handbook of Evaluated Reactor Physics Benchmark Experiments, ed. Paris: Nuclear Energy Agency (NEA DATA BANK), 2015, p. 1-142.

2.4-23 Dos Santos, A. et. al. "The Experimental Determination of the Relative Abundances and Decay Constants of Delayed Neutrons of the IPEN/MB-01 Reactor," PHYSOR 2004 -The Physics of Fuel Cycles and Advanced Nuclear Systems: Global Developments Chicago, Illinois, April 25-29, 2004, on CD-ROM, American Nuclear Society, Lagrange Park, IL. (2004).

2.4-24 G. D. Spriggs, " In-Pile Measurement of the Decay Constant and Relative Abundances of Delayed Neutrons," Nucl. Sci. and Eng., **114**, 342-351, (1993).

2.4-25 A. dos Santos, H. Pasqualeto, L.C.C.B. Fanaro, R. Fuga, and R. Jerez, "The Inversion Point of the Isothermal Reactivity Coefficient of the IPEN/MB-01 Reactor –1: Experimental Procedure," *Nucl. Sci. Eng*., **113**, 314 (1999).

2.4-26 T. Goorley, M. James, T. Booth, F. Brown, J. Bull, L.J. Cox, J. Durkee, J. Elson, M. Fensin, R. A. Forster, J. Hendricks, H.G. Hughes, R. Johns, B. Kiedrowski, R. Martz, S. Mashnik, G. Mckinney, D. Pelowitz, R. Prael, J. Sweezy, L. Waters, T. Wilcox, T. Zukaitis, "Initial MCNP6 Release Overview," *Nuclear Technology*, **1890**,3, 298-315 (2012).

2.4-27 Oblozinsky, O., Herman, M., Special Issue on Evaluated Nuclear Data File ENDF/B-VII.0. Nuclear Data Sheets. 107, No. 12, 2006.

2.4-28 K. Shibata, et al. "JENDL-4.0: A New Library for Nuclear Science and Engineering," *J. Nucl. Sci. Technol.* **48**, 1–30 (2011).

2.4-29 Dos Santos, A.; Diniz, R.: The Evaluation of the Effective Kinetic Parameters and Reactivity of the IPEN/MB-01 Reactor for the International Reactor Physics Experiment Evaluation Project. Nuclear Science and Engineering, v. 178, p. 459-478, 2014.

2.4-30 Patrick Blaise, Frédéric Mellier, Philippe Fougeras, "Application of the Modified Source Multiplication (MSM) Technique to Subcritical Reactivity Worth Measurements in Thermal and Fast Reactor Systems," ANIMMA International Conference– IEEE Transactions in Nuclear Science, 2009.

2.4-31 Williams, T., et al., "Critical Experiments and Reactor Physics Calculations for Low-Enriched High Temperature Gas Cooled Reactors," IAEA-TECDOC-1249, International Atomic Energy Agency, Vienna (2001).

2.4-32 C. Jammes, et al., "Comparison of Reactivity Estimations Obtained from Rod-Drop and Pulsed Neutron Source Experiments," *Ann. Nucl. Energy*, **32**, 1131 (2005).

2.4-33 G. Perret, et al., "Determination of Reactivity by a Revised Rod-Drop Technique in the MUSE-4 Programme – Comparison with Dynamic Measurements," *Proc. 7th Information Exchange Mtg. Actinide and Fission Product Partitioning and Transmutation*, Jeju, Korea, October 14-16, 2002.

2.4-34 I. Mele, et al., "TRIGA Mark II Benchmark Experiment, Part II: Pulse Operation," *Nucl. Technol.*, **105**, 52 (1994).

2.4-35 A. Trkov, et al., "Application of the Rod-Insertion Method for Control Rod Worth Measurements in Research Reactors," *Kerntechnik*, **60**, 225 (1995).

2.4-36 J. D. Bess, et al., "Benchmark Evaluation of HTR-PROTEUS Pebble Bed Experimental Program," *Nucl. Sci. Eng.*, **178**, 387 (2014).

2.4-37 R. E. Alcouffe, et al., "User's Guide for TWODANT: A Code Package for Two-Dimension, Diffusion-Accelerated, Neutral-Particle Transport," LA-10049, Rev. 1, Los Alamos National Laboratory, Los Alamos, NM (1984).

2.4-38 B. C. Kiedrowski, et al., "MCNP5-1.60 Feature Enhancements & Manual Clarifications," LA-UR-10-06217, Los Alamos National Laboratory, Los Alamos, NM (2010).

2.4-39 R. K. Meulekamp and S. C. Van der Marck, "Calculating the Effective Delayed Neutron Fraction with Monte Carlo," *Nucl. Sci. Eng.*, **152**, 142 (2006).

2.5 Reactivity Coefficient Measurements

Guidance for the determination of uncertainties for Reactivity Coefficient Measurements has not yet been formalized; however, such guidance is expected to be essentially the same as that for Reactivity Effects Measurements.

2.6 Kinetics Measurements

There are many types of Kinetic Measurements. Only guidance for the determination of uncertainties for β_{eff} Measurements are provided in this edition of the Guide. Guidance for the determination of uncertainties for other types of Kinetics Measurements has not yet been formalized.

2.6.1 Uncertainties in Measurement Methods

2.6.1.1 *Uncertainties in Measurements* of β_{eff}

The effective delayed neutron fraction (β_{eff}) plays an important role in the safety analyses of nuclear reactors because it is equal to the reactivity increment between delayed and prompt critical. Besides that, β_{eff} is important in the conversion of detector signals into reactivity through the inverse kinetics method or in the conversion of the reactor period into reactivity as in the doubling time method. Both of these methods are routinely employed in several routines during the operation of nuclear reactors. Finally, β_{eff} is also important to compare reactivity between the calculation values and the experimental values, by changing the unit of Δk obtained with transport calculation to the unit of dollars obtained from kinetics experiment.

There are several measurement techniques for the experimental determination of the delayed neutron fraction. The most common are: Cf source[2.6-1], Spectral Density (CPSD)[2.6-2], Rossi-α[2.6-3], Nelson Number[2.6-4], Feynman-α [2.6-5], and Modified Bennet[2.6-6]. However, these

measurement techniques do not directly give the β_{eff}. Instead β_{eff} is inferred from several other parameters. The most common parameters employed to infer the effective delayed neutron fraction are: adjoint fluxes, spatial-correction factors, fission rates, reactivity, neutron source strength and detector efficiency. Among those parameters, the fission rate is measured, while semi-experimental values are obtained for most of the other parameters by combination of measured results and calculated corrections. Uncertainties of these parameters and biases from several calculated factors are crucial and represent the main sources of uncertainty in these techniques.

A very brief description of each technique for β_{eff} measurements follows.

2.6.1.1a The Cf Source Method

According to the Cf source method [2.6-1], the parameter β_{eff} is obtained by:

$$\beta_{eff} = \frac{S_{Cf}}{\rho_{Cf}\, \nu\, F_{cr} F_r} \left(\frac{\Phi^{\dagger}_{Cf}}{\Phi^{\dagger}_{f}} \right) \qquad 2.6\text{-}1$$

where:

S_{Cf} = intensity of the Cf source (s^{-1})
ρ_{Cf} = reactivity introduced by the Cf source at the core center ($)
F_{cr} = fission rate at the center of the core per volume unit (s^{-1} cm^{-3})
ν = mean number of neutrons per fission at the core center
$\Phi^{\dagger}_{Cf}$ = adjoint flux of source neutrons at the core center
$\Phi\dagger_{f}$ = adjoint flux of fission neutrons at the core center
F_r = normalization factor, defined by:

$$F_r = \frac{\int_{reactor} \left(\int \chi\, \Phi^{\dagger}\, dE \right) \left(\int \nu\, \Sigma_f\, \Phi\, dE \right)}{\left(\int \chi\, \Phi^{\dagger}\, dE \right)_0 \left(\int \nu\, \Sigma_f\, \Phi\, dE \right)_0} \qquad 2.6\text{-}2$$

where the sub-index 0 in the denominator means that the integration should be performed in the core center. $\Phi^{\dagger}$ and Φ are the adjoint and direct neutron fluxes, respectively.

The measured parameters are: S_{Cf} , ρ_{Cf}, and F_{cr}. The normalization integral can be obtained by reactor power measurement or by calculations employing a calibrated miniature fission chamber at the center. The parameters ν and $\left(\frac{\Phi^{\dagger}_{Cf}}{\Phi^{\dagger}_{f}} \right)$ are calculated.

2.6.1.1b Spectral Densities

In the spectral density method, β_{eff} is obtained employing measurements of CPSD (Cross Power Spectral Density) and it is given by the following expression [2.6-3]:

$$\beta_{eff} = \frac{1}{1-\rho_{\$}} \sqrt{\frac{2D}{F_{cr}\, F_r} \left(\frac{V_1 V_2}{CPSD} \right)} \qquad 2.6\text{-}3$$

where V_1 and V_2 are quantities proportional to the signals of Detectors 1 and 2 (currents or counts, depending on the type of detectors employed), CPSD is the mean value of the cross power spectral density in the plateau region and $\rho_{\$}$ the reactivity in units of $. The other symbols have the same meaning as before. Parameters D (called Diven factor) and F_r are obtained semi-empirically; i.e., part comes from experiments and part comes from calculations. V_1, V_2, CPSD and $\rho_{\$}$ are obtained directly from measurements. It can be demonstrated that $P = (\gamma\, F_{cr}\, F_r)$, where P is the power of the facility.

This is important because most of the applications of the spectral density method employ the reactor power in the denominator of Equation 2.6-3.

2.6.1.1c Rossi-α Method

In the Rossi-α method [2.6-3].the parameter β_{eff} is obtained through the ratio of correlated to uncorrelated (background) components of the Rossi-α distribution as:

$$\beta_{eff} = \frac{1}{1+(1-\rho_\$)\sqrt{\frac{2F_{cr}\,Fr}{D}\left(\frac{C_{corr}}{C_{rand}}\right)\left(\frac{\alpha+C}{\alpha}\right)\Delta t}} \qquad 2.6\text{-}4$$

where:

C_{corr} = total counts in the correlated portion of the Rossi-α curve
C_{rand} = average number of counts per channel in the uncorrelated background
Δt = channels width
C = count rate of the detector
α = prompt neutron decay constant.
All other symbols have the same meaning as before.

Again, D and F_r are obtained in a semi-empirical way. The other parameters come from experiments, being C_{corr}, C_{rand}, Δt, C and α obtained directly from the Rossi-α experiment.

2.6.1.1d The Nelson Number Method

In the Nelson Number Method [2.6-4], the fundamental data are obtained from the Rossi-α distributions. In this method, an external neutron source of intensity *S* is inserted in the multiplicative medium in order to start the fission chains. The area under the Rossi-α curve gives the parameter β_{eff} as:

$$\beta_{eff} = \frac{-\rho_\$}{N(1-\rho_\$)^2 - \rho_\$} \qquad 2.6\text{-}5$$

where N is the Nelson number defined by:

$$N = \left(\frac{2\,g^*\,S}{g\,\nu_p D}\right)\left(\frac{A}{\alpha\,C}\right) \qquad 2.6\text{-}6$$

where:

g and g^* = spatial correction factors
ν_p = mean number of prompt neutrons per fission
A = value of the Rossi-α distribution at τ = 0 (the point where the curve intercepts the ordinate)
C = count rate of the detector
α = decay constant of prompt neutrons

The parameters A, C, α are obtained through the analysis of the Rossi-α curves. All the other parameters are obtained either by calculations or by a semi empirical way.

2.6.1.1e Feynman-α Method or Covariance-to-mean Method

In this method the β_{eff} parameter is obtained as [2.6-5]:

$$\beta_{eff} = \frac{1}{1+(1-\rho_{\$})\sqrt{\frac{a_p}{\varepsilon D}}} \qquad 2.6\text{-}7$$

where $\mathbf{a_p}$ is the amplitude of the Feynman-α distribution and **ε** is the detector efficiency defined as the ratio of detector count rate to the total fission rate integrated in the reactor. The other parameters have the same meaning as before. The measured parameters are $\mathbf{a_p}$ and $\rho_{\$}$.

2.6.1.1f Bennet Method

In the Bennet method, also called covariance method, the quantity measured is the covariance of the counts for two distinct detectors [2.6-6]. The β_{eff} parameter is given by:

$$\beta_{eff} = \sqrt{\frac{D}{F\,A_0\,(1+\rho_{\$})^2}} \qquad 2.6\text{-}8$$

where $F = (F_{cr}\,F_r)$ is the total fission rate of the reactor and A_0 is obtained through the fitting of the covariance curve versus the channel width.

2.6.1.1g Void Reactivity Measurements (VRM)

The Void Reactivity Measurement (VRM) method determines β_{eff} by measuring and calculating the worth of a void in a homogenous system and deriving β_{eff} as the ratio of the two measurements. This method is similar to methods used by Gordon Hansen to determine β_{eff} at Los Alamos National Laboratory (Reference 2.6-7). The measurement of the worth of the void is performed using stable reactor period measurements. A modified version of the In-Hour equation, shown in Equation 2.6-9, is used to derive the worth of the central void from the stable reactor period independent of β_{eff}.

$$\rho^{\$} = \sum_j ff^j \left(\sum \frac{\alpha_i^j}{1 + \lambda_i^j T_p} \right) \qquad 2.6\text{-}9$$

where:

$\rho^{\$}$	System Reactivity, $
ff^j	Fission Fraction of the j^{th} isotope
T_p	Stable Reactor Period, s
α_i	Relative Yield of i^{th} group for the j^{th} isotope
λ_i	Decay constant for i^{th} group for the j^{th} isotope

The ratio of the calculated worth and the measured worth of the void will then yield the β_{eff} for the system, as shown in Equation 2.6-10.

$$\beta_{eff} = \rho(\Delta k)/\rho(\$) \qquad 2.6\text{-}10$$

It is important to note that this method is limited to use in systems with a uniform composition where worth measurements can be very accurately measured and calculated.

The uncertainty in the β_{eff} is driven by the uncertainty in the stable reactor period measurement, the uncertainty in the delayed neutron parameters used in Equation 2.6-9, and the calculation of the void worth.

An example of the VRM method of determining β_{eff} for the Oak Ridge ORALLOY Sphere (ORSphere) is given in Example 2.6-2.

2.6.1.1h Common Functions/Parameters in Several Methods

Table 2.6-1 shows the functions/parameters that are peculiar for each method and the common parameters utilized in these methods. This table was extracted from the work of T. Sakurai et. al.[2.6-8].

Table 2.6-1. Main parameters used in different methods for β_{eff} determination

Peculiar Parameters for each method	^{252}Cf	APSD CPSD	Rossi-α	Feynman-α	Nelson	Bennet
Variance/Mean				✓		
Local Covariance						✓
Spectral Densities		✓				
Amplitude Rossi-α			✓		✓	
Cf Source Intensity	✓				✓	
Cf Source Reactivity	✓					
Detector Efficiency				✓		
Average number of Neutrons/Fission	✓					
Common Parameters to the Methods						
Fission Rate at the Center of the Core	✓	✓	✓	✓		✓
Reactivity in $		✓	✓	✓		✓
Diven Factor		✓	✓	✓	✓	✓
Normalization Factor (Power)		✓	✓	✓	✓	✓

The introduction of quantities that are external to the experiments, mainly the calculated values, hinders extremely the error propagation of the final parameter that is the object of the measurement. The case under consideration is β_{eff}. Table 2.6-1 shows several examples of these sorts of parameters. In addition to that, the Diven factor is common to all techniques excepting the Cf-source method and it introduces an uncertainty in measured β_{eff} values of about 1.3% [2.6-9].

In the context of the methods to determine β_{eff}, this parameter can be illustratively written as a product of two parts:

$$\beta_{eff} = P_c \cdot P_m,$$

where P_c refers to the calculated part and P_m to the measured part. Typical uncertainties in the calculated part, P_c , varies from 1.20 % to 3.09 %, and in the measured part, P_m, from 2.30 % to 4.30 % [2.6-10]. It is apparent from the description given so far that the number of experimental methods to infer β_{eff} are numerous and there are too many parameters to be considered. Consequently its uncertainty analysis has to be cast in a generic way.

There are other methods developed at the research reactor facility IPEN/MB-01 with which β_{eff} can be obtained directly by employing an absolute experimental determination. The developed methods employ macroscopic [2.6-11] and microscopic noise [2.6-12 and 2.6-13] and were approved as an

IRPhEP benchmark [2.6-14]. Besides the measurements of the curves APSD, CPSD and Rossi-α there are no other parameters needed in the process. The proposed method does not utilize Diven Factor, Power normalization, or any parameter from calculations or from another experiment. The experimental procedure relies solely on the measured quantities and models based on point kinetics and on the reflected-core kinetics. The process is extensively complex to be described in simple expressions as in the previous methods and they will be referred to as β_{eff} absolute measurements.

2.6.1.1i Effective Delayed Neutron Fraction Measurement Uncertainty Analysis

The uncertainties in the effective delayed neutron fraction can be classified into six categories:

1. Uncertainties in the measured parameters,
2. Uncertainties in the power normalization,
3. Uncertainty in the calculated factors,
4. Uncertainty in calibration,
5. Uncertainties in the parameters from other experiments,
6. Uncertainties from the least square approach.

The uncertainties in the measured parameters arise from the uncertainties of the CPSD/APSD, Rossi-α, and Feynman-α curves and reactivities. The uncertainty in the power normalization arises from the specific procedure to get this quantity. The uncertainty in the calculated factors arises from several sources: a) from the uncertainties in the nuclear data, b) from the calculation model, and c) from the mathematical method employed to solve the neutron transport equation. The uncertainty in calibration arises from the calibration of the ^{252}Cf source for instance. There are other sources of this type of uncertainty that may arise from the equipment employed in the experiment. The calibration of the equipment that compounds the measurement chain of a CPSD or APSD measurement should be taken into account, but in most cases this is not an easy task. The calibration of electronic equipment (such as electrometers and Dynamic Signal Analyzers) requires some certified standard equipment, but those standard equipment are not always available in reactor physics laboratories. Uncertainties from other experiments shall be considered whenever such data are employed in the determination of the β_{eff}. Example of this uncertainty category is the utilization of the Diven factor. Uncertainties from the least-square approach are those considered for the determination of some specific parameter. The uncertainty in the decay constant of prompt neutrons obtained from the Rossi-α curve is a good example of this category.

In order to get the uncertainty in the effective delayed neutron fraction for a generic method consider the general equation for the propagation of the associated uncertainties [2.6-15 and 2.6-16]. Let x_i be an independent or correlated set of variables and w(x_i) a dependent function of this set of variables. Accordingly, the uncertainty of w(x_i) is:

$$\sigma_w^2 = \sum_{i=1}^{n} \left(\frac{\partial w}{\partial x_i}\right)^2 . \sigma_i^2 + 2. \sum_{i>j}^{n} \frac{\partial w}{\partial x_i} . \frac{\partial w}{\partial x_j} . cov(x_i, x_j), \qquad 2.6\text{-}11$$

where x_i is a generic independent variable, σ_i is the uncertainty of x_i, and $\mathrm{cov}(x_i, x_j)$, is the covariance matrix of x_i and x_j.

In most of the uncertainty analyses of this section all independent variables are assumed uncorrelated. However, it is left to the evaluator judgement to perform additional analyses if necessary.

Practical examples will be illustrated in Section 2.6.4 in order to apply Equation, 2.6-11 in a real situation.

2.6.1.1j Other Uncertainty Considerations

Uncertainty in Dates

Uncertainties of dates must be considered in the case of experiments carried out with decaying isotopes. All important dates should be reported in order to better determine the isotopes' concentrations when the experiment was performed.

This uncertainty has to be propagated to the β_{eff} uncertainty through a sensitivity calculation and can be expressed as:

$$\sigma^{D}_{\beta_{eff}} = S^{D}_{\beta_{eff}} \cdot \frac{\sigma_D}{D}, \qquad 2.6\text{-}12$$

where $\sigma^{D}_{\beta_{eff}}$ is the uncertainty of the β_{eff} due to the uncertainty in date, S^{D}_{RR} is the β_{eff} sensitivity coefficient to the date, and σ_D is the date uncertainty. The subscript β_{eff} represents a generic measurement method.

Uncertainty of Temperature

The temperature uncertainty has to be propagated to the β_{eff} uncertainty through a sensitivity calculation.

This uncertainty has to be propagated to the β_{eff} uncertainty through a sensitivity calculation and can be expressed as:

$$\sigma^{T}_{\beta_{eff}} = S^{T}_{\beta_{eff}} \cdot \frac{\sigma_T}{T}, \qquad 2.6\text{-}13$$

where $\sigma^{T}_{\beta_{eff}}$ is the uncertainty of the β_{eff} due to the uncertainty in the temperature, $S^{T}_{\beta_{eff}}$ is the β_{eff} sensitivity coefficient to the temperature, and σ_T is the temperature uncertainty.

Systematic Uncertainties

The evaluation of systematic uncertainties can be presented in several ways: a) in the calibration of the equipment employed in the CPSD/APSD or Rossi-α curves, b) in the power normalization as extensively discussed in Section 2.7, c) in the Diven factors, and several other parameters. The experiment report should provide enough information so that the evaluator can judge the possible sources of systematic uncertainties.

2.6.1.1k Final β_{eff} Measurement Uncertainty

The final β_{eff} measurement uncertainty is obtained combining quadratically all uncertainty types and assuming no correlation among them. Let this uncertainty be denoted by $\sigma_{\beta_{eff_{MM}}}$; i.e., the measured method β_{eff}uncertainty for a generic measurement method. The final benchmark uncertainty for the β_{eff} measurement is given by:

$$\sigma_{\beta_{eff_{MM}}} = \sqrt{\sigma^{2}_{\beta_{eff}} + \left(\sigma^{D}_{\beta_{eff}}\right)^{2} + \left(\sigma^{T}_{\beta_{eff}}\right)^{2} + \left(\sigma^{sys}_{\beta_{eff}}\right)^{2}}, \qquad 2.6\text{-}14$$

where the subscript β_{eff} represents the β_{eff} uncertainty of any of the several measurement techniques described in this Guide or any other technique employed for the same purpose and $\sigma_{\beta_{eff}}^{sys}$ is the systematic uncertainty.

2.6.1.1l Sources of Uncertainty and Bounding Values for β_{eff} Measurements

Since there are too many methods to be considered in the uncertainty analyses and also different types (measured, calculated, semi empirical, etc.) of parameters the approach here will be to make a summary of the uncertainties by category. This is shown in Table 2.6-2a for thermal reactors and in Table 2.6-2b for fast reactors. This table shows a summary for the uncertainties and bounding values for the effective delayed neutron fraction measurements. The list is not exhaustive, but it addresses most of the uncertainties employed in the methods described previously.

Table 2.6-2a. Summary of uncertainties and bounding values for thermal reactors

Sources of Uncertainty	Typical Value	Minimum Value	Maximum Value	Type of Uncertainty (A or B) [(a)]
Measured Parameters	3.0 %	0.5 %	4.5 %	Variable
Power normalization	2.0 %	1.5 %	5.0 %	Variable
Calculated Factors	2.0 %	1.0 %	3.5 %	Variable
Calibration	2.0 %	0.5 %	5.0 %	Variable
Least Square approach	2.0 %	1.0 %	4.0 %	Variable
Measured β_{eff}	3.5 %	0.5 %	4.5 %	Variable

(a) The Uncertainty Type (A or B) has the same meaning as in ICSBEP Uncertainty Guide.

Table 2.6-2b. Summary of Uncertainties and Bounding Values for Fast Reactors

Sources of Uncertainty	Typical Value	Minimum Value	Maximum Value	Type of Uncertainty (A or B) [(a)]
Measured Parameters	3.0 %	0.5 %	4.5 %	Variable
Power normalization	2.0 %	1.5 %	5.0 %	Variable
Calculated Factors	2.0 %	1.0 %	3.5 %	Variable
Calibration	2.0 %	0.5 %	5.0 %	Variable
Least Square approach	2.0 %	1.0 %	4.0 %	Variable
Measured β_{eff}	4.0 %	1.5 %	8.0 %	Variable

(a) The Uncertainty Type (A or B) has the same meaning as in ICSBEP Uncertainty Guide.

2.6.2 Uncertainties in Experimental Configuration

This kind of uncertainty follows closely the procedure of the *ICSBEP Uncertainty Guide* [2.6-16]. Here the uncertainties are divided primarily into three categories: a) uncertainty in geometry, b) uncertainty in physics, chemistry, and isotopics of materials and c) uncertainty in the experimental configuration.

Uncertainties in the experimental configuration are the uncertainties that arise from the fact that the experiment setup is not in perfect agreement with its design, i.e. there is an uncertainty connected to the position of the detectors and auxiliary instrumentation, uncertainty of the experiment equipment composition etc., which is presented in a practical example in Section 2.7 (Example 2.7-2). The category also includes uncertainties in the environmental conditions, namely the uncertainties in basic

parameters of the experiment system which might not be of direct interest, but nevertheless affect the measured. This includes uncertainties such as those in the geometry, composition or integral physical parameters of the criticality system. An example of the evaluation of an experiment configuration uncertainty is given in Section 2.7 (Example 2.7-2).

The Effect of the Parameter Uncertainty of the Facility

This kind of uncertainty follows closely the procedure of the *ICSBEP Uncertainty Guide* [2.6-16]. Here the uncertainties are divided primarily into two categories: a) uncertainty in geometry, and b) uncertainty in physics, chemistry, and isotopic content of materials.

As an illustration, Tables 2.6-3 and 2.6-4 show, respectively the uncertainties in geometry and the uncertainties in materials. The empty columns may be filled as an aid to clarify the uncertainties. This list is not exhaustive. Different parameters will be listed for other types of configurations. Besides of the uncertainties commonly derived from the *ICSBEP Uncertainty Guide* for the facility parameters, the geometric and material uncertainties of the device (foil, fuel rod or miniature fission chamber) employed to infer the spectral indices shall be taken into consideration. The geometry and material details of the device has to be known in order to assign their specific uncertainties. Some details are shown in Tables 2.6-3 and 2.6-4. A sensitivity analysis is performed in order to propagate the geometric and material uncertainties of the facility and of the measurement device utilized to infer the β_{eff}. The final total uncertainty arising from the parameters of the facility is the square root of the sum of the squares of each component. Let this type of uncertainty be represented by σ_{PF}.

Table 2.6-3. Uncertainties in geometry

Parameter Identification	Mean Measured Value	Reported Uncertainty in Parameter	Type of Uncertainty (A or B) [(a)]	Number of Degrees of Freedom	Standard Uncertainty
Active Fuel Height					
Fuel Pellet Diameter					
Clad Outer Diameter					
Clad Inner Diameter					
Fuel Rod Pitch					
Bottom Alumina Height					
Other Relevant Parameters					

(a) The Uncertainty Type (A or B) has the same meaning as in ICSBEP Uncertainty Guide.

Table 2.6-4. Uncertainties in materials

Parameter Identification	Mean Measured Value	Reported Uncertainty in Parameter	Type of Uncertainty (A or B) [(a)]	Number of Degrees of Freedom	Standard Uncertainty
^{235}U Enrichment (%)					
UO_2 Density (g/cm^3)					
Cladding Density (g/cm^3)					
^{55}Mn in Cladding SS (wt.%)					
Cladding composition					
^{234}U (wt.%)					
UO_2 stoichiometric factor (%)					
Other Relevant Parameters					

(a) The Uncertainty Type (A or B) has the same meaning as in ICSBEP Uncertainty Guide.

2.6.3 *Uncertainties in Biases and Benchmark Models*

Biases in Benchmark Models

The determination of the biases arising from the β_{eff} measurement methods is a very complicated problem and some of them may never be found. The bias determination for the calculated quantities requires the availability of well-defined experiments for these quantities to serve as benchmarks; here referred to as Reference Values. The bias induced by these calculated factors can be understood calculating the ratio C/R, where C is the calculated quantity and R is the reference value provided by the specific available benchmarks. If C/R is higher than 1, the calculated factor overestimates the measured β_{eff}. On the other way around, the calculated factor underestimates the measured β_{eff}.

The bias in the β_{eff} measurements for a particular correction factor is given as:

$$B_{CF} = \frac{(R-C)}{C} \cdot SI_{MM} \,, \qquad 2.6\text{-}15$$

where B_{CF} is the bias for the specific calculated factor and its uncertainty arises from a standard error propagation.

The benchmark model value for the β_{eff} experiment after applying all possible biases and correction factors is given by:

$$SI_{Be} = SI_{MM} + B_{SL} + \frac{(R-C)}{C} \cdot SI_{MM}, \qquad 2.6\text{-}16$$

where $SI_{\boldsymbol{Be}}$ is the benchmark β_{eff} model, the subscript MM represents a generic measurement method, SI_{MM} is the measured reactivity, and B_{SL} is the bias from the benchmark model simplification (typically derived in Section 3 of and IRPhEP Evaluation), or by modelling limitations (typically derived in Section 4 of IRPhEP Evaluation).

Equation 2.6-16 reduces to:

$$SI_{Be} = SI_{MM} \cdot \frac{R}{C} + B_{SL}, \qquad 2.6\text{-}17$$

The ratio $\frac{R}{C}$ is defined as the bias-factor. Equation 2.6-17 can be generalized for a specific number of measurement bias as:

$$SI_{Be} = SI_{MM} \cdot B_{MM} + B_{SL}, \qquad 2.6\text{-}18$$

where $B_{MM} = \prod_{i=1}^{N_B} B_i$ is the total measurement method bias-factors , N_B is the total number of bias-factors applied to the measurement method, and B_i is the specific measurement method bias-factor. Bias in simplifications also includes the exclusion of the auxiliary devices to fix the detectors in the reactor system if not modelled in the benchmark model.

Uncertainties in Biases

Bias in measurement methods is always the inverse of the ratio of two quantities. The numerator is the calculated quantity while the denominator is the reference value. Its uncertainty can be found applying a standard propagation of the associated uncertainties assuming no correlations. The final result is given by:

$$\sigma_{B_{CF}} = \sqrt{((1/C)\cdot\sigma_R)^2 + ((R/C^2)\cdot\sigma_C)^2}, \qquad 2.6\text{-}19$$

where R and C represents the reference and the calculated values, respectively, and σ_R and σ_C are respectively the uncertainties in the specific experiment and in the calculations.

The total uncertainty in the benchmark simplification and in the benchmark limitation is given by:

$$\sigma_{B_{SL}} = \sqrt{\sigma_{B_S}^2 + \sigma_{B_L}^2}, \qquad 2.6\text{-}20$$

where σ_{B_S} is the uncertainty in the bias from simplifications and σ_{B_L} is the uncertainty in the bias from limitations.

As a starting point, the following paragraph was taken from the *ICSBEP Uncertainty Guide* [2.6-16] and adapted for β_{eff} measurements.

The evaluator should strive for a reasonable balance between making the benchmark model amenable to calculation and keeping the total β_{eff} uncertainty of the model as small as practical. Obviously, simplifications that make the benchmark model easier to use tend to make it more attractive to reactor physicist analysts. However, each simplification introduces an additional benchmark-model bias and a correlated uncertainty contribution. The use of benchmark models to validate a reactor physics analysis or to identify weaknesses in cross section data and calculational methods is more effective and reliable if the uncertainties are small. The only stage in the evaluation process where the evaluator legitimately can influence the magnitude of the total uncertainty is in deciding what simplifications to make to create the benchmark model. The **benchmark-model** is the best estimate of the value of β_{eff} that would be observed for an isolated experiment having exactly the geometry and materials described in the benchmark model. Thus one should aim at developing a benchmark model of the experiment which is simultaneously pragmatic for further evaluator's use, computationally not too demanding and free of major computational biases. This means that constructing a model with a great level of detail, which has a negligible contribution to the total benchmark-model uncertainty but significantly increases the complexity of the model and associated computational time, is not advisable. Additionally the evaluator should construct a benchmark-model including all parts of experiment that could potentially lead to the introduction of major β_{eff} biases, if not modelled. In the opposite case a rigorous study of the effect of the benchmark-model simplification on the computed β_{eff} should be performed.

Uncertainties in Benchmark Model

The uncertainties in the β_{eff} benchmark model are composed of three major parts: a) uncertainties in measurement method, b) uncertainties in biases, and c) uncertainty from the experimental configuration. These three components shall be combined quadratically in order to get the whole benchmark uncertainty.

The final benchmark uncertainty for the β_{eff} measurement method is given by:

$$\sigma^{Be}_{\beta_{eff_{MM}}} = \sqrt{\left(\sigma_{\beta_{eff_{MM}}}\cdot B_{MM}\right)^2 + \left(\beta_{eff_{MM}}\cdot\sigma_{B_{MM}}\right)^2 + \left(\sigma_{B_{SL}}\right)^2 + {\sigma_{PF}}^2}, \qquad 2.6\text{-}21$$

where $\sigma^{Be}_{\beta_{eff_{MM}}}$ is the β_{eff} benchmark uncertainty for the measurement method MM, $\sigma_{\beta_{eff_{MM}}}$ is the measured β_{eff} uncertainty from Equation 2.6-14, $\sigma_{B_{SL}} = \sqrt{\sigma^2_{B_S} + \sigma^2_{B_L}}$, σ_{B_S} is the uncertainty in the bias from simplifications and σ_{B_L} is the uncertainty in the bias from limitations.

Tables 2.6-5a and 2.6-5b show summary tables listing the uncertainties, typical values, and minimum – maximum range of values that are considered bounding for thermal and fast reactors, respectively.

Table 2.6-5a. Summary of uncertainties and bounding values for the benchmark model for thermal reactors

Sources of Uncertainty	Typical Value (%)	Minimum Value (%)	Maximum Value (%)
β_{eff} Measurement	3.5	0.5	4.5
Facility and Device Parameters	0.5	0.2	1.0
Bias	1.0	0.1	3.0
Benchmark model β_{eff}	4.0	1.2	5.0

Table 2.6-5b. Summary of uncertainties and bounding values for the benchmark model for fast reactors

Sources of Uncertainty	Typical Value (%)	Minimum Value (%)	Maximum Value (%)
β_{eff} Measurement	4.0	1.5	8.0
Facility and Device Parameters	2.0	2.0	4.0
Bias	1.0	0.1	3.0
Benchmark model β_{eff}	5.0	3.0	8.0

2.6.4 Practical Examples

Example 2.6-1: Determination of β_{eff} in *the IPEN/MB-01 Reactor*

Presented in this section is an example of the experimental determination of β_{eff} in the IPEN/MB-01 reactor [2.6-17]. In this experiment the reactor was made critical at 4.0 W and 100 W as indicated by the control room instrumentation and the control rods were kept in the automatic control mode since their movements do not interfere in the frequency region of interest. Later, these power levels were corrected by the results of the fuel rod scanning technique. The reactor was in its standard core configuration of 28 × 26 fuel rods.

The experimental procedure for the β_{eff} measurements considered here consists of obtaining the CPSD from the signals of two compensated ionization chambers (operating in current mode) in the frequency range $\lambda_i << f << \beta_{eff}/\Lambda$, where λ_i is the decay constant of the ith group of delayed neutrons

and Λ is the prompt neutron generation time. This frequency range is known as the plateau of the CPSD.

The most common form to get the CPSD is employing two detectors operating in current mode, transforming the current of the detectors into voltage signals, cutting off the DC component and sending the fluctuating component to a dynamic signal analyzer (DSA) to perform the mathematical operations to obtaining the CPSD. A typical measurement chain can be seen in Fig. E2.6-1.1. The detector currents are read by the picoameters (or electrometers), which also change the currents into voltage signals.

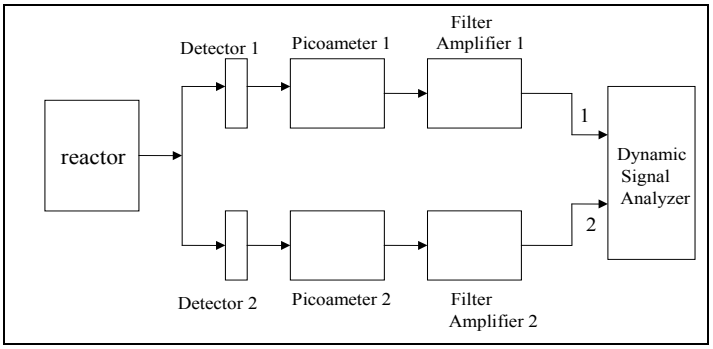

Figure E2.6-1.1. Measurement chain for obtaining the CPSD

For other types of measurement chains, the procedure for uncertainty analysis follows the one that will be presented here.

Following the Cohn's approach [2.6-18], the CPSD for the measurement chain of Fig. E2.6-1.1, assuming six groups of delayed neutrons and the point reactor model, is given by,

$$\Phi_{12}(w) = \left| \frac{\Lambda}{j\omega\Lambda + \sum_{i=1}^{6} \frac{j\omega\beta_i}{(j\omega+\lambda_i)}} \right|^2 \left(\frac{2D\gamma}{P\Lambda^2}\right) (I_1 I_2)(H_{e1}H_{f1})(H_{e2}H_{f2}) \,, \qquad \text{E2.6-1.1}$$

where,

Λ = prompt neutron generation time,
β_i = delayed neutron abundance for group i,
λ_i = decay constant of delayed neutron precursor for group i,
D = Diven factor,
γ = energy released per fission,
P = reactor power,
I_1 (I_2) = current of detector 1 (2) as read by the picoameters,
H_{e1} (H_{e2}) = transfer function of picoameter 1 (2),
H_{f1} (H_{f2}) = transfer function of filter-amplifier 1 (2),
ω = angular frequency = $2\pi f$, being f the frequency in Hz,
and j is the imaginary unit.

The transfer function of the picoameter (or electrometer) is simply the conversion factor from current to voltage, given in (Volt/Ampere) units. For instance, the conversion factor of the Keithley 614 electrometer is (2.0 Volts)/(Current Scale), so that a reading corresponding to a full scale will result in a voltage signal of 2.0 volts. The transfer function of the filter-amplifier is given only by the gain of the amplifier. The low cut off frequency of the filter, responsible for removing the DC component of

the detector's currents, does not need to be taken into account because the frequency range of interest is very away from this cut off value ($1x10^{-3}$ Hz).

In the frequency range of interest for β_{eff} determination, i.e. $\lambda_i << f << \beta_{eff}/\Lambda$, Eq. (2.6-1.1) can be written as,

$$\overline{\Phi}_{12} = \frac{2(H_{e1}H_{f1})I_1(H_{e2}H_{f2})I_2(\gamma D)}{(\beta_{eff})^2 P} \qquad \text{E2.6-1.2}$$

where now $\overline{\Phi_{12}}$ refers to the mean value of the CPSD in the plateau region. Note that the Equation E2.6-1.2 is identical to Equation 2.6-3 in Section 2.6.1:

$$\beta_{eff} = \frac{1}{1-\rho_\$}\sqrt{\frac{2D}{F_{cr}\,F_r}\left(\frac{V_1V_2}{CPSD}\right)}$$

when $\rho_\$ = 0$, since $P = (\gamma\, F_{cr}\, F_r)$, $V_x = (I_x\, H_{ex})$ and $H_{fx} = 1$.

The mean value of Φ_{12} can be obtained by averaging all points in this region and taking the standard deviation of the mean as the respective uncertainty. However, since the CPSD has intrinsic uncertainties (error bars in each frequency point) due to the measurement procedure, it seems better to obtain the mean value by a weighted least-squares fit of a constant. In this way the mean value will have an uncertainty given only by the fitting procedure. For each frequency bin, the error bar is given by[2.6-19]:

$$\varepsilon(\Phi_{12}) = \frac{1}{\sqrt{\gamma_{12}N}}(\%) \qquad \text{E2.6-1.3}$$

where γ_{12} is the measured coherence function and N is the number of RMS averages to get the final CPSD.

The two compensated ionization chambers (CC-80 from Merlin Gerin) were placed symmetrically in the west and east face of the core, approximately 11 cm away from the most external fuel rods. In this way the detectors are located in the reflector region and about 8.0 cm away from the reflected thermal neutron peak as shown in Fig. E2.6-1.2.

For these two experiments the settings of the DSA were as follow:

Input range in automatic detection
Overload rejection enabled
Anti-aliasing filter enabled
Hanning windowing enabled
DC coupling in float mode

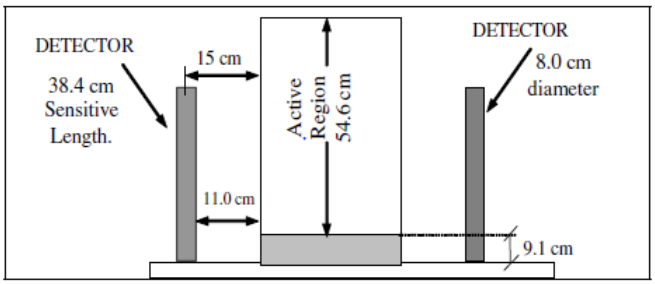

Figure E2.6-1.2. Side view of the active region and the detectors positioning

For the 4.0 W experiment, the scale of the electrometers was 2000×10^{-9} A, so that the conversion factor from current to voltage was $H_{e1} = H_{e2} = 2/2000\times10^{-9} = 1\times10^{6}$ V/A.

For the 100W experiment, the electrometers scales were 20×10^{-6} A, so that $H_{e1} = H_{e2} = 2/20\times10^{-6} = 1\times10^{5}$ V/A. The gain of the filter-amplifiers was 30 for both experiments, thus $H_{f1} = H_{f2} = 30$. The energy released per fission and the Diven factor employed in this work were $\gamma = 3.2\times10^{-11}$ J and D = 0.795 [2.6-20].

It should be stressed here that for fast reactors the Diven factor must be evaluated accordingly. The work of Shigeaki OKAJIMA, Yoshihiro YAMANE, Yoshinari TAKEMOTO and Takeshi SAKURAI [2.6-21] is a good reference for that. Regarding the Diven factor, or the neutron dispersion factor, ref. [2.6-22] gives a very complete analysis of this parameter as well as some original references about it.

One of the key parameters in Eq. (2.6-12) is the reactor power, and the details for obtaining this parameter can be found in Ref. 2.6-23. The procedure for obtaining the uncertainty in the reactor power follows closely Section 2.7 of this document.

The uncertainty of $\overline{\Phi_{12}}$ is obtained employing a least-squares approach by fitting the CPSD in the plateau region through a constant function. Here, the uncertainty sources of the Dynamic Signal Analyzer were taken into account only by the error bars of the CPSD, Eq. 2.6-3, through the coherence function. The error introduced by the windowing of the input signal of the DSA and other systematic errors, if any, were not considered explicitly in this analysis.

The uncertainties of reading the detector currents arise in two forms. Firstly the picoameters or electrometers have systematic uncertainties of around ± 1% of the reading according to the equipment data sheet. Secondly, the detectors currents present random fluctuations even for steady-state irradiation of the detector, (this is equivalent to the square root of counts when pulse mode detectors are employed). This statistical uncertainty can be estimated according to Knoll's book [2.6-24]. The contribution of the control banks motion (up and down) to the uncertainty in the absolute value of the currents reading, when in the automatic reactor control, can be neglected, since the mean value of the uncertainty generated in this way is zero (the upward motion is equally likely the downward motion). The uncertainties of all other parameters come from equipment data sheet, measurement or literature.

For the uncertainty estimate in the β_{eff} measurements, the following uncertainties were assumed (at 1σ):

- 1.0 % for the ionization chambers currents readings (from Keithley 614 electrometer data sheet).
- 1.0 % for the gain of the amplifiers (as measured in this work).
- 1.0 % for the current to voltage factor (from Keithley 614 electrometer data sheet).

- 2.0 % for the Diven factor [2.6-20 and 2.6-25].
- 1.0 % for the energy released per fission (estimated).
- 2.5 % for the reactor power (as measured in this work).

The expression for the uncertainty in the measured β_{eff} is obtained employing Eq. (2.6-9) to Eq. (2.6-12) of Section 2.6.1 and assuming no correlation among all variables, i.e. $cov(x_i,x_j)$ =0. The expression is:

$$\sigma_\beta^2 = \left(\frac{A}{2I_1^2}\sigma_{I1}^2 + \frac{A}{2I_2^2}\sigma_{I2}^2 + \frac{A}{2H_{e1}^2}\sigma_{He1}^2 + \frac{A}{2H_{e2}^2}\sigma_{He2}^2 + \frac{A}{2H_{f1}^2}\sigma_{Hf1}^2 + \frac{A}{2H_{f2}^2}\sigma_{Hf2}^2\right)\frac{\gamma D}{P\overline{\Phi_{12}}} + \left(\frac{A}{2P^2}\sigma_P^2 + \frac{A}{2\,\overline{\Phi_{12}}^2}\sigma_{\Phi 12}^2 + \frac{A}{2\gamma^2}\sigma_\gamma^2 + \frac{A}{2D^2}\sigma_D^2\right)\frac{\gamma D}{P\overline{\Phi_{12}}} \qquad \text{E2.6-1.4}$$

where $A = (H_{e1}H_{f1})I_1(H_{e2}H_{f2})I_2$.

Table E2.6-1.1 shows the results for β_{eff} and its uncertainty as well as other parameters of interest and their uncertainties. In Table E2.6-1.1 the values of the reactor power are the ones corrected by the gamma scanning method. The mean value $\overline{\Phi_{12}}$ was obtained through a fitting procedure of a constant in the plateau region of the CPSD (2 to 9 Hz approximately) and its uncertainty is only due to the least-squares approach. For both cases, 4.0 W and 100 W, the CPSD's were obtained with about 500 averages. An example of an experimental CPSD is shown in Fig. E2.6-1.3.

Table E2.6-1.1. β_{eff} and reactor noise data for the experiments

P (W)	I_1 (A)	I_2 (A)	$\overline{\Phi_{12}}$ (V^2/Hz)	β_{eff} (pcm)
4.35±0.11	(456.0±4.5)E-9	(458.0±4.6)E-9	(4.01±0.02)E-5	741±16
108.7±2.7	(11.20±0.11)E-6	(11.30±0.11)E-6	(9.74±0.09)E-6	740±16

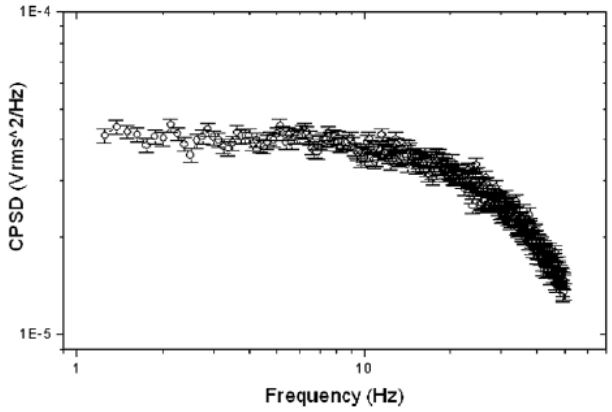

Figure E2.6-1.3. Experimental CPSD for the reactor in 4 watts. Scan rate of 100 Hz, 800 lines of resolution and 500 averages

Example 2.6-2: Determination of β_{eff} in the ORSphere using VRM

The ORSPHERE (Oak Ridge ORALLOY Sphere) measurements were performed at Oak Ridge National Laboratory in the early 1970s by Dr. John T. Mihalczo (team leader), J.J. Lynn, and J.R. Taylor. The critical and reactor physics measurements have been evaluated and found to be acceptable benchmark experiments and are evaluations HEU-MET-FAST-100 and ORSPHERE FUND-EXP-001 in the ICSBEP and IRPhEP Handbooks, respectively. The VRM Method was used to determine β_{eff} of the system.

The central void reactivity was measured and results were reported in Reference 2.6-26 and 2.6-27. The reactivity of the central void was measured by determining system reactivity for the 3.4420-inch-average-radius sphere with and without a 0.460-inch diameter uranium metal sphere present at the center of the sphere. By comparison of the sphere reactivity with and without the sphere present at the center of the ORSphere the worth of the central void was determined. The benchmark central void reactivity was 9.65 ± 0.123 ¢. The measurement process and uncertainty associated with the measured central void reactivity measurement are described below. The calculated void worth was 6.02 x10^{-4} ± 0.023 x10^{-4} Δk_{eff}. The calculation and uncertainty associated with the measured central void reactivity measurement are described below. The ratio of the measured worth in dollars and the calculated worth in Δk, with uncertainty appropriately propagated, yields the effective delayed neutron fraction, $\beta_{eff} = \rho(\Delta k)/\rho(\$)$. The benchmark β_{eff} value measured using the Void Reactivity Method was 0.00657 ± 0.00009

Measurement of the Central Void Worth

The central void worth was measured by comparing the system reactivity with and without a small sphere of uranium present at the center of the ORSPHERE. The system reactivity was determined from the measured stable reactor period using Equation 2.6-9. The measurement process to obtain the stable reactor period is described in Reference 2.6-26 as follows:

> The system was assembled with the small central sphere in place to slightly above delayed criticality by use of a small removable reflector. When the power or fission rate reached the appropriate level, the small reflector was removed in ~0.2 s. The positive stable reactor period was obtained from the reaction rate as a function of time in seven external detectors containing BF_3 that were either neutron counters or neutron sensitive ionization chambers. For the four neutron counters, the count rate was measured as a function of time; for the three ionization chambers, the output current was recorded on strip-chart recorders as a function of time. All detectors were external to the sphere at distances from 6 to 15 feet and were surrounded by at least 2 inches of paraffin moderator. The stable reactor periods were obtained graphically. The shorter reactor periods were measured over at least two decades of purely exponential change. The longer stable reactor periods were measured for at least a time period of 30 minutes of purely exponential change. The sphere was then disassembled by either raising the upper polar cap or lowering the lower section. The small, central uranium sphere was removed manually, and the system was reassembled with the small reflector in place to a power level from which the reactor period could again be measured after the small additional reflector was removed.

Multiple runs, 43, with a variable number of mass adjustment buttons on the surface of the sphere were performed on ten separate days between May 19 and August 10, 1972. Once the stable reactor periods were obtained, the Inhour equation was used to determine the system reactivity in dollars. This required the use of delayed neutron parameters. The relative yield and decay constants from

Keepin et al. for ^{235}U and ^{238}U were used.[6] The fraction of fission for ^{234}U and ^{236}U were split 50/50 between ^{235}U and ^{238}U. The fraction of fissions, obtained from neutron transport calculations by the experimenter, and Keepin data was provided in Reference 2.6-26. The system reactivity of the ORSphere with the small central sphere present, versus the reactivity with the small central sphere removed, yielded the worth of the small central sphere, or inversely, the worth of the central void region. Sample calculations of the central void region worth are given in Appendix B of ORSPHERE FUND-EXP-001. The average central void region worth given by the experimenter was 9.165 ± 0.023 ¢. According to the experimenter, J.T. Mihalczo, this value is the variance weighted average of the daily averages and standard deviations.[7] The given error is the standard deviation of the mean of all measurements with all detectors.

When evaluating the central void worth measurements additional parameters had to be taken into account. The effect of material and geometry properties were considered. These were evaluated by perturbing the model by the uncertainty in each parameter; for ORSPHERE this included isotopic composition, mass, and diameter of the central sphere. Additionally, uncertainty introduced when converting the stable reactor period to reactivity were considered. This included the effect of the delayed neutron parameters and the fission fraction. The uncertainty given in the Keepin delayed neutron parameters was assumed to be a random uncertainty. It was evaluated by propagation through Equation 2.6-9 along with a 5% uncertainty in the stable reactor period. The systematic uncertainty in the delayed neutron parameter data was evaluated by switching the Keepin data for delayed neutron parameters provided in the ABBN cross section library[8] that were derived from the delayed neutron parameters recommended by Spriggs, Campbell and Piksaikin.[9] The change in the worth using ABBN delayed neutron parameters versus the Keepin delayed neutron parameters is judged to be a bounding, systematic uncertainty effect due to uncertainty in the delayed neutron parameters. The effect due to uncertainty in the fission fraction was evaluated by switching fission fraction between those calculated using ENDF/B-VI and ENDF/B-VII. Finally, there is also an uncertainty in the treatment of the ^{234}U and ^{236}U isotopes. Because Keepin data for the delayed neutron parameters is only given for ^{235}U and ^{238}U, "half the ^{234}U fissions and half the ^{236}U were [added to] ^{235}U and the other half were in ^{238}U" (Reference 2.6-26). The uncertainty effect of this assumption is evaluated by attributing 100% of the ^{234}U and ^{236}U fissions to first ^{235}U and then to ^{236}U. The effect of all of these additional uncertainties increased the central void worth uncertainty from ±0.023 ¢ to ±0.123 ¢ with the largest contributor being the systematic uncertainty in the delayed neutron parameters.

Calculation of the Central Void Worth

The void worth was calculated by the experimenter in units of Δk using S_n transport theory, extrapolated to infinite order S_n, with a precision of at least 10^{-7} Δk. ONEDANT and XSDRNPM codes with Hansen-Roach and ENDF/B-VI cross section libraries were used. The average reactivity of the central void was $6.02 \pm 0.01 \times 10^{-4}$ Δk. According to Reference 2.6-26 this uncertainty "essentially includes all the variation in these calculated values (this choice is somewhat arbitrary but conservative)". Using deterministic methods the worth was re-calculated by the evaluator using ENDF/B-V.0, ENDF/B-VI.0 and ENDF.B-VII.0. The average re-calculated worth is 6.06×10^{-4} Δk which is 0.4 pcm above the given calculated worth of $6.02 \pm 0.01\times10^{-4}$. The 0.4 pcm difference is used as the bounding uncertainty in the calculated central void reactivity (0.23 pcm 1σ uncertainty).

[6] The Keepin et al. delayed neutron parameters were obtained from: G.R. Keepin, T.F. Wimmett, and R.K. Zeigler, *Phys. Rev.*, **107**, 1044 (1975).

[7] Personal communication with J.T. Mihalczo, November 25, 2013.

[8] Values provided by Yevgeniy Rozhikhin, December 6, 2013.

[9] G.D. Spriggs, J.M. Campbell, and V.M. Piksaikin, "An 8-Group Delayed Neutron Model Based on a Consistent Set of Half Lives," *Progress in Nuclear Energy*, **41**, No. 1-4, 223-251 (2002).

According to expert judgment[10] the uncertainties in nuclear data could contribute approximately 0.5% to the relative reactivity uncertainty for fast high enriched non-reflected uranium systems. And it was judged that by re-calculating using the three ENDF/B libraries the spread in the calculated reactivity due to discrepancies in nuclear data is accounted for and 0.23 pcm uncertainty in the calculated central void reactivity accounts for nuclear data sensitivities.

Derivation of β_{eff}

Using Equation 2.6-10, the measured and calculated central void worth and the evaluated uncertainties in each a β_{eff} of 0.00657 ± 0.00009 is derived for ORSPHERE. This method is applicable for ORSPHERE because the system is uniform and the void reactivity can be accurately calculated.

2.6.5 *References*

2.6-1 T. Sakurai and S. Okajima, "Measurement of Delayed Neutron Fraction β_{eff} by ^{252}Cf Source Method for Benchmark Experiments of β_{eff} at FCA," Prog. Nucl. Energy, v. 35, n. 2, pp. 195-202, 1999.

2.6-2 P. Chaussonet et. al., "International β_{eff} Benchmark Experiment in FCA CEA Results," Prog. Nucl. Energy, v. 35, pp. 157-162, 1999.

2.6-3 V. Doulin et, al., "The β_{eff} Measurement Results on FCA-XIX Cores," Prog. Nucl. Energy, v.35, n.2, pp. 163-168, 1999.

2.6-4 G.D. Spriggs, T. Sakurai, S.Okajima, "Rossi-α and β_{eff} Measurements in a Fast Critical Assembly," Prog. Nucl. Energy, v.35, n.2, pp.169-181, 1999.

2.6-5 T. Sakurai, H. Sodeyama and S. Okajima, "Measurement of Effective Delayed Neutrons Fraction β_{eff} by Covariance-to-Mean Method for Benchmark Experiments of β_{eff} at FCA," Prog. Nucl. Energy, v.35, n.2, pp. 203-208, 1999.

2.6-6 Y. Yamane, Y. Takemoto, T. Imai, "Effective Delayed Neutron Fraction Measurements in FCA-XIX Cores by using Modified Bennet Method," Prog. Nucl. Energy, v.35, n.2, pp. 183-194, 1999.

2.6-7 G.E. Hansen, C. Maier, "Material Replacement Experiments: Theory and Measurements for the Lady Godiva Assembly," LA-1525 (1953).

2.6-8 T. Sakurai et. Al.. "Experimental Cores for Benchmark Experiments of Effective Delayed Neutron Fraction β_{eff} at FCA," Prog. Nucl. Energy, v. 35, n. 2, p. 131, 1999.

2.6-9 A. D'angelo and J. L. Rowlands., "Conclusions Concerning the Delayed Neutron Data for the Major Actinides," *Prog. Nucl. Energy*, **41**, 1-4, p. 391 (2002).

[10] Personal email communication with E. Ivanov, February 3, 2015.

2.6-10 E. Fort et al., "Recommended Values of the Delayed Neutron Yield for: U-235; U-238 and Pu-239," *Prog. Nucl. Energy*, **41**, 1-4, p. 317 (2002).

2.6-11 R. Diniz and A. Dos Santos, "Experimental Determination of the Decay Constants and Abundances of Delayed Neutrons by Means of Reactor Noise Analysis," *Nucl. Sci. Eng*., **152**, 125-141 (2006).

2.6-12 R. Y. R. Kuramoto et al., "Absolute Measurement of β*eff* Based on Rossi-α Experiments and the Two-Region Model in the IPEN/MB-01 Research Reactor," *Nucl. Sci. and Engr* , v.158, p.272 - 283, 2008.

2.6-13 R. Y. R. Kuramoto et al., "Absolute Measurement of β*eff* based on Feynman-α experiments and the Two-Region Model in the IPEN/MB-01 Research Reactor," *Ann. Nucl. Energy*, **34**, 6, pp.433-442 (2006).

2.6-14 Dos Santos, A., Silva, Graciete Simões de Andrade e, Fanaro, L.C.C.B., Yamaguchi, Mitsuo, Jerez, Rogério, Diniz, Ricardo, Kuramoto, Renato Yoichi Ribeiro IPEN(MB01)-LWR-COEF-KIN-RESR-001: Reactor Physics Experiments In The IPEN/MB-01 Research Reactor Facility, International Handbook of Evaluated Reactor Physics Benchmark Experiments, ed. Paris: Nuclear Energy Agency (NEA Data Bank), 2009, p. 1-142.

2.6-15 U.S. Guide to the Expression of Uncertainty in Measurement, ANSI/NCSL Z540-2-1997, p11.

2.6-16 V. F. Dean, "ICSBEP Guide to the Expression of Uncertainties," Rev. 5, September 30, 2008.

2.6-17 Santos, A.; Diniz, Ricardo ; Fanaro, L.C.C.B. ; Jerez, R. ; Silva, Graciete Simões de Andrade e ; Yamaguchi, Mitsuo. A Proposal of a Benchmark for β_{eff}, β_{eff}/Lambda, Lambda of Thermal Reactors Fueled with Slightly Enriched Uranium. Annals of Nuclear Energy, v. 33, n.1, p. 848-855, 2006.

2.6-18 C.E.Cohn, A Simplified Theory of Reactor Noise, Nucl. Sci. and Eng. V.7, p.472 (1960).

2.6-19 J. S. Bendat and A. G. Piersol, "Random Data - Analysis and Measurement Procedures," Second Edition (Revised and Expanded), John Wiley, New York (1986).

2.6-20 E. F. Bennet, "An Experimental Method for Reactor-Noise Experiments of Effective Beta," Argone National Laboratory – ANL-81-72, 1981.

2.6-21 Shigeaki Okajima , Yoshihiro Yamane , Yoshinari Takemoto and Takeshi Sakurai, "A Note on the Diven Factor in Fast Systems," Journal of Nuclear Science and Technology, 37:8, 720-723, 2000.

2.6-22 Haifu Pang, "Développment des Méthodes Stochastiques et Déterministes pour la Détermination des Rendements des Neutrons Différés et du $\beta_{effectiif}$" PhD Thesis, Universite De Paris-SUD, Centre D'orsay, 1995.

2.6-23 Santos, A.; Diniz, Ricardo ; Fanaro, L.C.C.B. ; Jerez, R. ; Silva, Graciete Simões de Andrade e ; YAMAGUCHI, Mitsuo, "The Experimental Determination of the Delayed Neutron

Parameters: Beff, Beff/Lambda and Lambda of the IPEN/MB-01 Reactor," In: PHYSOR 2004- The Physics of Fuel Cycle and Advanced Nuclear Systems: Global Developments, 2004, Chicago. Illinois. PHYSOR 2004, 2004. v. 1. p. 1-1.

2.6-24 Glenn F. Knoll, "Radiation Detection and Measurement," Fourth Edition, John Willey, 2010.

2.6-25 A. M. Avramov et al, "The Measurement of the Effective Delayed Neutron Fraction in the Fast Critical Assembly BFS with Uranium-Plutonium Metal Fuel," Int. Conf. On the Physics of Reactor Operation, Design and Computation (PHYSOR 90), April (1990).

2.6-26 J.T. Mihalczo, J.J. Lynn, and J.R. Taylor, "The Central Void Reactivity in the Oak Ridge National Laboratory Enriched Uranium (93.2) Metal Sphere," *Nuc. Sci. and Eng.*, **130**, 153-163 (1998).

2.6-27 J. T. Mihalczo, J. J. Lynn, and J. R. Taylor, "The Central Void Reactivity in the Oak Ridge Enriched Uranium (93.2) Metal Sphere," ORNL/TM-13349, Oak Ridge National Laboratory (1997).

2.7 Reaction-Rate Distribution Measurements

Reaction rate measurements from neutron interactions cover a wide range of nuclear reactions. Reaction-rate measurements are flux maps, fission chamber scans, and wire-activation fine-structure and macro-structure measurements. They provide validation of the ability of the codes and nuclear data to predict the spatial distribution of neutron flux. Different materials can be employed, especially when seeking sensitivity to specific neutron spectra. Measurements can either be absolute, or relative, either to a normalizing position or average.

2.7.1 *Uncertainties in Measurement Methods*

To date, three major experimental techniques are employed to measure the reaction rates from neutron interactions:

1) Foil activation,
2) Fuel rod scanning and
3) Miniature fission chambers.

A fourth technique would be radiochemistry which is generally not common. ANL-5800 [2.7-1]. provides a good comparison with other methods (see Table 7-34 of this reference).

Techniques (1) and (2) are classified as indirect approach while Technique (3) is considered a direct approach. These three methods are employed widely in Reactor Physics. The uncertainties associated with reaction rate measurements are strongly dependent on the experimental techniques.

The goal of indirect approaches is to produce, as a product of the nuclear reaction, a radioactive isotope which emits beta or gamma rays. The reaction rate is inferred from the detector counts of the emitted radiations. Each one of those experimental techniques will be briefly described in the following subsections.

Reaction Rate Measurement Uncertainty Analysis

The uncertainties in the reaction rate measurements, i.e. experimental uncertainty, can be classified into five categories:

1. Uncertainties in the physical properties of nuclides,
2. Uncertainties in the measured quantities,
3. Uncertainties in calibration,
4. Uncertainties in the correction factor, and
5. Uncertainties arising from the least-square process.

Uncertainties in the physical quantities of nuclides are the ones arising from basic nuclear properties such as decay constants, gamma emission probabilities, gamma emission energies, isotope abundances, etc.. They are in general known from the nuclear structure and decay data available in several sites (for example http://www.nndc.bnl.gov/nudat2). They are intrinsic properties of the isotope under consideration and can be considered uncorrelated.

Uncertainties in the measured quantities are those arising from the detector counts, time, and temperature. The uncertainty in the detector counts is of statistical nature.

Uncertainties in calibration are those arising from the calibration of some specific quantities. The reactor power and the miniature fission chamber calibrated mass are good examples of this kind of uncertainty.

The uncertainty in the correction factor is that obtained when a calculation approach is employed for the determination of correction factors such as the gamma self-absorption in the foil or perturbation of the miniature fission chambers. The uncertainties arise from both: the basic nuclear data used in the process and from either the transport code or from the approximations with which the gamma or neutron flux is calculated.

Uncertainties from the least-square approach are those considered for the determination of some specific parameter or a calibration curve. The global detector efficiency (*GDE*) and the radioactive reaction product activity at the end of the irradiation, A_o, are classical examples that employ this approach. In the specific case of GDE, the covariance matrix of the fitted parameters has to be taken into consideration in the uncertainty analysis.

The categorization of uncertainties presented above offers broad guidelines for the evaluation of the experimental uncertainty of reaction rate measurements and the identification of different uncertainty sources. The categorized reaction rate uncertainties are in general considered uncorrelated. However, it is left to the evaluator judgement to perform additional analyses if necessary.

In order to get the uncertainty in the reaction rate consider the general equation for the propagation of the associated uncertainties [2.7-2 and 2.7-3]. Let x_i be an independent or correlated set of variables and $w(x_i)$ a dependent function of this set of variables. In linear approximation, the uncertainty of $w(x_i)$ is:

$$\sigma_w^2 = \sum_{i=1}^{n} \left(\frac{\partial w}{\partial x_i}\right)^2 . \sigma_i^2 + 2. \sum_{i>j}^{n} \frac{\partial w}{\partial x_i} . \frac{\partial w}{\partial x_j} . cov(x_i, x_j) \qquad 2.7\text{-}1$$

where x_i is a generic independent variable, , σ_i is the uncertainty of x_i, and $cov(x_i, x_j)$ is the covariance matrix of x_i and x_j.

2.7.1a *Foil Activation Technique*

In order to describe the uncertainty analysis of the reaction rate measurements consider initially the foil activation method, which is the simplest of the three techniques. The technique described here for foil utilization can be extended without any difficulties for wires and targets containing thin deposits

of fissile or activation materials (see ZPR-TM-424**)** which are also extensively employed for the reaction rate measurements in a reactor environment. Suppose that a foil containing some specific nuclide is exposed to a neutron flux and the nuclear reaction induced by the neutrons in the foil is represented as:

$X + n \rightarrow RRP + EP$,

where X is the foil nuclide, n is the incident neutron, RRP is the radioactive reaction product produced in the foil, and EP is the emitted particle. In this nuclear reaction the goal is to produce a radioactive nuclide, RRP , which decays either by gamma or beta emission. The emitted particle (EP) can be either gamma radiation, a proton or an alpha particle, etc. and the reaction rate is classified accordingly. Figure 2.7-1 shows schematically the behaviour of the activity of the radioactive reaction product produced (RRP) for a particular reaction type as a function of time and for a constant power history irradiation. A_0, A^∞ , t_I, t_d, and t_c shown in Figure 2.7-1 represent respectively, the activity of the RRP at the end of the irradition, the RRP saturation activity, the irradiation time, the decay time, and the detector count time.

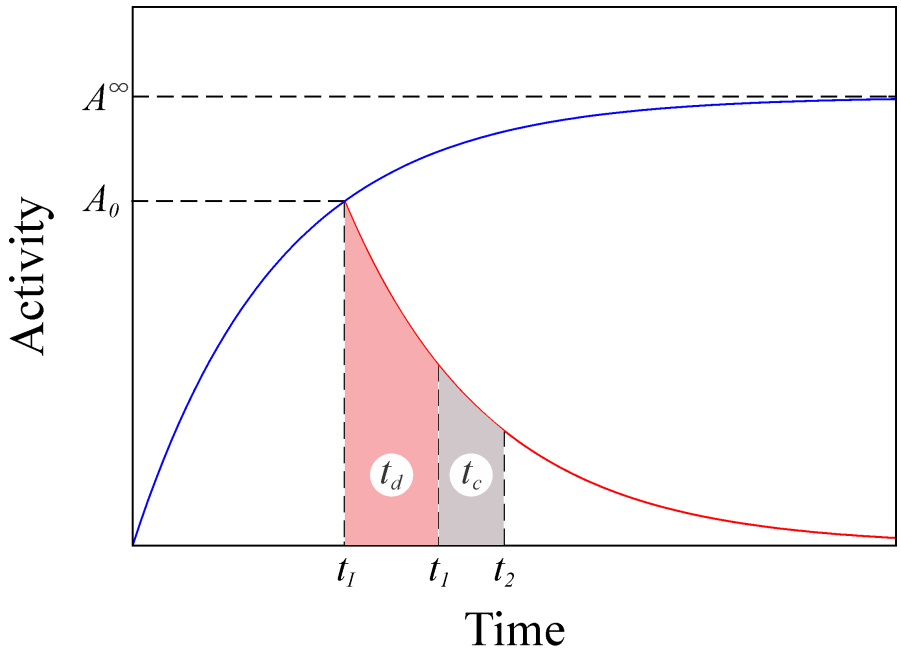

Figure 2.7-1. Radioactive reaction product activity as a function of time

Figure 2.7-1 shows clearly that the activity of the radioactive reaction product reaches a saturation value as the irradiation time goes to infinity. This saturation activity is the reaction rate that is being sought. However, the foil activation experiments are always performed in a finite irradiation time. Setting up the governing differential equation for production and destruction of the radioactive reaction product and making the following assumptions: a) the reaction rates in the target nuclide are small enough so that the atom density can be considered constant during the irradiation, b) the reactor power is constant during the irradiation period, c) the sample is inserted prior to the reactor start-up, and d) homogeneous initial condition, it can be shown that the reaction rate for the foil activation method (RR_{FAM}) is given by:

$$RR_{FAM} = \frac{A_0 \cdot F_{ramp} \cdot F_{abs} \cdot F_{SS}}{[1 - \exp(-\lambda_{RRP} \cdot t_I)]}, \qquad 2.7\text{-}2$$

with

$$A_0 = \frac{\lambda_{RRP}.C_{RRP}}{exp(-\lambda_{RRP}.t_d).\varepsilon_{RRP}.g_{RRP}.\eta_{RRP}.[1-exp(-\lambda_{RRP}.t_c)]} \quad , \qquad 2.7\text{-}3$$

where RR_{FAM} is the reaction rate for the foil activation method, all quantities with subscript (RRP) refers to the radioactive reaction product, λ_{RRP} is its decay constant, C_{RRP} is its net photopeak area (counts in the detector) for the characteristic transition at the end of the irradiation, ε_{RRP} is either the fission product yield of the radioactive reaction product (Y_{RRP}) or equal to 1.0 for other types of reactions, g_{RRP} is its gamma emission intensity, η_{RRP} is its global gamma detector efficiency, F_{ramp} is the ramp factor; i.e., a factor that transforms the real power history (from start-up and shutdown) into a constant power history for the time period when the reactor is critical, F_{abs} is the gamma self-absorption correction factor in the irradiated foil, F_{SS} is the self-shielding factor, i.e., a factor that transforms the perturbed reaction rate in the foil (due to the neutron flux depression inside of the foil) into an unperturbed reaction rate, and t_I, t_d and t_c are respectively the irradiation, the decay time and the count times. If the benchmark model models the foil explicitly there is no need to take into account F_{SS} and in this case this correction factor is equal to one.

The development above assumes that the samples are inserted prior to the reactor start-up. However, reactors often are equipped with pneumatic systems for sample irradiation, manual irradiations may be possible as well. In these cases methods shall be developed to take into account the time period when the sample is being inserted into the irradiated position and time period when sample is removed from that. The insertion and removal times are finite quantities and the sample is continuously being irradiated until it is completely inserted into the irradiated position or removed from it. Another assumption made that covers most of the cases employed in the reaction rate measurements is a linear transmutation chain with just one coupling between production and destruction of the radioactive reaction product. More complex transmutation chains shall require more complex development than that considered in this Guide. These complex cases should be considered case by case and specific analyses must be justified.

The determination of the reaction rates requires the knowledge of several parameters and correction factors. Each one of them will be considered separately in the coming subsections.

The Determination of the Global Detector Efficiency

The detection system is an integral part of the experimental setup. The measurements of the foil activity are performed in this device. This system has in the majority of cases a cylindrical form. As an illustrative example, its axial layout is schematically shown in Figure 2.7-2. The detection system is surrounded by shield materials (usually Pb) to avoid external radiation to contaminate the foil counts. The detector is usually an HPGe (High Pure Germanium Detector), but some other detectors such as NaI (Sodium Iodide) can be employed for this task. Figure 2.7-2 shows that below the detector there are sets of drawers that make it possible to change the distance to foil-detector. The foil is usually positioned in the center of the acrylic holder as shown in Figure 2.7-2. The detector is placed above the foil also as shown in Figure 2.7-2. The associated electronics are not shown in Figure 2.7-2, but they are also part of the detection system. Also, the unfolding software employed to resolve the gamma peaks is important part of the whole process of the gamma counts in a specific gamma energy photopeak.

The global detector efficiency (GDE) for gammas of energy E_γ is defined as:

$$GDE(E_\gamma) = \frac{Number\ of\ gamma\ of\ energy\ (E_\gamma)\ detected}{Number\ of\ gamma\ of\ energy\ (E_\gamma)\ emitted\ by\ the\ source} \qquad 2.7\text{-}4$$

The GDE depends on the product of two quantities: the detector efficiency and the geometric efficiency of the whole detection system. The detector intrinsic efficiency is related to the capacity of the detector to detect gamma rays. It is a property of the detector itself. The geometric efficiency depends on the geometric characteristics of the whole environment between source and detector. Quantities such as distance from source to detector, source and detector dimensions, presence of shielding and/or collimators, etc., are fundamental for the determination of the geometric efficiency.

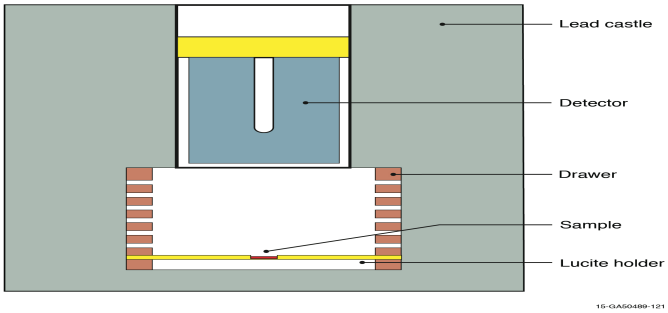

Figure 2.7-2. Foil detection system

The global detector efficiency is typically not calculated; instead it is determined by an experimental approach. This is accomplished by employing a set of calibrated standard radioactive sources that emit gammas at well-defined energies and emission intensities. Example E2.7-1 shows an example how the GDE is determined.

A_0; Foil Activity at the End of Irradiation

The determination of the foil activity at the end of irradiation $\boldsymbol{A(t_0)}$ is accomplished by performing measurements of detector counts as a function of the decay time (t_d). For each one of these measurements, the corresponding activity can be determined as:

$$A(t_d) = \frac{\lambda_{RRP}.C_{RRP}}{\varepsilon_{RRP}.g_{RRP}.\eta_{RRP}.[1-exp(-\lambda_{RRP}.t_c)]} \qquad 2.7\text{-}5$$

The corresponding $A(t_d)$ uncertainty is determined by employing standard error propagation and assuming that all independent variables are uncorrelated. The final result is:

$$\sigma_{A(t_d)} = A(t_d).\sqrt{\left(\frac{\sigma_{C_{RRP}}}{C_{RRP}}\right)^2 + \left(\frac{\sigma_{g_{RRP}}}{g_{RRP}}\right)^2 + \left(\frac{\sigma_{\eta_{RRP}}}{\eta_{RRP}}\right)^2 + \left(\frac{\sigma_{\varepsilon_{RRP}}}{\varepsilon_{RRP}}\right)^2 + B^2}, \qquad 2.7\text{-}6$$

where

$$B^2 = \left(\frac{\sigma_{\lambda_{RRP}}}{\lambda_{RRP}}\right)^2 . \left(1 - \frac{\lambda_{RRP}.t_c.e^{-\lambda_{RRP}.t_c}}{1-e^{-\lambda_{RRP}.t_c}}\right)^2 + \left(\frac{\lambda_{RRP}.\sigma_{t_c}.e^{-\lambda_{RRP}.t_c}}{1-e^{-\lambda_{RRP}.t_c}}\right)^2 . \qquad 2.7\text{-}7$$

The corresponding set of data is least-square fitted in an exponential function as:

$$A(t) = A_0 \exp\left(-\lambda_{RRP} t\right) \qquad 2.7\text{-}8$$

where the only parameter to be fitted is A_0. The decay constant of the radioactive reaction product (λ_{RRP}) given by the nuclear structure and decay library is kept constant. The $\boldsymbol{A(t_0)}$ uncertainty is given as a result of the least-square fitting process.

The Ramp Factor

F_{ramp} is a factor that transforms the real power history (from start-up and shutdown) into a constant power history for the time period that the reactor is critical. Figure 2.7-3 shows graphically the power history from a real irradiation experiment. This figure shows the sharp power rise until the desired power for the irradiation experiment and the time period when the power is maintained constant. During the sharp rise the reactor is slightly supercritical and during the constant power period the reactor is critical. When the reactor is being shut down the power drops sharply to zero.

This is the complex power history to be proposed for the benchmark model. F_{ramp} transform the real power history into a more appropriate one depicted by the area $\boldsymbol{A_I}$ in Figure 2.7-3. The quantities, A_{rp}, and A_I, in Figure 2.7-3 represent respectively, the area under the ramp and the area under the constant power region. During the ramp the reactor is slightly supercritical and in the region of constant power the reactor is critical. Figure 2.7-3 shows the signal (typically counts per second) of the detector that monitors the reactor power as a function of time. The reactor power shows a sharp ramp before reaching its stabilization. When saturation occurs at constant power, the saturation activity (A_∞) is independent of the power history during the ramp. If saturation is not reached during the irradiation period, the production of the radioactive reaction product during the ramp has to be subtracted from the total activity at the end of irradiation.

Strictly speaking, this effect has to be taken into consideration when the radioactive reaction product has a lifetime that is much longer than the irradiation period. Usually ten lifetimes is a good reference to assume that the radioactive reaction product reach equilibrium in the irradiation period. In the great majority of the reaction rate measurements this equilibrium never occurs and F_{ramp} has to be taken into consideration.

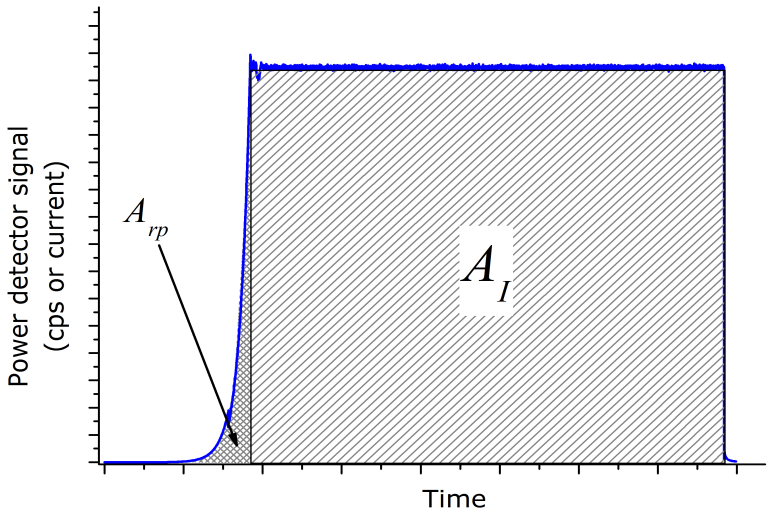

Figure 2.7-3. Power detector signal as a function of time in a typical reaction rate experiment

This transformation can be performed in the following way. Consider the transmutation equation for the radioactive reaction product, assuming homogeneous initial conditions. In the following development. It can be shown that the activity for the radioactive reaction product at time t higher than t_f, is given by:

$$A(t) = e^{-\lambda_{RRP} \cdot t} \cdot \int_0^{t_f} RR(t') \cdot e^{\lambda_{RRP} \cdot t'} \cdot dt' \quad , \qquad 2.7\text{-}9$$

where the irradiation starts at time t=0, t_I and t_f are, respectively, the time for the beginning and the end of constant power period (the reactor is critical), $A(t)$ is the radioactive reaction product activity at time t , and $RR(t')$ is the reaction rate at time t'. Since $RR(t')$ is proportional to $P(t')$; the power at time t', and noting that the activity $A(t)$ is proportional to the integral involving $RR(t')$ in Equation 2.7-9, F_{ramp} can be determined as:

$$F_{ramp} = \frac{\int_{t_i}^{t_f} P(t') \cdot e^{\lambda_{RRP} \cdot t'} \cdot dt'}{\int_0^{t_f} P(t') \cdot e^{\lambda_{RRP} \cdot t'} \cdot dt'} \approx \frac{A_I}{A_I + A_{rp}} \qquad 2.7\text{-}10$$

The ramp effect can be determined by performing the integrals in Equation 2.7-10 and it will transform the real power history into a constant power history for the time period when the reactor is critical.

One last point is the average power to be utilized in the theoretical analysis. This can be done by preserving the total number of radioactive reaction products produced between t_f and t_i. Consider $P(t')$ the power at time t' and note that $RR(t')$ is proportional to $P(t')$. Consequently:

$$\bar{P} = \frac{\int_{t_i}^{t_f} P(t') e^{\lambda t'} \lambda dt'}{e^{\lambda t_f} - e^{\lambda t_i}} \, , \qquad 2.7\text{-}11$$

where $\bar{P}$ represents the average power between t_f and t_i.

The Gamma Self-absorption Correction Factor

The gamma self-absorption correction factor (F_{abs}) corrects the reaction rate measurements due to the gamma intensity attenuation in the irradiated foil. Although the irradiation foil is in general very thin, this effect is important and has to be taken into consideration. F_{abs} can be calculated employing a Monte Carlo code such as MCNP5 [2.7-4]. However, a simple expression [2.7-5] has been found to give satisfactory results for this correction factor:

$$F_{abs} = \frac{\left(\mu/\rho\right).m}{S.\left[1 - e^{(-\mu/\rho)/(m/S)}\right]} \, , \qquad 2.7\text{-}12$$

where μ is the linear attenuation factor, and S, m, ρ, and μ/ρ are, respectively, the surface area, the mass, the density, and the mass attenuation factor of the foil.

The Self-shielding Factor

The depression of the neutron flux inside of the irradiated foil is taken into consideration by F_{SS}. This feature is depicted in Figure 2.7-4.

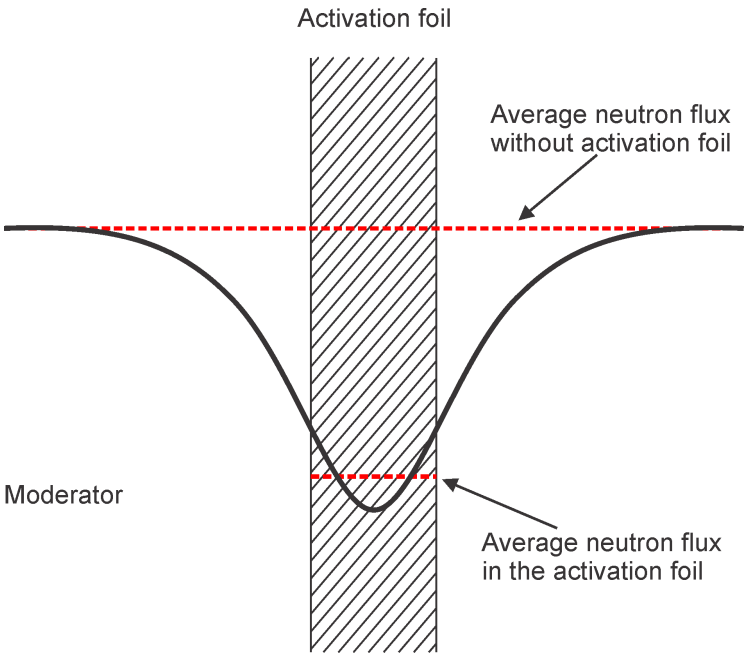

Figure 2.7-4. Neutron flux depression in the foil

Figure 2.7-4 shows that the neutron flux is attenuated inside of the foil due to the occurrence of neutron reactions. Also, there are other effects such as self-shielding in the resonances of the nuclides that takes part of the foil composition. F_{SS} is defined by:

$$F_{SS} = \frac{\int_0^\infty \sigma_{act}(E)\cdot\phi_{unp}(E)dE}{\int_0^\infty \sigma_{act}(E)\cdot\phi_{pert}(E)dE}, \qquad 2.7\text{-}13$$

where σ_{act} is the activation cross section to produce the radioactive reaction product, $\emptyset_{unp}(E)$ is the unperturbed neutron flux or the neutron flux without the foil, and $\emptyset_{pert}(E)$ is the perturbed neutron flux or the neutron flux in the presence of the foil. F_{SS} is a calculated quantity and can be determined employing a Monte Carlo code such as MCNP5 or similar, such as MATSSF [2.7-6].

The results of the reaction rate experiments are then the reaction rates without the presence of the activation foil. If the benchmark model explicitly models the activation foil, there is no need to determine F_{SS} and in this case this correction factor is equal to 1.

The Reaction Rate Measurement Uncertainty Analysis of Foil Activation Method

Applying Equation 2.7-1 to the reaction rate expression (Equation 2.7-2) and treating all independent variables as uncorrelated, the final result for the reaction rate uncertainty is:

$$\sigma_{RR_{FAM}} = RR_{FAM}\cdot \sqrt{\left(\frac{\sigma_{A_0}}{A_0}\right)^2 + \left(\frac{\sigma_{F_{ramp}}}{F_{ramp}}\right)^2 + \left(\frac{\sigma_{F_{abs}}}{F_{abs}}\right)^2 + \left(\frac{\sigma_{F_{SS}}}{F_{SS}}\right)^2 + \left(\frac{\sigma_{\lambda_{RRP}}\cdot t_I\cdot e^{-\lambda_{RRP}\cdot t_I}}{1-e^{-\lambda_{RRP}\cdot t_I}}\right)^2 + \left(\frac{\lambda_{RRP}\cdot\sigma_{t_I}\cdot e^{-\lambda_{RRP}\cdot t_I}}{1-e^{-\lambda_{RRP}\cdot t_I}}\right)^2} \qquad 2.7\text{-}14$$

The determination of σ_{RR} depends on the knowledge of the uncertainties $\sigma_{(A_0)}$, $\sigma_{F_{ramp}}$,$\sigma_{F_{abs}}$, $\sigma_{F_{SS}}$, σ_λ , and σ_{t_i}. Each one of these uncertainties will be described succinctly in the coming paragraphs.

The uncertainty in the foil activity at the end of irradiation ($\sigma_{(A_0)}$) is obtained employing a least square approach. As described in the section entitled, *Foil Activation Technique*, the measurements of

detector counts are performed for several decay times (t_d). For each one of those measurements, the corresponding activity can be determined as:

$$A(t_d) = \frac{\lambda_{RRP}.C_{RRP}}{\varepsilon_{RRP}.g_{RRP}.\eta_{RRP}.[1-\exp(-\lambda_{RRP}.t_c)]} \quad 2.7\text{-}15$$

The corresponding $A(t_d)$ uncertainty is determined by the standard error propagation as given by Equation 2.7-1. Assuming that all independent data are uncorrelated, the final result is:

$$\sigma_{A(t_d)} = A(t_d).\sqrt{\left(\frac{\sigma_{C_{RRP}}}{C_{RRP}}\right)^2 + \left(\frac{\sigma_{g_{RRP}}}{g_{RRP}}\right)^2 + \left(\frac{\sigma_{\eta_{RRP}}}{\eta_{RRP}}\right)^2 + \left(\frac{\sigma_{\varepsilon_{RRP}}}{\varepsilon_{RRP}}\right)^2 + B^2}, \quad 2.7\text{-}16$$

where:

$$B^2 = \left(\frac{\sigma_{\lambda_{RRP}}}{\lambda_{RRP}}\right)^2.\left(1 - \frac{\lambda_{RRP}.t_c.e^{-\lambda_{RRP}.t_c}}{1-e^{-\lambda_{RRP}.t_c}}\right)^2 + \left(\frac{\lambda_{RRP}.\sigma_{t_c}.e^{-\lambda_{RRP}.t_c}}{1-e^{-\lambda_{RRP}.t_c}}\right)^2, \quad 2.7\text{-}17$$

$\sigma_{C_{RRP}}$ is the uncertainty in the net detector counts. This uncertainty is given by the software (MAESTRO [2.7-7] for example) that comes with the multichannel analyser. The software considers only the net counts. Background counts are eliminated. The uncertainty in the net counts is the standard deviation of the gamma photopeak area counts. $\sigma_{\varepsilon_{RRP}}$ is the uncertainty in the fission yield for fissile or fissionable nuclides otherwise is zero. This uncertainty is available for example in the ENDF/B files (Section 8 under the reaction number (MT) 456). $\sigma_{g_{RRP}}$ and $\sigma_{\lambda_{RRP}}$ can be found in the structural and decay libraries available at the IAEA website (www-nds.iaea.org). σ_{t_l} is the uncertainty in the time scale. This uncertainty is property of the multichannel analyser employed to get the pulses from the detector to the unfolding software analysis.

The uncertainty of $\eta_{RRP}(E_\gamma)$ is determined employing the calibration curve of the detector system (GDE). This curve is built from the calibrated source data.

The global detector efficiency (GDE) is calculated for each gamma energy from Equation 2.7-4. The GDE uncertainty can be determined employing the standard error propagation given by equation 2.7.1-1 as:

$$\sigma_{GDE} = GDE\sqrt{\left(\frac{\sigma_C}{C}\right)^2 + \left(\frac{\sigma_{A_c}}{A_c}\right)^2 + \left(\frac{\sigma_i}{I}\right)^2 + \sigma_\lambda^2\left(t_s^2 + \left(\frac{t_c e^{-\lambda t_c}}{1-e^{-\lambda t_c}}\right)^2\right) + \left(\frac{\lambda\sigma_{t_c}e^{-\lambda t_c}}{1-e^{-\lambda t_c}}\right)^2 + \left(\lambda\sigma_{t_s}\right)^2}, \quad 2.7\text{-}18$$

where all independent data were assumed uncorrelated.

Here σ_{GDE} is the uncertainty in the global detector efficiency, σ_c is the uncertainty in the net detector counts provided by the unfolding software, σ_{A_c} is the uncertainty in the activity of the calibrated source. This uncertainty is provided by the source manufacturer. σ_I is the uncertainty of the gamma emission intensity. This set of data is then least-square fitted in an adequate function and the global detector efficiency can be determined for any specific gamma energy, E_γ , including that of the gamma emitted by the radioactive reaction product considered in the analysis under consideration. Let the fitting function be denoted by $\eta_{RRP}(E_\gamma)$. However, the uncertainty in $\eta_{RRP}(E_\gamma)$ for any generic gamma energy E_γ now arises from the application of the standard error propagation equation given by Equation 2.7.1 with the covariance matrix from the least-square approach. For example, for the case of $ln(\eta_{RRP}(E_\gamma)) = A + B \cdot ln(E_\gamma)$, $\sigma_{\eta_{RRP}}(E_\gamma)$ is given by:

$$\sigma_{\eta_{RRP}}(E_\gamma) = \sqrt{\left(\frac{\partial\eta_{RRP}}{\partial A}\right)^2 \cdot \sigma_A^2 + \left(\frac{\partial\eta_{RRP}}{\partial B}\right)^2 \cdot \sigma_B^2 + 2 \cdot \frac{\partial\eta_{RRP}}{\partial A} \cdot \frac{\partial\eta_{RRP}}{\partial B} \cdot cov(A,B)} \quad , \quad 2.7\text{-}19$$

where:

$$\frac{\partial \eta_{RRP}}{\partial A} = \eta_{RRP}(E_\gamma), \qquad 2.7\text{-}20$$

$$\frac{\partial \eta_{RRP}}{\partial B} = \eta_{RRP}(E_\gamma) \cdot \ln(E_\gamma), \qquad 2.7\text{-}21$$

σ_A , σ_B, cov (A,B) are given by the least square approach and cov (A,B) is the covariance of the variables A and B.

The final set of data ($A(t_d)$ and $\sigma_{(t_d)}$) is, then, least-square fitted in an exponential function as:

$$A(t) = A_0.\exp(-\lambda_{RRP}.t)\,, \qquad 2.7\text{-}22$$

where the only fitted parameter is A_0. The decay constant of the radioactive reaction product (λ_{RRP}) is given by the nuclear structure and decay library and kept constant during the fitting process. The A_0 uncertainty is given by the least-square fitting process.

$\sigma_{F_{ramp}}$ is the uncertainty in the ramp factor and can be addressed in the following way. Consider Equation 2.7-10.

$$F_{ramp} = \frac{\int_{t_i}^{t_f} P(t').e^{\lambda_{RRP}-t'}dt'}{\int_0^{t_f} P(t').e^{\lambda_{RRP}-t'}dt'} \qquad 2.7\text{-}23$$

The integrals in the numerator and denominator of F_{ramp} is performed numerically as:

$$F_{ramp} = \frac{\sum_{i=i_{init}}^{i=i_f} P(t_i).e^{\lambda_{RRP}.t_i}.\Delta t_i}{\sum_{i=i_0}^{i=i_f} P(t_i).e^{\lambda_{RRP}.t_i}.\Delta t_i}, \qquad 2.7\text{-}24$$

where Δt_i is the time interval between successive acquisitions of the detector that monitors the power, i_{init} and i_f are the index of the initial and final times for constant power regime, respectively and i_0 is the index of the initial operation time.

Now, noting that there is a linear relationship between power $P(t_i)$ and the count $C(t_i)$ of the detector that monitors the power at time count t_i , and for Δt_i constant, Equation 2.7-24 can be written as:

$$F_{ramp} = \frac{\sum_{i=i_{init}}^{i=i_f} C(t_i).e^{\lambda_{RRP}.t_i}}{\sum_{i=i_0}^{i=i_f} C(t_i).e^{\lambda_{RRP}.t_i}} \qquad 2.7\text{-}25$$

This is the starting point for the determination of $\sigma_{F_{ramp}}$. Applying a standard error propagation as given by Equation 2.7-1 in Equation 2.7.25, $\sigma_{F_{ramp}}$ can be written as:

$$\sigma_{F_{ramp}} = F_{ramp}.\sqrt{\left(\frac{\sigma_{A_1}}{A_1}\right)^2 + \left(\frac{\sigma_{A_2}}{A_2}\right)^2}, \qquad 2.7\text{-}26$$

where:

$$A_1 = \sum_{i=i_{init}}^{i=i_f} C(t_i).e^{\lambda_{RRP}.t_i}, \quad 2.7\text{-}27$$

$$A_2 = \sum_{i=i_0}^{i=i_f} C(t_i).e^{\lambda_{RRP}.t_i}, \quad 2.7\text{-}28$$

$$\sigma_{A_1} = \sqrt{\sum_{i=i_{init}}^{i=i_f} (\sigma_c.e^{\lambda_{RRP}t_i})^2 + \sum_{i=i_{init}}^{i=i_f} \left(\sigma_{\lambda_{RRP}}.t_i.e^{\lambda_{RRP}t_i}\right)^2 + \sum_{i=i_{init}}^{i=i_f} \left(\sigma_{t_i}.\lambda_{RRP}.e^{\lambda_{RRP}t_i}\right)^2}, \quad 2.7\text{-}29$$

and

$$\sigma_{A_2} = \sqrt{\sum_{i_0}^{i=i_f} (\sigma_c.e^{\lambda_{RRP}t_i})^2 + \sum_{i_0}^{i=i_f} \left(\sigma_{\lambda_{RRP}}.t_i.e^{\lambda_{RRP}t_i}\right)^2 + \sum_{i_0}^{i=i_f} \left(\sigma_{t_i}.\lambda_{RRP}.e^{\lambda_{RRP}t_i}\right)^2}. \quad 2.7\text{-}30$$

σ_c in Equations 2.7-29 and 2.7-30 represents the uncertainty of $C(t_i)$.

The uncertainties in F_{abs} and F_{SS} are more difficult to obtain because they are calculated quantities and some subjective judgements should be considered. F_{SS} is the ratio of the unperturbed to the perturbed reaction rates. In this case, it would be advisable to assign the uncertainty in each of these calculated reaction rates the error found in the literature for the comparison between theory and experiments for these reaction rates. In this case, $\sigma_{F_{corr}}$ would be given as:

$$\sigma_{F_{SS}} = F_{SS} \cdot \sqrt{\left(\frac{\sigma_{RR_{unpert}}}{RR_{unpert}}\right)^2 + \left(\frac{\sigma_{RR_{pert}}}{RR_{pert}}\right)^2}, \quad 2.7\text{-}31$$

where the subscripts, unpert and pert, refer respectively to the unperturbed and perturbed cases.

In the case of F_{abs}, Nakajima made some measurements for this correction factor [2.7-8] and concludes that the uncertainties ranges from 2 % to 3 %. This will be the range of the values adopted in this Uncertainty Guide.

The uncertainty in the irradiation time (σ_{t_i}) is usually given by the internal clock of the reactor data acquisition system. Time and power detector signal are acquired simultaneously. Generally, this equipment is very accurate and the uncertainty in the irradiation time can be considered negligible.

2.7.1b *Fuel Rod Scanning*

The fuel rod scanning technique consists of irradiation of an experimental fuel rod for a certain period of time at a specified power. After irradiation, the experimental fuel rod is taken to scanning equipment that has an opening collimator of specific size (usually 1.0 cm). The experimental approach follows closely that of the foil activation technique. The differences are that now the radioactive source is the fuel rod and there are plenty of actinides, fission products and activation nuclides formed during irradiation. The whole pattern of experimental gamma detection system, described in the section entitled *Foil Activation Technique*, can be extended to the case of fuel rod scanning. The basic measured quantities are the gamma spectra arising from the radioactive decay of fission products, actinides and structural materials of the irradiated fuel rod. The gamma spectra are usually obtained by an HPGe (High Purity Germanium) detector system. Another type of detector such as NaI can also be employed to cope with this task. This experimental technique is employed mostly to infer the neutron capture rates in the fertile nuclides and the total fission rates in the fissile and fissionable nuclides. These quantities are determined as a function of the axial position in the experimental fuel rod.

The following paragraphs describe the way to obtain the capture and fission rate distribution in an experimental fuel rod.

The essence of the proposed method to measure the reaction rates starts with the works of Nakajima [2.7-8 and 2.7-9]. The description that follows considers a fuel rod containing uranium and the measured quantities are the ^{238}U capture and total fissions. The same approach can be extended to a fuel rod containing a mixture of ^{232}Th and uranium. Furthermore, the case of mixed oxide (UO_2-PuO_2) can be performed in a straightforward fashion. In the following equations ^{143}Ce is taken as the fission product tracer. However, the equations are general and this fission product can be replaced by others such as ^{149}La. According to Nakajima the ^{238}U capture rate ($C8$) and total fission rate (F) inferred from the scanning counts are given respectively by Equations 2.7-32 and 2.7-33 as:

$$RR_{C8} = \frac{\lambda_{U9}-\lambda_{Np}}{\lambda_{U9}} \cdot \frac{A_{0Np} \cdot F_{ramp}}{f_{\gamma Np} \cdot [1-\exp(-\lambda_{Np} \cdot t_I)]}, \quad 2.7\text{-}32$$

$$RR_F = \frac{A_{0Ce} \cdot F_{ramp}}{f_{\gamma Ce} \cdot [1-\exp(-\lambda_{Ce} \cdot t_I)]}, \quad 2.7\text{-}33$$

where:

$$A_{0i} = \frac{\lambda_i C_i}{\varepsilon_i . g_i . \eta_i . [1-exp(-\lambda_i . t_c)]} \quad 2.7\text{-}34$$

is the activity of nuclide i at the end of the irradiation, the subscript i refers to nuclide i (Np for ^{239}Np, U9 for ^{239}U, or Ce for ^{143}Ce), λ_i is the decay constant of nuclide i, C_i is the photo peak intensity (counts) at the end of the irradiation for a characteristic transition of nuclide i, g_i is the gamma emission intensity of nuclide i, f_i is the fuel rod gamma self-absorption factor of nuclide i, η_i is the gamma detector efficiency for nuclide i, t_I and t_c are respectively the irradiation time, and the count time, and F_{ramp} is the ramp factor; i.e. correction due to the reactor power rise from 0 to the specified power and ε_i is either 1.0 for $C8$ or $\bar{Y}_{Ce}$;; the effective fission yield of ^{143}Ce defined by:

$$\bar{Y}_{Ce} = \frac{Y_{Ce}^{25}(\Sigma_f \Phi)_{25} + Y_{Ce}^{28}(\Sigma_f \Phi)_{28}}{(\Sigma_f \Phi)_{25} + (\Sigma_f \Phi)_{28}}, \quad 2.7\text{-}35$$

where Y_{Ce}^{i} is the ^{143}Ce fission yield for nuclide, i (25 for ^{235}U and 28 for ^{238}U), and $(\Sigma_{f\Phi})_i$ is the fission rate of nuclide i.

The determination of F_{ramp} follows the same procedure as described for the foil activation technique.

The measured quantity is C_i. The detector efficiency is obtained similarly to the foil technique. First, the detection system is gamma energy calibrated employing standard calibrated sources. A least square approach is employed to get the functional dependence of the detector efficiency and gamma energy. After that, the efficiency for any specific gamma energy and its corresponding uncertainty can be obtained, respectively, from the fitted equation and from the uncertainties of the fitted parameters and the covariance matrix among them arising from the least-square approach.

The fuel rod gamma self-absorption factor is a calculated factor and must be taken into consideration in order to have good estimates of the reaction rates in the fuel rod. The task to determine the gamma self-absorption factor for the fuel rod is not straightforward. Nakajima [2.7-8] has proposed an approach based on the Japanese MVP continuous energy Monte Carlo code that was successful for his experiment. The method to obtain this factor is described in some details by Nakajima [2.7-8 and 2.7-9]. The gamma-ray source is the gamma emitted by the radioactive decay of ^{239}Np in the case of the ^{238}U captures or the gamma-ray emitted by a specific fission product (^{143}Ce for example) in the case of the measurements of the fission rates. For the equilibrium case, the gamma source is proportional either to the ^{238}U captures or to the total fissions. These gamma sources are not radially constant

inside of the pellet. The spatial dependence along the pellet radius for the case of ^{239}Np in the equilibrium is shown in Figure 2.7-5. This Figure was extracted from Ref. 2.7-10 (Figure 1.3.2-6) and considers as an example for the case of the IPEN/MB-01 pellet. This curve is the result of simulations employing MCNP5. The radial ^{238}U neutron capture profile was calculated inside of the UO_2 pellet which was divided in 10 concentric regions of equal volume. A similar curve is found for the case of the total fission profile.

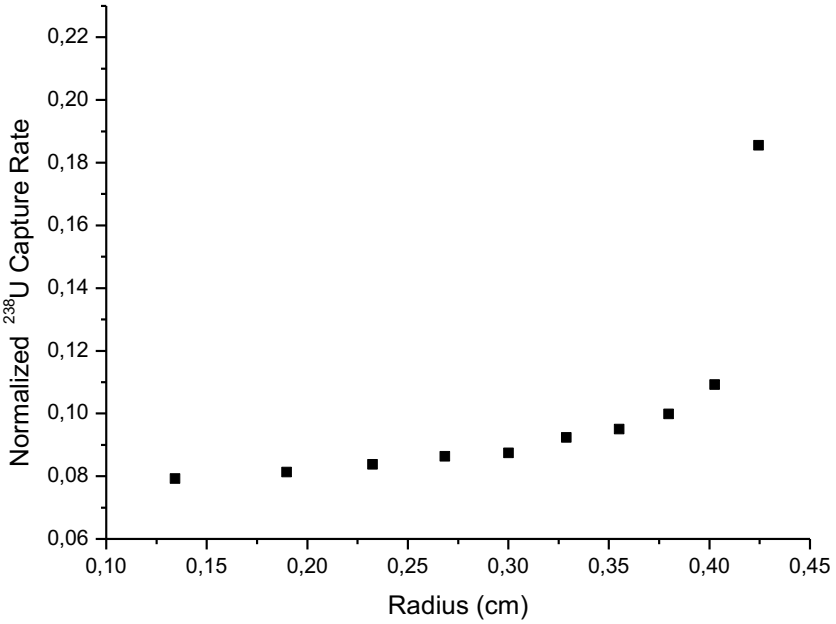

Figure 2.7-5. Normalized radial ^{238}U neutron capture profile inside the fuel rod

A typical geometry for the calculation of the fuel rod gamma self-absorption factor is shown in Figure 2.7-6. This is the scanning equipment of the IPEN/MB-01 reactor facility and it is shown here just for an illustration. This figure shows the fuel rod location in the scanning equipment, the surrounding shielding, the collimator opening and the detector. The radial gamma source is in the fuel pellets and its radial distribution is given in Figure 2.7-5. Simulations with a Monte Carlo code are performed in two distinct situations; the fuel rods with and without the fuel inside. In both cases the gamma source is present in the simulations and the tally is the gamma absorption rate in the detector. The fuel rod gamma absorption is given as the ratio of these two tallies. The procedure presented here is just to illustrate how to determine the gamma self-absorption and some other approaches can be adopted.

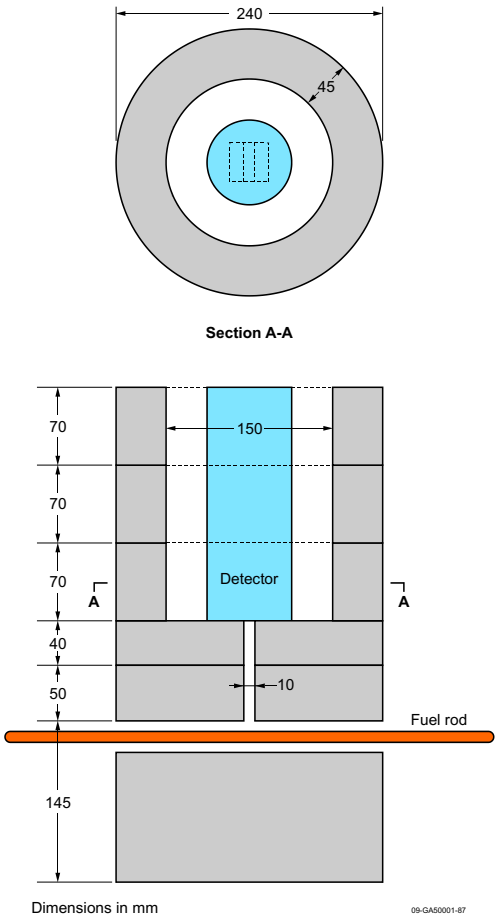

Figure 2.7-6. Schematic drawing of the scanning equipment

Reaction Rate Measurement Uncertainty Analysis of the Fuel Rod Scanning Method

The uncertainty analyses described here for the fuel rod scanning method consider the irradiation of a fuel rod containing uranium. Here only the neutron capture reaction in ^{238}U and total fissions are considered for the uncertainty analyses. The formalism described here can be extended to other types of fuel in a straightforward fashion. Applying Equation 2.7-1 to the reaction rate expression of the fuel rod scanning technique (Equations 2.7-32 and 2.7-33) and treating all independent variables uncorrelated, the final result for the reaction rate uncertainties are:

$$\sigma_{RR_{C8}} = RR_{C8} \cdot \sqrt{\left(\frac{\lambda_{Np}}{\lambda_{U9}-\lambda_{Np}} \cdot \frac{\sigma_{\lambda_{U9}}}{\lambda_{U9}}\right)^2 + \left(\frac{\sigma_{\lambda_{Np}}}{\lambda_{U9}-\lambda_{Np}}\right)^2 + \left(\frac{\sigma_{A_0}}{A_0}\right)^2 + \left(\frac{\sigma_{F_{ramp}}}{F_{ramp}}\right)^2 + \left(\frac{\sigma_{f_{\gamma Np}}}{f_{\gamma Np}}\right)^2 + B^2}, \quad 2.7\text{-}36$$

with

$$B^2 = \left[\frac{\sigma_{\lambda_{Np}\cdot t_I \cdot e^{-\lambda_{Np}\cdot t_I}}}{1-e^{-\lambda_{Np}\cdot t_I}}\right]^2 + \left[\frac{\lambda_{Np}\cdot\sigma_{t_I}\cdot e^{-\lambda_{Np}\cdot t_I}}{1-e^{-\lambda_{Np}\cdot t_I}}\right]^2,$$

$$\sigma_{RR_F} = RR_F \cdot \sqrt{\left(\frac{\sigma_{A_0}}{A_0}\right)^2 + \left(\frac{\sigma_{F_{ramp}}}{F_{ramp}}\right)^2 + \left(\frac{\sigma_{f_{\gamma Ce}}}{f_{\gamma Ce}}\right)^2 + \left[\frac{\sigma_{\lambda_{Ce}\cdot t_I \cdot e^{-\lambda_{Ce}\cdot t_I}}}{1-e^{-\lambda_{Ce}\cdot t_I}}\right]^2 + \left[\frac{\lambda_{Ce}\cdot\sigma_{t_I}\cdot e^{-\lambda_{Ce}\cdot t_I}}{1-e^{-\lambda_{Ce}\cdot t_I}}\right]^2}, \quad 2.7\text{-}37$$

The uncertainties $\sigma_{\lambda_{U9}}$, $\sigma_{\lambda_{Np}}$, and $\sigma_{\lambda_{Ce}}$ are obtained from the structural and decay data libraries. The uncertainties $\sigma_{A_{0Np}}$, $\sigma_{f_{\gamma Ce}}$, σ_{t_I} are obtained similarly to the case of the foil activation method extensively described in Section 2.7.1a, under the heading ***"The Reaction Rate Measurement Uncertainty Analysis of Foil Activation Method."***

2.7.1c *Miniature Fission Chambers*

Generally speaking, a fission chamber, whatever its size, is an airtight container filled with an inert gas of high ionization potential. Inside the container, one finds an anode and a cathode, with a fissile deposit characterizing the fission chamber. Neutrons hitting the fissile deposit induce fissions. One of the fission fragments (the heaviest one) is absorbed by the cathode and the other one ionizes the surrounding gas. The anode collects these charges and the generated signal is transported through a coaxial cable to the pre-amplifier, and then to the charge amplifier associated with a multi-channel analyser that gives a pulse spectrum that can be treated afterward. The collected charge is directly proportional to the fission rate arising in the chamber, and consequently also to the macroscopic cross section of the material used in the deposit. The major advantages of using fission chambers for reaction rate measurements are the possibility of performing these experiments on-line and, in a zero-power research reactor facility, using them for years on end, constructing a database with the characteristics of a single detector. Miniature fission chambers function on a completely identical physical basis, but exhibit one important characteristic – they are greatly reduced in size. This results in the possibility of conducting local fission rate measurements since the detectors can be positioned at any zone of interest. Another important side effect is the reduction in the perturbation that the introduction of a fission chamber and its auxiliary instrumentation induces in the reactor.

Measurements with fission chambers usually require the use of two different signal acquisition systems: a spectroscopy amplifier for detector fission spectra analysis PHA (Pulse Height Analyzer) and a fast current amplifier for time-dependent count rate detection MCS (Multi-Channel Scaler). The PHA measurement is made to obtain the so-called PHA spectrum of the fission chamber, which is represented by discriminated fission chamber pulse amplitudes arranged according to their energies. It is essential to precisely determine the PHA spectrum due to the fact that the spectrum integral is proportional to the absolute fission rate in the detector, thus being one of the main characteristics of a specific fission chamber type used in the spectral index. The MCS is connected to the monitor fission chambers in the core. Figure 2.7-7shows an example of the measured spectrum for the ^{239}Pu fission chamber which is used during the Spectral Indices measurements. Those data were acquired in the IPEN/MB-01 research reactor facility in 2007 under an agreement collaboration project between France and Brazil. It can be noted that there are two peaks in this curve. The first one is due to the alpha decay of plutonium isotopes and the second one is due to the fission fragments whose energy was deposited in the fission chamber. The overall spectrum of the fission chambers was then fitted to Equation 2.7-38.

$$f(x) = (ax + b) + (d.exp[-c(x - x_0)] + \frac{A_1}{w_1\sqrt{\pi/2}} exp\left[-2\frac{(x-x_{01})^2}{w_1^2}\right] + \frac{A_2}{w_2\sqrt{\pi/2}} exp\left[-2\frac{(x-x_{02})^2}{w_2^2}\right] \quad 2.7\text{-}38$$

where a, b, d, c, x_0, A_1, w_1, x_{01}, A_2, w_2 and x_{02} are the fitting parameters and x is the independent variable, or channels of the spectrum. Figure 2.7-7 shows the experimental data in black and the fitted data in red. The purpose of the fitting is to get the channel where the amplitude (the fission chamber counts) reaches half of the maximum value. Since there are two channel numbers that satisfy this condition, the chosen one is the highest channel number in Figure 2.7-7. This channel is called R and the integral counts are generally performed for channels above 0.3R, 0.4R and so on. The mass calibration measurement is usually performed for the threshold corresponding to the (0.4R, see below). The integral counts from the Pulse Height Analyzer are obtained from the integral of Figure 2.7-7 above some threshold channel. Usually 0.4R is the lower limit to cope with this task.

The miniature fission chamber technique is employed to get the fission density of several actinides. The main utilization is in the determination of the spectral indices but it has been utilized to normalize the power and to get the fission rate profiles in critical facilities. Axial and radial buckling measurements are direct products of the radial and axial profiles from the miniature fission chambers.

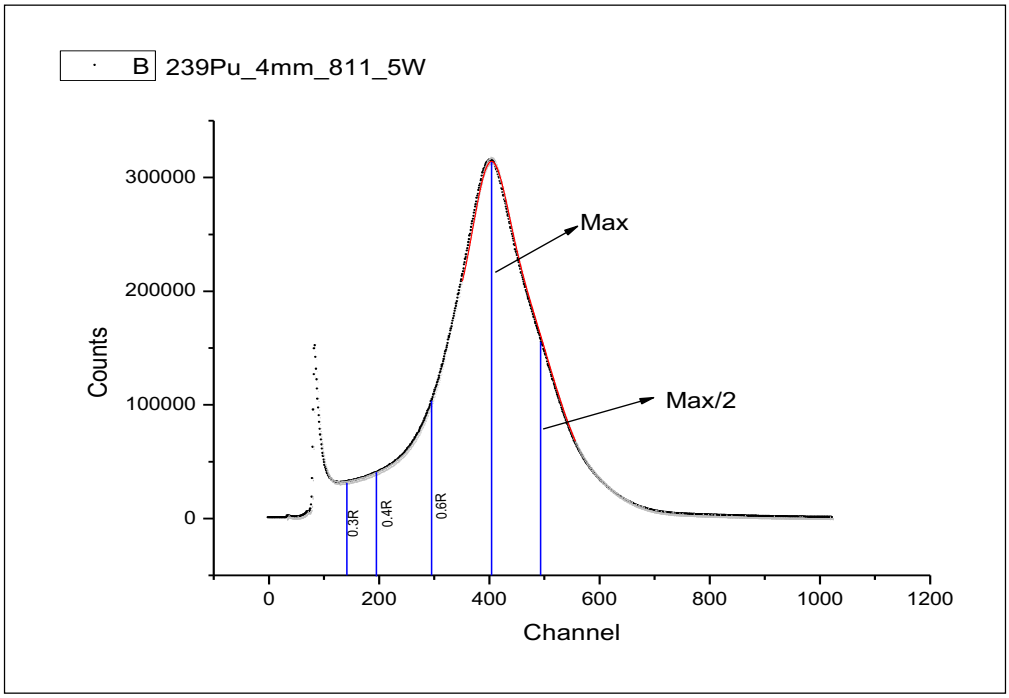

Figure 2.7-7. The miniature fission chamber spectra

The fission rates from the miniature fission chamber can be written as:

$$RR_{MFC} = C_{MFC} \cdot F_{corr} \cdot F_{cal}, \qquad 2.7\text{-}39$$

where RR_{MFC} is the fission rate of the miniature fission chamber, C_{MFC} is the miniature fission chamber counts, F_{corr} is the correction factor for perturbation induced by the miniature fission chamber and associated apparels to the local neutron flux, and F_{cal} is the calibration factor to get the absolute value of the fission rates.

The F_{corr} represents the correction factor one has to apply to the miniature fission chamber measurements for the absolute value of the fission rate at a certain location to be obtained. The meaning of the F_{corr} is similar to that discussed in the foil activation technique section in a way that it represents the perturbation which is induced in the reactor due to the presence of the measurement device and auxiliary instrumentation. Although the miniature fission chamber is relatively small it still influences the physical properties in its vicinity. Specifically a change in the material structure of the local area is induced which ultimately causes a difference in neutron transport, influencing neutron flux and spectrum. Depending on the size of the fission chamber, the experimental equipment used for the insertion in the measuring position and its material composition or the setup itself can not only affect the measured quantity, i.e. fission rate, but can have an impact on physical reactor parameters, such as the effective multiplication factor through reactivity induction. Another issue is the fact that if several pieces of measuring instrumentation is used these can be correlated through their individual local system perturbations. The extent to which the presence of the instrumentation will bias the results depends on the local conditions in the reactor as well, e.g. the unperturbed material composition of the reactor components and the neutron flux. It is therefore of great importance that

the perturbation which is introduced into the system due to the insertion of the fission chambers be estimated experimentally or through computations.

Calibration of miniature fission chambers is a complex but crucial element of uncertainty management in experimental techniques. As fission chambers are mainly used in pulse mode (count rates) in reactor physics applications (i.e., low power research reactors), we will only deal with this type of calibration. In pulse mode, each individual pulse carries information regarding the charge generated by the fission product within the fission ionization chamber. Signals can be processed as a pulse height distribution, called Pulse Height Analysis (PHA) spectrum [2.7.12.7-11. Its shape is entirely dependent on the detector characteristics like geometry and gas, and not at all on the electronics. It provides excellent signal-to-noise ratio by allowing discrimination of low amplitude pulses arising from gamma and electron interactions.

Calibration consists in establishing the relation between the measured indication and the physical quantity. Whatever mode is selected, this relation is linear for FC detectors used in saturation regime [2.7.12.7-12]. Therefore in pulse mode it can be expressed as a calibration factor representing the FC efficiency for a given discrimination threshold applied on the PHA spectrum. This factor has the dimension of a mass (g), so it is conventionally called effective mass, and is noted m_{eff}. It is an arbitrary representation depending only on the discrimination threshold. It takes into account not only fissile mass but also a number of other parameters such as detector geometry; it does not tend to the real mass of the FC deposit. The only hypothesis it requires is the stability of the PHA spectrum for reproducibility of the discrimination, whatever spectrum the FC is used in. For a fission chamber with a pure isotopic fissile deposit, it is written as:

$$m_{eff} = \frac{C(tresh)}{R_m} \qquad 2.7\text{-}40$$

where:

$C(tresh)$ is the FC count rate (s^{-1}) at a given threshold,

R_m stands for the fission rate per mass unit ($s^{-1}.g^{-1}$).

Thus, Equation 2.7-40 shows that accuracy of the calibration directly depends on the characterization of the irradiation facility at which it is performed, in terms of neutron spectrum and flux level. This is the first and main constraint which determines the choice of the irradiation facility.

Various facilities, such as the BR1 reactor at SCK-CEN, Belgium [2.7.12.7-13] or the (now closed) CALIBAN reactor at CEA Valduc Research Center [2.7-14], offer “reference” neutron fields, both in fast and purely thermal spectra. In BR1, the purely thermal spectrum is obtained into a 1m-large spherical cavity situated into the upper part of the large BR1 graphite reflector (Figure2.7-8). Both reactors are benchmarked in the ICSBEP database 2.7.12.7-15.

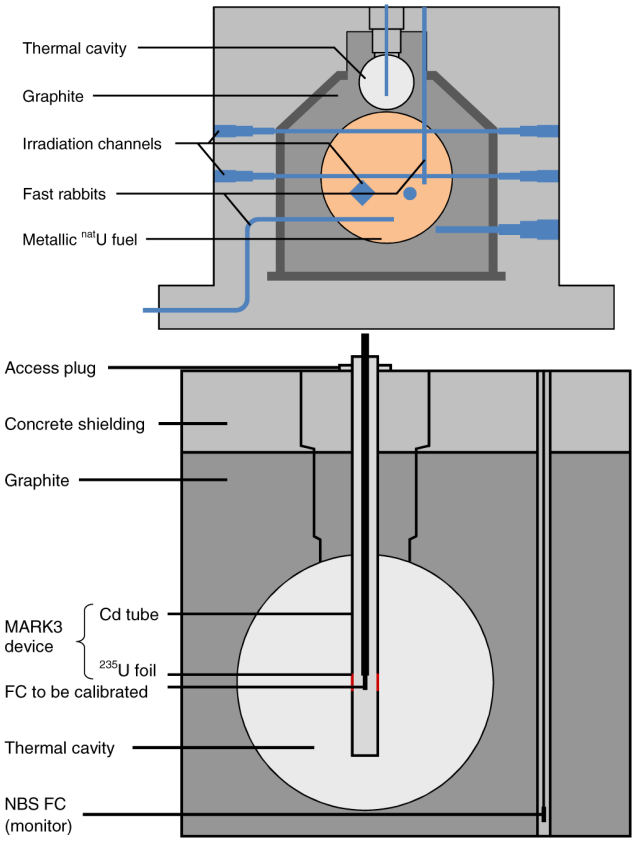

Figure 2.7-8. Schematic view of the irradiations channels and thermal column into the BR1 reactor and schematic view of the 1-m diameter BR1 spherical cavity with the MARK-3 device inserted (from 2.7.12.7-13)

Fast spectra are obtained using a conversion device called MARK-3 that allows the conversion of thermal neutrons into purely fast fission neutrons. It is made of a ^{235}U sheet surrounded by Cd-filter in order to minimize as much as possible the thermal part of the spectrum at the calibration location. The device is reproduced on Figure 2.7-8 right. More details of the miniature fission chamber calibration can be found in Appendix B.

A practical example of the evaluation of the bias in fission rates due to the use of guide tubes for the insertion of miniature fission chambers is presented in the Section 2.7.4, Example 2.7-2 (example Estimation of perturbation due to a miniature fission chamber).

With the development of advanced Monte Carlo methods for neutron transport calculations, which enable detailed experiment modelling, it is common practice to include as much of the basic information regarding fission chamber response and geometry as possible in order to avoid the need for the use of the Fcorr correction factor. An example of the detailed modelling of a miniature fission chamber and its response is described in Section 2.7.4, Example 2.7-2 (example Modelling of the miniature fission chamber response).

Reaction Rate Measurement Uncertainty Analysis for the Miniature Fission Chamber Technique

The uncertainty analysis applied to the miniature fission chamber measurements is accomplished applying Equation 2.7-1 to Equation 2.7-39 and assuming all independent data uncorrelated. The final result is:

$$\sigma_{RR_{MFC}} = \sqrt{\left(\frac{\sigma_{C_{MFC}}}{C_{MFC}}\right)^2 + \left(\frac{\sigma_{F_{corr}}}{F_{corr}}\right)^2 + \left(\frac{\sigma_{F_{cal}}}{F_{cal}}\right)^2}, \quad 2.7\text{-}41$$

where $\sigma_{C_{MFC}}$, $\sigma_{F_{corr}}$,and $\sigma_{F_{cal}}$ represent the uncertainties, respectively, in the miniature fission chamber counts, in the calculated correction factor, and in the calibration factor.

2.7.1d *Neutron Flux Determination*

Neutron flux is determined from the reaction rate as:

$$\Phi(r) = \frac{R_i^j(r)}{\overline{\sigma_i^J}}, \quad 2.7\text{-}42$$

where $\phi(r)$ is the neutron flux at position, r, $R_i^j(r)$ is the reaction rate per target nuclide of nuclide, i , at position, r, and $\overline{\sigma_i^J}$ is the flux weighted microscopic cross section of nuclide, i, for nuclear reaction, j, given by:

$$\overline{\sigma_i^J} = \frac{\int\int_0^\infty \sigma_i^j(E)\phi(r,E)dEd^3r}{\int\int_0^\infty \phi(r,E)dEd^3r}, \quad 2.7\text{-}43$$

where E is the neutron Energy, $\phi(r,E)$is the neutron flux at position r and energy E, and the space integral is performed in the volume where the reaction rate was measured. R_i^j is related to the reaction rate RR_i^j as defined in this section as:

$$R_i^j = \frac{RR_i^j}{N_i}, \quad 2.7\text{-}44$$

where i refers to nuclide i, RR_i^j is the reaction rate for nuclide i for nuclear reaction j, and N_i the total number of atoms of nuclide i in the measurement device (either foil, wire, fuel rod, or miniature fission chamber).

Neutron Flux Uncertainty Analysis

The uncertainty analysis applied to the neutron flux is accomplished applying Equation 2.7-1 to Equation 2.7-42, and assuming no correlation among the parameters. The final result is:

$$\sigma_{\Phi(r)} = \Phi(r)\sqrt{\left(\frac{\sigma_{RR_i^j(r)}}{RR_i^j(r)}\right)^2 + \left(\frac{\sigma_{N_i}}{N_i}\right)^2 + \left(\frac{\sigma_{\overline{\sigma_i^j}}}{\overline{\sigma_i^j}}\right)^2}. \quad 2.7\text{-}45$$

$\sigma_{RR_i^j(r)}$ is the reaction rate uncertainty of the several categories as defined in this section and $\sigma_{\overline{\sigma_i^J}}$ is the uncertainty in the average microscopic cross section, $\overline{\sigma_i^J}$.

2.7.1e *Relative Reaction Rates*

Relative reaction rates are defined as:

$$RR_{relt} = \frac{RR}{RR_{ref}}, \quad 2.7\text{-}46$$

where RR is the reaction rate of the several categories as defined in this section, and RR_{ref} is a reference reaction rate; which can be either a specific reaction rate in a specific position or an average value. If both RR and RR_{ref} arise from the same operation and if the device that perform the measurements (either foil, wire, fuel rod, or miniature fission chamber) is the same, Equation 2.7-46 yields the following expression for the relative reaction rate:

$$RR_{relt} = \frac{A_0}{A_{0ref}}. \qquad 2.7\text{-}47$$

Equation 2.7-47 was derived by substituting Equation 2.7-2 into 2.7-46. Several terms of Equation 2.7-2 cancel and the final expression for RR_{relt} became just the ratio of the activities or counts at the end of the irradiation. If the operation is the same but the measurement device is not, only F_{ramp} cancels in Equation 2.7-2 and the power uncertainty does not need to be taken into consideration. In the other way around all terms of Equation 2.7-2 must be considered and the procedure of Section 2.3 shall be adopted.

Relative Reaction Rate Uncertainty Analysis

Consider that the operation and the measurement device to be the same. In this case, applying Equation 2.7-1 to Equation 2.7-47, and assuming no correlation among the parameters yields:

$$\sigma_{RR_{relt}} = RR_{relt}\sqrt{\left(\frac{\sigma_{A_0}}{A_0}\right)^2 + \left(\frac{\sigma_{A_{0ref}}}{A_{0ref}}\right)^2} \qquad 2.7\text{-}48$$

If the operation is the same but the measurement device is not, the application of Equation 2.7-1 to Equation 2.7-47 and assuming no correlation among parameters yields:

$$\sigma_{RR_{relt}} = RR_{relt}\sqrt{\left(\frac{\sigma_{RR}}{RR}\right)^2 + \left(\frac{\sigma_{RR_{ref}}}{RR_{ref}}\right)^2} \qquad 2.7\text{-}49$$

where both σ_{RR} and $\sigma_{RR_{ref}}$ are given by Equation 2.7-14 but in this case F_{ramp} is equal to 1.0 and $\sigma_{F_{ramp}}$ is equal to zero. In the other way around all terms of Equation 2.7-2 must be considered and the procedure of Section 2.3 shall be adopted.

2.7.1f *Other Uncertainty Considerations*

Uncertainty in Dates

Uncertainties of dates must be considered in the case of experiments carried out with decaying isotopes. All important dates should be reported in order to better determine the isotopes' concentrations when the experiment was performed.
This uncertainty has to be propagated to the reaction rate uncertainty through a sensitivity calculation and can be expressed as:

$$\sigma_{RR}^{D} = S_{RR}^{D} \cdot \frac{\sigma_D}{D} \qquad 2.7\text{-}50$$

where σ_{RR}^{D} is the uncertainty of the reaction rate due to the uncertainty in date, $S_{RR}^{D}$is the reaction rate sensitivity coefficient to the date, and σ_D is the date uncertainty. The subscript RR represents a generic reaction from a generic measurement method.

Uncertainty of Temperature

The temperature uncertainty has to be propagated to the reaction rate uncertainty through a sensitivity calculation.

This uncertainty has to be propagated to the reaction rate uncertainty through a sensitivity calculation and can be expressed as:

$$\sigma_{RR}^{T} = S_{RR}^{T} \cdot \frac{\sigma}{T} \qquad 2.7\text{-}51$$

where σ_{RR}^{T} is the uncertainty of the reaction rate due to the uncertainty in the temperature, $S_{RR}^{D}$is the reaction rate sensitivity coefficient to the temperature, and σ_T is the temperature uncertainty.

Uncertainty of Power

The power uncertainty has three components. The first component is statistical or the spread of the counts of the detector that monitors this quantity. The second component is the uncertainty in calibration. The third component is the systematic uncertainty. These three components shall be combined quadratically. The power uncertainty has to be propagated to the reaction rate uncertainty. This can be accomplished noting that reaction rate and power are proportional quantities. Consequently, the relative uncertainty of the reaction rate due to the power uncertainty can be assumed to be equal to the relative uncertainty in the power. Mathematically this statement can be expressed as:

$$\frac{\sigma_{RR}^{P}}{RR} = \frac{\sigma_P}{P} \qquad 2.7\text{-}52$$

where σ_{RR}^{P} is the uncertainty of the reaction rate due to the power uncertainty, σ_P is power uncertainty, and P is the power. σ_{RR}^{P} can be extracted from Equation 2.7-44 as:

$$\sigma_{RR}^{P} = \frac{\sigma_P}{P} \cdot RR \qquad 2.7\text{-}53$$

Considering the relative reaction rate case, if both RR and RR_{ref} arise from the same operation, there is no need to take into account the power uncertainty in the uncertainty analysis.

Systematic Uncertainties

The bias from the experimental factors (ramp factor, power, and the unfolding software employed to resolve the gamma peaks) shall be evaluated. The experiment report should provide enough information so that the evaluator can judge the possible sources of systematic uncertainties. The systematic uncertainties can arise from the nonlinearity of the detector that monitors the power, in the method employed for the power normalization or in the unfolding software. Physical quantities employed such as energy released per fission employed in the power normalization can play a significant role in the systematic uncertainties determination.

2.7.1g *Final Reaction Rate Measurement Uncertainty*

The final reaction rate uncertainty is obtained combining all uncertainty types quadratically and assuming no correlation among them. Let this uncertainty be denoted by $\sigma_{RR_{MM}}$ i.e., the measured method reaction rate uncertainty for a generic reaction type and a generic measurement method. The final uncertainty for the reaction rate experiment is given by:

$$\sigma_{RR_{MM}} = \sqrt{\sigma_{RR}^2 + (\sigma_{RR}^D)^2 + (\sigma_{RR}^T)^2 + (\sigma_{RR}^P)^2 + \left(\sigma_{RR}^{sys}\right)^2}, \qquad 2.7\text{-}54$$

where the subscript RR represents the reaction rate uncertainty of any of the three measurement techniques described in this Guide or any other technique employed for the same purpose and σ_{RR}^{sys} is the systematic uncertainty. Equation 2.7-54 is also applied to the case of the neutron flux.

Again here, for the relative reaction rate case and for RR and RR_{ref} arising from the same operation there is no need to take into consideration the power uncertainty. Otherwise the procedure of Section 2.3 shall be applied.

2.7.1h Sources of Uncertainty and Bounding Values for the Reaction Rate Measurements

Tables 2.7-2a and 2.7-2b show summaries for the uncertainties and bounding values for the reaction rate measurements for thermal and fast reactor, respectively. The list is not exhaustive, but it will contemplate most of the uncertainties employed in the uncertainty analysis described in the coming subsections. The type of uncertainty (A or B) has the same meaning of Refs. 2.7-1 and 2.7-2.

Table 2.7-2a. Summary of uncertainties and bounding values for thermal reactors

Sources of Uncertainty	Typical Value	Minimum Value	Maximum Value	Type of Uncertainty (A or B) [a]
Radioactive Reaction Product Decay Constant (λ_{RRP})	0.05 %	0.01 %	0.5 %	B
Radioactive Reaction Product Gamma Intensity. (g_{RRP})	0.4 %	0.1 %	2.0 %	B
Calibrated Standard Source Activity (A_c)	1.0 %	0.1 %	5 %	B
Calibrated Standard Source Decay Constant (λ_{CSS})	0.05 %	0.01 %	0.5 %	B
Calibrated Standard Source Gamma Intensity (I_{CSS})	0.4 %	0.1 %	2.0 %	B
Time (t)	0.1 %	0.01 %	1 %	B
Detector Count; including A_0 (C)	0.5 %	0.1 %	30 %	B
Global Detector Efficiency (η_{RRP})	0.7 %	0.1 %	3 %	B
End of Irradiation Activity (A_0)	1.5 %	0.1 %	5 %	B
Ramp Factor (F_{ramp})	1.0 %	0.1 %	5 %	B
Gamma Self-Absorption Factor (F_{abs})	2.0 %	0.1 %	5 %	B
Depression Flux Correction factor (F_{corr})	1.0 %	0.1 %	5 %	B
Fission Yield (Y_{RRP})	2.0 %	0.1 %	5 %	B
Reactor Power	2.0 %	1.0 %	5.0 %	B
Power detector signal	0.5 %	0.1 %	1.0 %	B
Calibrated Mass (MFC)	2.5 %	1.0 %	4.0 %	A
Average Microscopic Cross Section ($\overline{\sigma_i^J}$)	2.5%	1.0%	4.0%	Variable
Reaction Rate (RR)	3.0 %	1.0 %	5.0 %	Variable
Neutron Flux	3.0 %	1.0 %	10.0 %	Variable
Relative Reaction Rate	1.0 %	0.1 %	4.0 %	B

(a) The Uncertainty Type (A or B) has the same meaning as in ICSBEP Uncertainty Guide.

Table 2.7-2b. Summary of uncertainties and bounding values for fast reactors

Sources of Uncertainty	Typical Value	Minimum Value	Maximum Value	Type of Uncertainty (A or B)
Radioactive Reaction Product Decay Constant (λ_{RRP})	0.05 %	0.01 %	0.5 %	B
Radioactive Reaction Product Gamma Intensity. (g_{RRP})	0.4 %	0.1 %	2.0 %	B
Calibrated Standard Source Activity (A_c)	1.0 %	0.1 %	5 %	B
Calibrated Standard Source Decay Constant (λ_{CSS})	0.05 %	0.01 %	0.5 %	B
Calibrated Standard Source Gamma Intensity (I_{CSS})	0.4 %	0.1 %	2.0 %	B
Time (t)	0.1%	0.01%	1%	B
Detector Count (C)	0.5 %[a]	0.1 %	30 %	B
Global Detector Efficiency (η_{RRP})	0.7 %	0.1 %	3 %	B
End of Irradiation Activity(A_0)	1.5 %	0.1 %	5 %	B
Ramp Factor (F_{ramp})	1.0 %	0.1 %	5 %	B
Gamma Self-Absorption Factor (F_{abs})	2.0 %	0.1 %	5 %	B
Depression Flux Correction factor (F_{corr})	1.0 %	0.1 %	5 %	B
Fission Yield (Y_{RRP})	2.0 %	0.1 %	5 %	B
Reactor Power	2.0 %	1.0 %	5.0 %	B
Power detector signal	0.5 %	0.1 %	1.0 %	B
Calibrated Mass (MFC[b])	1.5 %	1.0 %	4.0 %	A
Reaction Rate (RR)	3.0 %[c]	1.0 %	5.0 %	B

(a) Typical uncertainty for the measurements of reaction rates of the basic nuclides with fission chambers is ~1% in the core
(b) MFC stands for miniature fission chambers
(c) The value is typical for the absolute measurements. The typical uncertainty for the relative measurements is comparable with the detector count uncertainty (~1%) because other components of the uncertainty such as Reactor Power and Calibrated Mass are cancelled

2.7.2 *Uncertainties in Experimental Configuration*

This kind of uncertainty follows closely the procedure of the *ICSBEP Uncertainty Guide* [2.7-2]. Here the uncertainties are divided primarily into three categories: 1) uncertainty in geometry, 2) uncertainty in physics, chemistry, and isotopics of materials, and 3) uncertainty in the experimental configuration.

Uncertainties in the experimental configuration are the uncertainties that arise from the fact that the experiment setup is not in perfect agreement with its design, i.e. there is an uncertainty connected to the position of the activation foils, detectors and auxiliary instrumentation, uncertainty of the experiment equipment composition etc., which is presented in a practical example in Section 2.7.4 (Example 2.7-2). The category also includes uncertainties in the environmental conditions, namely the uncertainties in basic parameters of the experiment system which might not be of direct interest, but nevertheless affect the measured. This includes uncertainties such as those in the geometry, composition or integral physical parameters of the criticality system. An example of the evaluation of an experiment configuration uncertainty is given in Section 2.7.4 (Example 2.7-2).

As an illustration, Tables 2.7-3 and 2.7-4 show, respectively the uncertainties on geometry and the uncertainties on materials. The empty columns may be filled as an aid to clarify the uncertainties. This list is not exhaustive. Different parameters will be listed for other types of configurations. Besides of the uncertainties commonly derived from the *ICSBEP Uncertainty Guide* for the facility parameters, the geometric and material uncertainties of the device (foil, fuel rod or miniature fission chamber) employed to infer the reaction rates shall be taken into consideration. The geometry and material details of the device and its respective auxiliary devices such as holders, canister, etc. has to be known in order to assign their specific uncertainties. Tables 2.7-3 and 2.7-4 show some details for the foil activation technique. A sensitivity analysis is performed in order to propagate the geometric and material uncertainties of the facility and of the measurement device utilized to infer the reaction rates. Finally, the gamma detector system (GDS) is an integral part of the experiment. Its geometric and material details should be known as well as their corresponding uncertainties. These uncertainties shall be propagated to the gamma self-shielding factor employing a sensitivity calculation. The final total uncertainty arising from the parameters of the facility and from the parameters of the gamma detection system is the square root of the sum of the squares of each component. Let this type of uncertainty be represented by σ_{PF}.

Table 2.7-3. Uncertainties in geometry

Parameter Identification	Mean Measured Value (mm)	Reported Uncertainty in Parameter	Type of Uncertainty (A or B) [(a)]	Number of Degrees of Freedom	Standard Uncertainty
Active Fuel Height					
Fuel Pellet Diameter					
Clad Outer Diameter					
Clad Inner Diameter					
Fuel Rod Pitch					
Bottom Alumina Height					
Foil geometric data					
Foil location					
Auxiliary Set up for fixing the foil					
Other Relevant Parameters					

(a) The Uncertainty Type (A or B) has the same meaning as in ICSBEP Uncertainty Guide.

Table 2.7-4. Uncertainties in materials

Parameter Identification	Mean Measured Value	Reported Uncertainty in Parameter	Type of Uncertainty (A or B) [(a)]	Number of Degrees of Freedom	Standard Uncertainty
^{235}U Enrichment (%)					
UO_2 Density (g/cm^3)					
Cladding Density (g/cm^3)					
^{55}Mn in Cladding SS (wt.%)					
Cladding composition					
^{234}U (wt.%)					
UO_2 stoichiometric factor (%)					
Foil mass					
Target Nuclide Mass					
Target Nuclide abundance					
Other Relevant Parameters					

(a) The Uncertainty Type (A or B) has the same meaning as in ICSBEP Uncertainty Guide.

2.7.3 *Uncertainties in Biases and Benchmark Models*

Biases in Benchmark Model

Biases are introduced in the Benchmark Model in three distinct forms. By reaction rate measurement methods whenever parameters derived from calculations or from other experiments are employed to infer the measured reaction rate; by the desired simplification (typically derived in Section 3 of an IRPhEP Evaluation), or by modelling limitations (typically derived in Section 4 of IRPhEP Evaluation). Biases in the reaction rate measurement methods shown in this section arise from the calculated factors (e.g., gamma self-absorption factors and self-shielding factors), and from the structure and decay data library employed in the analysis. Section 2.7.1 shows how these factors were applied and how structure and decay data library was employed in the measurement method.

The determination of the biases arising from the reaction rate measurement methods is a very complicated problem. The bias determination for the calculated quantities requires the availability of well-defined experiments for these quantities to serve as benchmarks; here referred to as Reference Value. The bias induced by these calculated factors can be understood calculating the ratio C/R, where C is the calculated quantity and R is the reference value provided by the specific available benchmarks. If C/R is higher than 1, the calculated factor overestimates the measured reaction rate. On the other way around, the calculated factor underestimates the measured reaction rate.

The bias in the reaction rate measurements for a particular correction factor is given as:

$$B_{CF} = \frac{(R-C)}{C} \cdot SI_{MM} \,, \qquad 2.7\text{-}55$$

where B_{CF} is the bias for the specific calculated factor and its uncertainty arises from a standard error propagation.

The benchmark model value for the reaction rate experiment after applying all possible biases and correction factors is given by:

$$SI_{Be} = SI_{MM} + B_{SL} + \frac{(R-C)}{C} \cdot SI_{MM}, \quad 2.7\text{-}56$$

where SI_{Be} is the benchmark reaction rate model value, the subscript MM represents a generic measurement method, SI_{MM} is the measured reaction rate, and B_{SL} is the bias from the benchmark model simplification (typically derived in Section 3 of an IRPhEP Evaluation), or by modelling limitations (typically derived in Section 4 of an IRPhEP Evaluation).

Equation 2.7-56 reduces to:

$$SI_{Be} = SI_{MM} \cdot \frac{R}{C} + B_{SL}, \quad 2.7\text{-}57$$

The ratio $\frac{R}{C}$ is defined as the bias-factor. Equation 2.7-57 can be generalized for a specific number of measurement bias as:

$$SI_{Be} = SI_{MM} \cdot B_{MM} + B_{SL}, \quad 2.7\text{-}58$$

where $B_{MM} = \prod_{i=1}^{N_B} B_i$ is the total measurement method bias-factors , N_B is the total number of bias-factors applied to the measurement method, and B_i is the specific measurement method bias-factor. Bias in simplifications also includes the exclusion of the auxiliary devices to fix the detectors in the reactor system if not modelled in the benchmark model.

Uncertainties in Biases

Bias in measurement methods is always the inverse of the ratio of two quantities. The numerator is the calculated quantity while the denominator is the reference value. Its uncertainty can be found applying a standard propagation of the associated uncertainties assuming no correlations. The final result is given by:

$$\sigma_{B_{CF}} = \sqrt{((1/C) \cdot \sigma_R)^2 + ((R/C^2) \cdot \sigma_C)^2}, \quad 2.7\text{-}59$$

where R and C represents the reference and the calculated values, respectively, and σ_R and σ_C are respectively the uncertainties in the specific experiment and in the calculations.

The total uncertainty in the benchmark simplification and in the benchmark limitation is given by:

$$\sigma_{B_{SL}} = \sqrt{\sigma_{B_S}^2 + \sigma_{B_L}^2}, \quad 2.7\text{-}60$$

where σ_{B_S} is the uncertainty in the bias from simplifications and σ_{B_L} is the uncertainty in the bias from limitations.

As a starting point, the following paragraph was taken from the *ICSBEP Uncertainty Guide* [2.7-2] and adapted for reaction rate measurements.

The evaluator should strive for a reasonable balance between making the benchmark model amenable to calculation and keeping the total reaction rate uncertainty of the model as small as practical. Obviously, simplifications that make the benchmark model easier to use tend to make it more attractive to reactor physicist analysts. However, each simplification introduces an additional benchmark-model bias and a correlated uncertainty contribution. The use of benchmark models to validate a reactor physics analysis or to identify weaknesses in cross section data and calculational methods is more effective and reliable if the uncertainties are small. The only stage in the evaluation process where the evaluator legitimately can influence the magnitude of the total uncertainty is in

deciding what simplifications to make to create the benchmark model. The **benchmark-model** is the best estimate of the value of reaction rate that would be observed for an isolated experiment having exactly the geometry and materials described in the benchmark model. Thus one should aim at developing a benchmark model of the experiment which is simultaneously pragmatic for further evaluator's use, computationally not too demanding and free of major computational biases. This means that constructing a model with a great level of detail, which has a negligible contribution to the total benchmark-model uncertainty but significantly increases the complexity of the model and associated computational time, is not advisable. Additionally the evaluator should construct a benchmark-model including all parts of experiment that could potentially lead to the introduction of major reaction rate biases, if not modelled. In the opposite case a rigorous study of the effect of the benchmark-model simplification on the computed reaction rates should be performed.

Uncertainties in Benchmark Model

The uncertainties in the reaction rate benchmark model are composed of three major parts: a) uncertainties in measurement method, b) uncertainties in biases, and c) uncertainty from the facility and device parameters. These three components shall be combined quadratically in order to get the whole benchmark uncertainty.

The final benchmark uncertainty for the reaction rate measurement method is given by:

$$\sigma_{MM}^{Be} = \sqrt{\left(\sigma_{RR_{MM}} \cdot B_{MM}\right)^2 + \left(RR_{MM} \cdot \sigma_{B_{MM}}\right)^2 + \left(\sigma_{B_{SL}}\right)^2 + \sigma_{PF}{}^2}, \qquad 2.7\text{-}61$$

where σ_{MM}^{Be} is the reaction rate benchmark uncertainty for the measurement method MM, $\sigma_{RR_{MM}}$ is given by Equation 2.7-54 $\sigma_{B_{SL}} = \sqrt{\sigma_{B_S}^2 + \sigma_{B_L}^2}$, σ_{B_S} is the uncertainty in the bias from simplifications and σ_{B_L} is the uncertainty in the bias from limitations.

The benchmark uncertainty for the neutron flux and the relative reaction rate also follows Equation 2.7-60.

Table 2.7-5 shows a summary table listing the uncertainties, typical values, and minimum – maximum range of values that are considered bounding.

Table 2.7-5. Summary of uncertainties and bounding values for the benchmark model

Sources of Uncertainty	Typical Value (%)	Minimum Value (%)	Maximum Value (%)
Reaction Rate Measurement (RR)	3.0	1.0	5.0
Neutron Flux Measurement	2.5	1.0	10.0
Relative Reaction Rate Measurement	1.0	0.1	4.0
Facility and Device Parameters	1.0	0.5	2.0
Bias	1.0	0.1	5.0
Reaction Rate Benchmark model	4.0	1.2	7.0
Neutron Flux	3.0	1.0	12.0
Relative Reaction Rate	1.0	0.1	5.0

2.7.4 *Practical Examples*

Example 2.7-1: Determination of the ^{115}In Inelastic Scattering Reaction Rate in the Central Region of the IPEN/MB-01 Reactor

The example considered here concerns the determination of the ^{115}In inelastic scattering reaction rate in the central region of the IPEN/MB-01 reactor. The fuel rod scanning and the miniature fission chambers techniques are mostly employed in the spectral ratio measurements. Examples of the utilization of these two techniques will be reserved for the spectral ratio section.

The natural In foil is a cylinder with 8.49 mm of diameter and 0.516 mm height weighting 0.2134 g. The abundance of ^{115}In in the natural In is 0.9571 ± 0.0005 [2.7-16]. The irradiation was made in a constant power of 100W during one hour. The uncertainty in the power is 2.7 %. The moderator temperature was measured employing 12 thermocouples. The average value was: 20.23 ^{0}C ± 0.08 ^{0}C. After that the ^{115}In foil was taken to the HPGe detector systems to obtain the counts as a function of the decay time. The count time was around 0.5 hours.

Determination of the Global Detector Efficiency (GDE)

The Global Detector Efficiency plays an important role in the reaction rate determination. This example shows how this was accomplished in the IPEN/MB-01 facility.

From the definition of the global efficiency as given by Equation 2.7-3 and applying the decay correction for the source decay, it can be found [2.7-17] that GDE is given by:

$$GDE\left(E_\gamma\right) = \frac{\lambda \cdot C(E_\gamma) \cdot e^{\lambda \cdot t_s}}{I.A_c \cdot (1 - e^{-\lambda \cdot t_c})}, \qquad \text{E2.7-1.1}$$

where $C\left(E_\gamma\right)$ is the net detector counts for the gamma energy E_γ emitted by the standard source, λ and A_c are respectively, its decay constant and initial activity (the first calibration when certificate is issued), t_c is detector count time, t_s is the time span from the source calibration by the manufacturer and the beginning of the count, and I is the emission intensity for gammas of energy E_γ.

In a general sense, two kinds of standard calibrated source are employed to obtain the detector efficiency. The first is ^{152}Eu (half-life 13.517 ± 0.009 years). This is an ideal source because it decays by emission of several gammas with well-defined energies that cover a large part of the gamma energy spectra detected by the HPGe (120 keV to 1500 keV). Furthermore, its half-life is long enough to allow the utilization of this source for a long period. Table 2.7-1 shows the gamma energies emitted in the decay process of ^{152}Eu as well as the corresponding emission probabilities with uncertainties [for example http://www.nndc.bnl.gov/nudat2]. The second standard source is ^{133}Ba (half-life 10.559 ± 0.008 years). This standard source emits lower energy gammas that serve as the complement for ^{152}Eu. Table 2.7-2 shows the gamma energies emitted in the decay process of ^{133}Ba as well as the corresponding emission probabilities with uncertainties. The data of tables E2.7-1.1 and E2.7-1.2 are from http://www.nndc.bnl.gov/nudat2.

Table E2.7-1.1. Gamma energy characteristics and emission intensities for ^{152}Eu

Energy (keV)	Gamma Emission Intensity (I)
121.7817(3)[(a)]	0.2853(16)
244.6974(8)	0.0755(4)
344.2785(12)	0.2659(20)
411.1165(12)	0.02237(13)
443.9606(16)	0.02827(14)
778.9045(24)	0.1293(8)
964.057(5)	0.1451(7)
1112.076(3)	0.1367(8)
1408.013(3)	0.2087(9)

(a) Terms in parenthesis are uncertainties

Table E2.7-1.2. Gamma energy characteristics and emission intensities for ^{133}Ba

Energy (keV)	Gamma Emission Intensity (I)
4.29[(a)]	0.157(8)
30.625	0.339(10)
30.973	0.622(18)
34.92	0.0588(17)
34.987	0.114(3)
35.818	0.0351(10)
53.1622(6)	0.0214(3)
79.6142(12)	0.0265(5)
80.9979(11)	0.329(3)
160.6120(16)	0.00638(5)
223.2368(13)	0.00453(3)
276.3989(12)	0.0716(5)
302.8508(5)	0.1834(13)
356.0129(7)	0.6205
383.8485(12)	0.0894(6)

(a) Uncertainties not available

The HPGe detector calibration of the IPEN/MB-01 facility was performed employing a ^{152}Eu calibrated source. The ^{152}Eu calibrated source is a disk with 8 mm diameter and 0.5 mm height; very similar to the ^{115}In activation foils employed in this example. The initial activity of the ^{152}Eu source was 12.1 ± 0.11 kBq calibrated in March 1st 1991. Table E2.7-1.3 shows the gamma intensity, the HPGe detector counts, and the global detector efficiency as a function of the gamma energy. Equations 2.7-4 and 2.7-18 were utilized to obtain respectively the global efficiencies and their corresponding uncertainty. The uncertainties in the span and count times (t_s and t_c) were taken equal to 0.5 sec.

Table E2.7-1.3. Gamma intensity, HPGE detector counts, and the global detector efficiency as a function of the gamma energy

E_γ(keV)	I_γ	σ_{I_γ}	$C(E_\gamma)$	$\sigma_{C(E_\gamma)}$	GDE(E_γ)	σ_{GDE}
244.17	0.0751	0.0005	328967	884	0.01406	0.00016
344.62	0.2658	0.0018	909599	1089	0.01098	0.00013
411.36	0.02234	0.00013	64030	515	0.00920	0.00012
444.18	0.03120	0.00018	82309	498	0.00847	0.00010
778.97	0.1296	0.0007	221481	632	0.00548	0.00006
964.05	0.1462	0.0006	203857	623	0.00447	0.00005
1112.00	0.1356	0.0006	176351	606	0.00417	0.00004
1407.80	0.2085	0.0008	220897	530	0.00340	0.00003

Figure E2.7-1.1 shows the global detection efficiency as a function of gamma energy. The data on this figure were least-square fitted to a first order polynomial function as:

$$ln(\eta_{RRP}(E_\gamma)) = A + B \cdot ln(E_\gamma) \quad , \qquad \text{E2.7-1.2}$$

where E_γ is a generic gamma energy and A and B are constants to be determined from the least-square fit. The associated uncertainty for the global detector efficiency for a gamma of energy E_γ as given by Equation 2.7.1-41 can be found as:

$$\sigma_{\eta_{RRP}}(E_\gamma) = \sqrt{\left(\frac{\partial \eta_{RRP}}{\partial A}\right)^2 \cdot \sigma_A^2 + \left(\frac{\partial \eta_{RRP}}{\partial B}\right)^2 \cdot \sigma_B^2 + 2 \cdot \frac{\partial \eta_{RRP}}{\partial A} \cdot \frac{\partial \eta_{RRP}}{\partial B} \cdot cov(A,B)} \quad , \qquad \text{E2.7-1.3}$$

where:

$$\frac{\partial \eta_{RRP}}{\partial A} = \eta_{RRP}(E_\gamma), \qquad \text{E2.7-1.4}$$

$$\frac{\partial \eta_{RRP}}{\partial B} = \eta_{RRP}(E_\gamma) \cdot \ln(E_\gamma), \qquad \text{E2.7-1.5}$$

σ_A , σ_B, and cov(A,B) are given by the least square approach. Cov(A,B) is the covariance of the variables A and B.

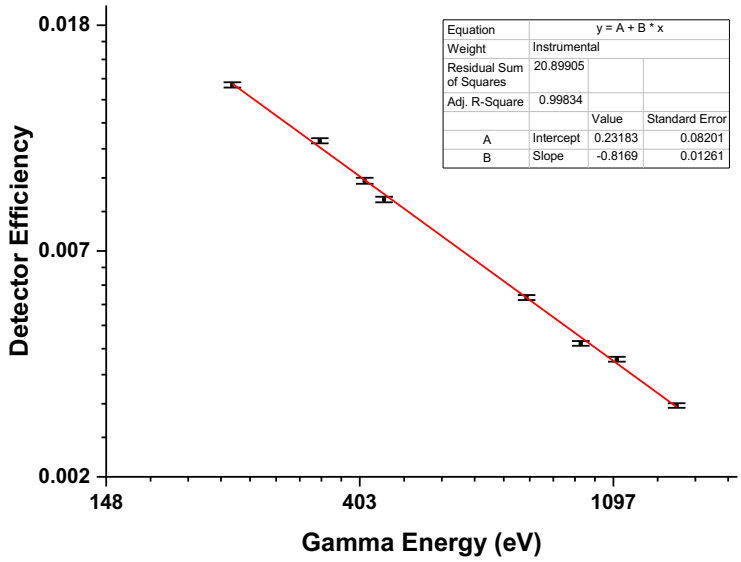

Figure E2.7-1.1. Detector efficiency as a function of the gamma energy

The covariance matrix arising from the least square approach is shown in Table E2.7-1.4.

Table E2.7-1.4. Covariance matrix for the global detector efficiency

	A	B
A	6.7256E-03	-0.00103
B	-0.00103	1.5901E-04

Determination of the ^{115m}In Reaction Rate

^{115m}In decays by gamma emission. Its half-life is 4.486 ± 0.004 hours and its gamma energy is 336.244 ± 0.017 eV. Its gamma efficiency is 0.458 ± 0.022. The global detection efficiency and its corresponding uncertainty at this energy was determined employing Equations E2.7-1.2 and E2.7-1.3 and the data of Table E2.7-1.4. The final value was 0.0109 ± 0.0001.

The determination of A_0 involves the calculation of $A(t_d)$ as a function of t_d as given by Equation 2.7-15. The corresponding uncertainty of $A(t_d)$is given by Equation 2.7-16. The uncertainty in the count time (t_c) was equal to 0.5 sec. Table E2.7-1.5 shows the ^{115m}In activity ($A(t_w)$) as a function of decay time (t_d).

Table E2.7-1.5. ^{115m}In activity and respective uncertainty as a function of decay time (t_d)

Decay Time t_d (sec.)	Count Time (t_c) (sec.)	Net Counts	Net Count Uncertainty	$A(t_d)$ (Bq)	$\sigma_{A(t_d)}$ (Bq)
103844	1798.14	2658	62	308	17
105649	1798.24	2372	62	275	16
107450	1798.22	2257	55	262	15
109251	1798.26	2053	53	238	13
111052	1798.36	1859	52	216	12
112853	1798.38	1701	49	197	11
114654	1798.34	1619	50	188	11
116455	1798.26	1527	49	177	11
118256	1798.30	1407	47	163	10
120057	1798.38	1196	42	139	9
121858	1798.38	1203	47	140	9
123659	1798.42	1110	40	129	8
125460	1798.32	1024	44	119	8
127261	1798.24	938	39	109	7
129062	1798.42	899	41	104	7
130863	1798.32	790	36	92	6
132664	1798.38	755	36	88	6
134465	1798.30	674	34	78	6
136266	1798.36	645	35	75	6
138067	1798.34	545	32	63	5
139868	1798.46	516	33	60	5
141669	1798.44	512	33	59	5
143470	1798.44	480	32	56	5
145271	1798.44	475	34	55	5
147072	1798.38	423	31	49	4
148873	1798.38	316	25	37	3
150674	1798.40	338	40	39	5
152475	1798.52	279	27	32	4
154276	1798.44	287	32	33	4
156077	1798.42	261	28	30	4
157878	1798.34	250	27	29	3
159679	1798.52	249	28	29	4
161480	1798.50	192	27	22	3
163281	1798.46	185	29	21	4
165082	1798.48	156	24	18	3
166883	1798.48	175	27	20	3
168684	1798.44	182	33	21	4
170485	1798.44	87	18	10	2
172286	1798.50	98	22	11	3
174087	1798.42	95	22	11	3
175888	1798.36	91	19	11	2
177689	1798.46	114	23	13	3
179490	1798.42	82	27	10	3
181291	1798.50	51	20	6	2
183092	1798.50	109	22	13	3

Figure E2.7-1.2 shows the ^{115m}In activity ($A(t_d)$) as a function of decay time (t_d). These data were least-square fitted in an exponential function given by Equation 2.7-22. The ^{115m}In decay constant was fixed in the fitting process. Only A_0 was determined and its value was 25,287 ± 279 Bq.

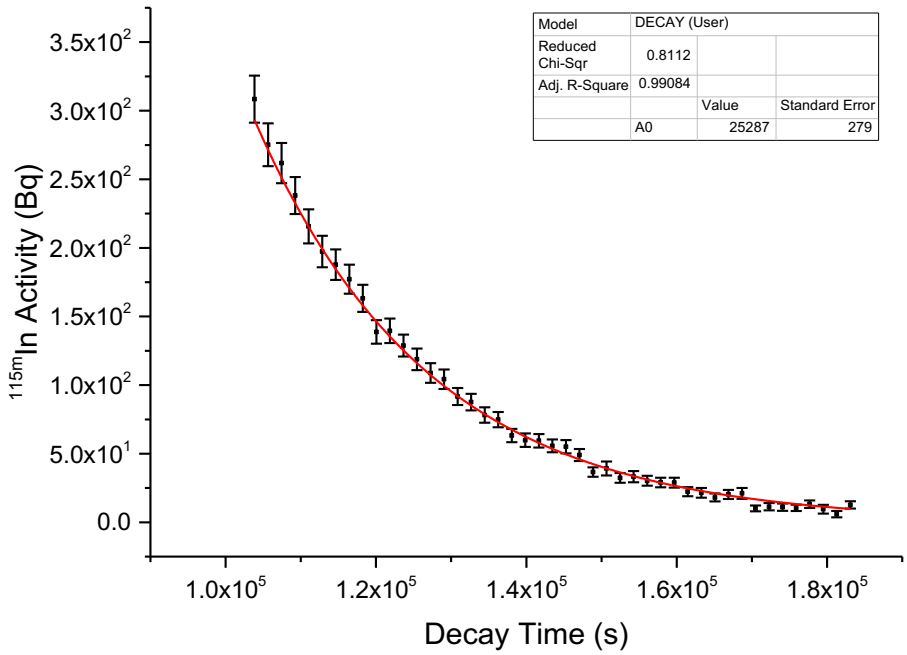

Figure E2.7-1.2. ^{115m}In activity versus decay time

The determination of the ^{115m}In inelastic reaction rate from Equation 2.7-2 requires the knowledge of the factors, F_{ramp} ; the ramp factor; and F_{abs} , the gamma self-absorption correction factor.

F_{corr} , the correction factor due to the neutron flux depression inside of the foil, was taken equal to 1.0 due to the fact that the inelastic reaction rate in ^{115m}In occurs only in the fast neutron energy region and for this case the neutron flux depression inside of the foil is marginal.

F_{ramp} and its corresponding uncertainty were determined by employing, respectively, Equations 2.7-10 and 2.7-26. Its final value was 0.986 ± 0.008.

F_{abs} was calculated employing Equation 2.7-12 with the mass attenuation factor for the ^{115m}In gamma energy from NIST. The final value was 1.012.

The final reaction rate and its corresponding uncertainties were determined employing Equations 2.7-1 and 2.7-14. The final result was 1.762×10^5 reactions/s with 1.4% uncertainty.

The final benchmark uncertainty for the ^{115m}In inelastic reaction rate experiment is given by Equation 2.7-60 or:

$$\sigma_{RR}^{Be} = \sqrt{(1.4)^2 + (2.7)^2} = 3.04\%,$$

where 1.4% is the experimental uncertainty and 2.7% is the power uncertainty.

The temperature contribution to the final benchmark uncertainty was negligible (less than 0.01 %). The effect of the parameter of facility contribution to the benchmark uncertainty was not considered in this example.

Example 2.7-2: Estimation of Perturbation Due to a Miniature Fission Chamber

The example considered in this chapter demonstrates how to estimate the perturbation of a miniature fission chamber and the estimation of the perturbation correction factor F_{corr}. It is based on fission rate axial profile measurements performed in the core of the Jožef Stefan Institute (JSI) TRIGA Mark II reactor, described in detail in the IRPhEP evaluation TRIGA-FUND-RESR-002. The miniature fission chambers used in the experiment were designed and manufactured by the Commisariat à l'énergie Atomique et aux énergies alternatives (CEA). These were inserted into the core of the TRIGA research reactor using a specially developed positioning system composed of a pneumatic drive mechanism and long aluminium guide tubes. A schematic of the fission chamber together with the guide tube and their dimensions is presented in **Figure** Figure E2.7-2.1.

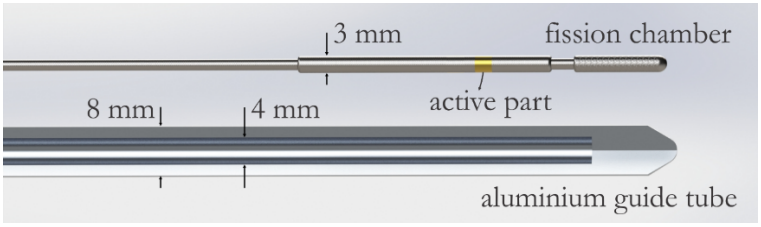

Figure E2.7-2.1. Scheme of the fission chamber and aluminium tube

The absolute values of in-core fission rate yield information that can be used to assess different reactor parameters, for example the reactor thermal power or the average deposited energy per fission event. Since the manipulation of the fission chambers had to be performed from the reactor platform, i.e. 5 m above the submerged core, guide tubes had to be utilized to increase the precision of the chamber's positioning. The insertion of the tubes, which can be generalized for any experiment where auxiliary instrumentation is utilized, in the reactor core introduced an experimental bias due to the fact that they alter the composition of the material in the vicinity of the fission chambers. Although aluminium is neither a good neutron absorber nor moderator, it displaces water surrounding the fission chambers, which significantly affects the local neutron spectrum. A smaller portion of thermal neutrons and a higher share of fast neutrons is thus expected to penetrate the tubes and reach the detectors. In order to assess the effect of the aluminium guides on the response of the fission chambers, Monte Carlo calculations were performed – in the first step the fission rates R_0 in an unbiased, i.e. instrumentation-free, core were calculated upon which the guide tubes were added to the model and the computations repeated to obtain R_P. The ratio of fission rates computed with and without the aluminium tubes, namely R_P/R_0-1, was calculated and is shown in the form of a profile at reactor core mid-plain in Figure E2.7-2.2.

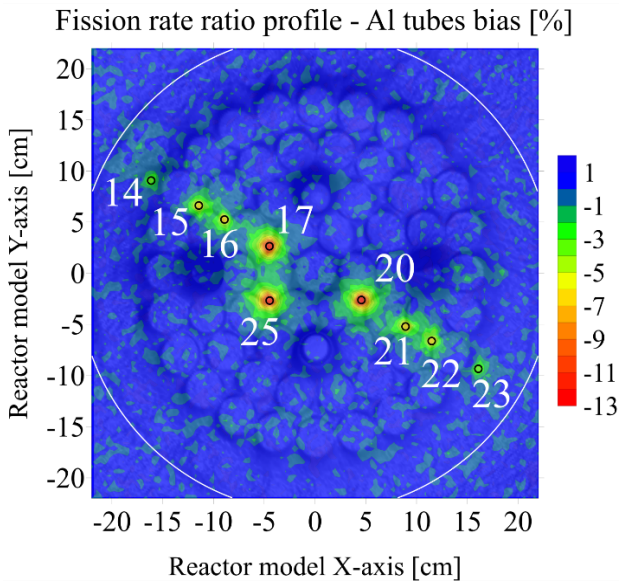

Figure E2.7-2.2. Profile of the relative difference between the computed reaction rates with aluminium guide tubes and without them at mid-plane of the reactor core. The smaller black circles denote measuring positions where aluminium guide tubes were inserted into the core. The edge of the core is denoted with a white line.

As can be seen in Figure E2.7-2.2 the presence of aluminium guide tubes results in significant changes of the fission rates around the measuring positions. As expected the tubes induce a reduction in neutron thermalization which results in a local increase of the number of fast neutrons compared to an instrumentation-free core. The rate of ^{235}U fissions, which is the main isotope contributor to the fission chamber signal, is consequently lowered. It can be observed that the decrease in fission chamber signal is largest, i.e. approximately 13 %, at measuring positions closest to the centre of the core, which is a consequence of a neutron spectrum which, in principle, is faster. With the increase of ambient neutron slowdown toward the edges of the core the effect of aluminium tubes on the fission rate is becoming less observable, reaching a value of around - 2 % at the outermost measuring positions. Thus if one wanted to obtain an absolute value of the reaction rate in the core, the measured value would have to be multiplied with the inverse of the calculated ratio, which in fact represents F_{corr}.

Table E2.7-2.1. Summary of fission rate ratios and F_{corr} factors for measurements of fission rates at different measuring positions in the core of the JSI TRIGA Mark II reactor. Miniature fission chambers were used together with aluminium guide tubes for precise in-core insertion.

Measuring Position	Radial Distance to Centre of Core [cm]	Fission Rate Ratio (%)	F_{corr}
MP14	18.259	- 2	1.02
MP15	13.189	- 6	1.06
MP16	10.367	- 6	1.06
MP17	5.246	- 12	1.14
MP20	5.246	- 13	1.15
MP21	10.367	- 6	1.06
MP22	13.189	- 5	1.05
MP23	18.259	- 3	1.03
MP25	5.246	- 12	1.14

Modelling of the Miniature Fission Chamber Response

The example considered in this chapter demonstrates how to estimate the response of a miniature fission chamber based on two fundamental criteria – constructing a detailed computational model of the experimental setup to minimize biases while account for the computational efficiency of the model. Namely estimating reaction rates inside voxels which are relatively small (order of millimetres) tends to be computationally demanding, i.e. in order to get benchmark grade statistics the calculations times are long. The practical example focuses on fission rate measurements performed with miniature fission chambers in the core of the JSI TRIGA Mark II research reactor, described in detail in the IRPhEP evaluation TRIGA-FUND-RESR-002. The fission chambers used in the experiment were miniature, with the active part length and diameter measuring several millimetres, as shown in Figure E2.7-2.1. The chambers were not modelled in detail since the active part is relatively small, resulting in prolonged neutron transport calculations times even in the core of the TRIGA reactor model, where neutron flux is the highest. In order to compensate for the effect of the fission chamber structure on the measurements of fission rates, a study of the simplification of the fission chambers' geometry was made and was found to be negligible[11]. The study was aimed at constructing a detailed and a simplified model of the fission chamber and comparing the computed values – the relative differences between the two cases were discovered to have values of around 0.5 %, which is of the order of statistical uncertainty of the Monte Carlo calculations.

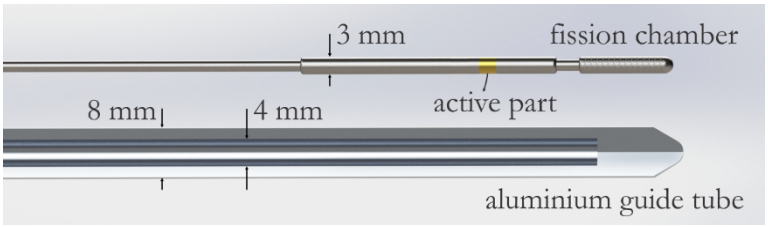

Figure E2.7-2.1. Scheme of the fission chamber and aluminium tube

The simplified benchmark model of the fission chamber was thus represented by a cylindrical mesh of the same height as the active part of the fission chamber and a diameter equal to the inner diameter of the aluminium guide tubes, which is shown in Figure E2.7-2.1. The mesh served the purpose of tallying the fission rates with a multiplier corresponding to the fission deposit material in the miniature chambers, shown in Table E2.7-2.2 for two types of fission chambers.

Table E2.7-2.2. Tallying material composition for two types of fission chambers – the first with the fission deposit composed mainly of ^{235}U and the other of ^{238}U

Chamber	^{234}U [% at.]	^{235}U [% at.]	^{236}U [% at.]	^{238}U [% at.]
FC ^{235}U	0.063	98.490	0.038	1.409
FC ^{238}U	0	0.036	0	99.964

In order to better understand the response of the fission chamber, a study was made in which the number of fission events on individual isotopes composing each of the fission chamber deposit was tracked. It was found that the response of the fission chamber with the coating composed mainly of ^{235}U is largely based on fission events on the latter isotope with the other uranium isotopes contributing only a small fraction to the signal. On the other hand although the second fission

[11] V. Radulović, L. Barbot, *Fission rate calculations for 3 mm and 4 mm CEA fission chambers inside irradiation locations BR1 and Minerve reactors*, CEA Technical note, DEN/CAD/DER/SPEx/LDCI/NT/2015/No11/1, 2015.

chamber has a coating composed mainly of ^{238}U, the ^{235}U isotope with an 0.0357 % atomic fraction contributes to almost one half of the recorded fission rates, depending on the position in the reactor core. The ratio between the fission events recorded solely on ^{238}U and the combined number of fission events, i.e. $^{235}U + ^{238}U$, for four different measuring positions in the TRIGA core is presented in Table E2.7-2.3 it can be seen that the average of the ratio is around 0.5, with the fission event fraction of ^{238}U increasing from the edge of the reactor towards the centre, which is a consequence of the hardening of the neutron spectrum.

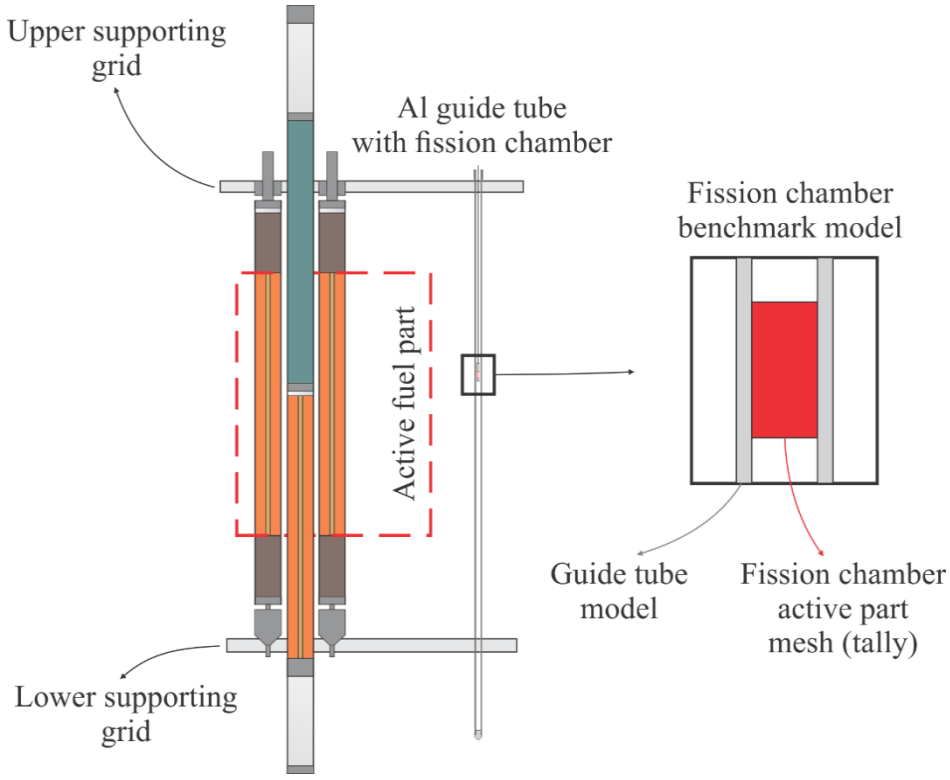

Figure E2.7-2.3. Schematic of the TRIGA reactor core on the left side and the fission chamber benchmark model on the right side

Table E2.7-2.3. Ratio between the fission events recorded solely on ^{238}U and the combined number of fission events, i.e. $^{235}U + ^{238}U$, for calculations on the ^{238}U fission chamber at four different measuring positions in the TRIGA core.

Fission Rate Ratio	MP14	MP15	MP16	MP17
$R(^{238}U) / R(^{235}U + ^{238}U)$	0.44	0.64	0.66	0.62

Evaluation of the Uncertainty in the Experiment Configuration with Miniature Fission Chambers

The example considered in this chapter describes the evaluation of uncertainties connected with the configuration of the experiment performed with miniature fission chambers in the JSI TRIGA Mark II research reactor. The example is based on the computed fission rate uncertainty due to the uncertainty in the axial and radial positions of the miniature fission chambers.

Fission chamber axial position – namely the fission chambers were inserted into the core using a pneumatic positioning system, which had an accuracy of ± 0.3 mm. Since precise knowledge of the distance between the positioning mechanism and the reactor core is crucial in determining the exact position of the fission chamber and because the reaction rates change significantly through the height of the reactor, the uncertainty in the position of the chamber directly influences the measurements. The uncertainty in the measured fission rates due to the uncertainty in the axial position of the chambers was estimated by calculating the gradient of the reaction rates computed with the Monte Carlo method, using the equation:

$$\frac{1}{R_i}\left|\frac{dR_i}{dz_i}\right| = \frac{1}{R_i}\left|\frac{R_{i+1} - R_{i-1}}{z_{i+1} - z_{i-1}}\right|, \qquad \text{E2.7-2.1}$$

where R_i is the reaction rate value on the i-th position of the axial profile. The results of a sample gradient calculation are shown in Figure E2.7-1.4. The gradients were averaged over a 25 mm interval to exclude statistical distortion, which is a consequence of the uncertainty being of the same order as the statistical uncertainties of the calculations. The active core region (fuel meat) is located on the axial interval from 140 mm to 520 mm. As can be observed, the gradient in the central area is of the order of 0.5 % / mm to approximately 1 % / mm. The largest fission rate gradient of approximately 2.5 % / mm can be seen at axial positions around 100 mm and 600 mm, where the graphite plugs and metal cladding are located inside the fuel element.

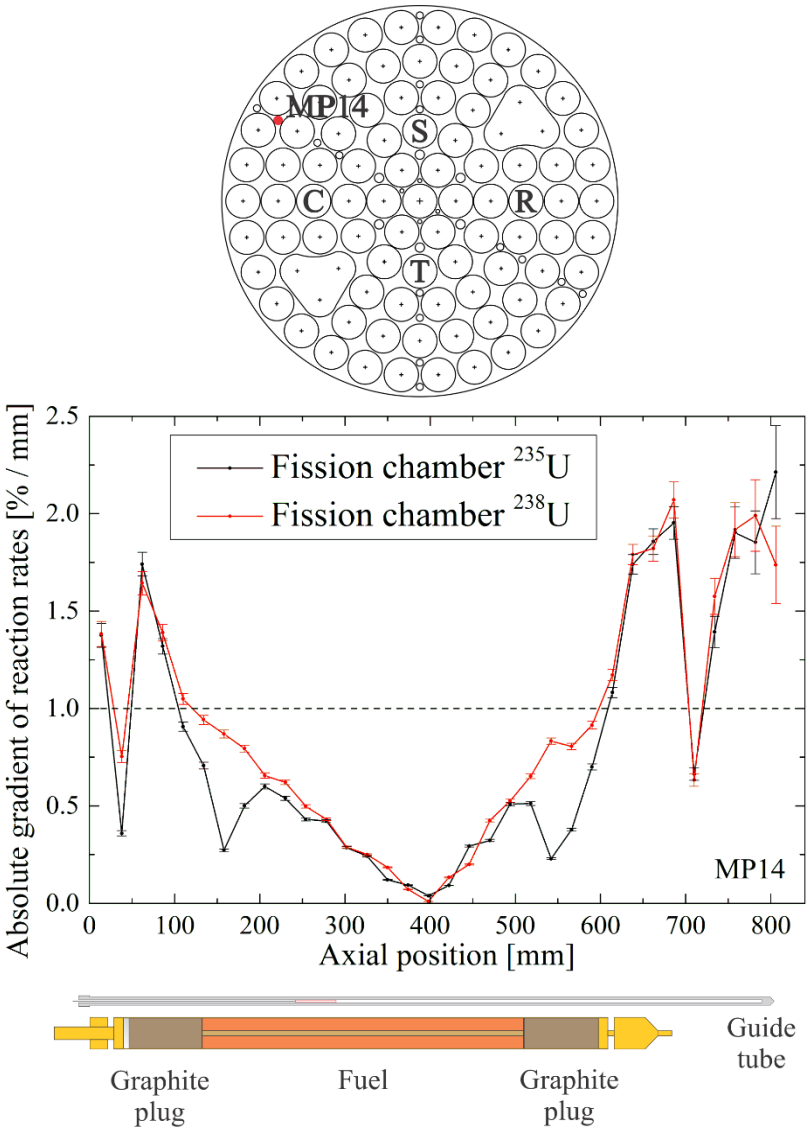

Figure E2.7-2.4. Fission rate axial gradient for ^{235}U and ^{238}U fission chambers at the MP14 measuring position, which is shown in a schematic of the upper support grid of the TRIGA reactor. A fuel element model and a model of the aluminium guide tube are shown in the bottom of the figure.

Fission chamber radial position – both fission chambers were inserted into the core using waterproof aluminium guide tubes with an inner diameter of 4 mm. Since the diameter of the fission chambers is 3 mm there is an upper limit for the uncertainty in the radial position of the chamber, which amounts to 0.5 mm. It was postulated that the part of the tube inserted into the core of the reactor was not additionally curved (thus contributing to the FC radial position uncertainty). Due to the relatively high heterogeneity of the reactor core in the radial direction, the radial reaction rate gradient is expected to be greater than the axial gradient. Hence to estimate the uncertainty contribution due to the radial position of the fission chamber the radial gradient throughout the TRIGA reactor core was calculated. Figure E2.7-2.5 shows the radial gradient profile for a fission chambers at a reactor core mid-plane.

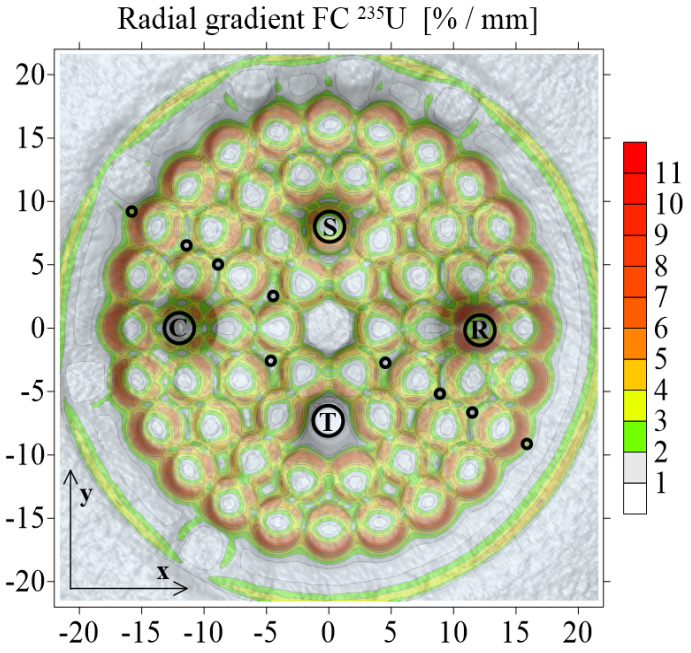

Figure E2.7-2.5. Radial reaction rate gradient profile at the mid-plane of the reactor core for the ^{235}U fission chamber. The small black rings in the picture represent the measuring positions used in the experiment. Additionally, the control rod positions (T, S, C, R) and the coordinate axes are denoted.

The calculations were performed using a rectangular mesh which was imposed over the whole reactor core calculating reaction rates at 250 points in the x- and y- directions and at 50 steps through the height of the reactor. The number of mesh steps in the axial direction was chosen in such a manner to obtain calculation steps which would not exceed axial lengths at which significant reaction rate gradients occur. Thus the axial reaction rate values were averaged over 1.37 cm axial slices of the height of the reactor with the origin at the centre of the active part of the fuel. The two-dimensional fission rate distribution was obtained using a two-dimensional gradient equation:

$$\left|\frac{dR}{dr}\right|_{i,j} = (x_i^2 + y_j^2)^{-\frac{1}{2}} \left(x_i \left| \frac{R_{i+1,j} - R_{i-1,j}}{x_{i+1} - x_{i-1}} \right| + y_j \left| \frac{R_{i,j+1} - R_{i,j-1}}{y_{i+1} - y_{i-1}} \right| \right), \qquad \text{E2.7-2.2}$$

and an advanced Kriging interpolation method [12] for a mesh of 62500 fission rate plane points. It can be seen, that the changes in fission rates when using the ^{235}U fission chamber are largest at the edges of the fuel elements and significantly smaller at the locations of measuring positions with an approximate value of 1 % / mm. Due to small variations the radial reaction rate gradients have been averaged over the height of the core (839 axial computational positions) for each of the measuring position which showed that the gradient values are relatively similar. Therefore a combined reaction rate gradient was calculated, which was averaged over all of the 9 measuring positions. The calculated values were 1.59 % / mm for the ^{235}U fission chamber. Taking into account that the upper uncertainty limit in the chamber radial position is 0.5 mm, the final estimate of the relative standard uncertainty due to radial position of the fission chambers is 0.8 % for ^{235}U fission chamber with an estimated absolute 'uncertainty of uncertainty' of 0.2 %.

[12] The Kriging method is widely used in engineering applications, providing an accurate linear unbiased prediction of the intermediate values. Reference: N. Cressie, *Statistics for Spatial Data*, Wiley, 1993.

An overview of the evaluation of uncertainty in the fission rate measurements due to the uncertainty in the axial and radial positions of the fission chambers is presented in Table E2.7-2.4. It can be seen that the uncertainty was estimated for two types of fission chambers with different response characteristics. The typical values of the relative fission rate uncertainty due to the uncertainty in the axial position were estimated to be around 2.5 %, while the contribution because of the uncertainty in the radial position of the chambers is below 1 %.

Table E2.7-2.4. Uncertainty in fission rate measurements due to uncertainties in the axial and radial positions for two different types of fission chambers (averaged over all chamber axial and radial positions)

Parameter Identification	Reported Parameter Uncertainty	Δk_{eff} x 10^5	Averaged Fission Rate Gradient [% / mm]	Relative Standard Uncertainty in Fission Rate Distribution
FC axial position (mm)	± 3 mm (positioning system and Al tubes)	Does not affect k_{eff}	0.82 (FC ^{235}U) 0.86 (FC ^{238}U)	± 2.5 % (FC ^{235}U) ± 2.6 % (FC ^{238}U)
FC radial position (mm)	± 0.5 mm (aluminium guide tube width)	Does not affect k_{eff}	1.59 (FC ^{235}U) 0.36 (FC ^{238}U)	± 0.8 % (FC ^{235}U) ± 0.2 % (FC ^{238}U)

Discussion on the axial and radial dependency of the reaction rate uncertainties – when evaluating the uncertainty of fission rate distribution measurements at different irradiation positions in a reactor, one has to take into account the fact that the neutron flux and neutron spectra can change significantly throughout the core. This has several major consequences – one of the most obvious being the variation in the neutron flux, which has an effect on the absolute values of the reaction rates and with it the uncertainty in the statistics of the measurements. This introduces an intrinsic axial and radial dependency to the measurements uncertainty. Additional sources of the variations in the axial and radial values of reaction rate uncertainty are the changes in neutron spectra, which, for example in combination with the response function of the fission chamber, result in an increase of the axial and radial gradient in reaction rate uncertainties. This means that there is a significant difference in the experimental uncertainty of the measurements performed at core mid-plain or on the other hand at the edges of the core (same applying for radial variations of fission chamber positions). The evaluations presented in this section are characteristic examples of such a dependency.

First let us consider the uncertainty in the axial position of the fission chamber – the method used to evaluate the uncertainty source was based on the computation of the axial fission rate gradient, the results of which can be seen in Figure E2.7-2.4. It is evident that the gradient varies considerably throughout the height of the reactor core, i.e. at the centre of the core and the active part of the fuel the gradient is of the value of approximately 0.1 %/mm, which is an order of magnitude lower than that computed at the edges of the core, where it has a value of up to 2 %/mm. It is clear that one cannot simply average the uncertainty over the whole height of the core, since the uncertainty would be greatly overestimated for the fuel part of the core and underestimated next to the core support grids. It is therefore necessary to establish a set of criteria which can serve as guidelines for determining whether the axial or radial dependency of the fission rates can be neglected and an average estimate of the uncertainty can be produced or the dependency has to be taken into account. One of the basic attributes of an uncertainty evaluation is the uncertainty connected with the method used to produce the uncertainty estimate. If for example a Monte Carlo neutron transport method is used, as is the case for the evaluations presented in this chapter, then one of the basic criteria is related to the statistical uncertainty of the computations. In the case of the fission chamber computations presented above, the computational uncertainty was of the order of 0.5 %. That means that the variations in the fission rate uncertainty in the axial direction are several times larger, thus simple averaging cannot be used. In

order to establish an unambiguous criterion for the analysis of the axial and radial distribution of reaction rate uncertainties and gaining a combined uncertainty assessment for individual fission rate uncertainty sources, free of these dependencies, two new quantities are introduced which describe the behaviour of calculated reaction rates during parameter variation. The first quantity, named the relative natural norm L_{nat}, represents the absolute value of the maximum relative difference in fission reaction rate between the reference case $R_{i,0}$ and the calculation with a perturbed value of a specific parameter $R_{i,var}$:

$$L_{nat} = \max_{i=1,..,N} \left| \frac{R_{i,var}}{R_{i,0}} - 1 \right| , \qquad \text{E2.7-2.3}$$

where the index i goes over all of the axial positions N at which the fission rate calculations were performed. L_{nat} can actually be used as a measure for the maximum deviation of the discrepancies between the reference benchmark calculation and that with perturbed parameter. With the second quantity L_{rs} a measure for the relative standard uncertainty of the reaction rate calculations was introduced, defined by:

$$L_{rs} = \sqrt{\frac{\sum_{i=1}^{N} \left(\frac{R_{i,var}}{R_{i,0}} - 1 \right)^2}{N}} . \qquad \text{E2.7-2.4}$$

The latter quantity basically represents a measure of the scatter of uncertainties around an average value – this means that in the case of small axial or radial dependency the value of L_{rs} will be small, the opposite being true when the gradient of the uncertainty distribution is large. It was discovered that the perturbation of most reactor parameters results in fission rate changes which are smaller than- or of the order of the statistical errors of calculations and are in general not dependent upon the axial and radial position of the fission chambers. This means that the two quantities, i.e. L_{nat} and L_{rs}, used for describing the uncertainty deviations are of approximately the same value. In such a case the evaluator can consider the uncertainty dependency to be neglected and produce a single L_{rs} value which is postulated to represent the standard uncertainty value. If the axial or radial deviations of the uncertainty source are larger than the computational statistics, a combined estimate characterized by the L_{rs} norms value should only be used for the estimation of the "maximum" value of the experimental uncertainties, whereas the dependencies should be taken into account when comparing the benchmark model and computational results for benchmarking purposes.

Evaluation of the Uncertainty in the Experiment Configuration with Miniature Fission Chambers – Control Rod Position

The example considered in this chapter describes the evaluation of fission rate measurement uncertainties connected with the configuration of the experiment performed with miniature fission chambers in the JSI TRIGA Mark II research reactor. The example is based on the computed fission rate uncertainty due to the uncertainty in the TRIGA reactor control rod position. The power of the TRIGA reactor is controlled by the insertion and withdrawal of four control rods – namely the safety (S), transient (T), compensating (C) and regulating (R) control rod. Their locations, relative to measuring positions utilized in the fission chamber experiment, are shown in Figure E2.7-2.5. The safety and transient control rods are generally completely withdrawn during steady state reactor operation, as was also the case during the fission chamber measurements. The power of the reactor was controlled with the compensating and regulating rods, which were inserted into the core to an approximately equal measure. The control rod positioning scale is divided into 900 steps, where step 200 denotes complete withdrawal (0 for the transient rod) and 900 complete insertion. The movement of the rods is controlled by an asynchronous motor with an uncertainty in positioning of 3 steps[13]. The

[13] M. Ravnik, *Technical description of TRIGA Mark II reactor at Jožef Stefan Institute*, Jožef Stefan Institute, http://www.rcp.ijs.si/ric/description-s.html, November 2011.

effect of the control rod position uncertainty on the fission rate profile measurements was studied by alternatively inserting and withdrawing the regulating control rod in the benchmark Monte Carlo computational model by 5, 10 and 50 steps as depicted in Figure E2.7-2.6.

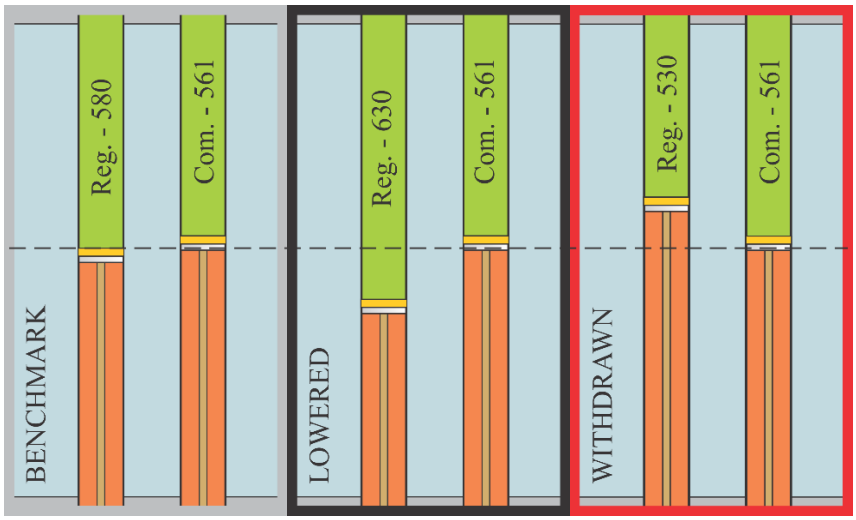

Figure E2.7-2.6. Schematic of the Monte Carlo benchmark computational model of the TRIGA reactor used in the evaluation of the uncertainty in fission rate measurements due to the uncertainty in control rod position. The leftmost frame depicts the initial control rod position during the experiment and the other two the perturbation steps, where the regulating rod was alternately lowered (black) and withdrawn (red) for either 5, 10 or 50 steps.

The calculated perturbed fission rate profiles R_p were compared to the original results R_0 and the relative dispersion of the perturbed computations was determined through the L_{rs} norm. It was found that the relative change in fission rate values $(R_p-R_0)/R_0$, after the control rod position was changed for 5 and 10 steps, was small and of the same value as the statistical uncertainty of the calculations. Therefore only the effect of 50 step change is presented and was, in order to gain the fission rate uncertainty estimate, scaled to a step perturbation approximately an order of magnitude lower. The results are shown in Table E2.7-2.5, where it can be seen that the position of the regulating control rod in the Monte Carlo computational model was varied for ± 50 steps which enabled the calculation of the multiplication factor defect and both L_{nat} and L_{rs} norms. The norm values were calculated on the basis of all axial reaction rate values – because the comparison between different radial positions throughout the core exhibited small discrepancies the final L_{nat} and L_{rs} estimations were gained through the averaging of their values over all of the measuring positions. The graphs in Figure E2.7-2.7 show the dependency of the fission rate relative difference for the regulating rod position perturbation calculation on the axial and radial position for the ^{235}U fission chamber. For all three measuring positions a standard discrepancy can be observed which is however dependent on the radial position of the regulating control rod relative to the studied measuring position (see Figure E2.7 -2.5 with denoted regulating control rod R and measuring positions). This occurs due to the so-called flux redistribution effect – i.e. the movement of control rods can induce a flux tilt in the relatively small core of the TRIGA reactor. This means that although for measuring positions close to the regulating control rod the fission rates will decrease if the rod is lowered and increase if the rod is withdrawn, for measuring positions close to the compensating control rod (opposite side of the reactor core) the change in fission rates will be the opposite as can be seen from Figure E2.7-2.7. The statistical error is of the order of 0.5 % for axial positions in the active part of the fuel and several percent at the edges of the core. The calculated L_{rs} norm averaged over all of the measuring positions and height of the reactor core is 0.028 with the regulating rod inserted for 50 steps and 0.034 with the regulating rod withdrawn for 50 steps. Since the reported error in control rod position is 3 steps the estimate of the relative standard uncertainty in fission rate distribution is concluded to be less than 0.3 %. Although the TRIGA reactor power is controlled by both compensating and regulating control rod only the

effect of the latter was studied because they are of similar integral worth and furthermore the core has a point cylindrical symmetry – hence the effect of the compensating control rod is postulated to be of similar value.

Table E2.7-2.5. Relative standard uncertainty in fission rate distribution due to uncertainty in control rod position

Parameter Identification	Parameter Variation in Calculation	Reported Parameter Uncertainty	ΔK_{eff} X 10^5	Averaged L_{nat} Norm	Averaged L_{rs} Norm	Relative Standard Uncertainty in Fission Rate Distribution
Regulating control rod lowered [steps]	+ 50	3 steps	approx. ± 300	0.090	0.028	(≤) ± 0.3 %
Regulating control rod withdrawn [steps]	- 50	3 steps		0.094	0.034	(≤) ± 0.3 %

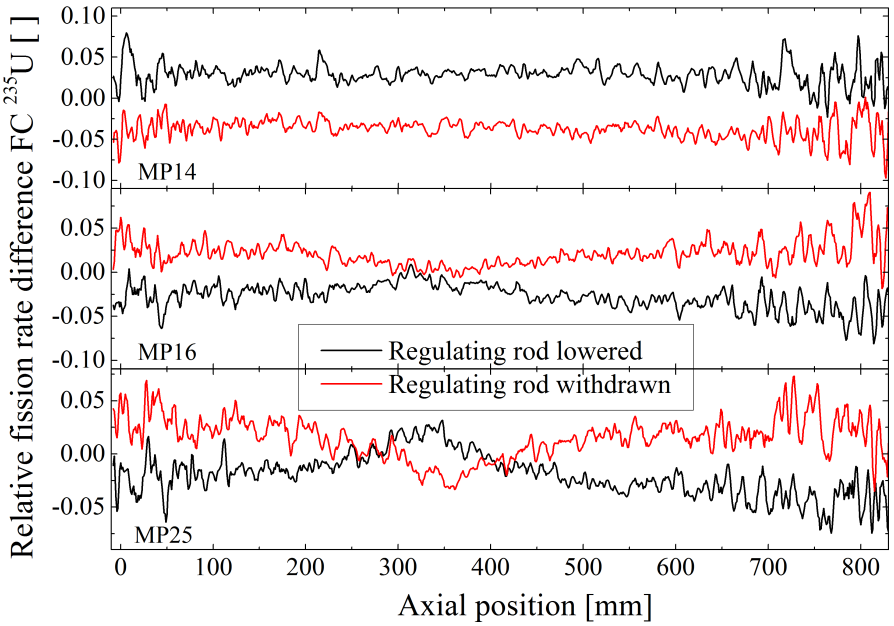

Figure E2.7-2.7. Axial distribution of the relative difference between fission rate calculations performed with the reference model and the model exhibiting perturbed regulating control rod position at three measuring positions for the ^{235}U fission chamber. The data denoted with the black curve represent the scenario with lowered regulating rod and the red curve data represent the scenario with the regulating rod withdrawn.

Example 2.7-3: Measurement of Reaction Rates for Bare Samples and Under Cd and BN (boron nitride) for a Selection of Nuclear Reactions in the Pneumatic Tube Irradiation Facility in the JSI TRIGA Mark II Reactor

The example presented hereby concerns the measurement of reaction rates for bare samples and under Cd and BN (boron nitride) for a selection of nuclear reactions in the Pneumatic Tube irradiation facility in the JSI TRIGA Mark II reactor in Ljubljana, Slovenia. The aim of the measurement

campaign was to characterize the neutron spectrum in the irradiation facility and investigate the applicability of boron nitride material for integral activation measurements in the epithermal energy range and cross-section validation.

Table E2.7-3.1. Sample materials and measured nuclear reactions

Sample Material	Nuclear Reaction
Al-0.1%Au	Au-197(n,γ), Al-27(n,p), Al-27(n,a)
Al-0.2%U	U-238(n,γ)
Al-1%Th	Th-232(n,γ)
Al-1%Mn	Mn-55(n,γ)
Al-0.1%Co	Co-59(n,γ)
Al-2%Sc	Sc-45(n,γ)
Fe	Fe-58(n,γ), Fe-54(n,p)
Sn enriched in ^{117}Sn	^{117}Sn(n,n')

The samples were in the form of foils, from around 3 mm to around 6 mm in diameter and from around 0.1 mm to 1 mm in thickness. The Al-0.1%Au material was obtained from the IRMM (Institute for Reference Materials and Measurements, Geel, Belgium) with a certified concentration of Au of 1.003 g/kg and a certified 2-σ uncertainty in the concentration of Au of 0.012 g/kg (IRMM-530R). The Al-0.2%U, Al-1%Th and Al-1%Mn materials were obtained from the CBNM (Central Bureau voor Nucleaire Metingen, Geel, Belgium – predecessor of the IRMM) and have quoted uncertainties in their compositions of 2 % with no indication on the coverage factor – 1-σ was assumed. The Al-0.1%Co and Al-2%Sc materials were obtained from the IRMM (IRMM-527 and IRMM-534, respectively). The certified Cobalt concentration is 1.001 g/kg with a certified 2-σ uncertainty of 0.024 g/kg. The certified Scandium concentration is 19.95 g/kg with a certified 2-σ uncertainty of 0.2 g/kg. The Fe samples were obtained as pure iron from the Goodfellow (Huntingdon, UK) and Leico Industries, Inc. (New York, US) companies. The quoted purity levels were 99.99 % and 99.9 %, respectively. The enriched Sn material was obtained from Campro Scientific GmbH, Berlin, Germany. The quoted ^{117}Sn enrichment was (92.8 ± 0.4) %.

The samples were irradiated bare, inside Cd and BN containers. The Cd containers were 10 mm in diameter and 6 mm in height, with a wall thickness of 1 mm, the BN containers were 13 mm in diameter and 14 mm in height, with a wall thickness of 4 mm.

The irradiation details (samples, containers, irradiation times) are reported in Table E2.7-3.2. The irradiations were performed at full reactor power (250 kW) using the pneumatic sample transport system the facility is equipped with.

Table E2.7-3.2. Sample / container irradiations performed

Irradiation	Irradiation Time	Irradiated Samples	Container
1	5 min	Al-0.2%U, Al-1%Mn, Al-0.1%Au	bare
2	10 min	Al-0.2%U, Al-1%Mn, Al-0.1%Au	Cd
3	10 min	Al-0.2%U, Al-1%Mn, Al-0.1%Au	BN
4	5 min	Sn (enriched in Sn-117), Al-0.1%Au	bare
5	5 min	Sn (enriched in Sn-117), Al-0.1%Au	Cd
6	5 min	Sn (enriched in Sn-117), Al-0.1%Au	BN
7	10 min	Fe, Al-0.1%Au	bare
8	15 min	Fe, Al-0.1%Au	Cd
9	10 min	Fe, Al-0.1%Au	BN
10	15 min	Al-0.1%Co, Al-2%Sc, Al-1%Th, Al-0.1%Au	bare
11	30 min	Al-0.1%Co, Al-2%Sc, Al-1%Th, Al-0.1%Au	Cd
12	10 min	Al-0.1%Co, Al-2%Sc, Al-1%Th, Al-0.1%Au	BN

The efficiency of the HPGe detector used for the measurements was calibrated using point wise ^{152}Eu and a ^{137}Cs sources with certified activities, obtained from the PTB (Physikalish-Technische Bundesanstalt, Braunschweig, Germany), using the k_0-IAEA program for k0-standardized neutron activation analysis [Rossbach, M., Blaauw, M., Bacchi, M. A., Lin, X., 2007, The k0-IAEA program, J. Radioanal. Nucl. Chem., 274 (3), 657_662 and Rossbach, M., Blaauw, M., 2006, Progress in the k0-IAEA program, Nucl. Instr. Meth. A, 564 (2), 698-701.]. The global detection efficiency fitting function used in this program is divided into three energy regions: 50-90 keV, 90-200 keV and above 200 keV, different mathematical functions being used in the three regions. The k0-IAEA program uses a Monte Carlo efficiency transfer algorithm to compute the efficiency vs. energy curve for a measured sample at a certain distance from the detector from the fitted reference efficiency vs. energy curve, measured at a reference distance from the detector. The overall (1-σ) uncertainty in the detection efficiency is 2 %.

The measurement data for the experimental campaign is reported in the datasets below. The datasets reports line by line, the measurement number ("ID"), the sample material, the container employed ("CV"), the target, product and decaying isotopes, the sample weight ("WGT") and its uncertainty in % ("DWG"), the mass fraction of the target isotope ("WPC"), the irradiation, cooling and measurement times in seconds ("TIR," "TCO" and "TME") along with their respective uncertainties in seconds ("DTI," "DTC" and "DTM"), the measured gamma line energy in keV ("EGM") the measured peak area and its uncertainty in counts ("PKA" and "DPK"), the detection efficiency ("EPS") and its uncertainty in % ("DEP") and lastly the coincidence correction factor ("COI"), and finally the calculated specific saturation activities in Bq / target atom (A_∞) and the calculated uncertainties in %.

Table E2.7-3.3. $^{238}U(n,\gamma)^{239}U$, $^{27}Al(n,\alpha)^{24}Na$, $^{197}Au(n,\gamma)^{198}Au$ reaction rate measurements

ID	Material	CV	Target	Product	Decaying	WGT [mg]	DWG [%]	WPC [%]	TIR [s]	DTI [s]	TCO [s]	DTC [s]	TME [s]	DTM [s]	EGM [keV]	PKA [counts]	DPK [counts]	EPS	DEP [%]	COI	SPCACT	Unc [%]
V023	Al-0.2%-U	bare	U-238	U-239	Np-239	8.06	0.2	0.2	300	1	434859	1	87100	1	103.7	82279	310	1.72E-02	2	1	3.38E-11	2.1
V023	Al-0.2%-U	bare	U-238	U-239	Np-239	8.06	0.2	0.2	300	1	434859	1	87100	1	106.1	104683	334	1.76E-02	2	1	3.07E-11	2.1
V023	Al-0.2%-U	bare	U-238	U-239	Np-239	8.06	0.2	0.2	300	1	434859	1	87100	1	209.8	11223	120	1.61E-02	2	1	2.92E-11	2.3
V023	Al-0.2%-U	bare	U-238	U-239	Np-239	8.06	0.2	0.2	300	1	434859	1	87100	1	228.2	34834	196	1.27E-02	2	1	3.42E-11	2.1
V023	Al-0.2%-U	bare	U-238	U-239	Np-239	8.06	0.2	0.2	300	1	434859	1	87100	1	277.6	38563	217	1.25E-02	2	1	3.00E-11	2.1
V023	Al-0.2%-U	bare	U-238	U-239	Np-239	8.06	0.2	0.2	300	1	434859	1	87100	1	285.8	2022	60	1.16E-02	2	1	3.10E-11	3.6
V023	Al-0.2%-U	bare	U-238	U-239	Np-239	8.06	0.2	0.2	300	1	434859	1	87100	1	315.9	3764	77	1.11E-02	2	1	2.99E-11	2.9
V023	Al-0.2%-U	bare	U-238	U-239	Np-239	8.06	0.2	0.2	300	1	434859	1	87100	1	334.2	4880	79	1.11E-02	2	1	3.02E-11	2.6
V024	Al-0.2%-U	Cd	Al-27	Na-24	Na-24	8.67	0.2	99.8	600	1	186903	1	172800	1	1368.6	29976	178	3.99E-03	2	1	8.05E-16	2.1
V024	Al-0.2%-U	Cd	Al-27	Na-24	Na-24	8.67	0.2	99.8	600	1	186903	1	172800	1	2754	16848	132	2.32E-03	2	1	7.79E-16	2.2
V024	Al-0.2%-U	Cd	U-238	U-239	Np-239	8.67	0.2	0.2	600	1	186903	1	172800	1	103.7	591304	884	1.72E-02	2	1	2.80E-11	2
V024	Al-0.2%-U	Cd	U-238	U-239	Np-239	8.67	0.2	0.2	600	1	186903	1	172800	1	106.1	755803	984	1.76E-02	2	1	2.56E-11	2
V024	Al-0.2%-U	Cd	U-238	U-239	Np-239	8.67	0.2	0.2	600	1	186903	1	172800	1	209.8	81621	369	1.61E-02	2	1	2.45E-11	2.1
V024	Al-0.2%-U	Cd	U-238	U-239	Np-239	8.67	0.2	0.2	600	1	186903	1	172800	1	226.4	5862	255	1.49E-02	2	1	2.86E-11	4.8
V024	Al-0.2%-U	Cd	U-238	U-239	Np-239	8.67	0.2	0.2	600	1	186903	1	172800	1	228.2	250249	596	1.27E-02	2	1	2.83E-11	2
V024	Al-0.2%-U	Cd	U-238	U-239	Np-239	8.67	0.2	0.2	600	1	186903	1	172800	1	277.6	279432	555	1.25E-02	2	1	2.51E-11	2
V024	Al-0.2%-U	Cd	U-238	U-239	Np-239	8.67	0.2	0.2	600	1	186903	1	172800	1	285.8	14749	139	1.16E-02	2	1	2.61E-11	2.2
V024	Al-0.2%-U	Cd	U-238	U-239	Np-239	8.67	0.2	0.2	600	1	186903	1	172800	1	315.9	28383	179	1.11E-02	2	1	2.60E-11	2.1
V024	Al-0.2%-U	Cd	U-238	U-239	Np-239	8.67	0.2	0.2	600	1	186903	1	172800	1	334.2	35482	200	1.11E-02	2	1	2.53E-11	2.1
V025	Al-0.2%-U	B	U-238	U-239	Np-239	7.96	0.3	0.2	600	1	532219	1	90000	1	103.7	46341	269	1.72E-02	2	1	1.31E-11	2.1

Table E2.7-3.3 (cont`d). $^{238}U(n,\gamma)^{239}U$, $^{27}Al(n,\alpha)^{24}Na$, $^{197}Au(n,\gamma)^{198}Au$ reaction rate measurements

ID	Material	CV	Target	Product	Decaying	WGT [mg]	DWG [%]	WPC [%]	TIR [s]	DTI [s]	TCO [s]	DTC [s]	TME [s]	DTM [s]	EGM [keV]	PKA [counts]	DPK [counts]	EPS	DEP [%]	COI	SPCACT	Unc [%]
V025	Al-0.2%-U	B	U-238	U-239	Np-239	7.96	0.3	0.2	600	1	532219	1	90000	1	106.1	59220	364	1.76E-02	2	1	1.19E-11	2.1
V025	Al-0.2%-U	B	U-238	U-239	Np-239	7.96	0.3	0.2	600	1	532219	1	90000	1	209.8	6313	97	1.61E-02	2	1	1.13E-11	2.5
V025	Al-0.2%-U	B	U-238	U-239	Np-239	7.96	0.3	0.2	600	1	532219	1	90000	1	228.2	19200	149	1.27E-02	2	1	1.29E-11	2.2
V025	Al-0.2%-U	B	U-238	U-239	Np-239	7.96	0.3	0.2	600	1	532219	1	90000	1	277.6	21643	157	1.25E-02	2	1	1.16E-11	2.2
V025	Al-0.2%-U	B	U-238	U-239	Np-239	7.96	0.3	0.2	600	1	532219	1	90000	1	285.8	1211	54	1.16E-02	2	1	1.27E-11	4.9
V025	Al-0.2%-U	B	U-238	U-239	Np-239	7.96	0.3	0.2	600	1	532219	1	90000	1	315.9	2141	60	1.11E-02	2	1	1.17E-11	3.5
V025	Al-0.2%-U	B	U-238	U-239	Np-239	7.96	0.3	0.2	600	1	532219	1	90000	1	334.2	2582	65	1.11E-02	2	1	1.09E-11	3.2
V029	Al-0.1%-Au	bare	Al-27	Na-24	Na-24	5.87	0.3	99.9	300	1	33252	1	36000	1	1368.6	29524	174	3.96E-03	2	1	7.88E-16	2.1
V029	Al-0.1%-Au	bare	Al-27	Na-24	Na-24	5.87	0.3	99.9	300	1	33252	1	36000	1	2754	16488	130	2.32E-03	2	1	7.52E-16	2.2
V029	Al-0.1%-Au	bare	Au-197	Au-198	Au-198	5.87	0.3	0.1	300	1	33252	1	36000	1	411.8	2109306	1536	9.48E-03	2	1	4.70E-10	2.1
V029	Al-0.1%-Au	bare	Au-197	Au-198	Au-198	5.87	0.3	0.1	300	1	33252	1	36000	1	675.9	12101	113	6.60E-03	2	1	4.59E-10	2.3
V030	Al-0.1%-Au	Cd	Al-27	Na-24	Na-24	5.91	0.3	99.9	600	1	23626	1	6000	1	1368.6	13822	119	3.96E-03	2	1	8.10E-16	2.2
V030	Al-0.1%-Au	Cd	Al-27	Na-24	Na-24	5.91	0.3	99.9	600	1	23626	1	6000	1	2754	7891	90	2.32E-03	2	1	7.90E-16	2.3
V030	Al-0.1%-Au	Cd	Au-197	Au-198	Au-198	5.91	0.3	0.1	600	1	23626	1	6000	1	411.8	330892	578	9.48E-03	2	1	2.04E-10	2
V030	Al-0.1%-Au	Cd	Au-197	Au-198	Au-198	5.91	0.3	0.1	600	1	23626	1	6000	1	675.9	1827	45	6.60E-03	2	1	1.92E-10	3.2
V035	Al-0.1%-Au	B	Al-27	Na-24	Na-24	2.83	0.7	99.9	600	1	114955	1	43200	1	1368.6	11084	106	3.96E-03	2	1	7.63E-16	2.3
V035	Al-0.1%-Au	B	Al-27	Na-24	Na-24	2.83	0.7	99.9	600	1	114955	1	43200	1	2754	6224	80	2.32E-03	2	1	7.32E-16	2.5
V035	Al-0.1%-Au	B	Au-197	Au-198	Au-198	2.83	0.7	0.1	600	1	114955	1	43200	1	411.8	204327	458	9.48E-03	2	1	5.07E-11	2.1
V035	Al-0.1%-Au	B	Au-197	Au-198	Au-198	2.83	0.7	0.1	600	1	114955	1	43200	1	675.9	1157	40	6.60E-03	2	1	4.89E-11	4.1

Table E2.7-3.4. $^{55}Mn(n,\gamma)^{56}Mn$ reaction rate measurements

ID	Material	CV	Target	Product	Decaying	WGT [mg]	DWG [%]	WPC [%]	TIR [s]	DTI [s]	TCO [s]	DTC [s]	TME [s]	DTM [s]	EGM [keV]	PKA [counts]	DPK [counts]	EPS	DEP [%]	COI	SPCACT	UNC [%]
V020	Al-1%-Mn	bare	25-Mn-55	25-Mn-56	25-Mn-56	10.67	0.2	1	300	1	77737	1	1000	1	846.8	15344	124	5.58E-3	2	1	3.69E-11	2.2
V020	Al-1%-Mn	bare	25-Mn-55	25-Mn-56	25-Mn-56	10.67	0.2	1	300	1	77737	1	1000	1	1810.7	2301	49	3.22E-3	2	1	3.53E-11	2.9
V020	Al-1%-Mn	bare	25-Mn-55	25-Mn-56	25-Mn-56	10.67	0.2	1	300	1	77737	1	1000	1	2113.1	1064	33	2.86E-3	2	1	3.48E-11	3.7
V021	Al-1%-Mn	Cd	25-Mn-55	25-Mn-56	25-Mn-56	8.97	0.2	1	600	1	76376	1	10000	1	846.8	9762	101	5.58E-3	2	1	1.75E-12	2.3
V021	Al-1%-Mn	Cd	25-Mn-55	25-Mn-56	25-Mn-56	8.97	0.2	1	600	1	76376	1	10000	1	1810.7	1491	41	3.22E-3	2	1	1.70E-12	3.4
V022	Al-1%-Mn	B	25-Mn-55	25-Mn-56	25-Mn-56	8.73	0.2	1	600	1	84874	1	15000	1	846.8	3791	66	5.58E-3	2	1	1.03E-12	2.7
V022	Al-1%-Mn	B	25-Mn-55	25-Mn-56	25-Mn-56	8.73	0.2	1	600	1	84874	1	15000	1	1810.7	550	28	3.22E-3	2	1	9.48E-13	5.5
V022	Al-1%-Mn	B	25-Mn-55	25-Mn-56	25-Mn-56	8.73	0.2	1	600	1	84874	1	15000	1	2113.1	268	23	2.86E-3	2	1	9.85E-13	8.8

Table E2.7-3.5. $^{117}Sn(n,n')^{117m}Sn$, $^{197}Au(n,\gamma)^{198}Au$ reaction rate measurements

ID	Material	CV	Target	Product	Decaying	WGT [mg]	DWG [%]	WPC [%]	TIR [s]	DTI [s]	TCO [s]	DTC [s]	TME [s]	DTM [s]	EGM [keV]	PKA [counts]	DPK [counts]	EPS	DEP [%]	COI	SPCACT	UNC [%]
V041	Sn (enriched)	bare	50-Sn-117	50-Sn-117m	50-Sn-117m	39.08	0.05	100	300	1	174182	1	1000	1	156	2327	76	1.83E-2	2	1	2.55E-12	3.8
V041	Sn (enriched)	bare	50-Sn-117	50-Sn-117m	50-Sn-117m	39.08	0.05	100	300	1	174182	1	1000	1	158.5	93966	319	1.83E-2	2	1	2.45E-12	2.1
V042	Sn (enriched)	Cd	50-Sn-117	50-Sn-117m	50-Sn-117m	41.44	0.05	100	300	1	157643	1	6000	1	156	14808	175	1.83E-2	2	0.997	2.54E-12	2.3
V042	Sn (enriched)	Cd	50-Sn-117	50-Sn-117m	50-Sn-117m	41.44	0.05	100	300	1	157643	1	6000	1	158.5	604783	842	1.83E-2	2	1	2.45E-12	2
V043	Sn (enriched)	B	50-Sn-117	50-Sn-117m	50-Sn-117m	13.02	0.15	100	300	1	163226	1	6000	1	156	4452	100	1.82E-2	2	0.997	2.45E-12	3
V043	Sn (enriched)	B	50-Sn-117	50-Sn-117m	50-Sn-117m	13.02	0.15	100	300	1	163226	1	6000	1	158.5	184903	467	1.81E-2	2	0.9994	2.42E-12	2
V031	Al-0.1%-Au	bare	79-Au-197	79-Au-198	79-Au-198	5.84	0.3	0.1	300	1	104547	1	300	1	411.8	14989	123	9.53E-3	2	1	4.70E-10	2.2
V032	Al-0.1%-Au	Cd	79-Au-197	79-Au-198	79-Au-198	5.91	0.3	0.1	300	1	103018	1	600	1	411.8	12729	113	9.53E-3	2	1	1.96E-10	2.2
V036	Al-0.1%-Au	B	79-Au-197	79-Au-198	79-Au-198	2.56	0.8	0.1	300	1	91505	1	5500	1	411.8	13628	119	9.53E-3	2	1	5.16E-11	2.3

Table E2.7-3.6. $^{58}Fe(n,\gamma)^{59}Fe$, $^{54}Fe(n,p)^{54}Mn$, $^{197}Au(n,\gamma)^{198}Au$ reaction rate measurements

ID	Material	CV	Target	Product	Decaying	WGT [mg]	DWG [%]	WPC [%]	TIR [s]	DTI [s]	TCO [s]	DTC [s]	TME [s]	DTM [s]	EGM [keV]	PKA [counts]	DPK [counts]	EPS	DEP [%]	COI	SPCACT	UNC [%]
V038	Fe	(bare)	26-Fe-58	26-Fe-59	26-Fe-59	220.69	0.01	100	600	1	612108	1	43200	1	142.7	15528	166	1.78E-2	2	1	3.21E-12	2.3
V038	Fe	(bare)	26-Fe-58	26-Fe-59	26-Fe-59	220.69	0.01	100	600	1	612108	1	43200	1	192.3	41650	232	1.61E-2	2	1	3.17E-12	2.1
V038	Fe	(bare)	26-Fe-58	26-Fe-59	26-Fe-59	220.69	0.01	100	600	1	612108	1	43200	1	334.8	2553	87	1.06E-2	2	1	3.19E-12	4
V038	Fe	(bare)	26-Fe-58	26-Fe-59	26-Fe-59	220.69	0.01	100	600	1	612108	1	43200	1	1099.3	251477	510	4.51E-3	2	1	3.52E-12	2
V038	Fe	(bare)	26-Fe-58	26-Fe-59	26-Fe-59	220.69	0.01	100	600	1	612108	1	43200	1	1291.6	170678	415	4.02E-3	2	1	3.51E-12	2
V038	Fe	(bare)	26-Fe-54	25-Mn-54	25-Mn-54	220.69	0.01	100	600	1	612108	1	43200	1	834.8	39439	220	5.48E-3	2	1	7.89E-14	2.1
V039	Fe	(Cd)	26-Fe-58	26-Fe-59	26-Fe-59	219.92	0.01	100	900	1	684161	1	73299.1	1	142.7	1835	89	1.78E-2	2	1	1.52E-13	5.2
V039	Fe	(Cd)	26-Fe-58	26-Fe-59	26-Fe-59	219.92	0.01	100	900	1	684161	1	73299.1	1	192.3	4565	107	1.61E-2	2	1	1.39E-13	3.1
V039	Fe	(Cd)	26-Fe-58	26-Fe-59	26-Fe-59	219.92	0.01	100	900	1	684161	1	73299.1	1	334.8	255	44	1.06E-2	2	1	1.28E-13	17.4
V039	Fe	(Cd)	26-Fe-58	26-Fe-59	26-Fe-59	219.92	0.01	100	900	1	684161	1	73299.1	1	1099.3	28847	173	4.51E-3	2	1	1.62E-13	2.1
V039	Fe	(Cd)	26-Fe-58	26-Fe-59	26-Fe-59	219.92	0.01	100	900	1	684161	1	73299.1	1	1291.6	19386	142	4.02E-3	2	1	1.60E-13	2.1
V039	Fe	(Cd)	26-Fe-54	25-Mn-54	25-Mn-54	219.92	0.01	100	900	1	684161	1	73299.1	1	834.8	102492	326	5.48E-3	2	1	8.11E-14	2
V040	Fe	(B)	26-Fe-58	26-Fe-59	26-Fe-59	22.56	0.1	100	600	1	776680	1	220000	1	142.7	699	107	1.78E-2	2	1	2.90E-13	15.4
V040	Fe	(B)	26-Fe-58	26-Fe-59	26-Fe-59	22.56	0.1	100	600	1	776680	1	220000	1	192.3	545	73	1.61E-2	2	1	8.33E-14	13.5
V040	Fe	(B)	26-Fe-58	26-Fe-59	26-Fe-59	22.56	0.1	100	600	1	776680	1	220000	1	1099.3	3204	63	4.51E-3	2	1	9.02E-14	2.8
V040	Fe	(B)	26-Fe-58	26-Fe-59	26-Fe-59	22.56	0.1	100	600	1	776680	1	220000	1	1291.6	2242	53	4.02E-3	2	1	9.28E-14	3.1
V040	Fe	(B)	26-Fe-54	25-Mn-54	25-Mn-54	22.56	0.1	100	600	1	776680	1	220000	1	834.8	20451	148	5.48E-3	2	1	7.91E-14	2.1
V033	Al-0.1%-Au	(bare)	79-Au-197	79-Au-198	79-Au-198	6.1	0.3	0.1	600	1	99017	1	200	1	411.8	19691	142	9.49E-3	2	1	4.38E-10	2.2
V034	Al-0.1%-Au	(Cd)	79-Au-197	79-Au-198	79-Au-198	5.63	0.4	0.1	900	1	152451	1	300	1	411.8	15552	126	9.49E-3	2	1	1.96E-10	2.2
V037	Al-0.1%-Au	(B)	79-Au-197	79-Au-198	79-Au-198	2.45	0.8	0.1	600	1	147126	1	3600	1	411.8	14222	120	9.49E-3	2	1	5.08E-11	2.3

Table E2.7-3.7. $^{59}Co(n,\gamma)^{60}Co$, $^{197}Au(n,\gamma)^{198}Au$ reaction rate measurements

ID	Material	CV	Target	Product	Decaying	WGT [mg]	DWG [%]	WPC [%]	TIR [s]	DTI [s]	TCO [s]	DTC [s]	TME [s]	DTM [s]	EGM [keV]	PKA [counts]	DPK [counts]	EPS	DEP [%]	COI	SPCACT	UNC [%]
V047	Co	bare	27-Co-59	27-Co-60	27-Co-60	7.51	0.3	0.1	900	1	2173237	1	151200	1	1173.2	48755	227	1.09E-2	2	1	1.04E-10	2.1
V047	Co	bare	27-Co-59	27-Co-60	27-Co-60	7.51	0.3	0.1	900	1	2173237	1	151200	1	1332.5	43951	214	9.87E-3	2	1	1.03E-10	2.1
V048	Co	Cd	27-Co-59	27-Co-60	27-Co-60	7.6	0.3	0.1	1800	1	2410947	1	350000	1	1173.2	18394	153	1.09E-2	2	1	8.42E-12	2.2
V048	Co	Cd	27-Co-59	27-Co-60	27-Co-60	7.6	0.3	0.1	1800	1	2410947	1	350000	1	1332.5	16595	144	9.87E-3	2	1	8.34E-12	2.2
V049	Co	B	27-Co-59	27-Co-60	27-Co-60	2.55	0.8	0.1	600	1	2767750	1	1311264	1	1173.2	4204	224	1.09E-2	2	1	4.61E-12	5.7
V049	Co	B	27-Co-59	27-Co-60	27-Co-60	2.55	0.8	0.1	600	1	2767750	1	1311264	1	1332.5	3973	208	9.87E-3	2	1	4.78E-12	5.7
V044	Al-0.1%-Au	bare	79-Au-197	79-Au-198	79-Au-198	5.83	0.3	0.1	900	1	440744	1	300	1	411.8	40775	203	2.40E-2	2	1	4.62E-10	2.1
V045	Al-0.1%-Au	Cd	79-Au-197	79-Au-198	79-Au-198	6.03	0.3	0.1	1800	1	438110	1	300	1	411.8	35854	190	2.40E-2	2	1	1.95E-10	2.1
V046	Al-0.1%-Au	B	79-Au-197	79-Au-198	79-Au-198	2.89	0.7	0.1	600	1	433324	1	3600	1	411.8	17860	134	2.40E-2	2	1	5.01E-11	2.3

Table E2.7-3.8. $^{45}Sc(n,\gamma)^{46}Sc$ reaction rate measurements

ID	Material	CV	Target	Product	Decaying	WGT [mg]	DWG [%]	WPC [%]	TIR [s]	DTI [s]	TCO [s]	DTC [s]	TME [s]	DTM [s]	EGM [keV]	PKA [counts]	DPK [counts]	EPS	DEP [%]	COI	SPCACT	UNC [%]
V050	Al-2%-Sc	bare	21-Sc-45	21-Sc-46	21-Sc-46	7.19	0.3	2	900	1	958860	1	3600	1	889.3	504961	746	1.34E-2	2	1	6.92E-11	2
V050	Al-2%-Sc	bare	21-Sc-45	21-Sc-46	21-Sc-46	7.19	0.3	2	900	1	958860	1	3600	1	1120.5	426046	659	1.12E-2	2	1	6.98E-11	2
V051	Al-2%-Sc	Cd	21-Sc-45	21-Sc-46	21-Sc-46	7.28	0.3	2	1800	1	961996	1	86400	1	889.3	497968	735	1.34E-2	2	1	1.41E-12	2
V051	Al-2%-Sc	Cd	21-Sc-45	21-Sc-46	21-Sc-46	7.28	0.3	2	1800	1	961996	1	86400	1	1120.5	420540	657	1.12E-2	2	1	1.42E-12	2
V052	Al-2%-Sc	B	21-Sc-45	21-Sc-46	21-Sc-46	2.47	0.8	2	600	1	1057386	1	172800	1	889.3	28556	198	1.34E-2	2	1	3.62E-13	2.3
V052	Al-2%-Sc	B	21-Sc-45	21-Sc-46	21-Sc-46	2.47	0.8	2	600	1	1057386	1	172800	1	1120.5	24083	165	1.12E-2	2	1	3.65E-13	2.3

Table E2.7-3.9. $^{232}Th(n,\gamma)^{233}Th$ reaction rate measurements

ID	Material	CV	Target	Product	Decaying	WGT [mg]	DWG [%]	WPC [%]	TIR [s]	DTI [s]	TCO [s]	DTC [s]	TME [s]	DTM [s]	EGM [keV]	PKA [counts]	DPK [counts]	EPS	DEP [%]	COI	SPCACT	UNC [%]
V026	Al-1%-Th	bare	90-Th-232	90-Th-233	91-Pa-233	10.32	0.2	1	900	1	1290264	1	14400	1	86.8	17043	165	4.03E-02	2	1	3.03E-11	2.2
V026	Al-1%-Th	bare	90-Th-232	90-Th-233	91-Pa-233	10.32	0.2	1	900	1	1290264	1	14400	1	94.7	84337	372	4.34E-02	2	1	2.52E-11	2.1
V026	Al-1%-Th	bare	90-Th-232	90-Th-233	91-Pa-233	10.32	0.2	1	900	1	1290264	1	14400	1	98.4	135592	479	4.45E-02	2	1	2.53E-11	2
V026	Al-1%-Th	bare	90-Th-232	90-Th-233	91-Pa-233	10.32	0.2	1	900	1	1290264	1	14400	1	103.9	8142	132	4.65E-02	2	1	3.36E-11	2.6
V026	Al-1%-Th	bare	90-Th-232	90-Th-233	91-Pa-233	10.32	0.2	1	900	1	1290264	1	14400	1	300.1	36770	206	3.06E-02	2	1	2.58E-11	2.1
V026	Al-1%-Th	bare	90-Th-232	90-Th-233	91-Pa-233	10.32	0.2	1	900	1	1290264	1	14400	1	311.9	205700	463	2.96E-02	2	1	2.59E-11	2
V026	Al-1%-Th	bare	90-Th-232	90-Th-233	91-Pa-233	10.32	0.2	1	900	1	1290264	1	14400	1	340.5	22489	160	2.76E-02	2	1	2.60E-11	2.1
V026	Al-1%-Th	bare	90-Th-232	90-Th-233	91-Pa-233	10.32	0.2	1	900	1	1290264	1	14400	1	375.4	3172	59	2.57E-02	2	1	2.57E-11	2.7
V026	Al-1%-Th	bare	90-Th-232	90-Th-233	91-Pa-233	10.32	0.2	1	900	1	1290264	1	14400	1	398.5	6235	81	2.45E-02	2	1	2.58E-11	2.4
V026	Al-1%-Th	bare	90-Th-232	90-Th-233	91-Pa-233	10.32	0.2	1	900	1	1290264	1	14400	1	415.8	7659	89	2.37E-02	2	1	2.63E-11	2.3
V027	Al-1%-Th	Cd	90-Th-232	90-Th-233	91-Pa-233	8.96	0.2	1	1800	1	1729086	1	21600	1	86.8	13864	153	4.03E-02	2	1	1.08E-11	2.3
V027	Al-1%-Th	Cd	90-Th-232	90-Th-233	91-Pa-233	8.96	0.2	1	1800	1	1729086	1	21600	1	94.7	69818	325	4.34E-02	2	1	9.13E-12	2.1
V027	Al-1%-Th	Cd	90-Th-232	90-Th-233	91-Pa-233	8.96	0.2	1	1800	1	1729086	1	21600	1	98.4	114101	430	4.45E-02	2	1	9.33E-12	2
V027	Al-1%-Th	Cd	90-Th-232	90-Th-233	91-Pa-233	8.96	0.2	1	1800	1	1729086	1	21600	1	103.9	7187	125	4.65E-02	2	1	1.30E-11	2.7
V027	Al-1%-Th	Cd	90-Th-232	90-Th-233	91-Pa-233	8.96	0.2	1	1800	1	1729086	1	21600	1	300.1	30573	183	3.06E-02	2	1	9.39E-12	2.1
V027	Al-1%-Th	Cd	90-Th-232	90-Th-233	91-Pa-233	8.96	0.2	1	1800	1	1729086	1	21600	1	311.9	171024	430	2.96E-02	2	1	9.41E-12	2
V027	Al-1%-Th	Cd	90-Th-232	90-Th-233	91-Pa-233	8.96	0.2	1	1800	1	1729086	1	21600	1	340.5	18630	149	2.76E-02	2	1	9.42E-12	2.2
V027	Al-1%-Th	Cd	90-Th-232	90-Th-233	91-Pa-233	8.96	0.2	1	1800	1	1729086	1	21600	1	375.4	2587	55	2.57E-02	2	1	9.18E-12	2.9
V027	Al-1%-Th	Cd	90-Th-232	90-Th-233	91-Pa-233	8.96	0.2	1	1800	1	1729086	1	21600	1	398.5	5194	75	2.45E-02	2	1	9.43E-12	2.5

Table E2.7-3.9 (cont`d). $^{232}Th(n,\gamma)^{233}Th$ reaction rate measurements

ID	Material	CV	Target	Product	Decaying	WGT [mg]	DWG [%]	WPC [%]	TIR [s]	DTI [s]	TCO [s]	DTC [s]	TME [s]	DTM [s]	EGM [keV]	PKA [counts]	DPK [counts]	EPS	DEP [%]	COI	SPCACT	UNC [%]
V027	Al-1%-Th	Cd	90-Th-232	90-Th-233	91-Pa-233	8.96	0.2	1	1800	1	1729086	1	21600	1	415.8	6255	81	2.37E-02	2	1	9.41E-12	2.4
V028	Al-1%-Th	B	90-Th-232	90-Th-233	91-Pa-233	8.12	0.2	1	600	1	1754450	1	136800	1	86.8	17309	175	4.03E-02	2	1	7.21E-12	2.3
V028	Al-1%-Th	B	90-Th-232	90-Th-233	91-Pa-233	8.12	0.2	1	600	1	1754450	1	136800	1	98.4	135914	434	4.45E-02	2	1	5.95E-12	2
V028	Al-1%-Th	B	90-Th-232	90-Th-233	91-Pa-233	8.12	0.2	1	600	1	1754450	1	136800	1	103.9	8145	141	4.65E-02	2	1	7.88E-12	2.7
V028	Al-1%-Th	B	90-Th-232	90-Th-233	91-Pa-233	8.12	0.2	1	600	1	1754450	1	136800	1	300.1	36693	210	3.06E-02	2	1	6.04E-12	2.1
V028	Al-1%-Th	B	90-Th-232	90-Th-233	91-Pa-233	8.12	0.2	1	600	1	1754450	1	136800	1	311.9	205099	490	2.96E-02	2	1	6.05E-12	2
V028	Al-1%-Th	B	90-Th-232	90-Th-233	91-Pa-233	8.12	0.2	1	600	1	1754450	1	136800	1	340.5	22129	156	2.76E-02	2	1	5.99E-12	2.1
V028	Al-1%-Th	B	90-Th-232	90-Th-233	91-Pa-233	8.12	0.2	1	600	1	1754450	1	136800	1	375.4	3197	70	2.57E-02	2	1	6.08E-12	3
V028	Al-1%-Th	B	90-Th-232	90-Th-233	91-Pa-233	8.12	0.2	1	600	1	1754450	1	136800	1	398.5	6415	89	2.45E-02	2	1	6.24E-12	2.4
V028	Al-1%-Th	B	90-Th-232	90-Th-233	91-Pa-233	8.12	0.2	1	600	1	1754450	1	136800	1	415.8	7624	95	2.37E-02	2	1	6.14E-12	2.4

The general expression for the specific saturation activity A_∞ for type 1 decay is:

$$A_\infty = \frac{N_p}{t_m} \frac{1}{SDC\ N_{at} \epsilon_p P_g F_{COI}},$$

where N_p is the measured peak area (equivalent to "PKA" in the datasets), t_m is the measurement time ("TME"), S, D and C are, respectively, the saturation, decay and cooling factors defined as follows:

$$S = 1 - e^{-\lambda t_{irr}}$$

$$D = 1 - e^{-\lambda t_{cool}}$$

$$C = \frac{1 - e^{-\lambda t_m}}{\lambda t_m},$$

where t_{irr} is the irradiation time ("TIR"), t_{cool} is the decay time ("TCO"), and N_{at} is the number of target atoms in the sample, given by:

$$N_{at} = \frac{m}{M} N_A w\ \Theta,$$

Where m is the sample mass ("WGT"), M is the molar mass of the target atom, N_A is Avogadro's number, w is the mass fraction of the target atoms constituting the sample ("WPC") and Θ is the isotopic abundance of the target atoms; ϵ_p is the detection efficiency ("EPS"), P_g is the gamma emission intensity, or intensity and F_{COI} is the coincidence correction factor for the measured gamma ray and the measurement geometry.

The uncertainties in the calculated activities were computed from the uncertainties in all the input quantities stated above, i.e. in the sample mass ("DWG"), the irradiation, cooling and measurement times ("DTI," "DTC" and "DTE"), in the measured peak areas ("DPK") and detection efficiency ("DEP"). The expression used to compute the uncertainties follows from the standard uncertainty propagation expression, assuming uncorrelated variables:

$$\left(\frac{\sigma_{A_\infty}}{A_\infty}\right)^2 = \left(\frac{\sigma_m}{m}\right)^2 + \left(\frac{\sigma_{N_p}}{N_p}\right)^2 + \left(\frac{\sigma_\epsilon}{\epsilon}\right)^2 + \frac{1}{A_\infty^2}\left[\left(\frac{\partial A_\infty}{\partial t_{irr}}\right)^2 \sigma_{t_{irr}}^2 + \left(\frac{\partial A_\infty}{\partial t_d}\right)^2 \sigma_{t_d}^2 + \left(\frac{\partial A_\infty}{\partial t_m}\right)^2 \sigma_{t_m}^2\right]$$

The last three terms in brackets including the partial derivatives of A_∞ with respect to the irradiation, decay and measurement times were approximated by computing the quantities ΔA_∞, i.e. the differences in A_∞ obtained by perturbing the irradiation, decay and count times by their uncertainties. As the relative uncertainties in the times are very small, so are their contributions to the uncertainties in the measured specific saturation activities.

2.7.5 References

2.7-1 "Reactor Physics Constants," 2nd ed., *Argonne* National Laboratory, *ANL-5800*, U.S. Atomic Energy Commission, July 1963.

2.7-2 U.S. Guide to the Expression of Uncertainty in Measurement, ANSI/NCSL Z540-2-1997, p11.

2.7-3 V. F. Dean, "ICSBEP Guide to the Expression of Uncertainties," Rev. 5, September 30, 2008.

2.7-4 M.-5. X.-5. M. C. TEAM, MCNP – A General Monte Carlo N-Particle Transport Code, Version 5, Los Alamos: Argonne National Laboratory, 2003.

2.7-5 Nakajima, K.; Akai, M.; Yamamoto, T. and Suzaki, T. "Measurements and Analyses of the Ratio of ^{238}U Captures to ^{235}U Fission in Low-Enriched UO2 Tight Lattices," *Joumal of Nuclear Science and Technology*, **31**, 1160-1170 (1994).

2.7-6 A. Trkov et al.; "On the Self-shielding Factors in Neutron Activation Analysis," Nuclear Instruments and Methods in Physics Research A 610 (2009) 553–565, DOI: doi:10.1016/j.nima.2009.08.079.

2.7-7 ORTEC "MAESTRO-32 MCA Emulator for Microsoft Windows 2000 Professional and XP" Professional A65-B32 Software User's Manual Software Version 6.0.

2.7-8 Nakajima, K.; Akai, M. and Suzaki, T. "Measurements of the Modified Conversion Ratio by Gamma-Ray Spectrometry of Fuel Rods for Water-Moderated UQ2 Cores". *Nuclear Science and Engineering*, **116**, 138-146 (1994).

2.7-9 K. Nakajima e-M. Akai, "Modified Conversion Ratio Measurement in Light Water-Moderated UO2 Lattices," *Nuclear Technology,* vol. 113, pp. 375-379, 1996.

2.7-10 Dos Santos, A. et al., IPEN(MB01)-LWR-CRIT-COEF-KIN-RRATE-SPECT-POWDIS-RESR-001: Reactor Physics Experiments in the IPEN/MB-01 Research Reactor Facility. International Handbook of Evaluated Reactor Physics Benchmark Experiments. NEA/NSC, 2012.

2.7-11 G. F. Knoll, Ed., "General Properties of Radiation Detectors," in *Radiation Detection and Measurement*, 4th ed. ed. USA: Wiley, 2010.

2.7-12 S. Chabod, "Saturation Current of Miniaturized Fission Chambers,"*Nucl. Instrum. Methods Phys. Res.*, vol. 598, no. 2, pp. 577–590, Jan. 2009.

2.7-13 J. Wagemans, G. Vittiglio, E. Malambu, and H. Aït Abderrahim, "The BR1 Reactor: A Versatile Irradiation Facility for Fundamental Research and Industrial Applications," in *Proc. ANIMMA*, Marseille, France, Jun. 7–10, 2009.

2.7-14 N. Authier and B. Mechitoua, "Bare, Highly Enriched Uranium Fast Burst Reactor CALIBAN," NEA/NSC/DOC/(95)03/II vol. II, HEU-MET-FAST-080, 1995.

2.7-15 NEA Nuclear Science Committee, International Criticality Safety Benchmark Experiment Handbook NEA/NSC/DOC(95)03/I-IX Sep. 2012.

2.7-16 https://www-nds.iaea.org/relnsd/vcharthtml/VChartHTML.html

2.7-17 Harb, S., Din K. S., and Abbady A., "Study of Efficiency Calibrations of HPGe Detectors for Radioactivity Measurements of Environmental Samples," in *Proceedings of the 3rd Environmental Physics Conference*, Aswan, Egypt, 2008.

2.8 Power Distribution Measurements

Guidance for the determination of uncertainties for Power Distribution Measurements has not yet been formalized; however, such guidance is expected to be essentially the same as that for Reaction-Rate Distribution Measurements.

Radial and axial power distributions are generally performed using integral or peak check spectrometry.

2.9 Isotopic Measurements

Guidance for the determination of uncertainties for Isotopic Measurements has not yet been formalized.

2.10 Other Miscellaneous Types of Measurements

Guidance for the determination of uncertainties for other Miscellaneous Types of Measurements has not yet been formalized.

APPENDIX A: DETERMINATION OF AN EXPERIMENTAL ERROR MATRIX

(Extracted directly from Sections 4.2 and 4.3 of *Methods and Issues for the Combined Use of Integral Experiments and Covariance Data*, A report by the Working Party on International Nuclear Data Evaluation Co-operation of the NEA Nuclear Science Committee, NEA/NSC/WPEC/DOC(2013)445)

4.2. Experimental error matrix

Experimental uncertainties of an integral parameter are usually given by the experimenters in the form of components. However, correlations between integral parameters are scarcely found in the experiment reports; therefore, we have to estimate them from the experimental information available. The method adopts the following three steps.

(Stage 1) Classification of Error Components to either Common or Independent

First, all-related components of the experimental errors for "Data A" and "Data B" with quantitative values reported are listed, and each individual component identified either as a "Common error (i.e. the correlation factor is 1.0) between Data A and B," or an "Independent error (i.e. the correlation factor is 0.0)"[14]. If an error component is judged as a mixture of common and independent errors, that is, the correlation factor is not considered as either 1.0 or 0.0, then the error component must be divided into more detailed subcomponents until the error component becomes either a common or independent error. This classification requirement is difficult for the experimenters who evaluate the error components in their report, but today this kind of rigor is essential to retain full value of these experimental quantities. Recent experimental databases like the OECD/NEA ICSBEP and IRPhEP handbooks [47] [48] now include such detailed experimental error evaluation by the continuous efforts of the authors and reviewers.

(Stage 2) Summation of Common and Independent Errors

Next, the common and independent errors, respectively, are summed-up statistically to obtain standard deviation, σ_{Total}, the diagonal term of the matrix. The statistical treatment is justified by the assumption that all error components have already been divided until there are no correlations between any error items in the measurement of an integral parameter. The total errors of Data A and B, that is, the diagonal term of error matrix, ***Ve***, are the summation of common and independent errors as below:

Standard deviation of Data A: $$\sigma_{Total,A} = \sqrt{\sigma^2_{Common,A} + \sigma^2_{Independent,A}} \qquad (4.5)$$

Standard deviation of Data B: $$\sigma_{Total,B} = \sqrt{\sigma^2_{Common,B} + \sigma^2_{Independent,B}} \qquad (4.6)$$

where σ_{Common}: Summing up of all Common error components,

[14] The words "Common" and "Independent" adopted here are usually referred as "Systematic" and "Statistical," respectively, in many experimental reporting literatures. However, the use of the former labels more clearly expresses the intention of this classification to evaluate their correlation factor for a specific pair of data in a large matrix than the latter labels.

$\sigma_{Independent}$: Summing up of all Independent error components.

(Stage 3) Evaluation of correlation factor

Finally, the correlation factor, non-diagonal term, of Data A and B is derived as the ratio of common errors to the total errors as Equation (4.7). Steps 1 to 3 must be repeated for all matrix elements to generate a full experimental error matrix as the input of adjustment exercise. It should be noted that the correlation factors between several sodium void reactivity measurements would be changed depending on the combination of void steps, even in the same experimental core.

Correlation Factor of Data A and Data B: $$\rho_{A,B} = \frac{\sum_i \sigma_{Common,A,i} \times \sigma_{Common,B,i}}{\sigma_{Total,A} \times \sigma_{Total,B}} \qquad (4.7)$$

where, the suffix *i* represents common error components between Data A and Data B.

4.3. Examples to evaluate experimental error matrix

Typical examples to estimate the experimental error matrix are shown for the sodium void reactivity (SVR) measurement and the reaction rate ratio (RRR) measurement in the ZPPR-9 core.

4.3.1. Sodium void reactivity measurement

Figure 17 summarises the evaluation procedure for the SVR measurement in the ZPPR-9 core. Table 3 shows the measured void step in the ZPPR-9 experiment [49]. Treatment of the error values and their correlation between Step 3 and Step 5 of the SVR measurement in ZPPR-9 is provided as an example. Step 3 is a central void case in the core where neutron non-leakage term is dominant for the reactivity change by sodium voiding, on the other hand, Step 5 is an axially whole-core void case where the non-leakage term of the reactivity is largely cancelled by the leakage term. The net reactivity of both steps is almost the same with the value around +30 cents, though the mass of the removed sodium to simulate sodium voiding is quite different by more than factor 2, that is, 31 kg for Step 3 and 78 kg for Step 5, respectively. The left part of Figure 17 is the result of the experimental error evaluation [49] following the IRPhEP evaluation guidance [50], where the error sources are classified into the three categories, (1) measurement technique, (2) geometry, and (3) composition.

(Stage 1) The detailed explanation of the error evaluation for the SVR measurement can be found in "Section 2.4: Evaluation of Reactivity Data" of [49]. First, the quality of the error analysis is assessed and the experimental error components are categorised in order to fulfil the requirement of the necessary error matrix evaluation, that is, the correlation factor of each error component between the two measurements must be 1.0 or 0.0.

Table 3: Results of zone sodium-voiding measurements in ZPPR-9 [41]

Step No.	Total Zone Size Drawers	Zone Depth mm	Total Na Mass[a] kg	Reactivity Change[b] cent		Reactivity Adjustment[c] cent
				Cumulative $\pm\sigma_m$ (σ_t)	Step $\pm\sigma_m$ (σ_t)	
1	9	203.2	2.90	3.03±0.05 (0.10)	3.03±0.05 (0.10)	-0.04
2	37	203.2	11.94	11.56±0.04 (0.19)	8.53±0.06 (0.17)	-1.36
3	97	203.2	31.30	29.39±0.02 (0.36)	17.83±0.04 (0.32)	1.22
4	97	406.4	62.60	37.26±0.01 (0.43)	7.87±0.02 (0.10)	0.84
5	97	508.0	77.88	31.68±0.02 (0.36)	-5.58±0.04 (0.15)	0.13
6	97	685.8	105.11	24.44±0.03 (0.29)	-7.24±0.04 (0.15)	-0.82
Outer core zones						
1	25 (x axis)	203.2	8.07	0.93±0.06 (0.12)		
2	25 (y axis)	203.2	8.07	0.20±0.06 (0.12)		

a: A random uncertainty of 1% is assigned to any mass or mass difference.

b: Counting statistics only are included in σ_m. The value of σ_t includes uncertainties in the reactivity adjustment and a 1.1% uncertainty in the detector calibration.

c: This uncertainty adjustment accounts for differences in experimental conditions between the reference and the particular step. When comparing the reactivity between steps, an uncertainty is assigned based on the magnitude of the adjustment.

Figure 17: Summary of uncertainties in the zone sodium void measurement in ZPPR-9

Source of Uncertainty				Uncertainty		Common error	Independent error
				cents	% of measured reactivity*		
Measurement technique	MSM method	Rod drop method	Counting statistics		±(0.2)**		0.2 % for Step3 and Step5
			λi and $\beta i/\beta$		±1.0	1.0 % for Step3 and Step5	
		$\frac{R_1 \cdot \varepsilon_2}{R_2 \cdot \varepsilon_1}$			±0.2		0.2 % for both step
		$\frac{\beta_{eff,1}}{\beta_{eff,2}}$		negligible			0.0 % for both step
		$\frac{S_{eff,2}}{S_{eff,1}}$			±0.5		0.5 % for both step
	Adjustment	Interface gap		±0.03			Step3: 0.10 %, Step5: 0.09 %
		Temperature		±0.27			0.9 % for both step
		Pu decay		±0.0015		0.00 % for both step	
Geometry		Interface gap (included in adjustment of measurement technique)			--		--
Composition	Assumed deviation of material mass	Pu mass			Depend on measured void zones	Step3: 0.72 %, Step5: 0.67 %	
		U mass					1.0 % for both step
		Stainless steel weight				0.16 % for both step	
		Sodium mass					
		O mass					
		C mass					
		^{239}Pu isotope ratio					
		^{235}U isotope ratio					
	Removed sodium mass				±1.0		
	Difference of stainless steel weight between the sodium-filled plates and the empty plates				±0.16		
						(Sub total - Common) Step3: 1.24 %, Step5: 1.21 %	(Sub total - Independent) Step3: 1.46 %, Step5: 1.46 %
						(Total error) Step3: 1.92 %, Step5: 1.90 %	

*: Every value in this column depends on the individual measurement case and is a relative uncertainty.
**: Generalised uncertainty.

$$\rho\ (between\ Step3\ and\ Step5) = \frac{\sum_i \sigma_{Common}(Step3,i) \times \sigma_{Common}(Step5,i)}{\sigma_{Total}(Step3) \times \sigma_{Total}(Step5)} = 0.41$$

The following are brief comments for the important error components in Figure 17 and Table 3. λ_i and β_i/β: To obtain the cent-unit reactivity by solving the inverse kinetics equation from the flux change measured, the family-wise decay constant (λ_i) values of the delayed neutron precursors and the family-wise delayed neutron fraction ratio (β_i/β) were needed as the input data[1]. This error component greatly contributes to the total error with the common characteristics between two measurements, since ANL experimenters used the same λ_i and β_i/β values throughout the measurement.

Temperature adjustment: The correction of temperature difference was needed between two measurements. According to the ANL document, the temperature difference is usually 2 degree-C at maximum, and the uncertainty of the temperature coefficient would be 10%. The resulted error

[1] Note this is not concerned with the conversion factor (β_{eff}) of the reactivity from cent-unit to delta k, which is needed to compare the reactivity value of an experiment with that of calculation.

values are quite large with the independent characteristics, since the temperature change between two measurements could be considered as random.

Material mass-induced error: The assumed mass uncertainties were derived from some ANL documents, that is, 0.079% for plutonium, 0.15% for uranium, etc. The mass uncertainties were converted to the reactivity-unit errors using the sensitivity coefficients of each element to each void step, therefore, the error values were slightly changed in Steps 3 and 5. This mass-induced error can be considered as a common component, since the shape of sensitivity coefficients for two measurements are quite similar.

(Stage 2) Summation of the results of the error values for Steps 3 and 5 is shown in Figure 17. The total error for Step 3 is 1.92%, and for Step 5, 1.90%. The contributions of common and independent errors are quite comparable.

(Stage 3) Finally, the correlation factor between Steps 3 and 5 is shown at the bottom of Figure 17. The value is 0.41, which might be physically plausible from the quantitative evaluation of the common and independent error components.

4.3.2. Reaction rate ratio measurement

Figure 18 and Tables 4-7 show the error matrix evaluation process for the RRR measurement in the ZPPR-9 core. Here, the foil activation method for the RRR measurement adopted in the ZPPR facility is provided as an example. Thin metallic activation foils were used to measure reaction rates in ZPPR-9 as illustrated in Figure 18. Uranium and plutonium metal foils were placed between plates in various drawers in the assembly, irradiated and then removed from the drawers. Capture and fission rates in the irradiated foils were determined by counting gamma rays emitted by capture or fission products.

(Stage 1) The error evaluation for the RRR measurement in ZPPR-9 is described in detail in "Section 2.7: Evaluation of Reaction Rate Distributions" [49]. Tables 4-7 show the result of the experimental error evaluation.

Error caused by mapping foil activity measurement: This error component consists of (1) the counting statistics, (2) the positioning of a sample above a gamma-ray counter, (3) the foil mass and (4) the discrete channel boundary in peak integration, whose characteristics are all statistical.

Figure 18: Example of reaction rate ratio measurement in ZPPR-9

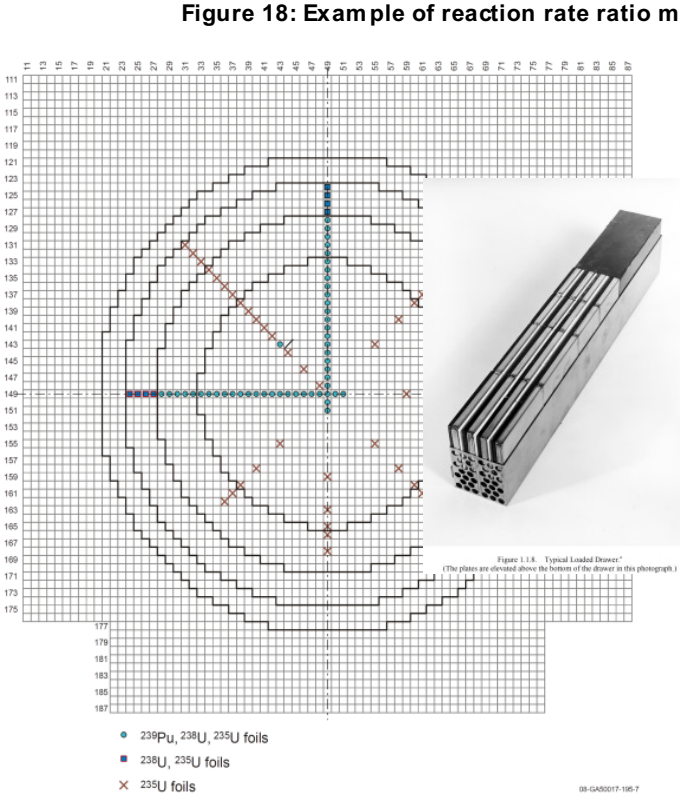

Figure 1.31. Measured Radial Reaction Rate Positions in ZPPR-9.
(Ref. D. N. Olsen, "ZPPR Assembly 9 – Detailed Work Plan No. 3", ZPR-I-306, Argonne National Laboratory (Jun. 1978).)

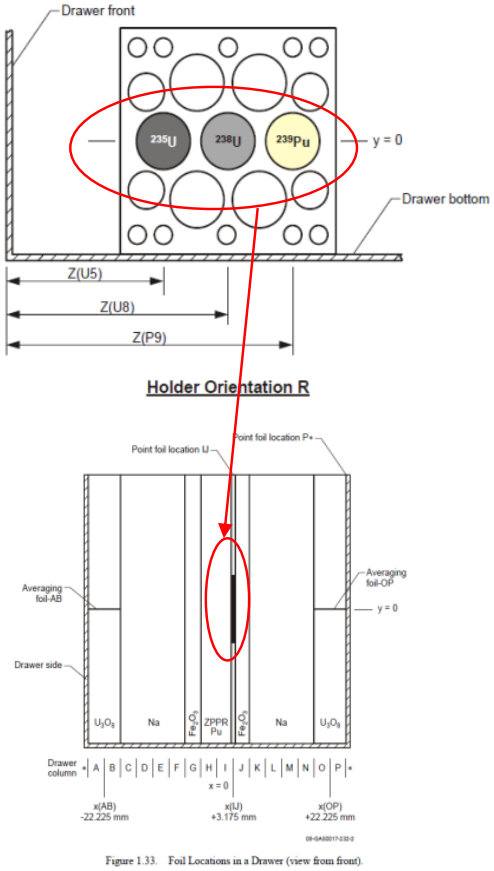

Figure 1.33. Foil Locations in a Drawer (view from front).

Table 4: Uncertainties assigned to the detector calibration

Typical uncertainty (% of measured reaction rate)						
Reaction Rate				Reaction Rate Ratio		
^{239}Pu(n, f)	^{235}U(n, f)	^{238}U (n, f)	^{238}U(n, γ)	^{235}U(n, f)/ ^{239}Pu(n, f)	^{238}U (n, f)/ ^{239}Pu(n, f)	^{238}U(n, γ)/ ^{239}Pu(n, f)
1.5	1.3	1.9	1.0	1.0	1.8	1.2

Table 5: Combined uncertainties of mapping foil data

	Typical uncertainty (% of measured reaction rate)							
	^{239}Pu fission		^{235}U fission		^{238}U fission		^{238}U capture	
	Core	Radial blanket	Core	Radial blanket	Core	Radial blanket	Core	Radial blanket
Measurement technique	1.3*		1.1*		1.7*		1.0*	
Geometry	negligible	--	negligible	1.0	negligible	0.1	negligible	0.9
Composition	0.18	---	0.17	0.08	0.22	0.27	0.18	0.06
Total	1.3	1.3	1.1	1.5	1.7	1.7	1.0	1.3

Table 6: Combined uncertainties of reaction rate ratio (in core region)

			Typical uncertainty (% of measured reaction rate ratio)					
			F25/F49		F28/F49		C28/F49	
			F25	F49	F28	F49	C28	F49
Measurement technique	Mapping foil		1.1	1.3	1.7	1.3	1.0	1.3
		Sub-total	1.7		2.1		1.6	
	Detector calibration		1.0*		1.8*		1.2*	
Geometry			negligible		negligible		negligible	
Composition			0.06		0.22		0.05	
Total			2.0		2.8		2.0	

In ZPPR-9, the reaction rates were measured in the same run and at the same foil place. Common errors of two reaction rate ratios (e.g. F49/F25 and C28/F25) come from the error of the common reaction rate (F25), as shown in the following table and equation.

Table 7: Final values for uncertainties and correlations of reaction rate ratio

Reaction Ratio		F28/F25	F49/F25	C28/F25
Total Error		2.7%	2.0%	1.9%
Correlation factor	F28/F25	1.0		
	F49/F25	0.23	1.0	
	C28/F25	0.23	0.32	1.0

$$\rho\ (between\ F49/F25\ \ and\ C28/F25) \approx \frac{1.1\% \times 1.1\%}{\sigma_{Total}(F49/F25) \times \sigma_{Total}(C28/F25)} = 0.32$$

Error caused by detector calibration: The absolute calibration of each reaction is necessary to measure the RRR value, which was made by gamma-ray counting of ^{239}Pu, ^{235}U and ^{238}U foils and deposits in back-to-back fission chambers. Note that the error induced by the detector calibration has the systematic characteristics to determine the absolute value of a kind of RRR, such as by averaging the F49/F25 values in the whole core, however, it has a statistical characteristic when the correlation between two kinds of RRRs, such as between F49/F25 and C28/F25, is considered.

Composition-induced error: Since the error caused by the foil composition is included in the mapping foil error, the composition row in Table 5 is related to the chemical analysis error of the core fuel and other core materials, and possesses the common characteristics between two RRRs. The composition error to the reactivity was converted with the sensitivity coefficients like the SVR case, but the magnitude was found to be negligible, compared with other common error mentioned below.

(Stage 2) In the ZPPR experiment, the activation foils of ^{239}Pu, ^{235}U and ^{238}U were irradiated in the same run, and at the same foil folders in a drawer. This means that the common error of two RRRs such as F49/F25 and C28/F25 must include the contribution from the common denominator, F25 in this case. The results of the error values for F49/F25 and C28/F25 are shown in Table 7. The total error for F49/F25 is 2.0%, and for C28/F25, is 1.9%.

(Stage 3) The correlation factors between F49/F25 and C28/F25 become 0.32 as shown in the last row of Table 7.

References

[41] "ZPPR-11 Monthly Report for February 1980," ZPR-TM-361, Argonne National Laboratory.

[47] OECD/NEA (2012), "International Handbook of Evaluated Criticality Safety Benchmark Experiments," NEA/NSC/DOC(95)03, September 2012 Edition.

[48] OECD/NEA (2013), "International Handbook of Evaluated Reactor Physics Benchmark Experiments," NEA/NSC/DOC(2006)1, March 2013 Edition.

[49] T. Ikegami (2011), "ZPPR-9 Experiment: A 650 MWe-class Sodium-cooled MOX-fuelled FBR Core Mock-up Critical Experiment with Clean Core of Two Homogeneous Zones," International Handbook of Evaluated Reactor Physics Benchmark Experiments (IRPhE), ZPPR-LMFR-EXP-002, NEA/NSC/DOC(2006)1, OECD/NEA.

[50] V.G. Dean (2003), "The Benchmark Evaluation Process: From Experimental Data to Benchmark Model," *Nuclear Science and Engineering* 145, pp.20-38.

[51] R.M. Lell, J.A. Morman, R.W. Schaefer, R.D. McKnight (2011), "ZPR-6 Assembly 7 Experiments: A Fast Reactor Core with Mixed (Pu,U)-Oxide Fuel and Sodium with a Thick Depleted Uranium Reflector," International Handbook of Evaluated Reactor Physics Benchmark Experiments (IRPhE), ZPR-LMFR-EXP-001, NEA/NSC/DOC(2006)1, OECD/NEA.

APPENDIX B: CALIBRATION OF MINIATURE FISSION CHAMBERS

Calibration of Miniature Fission Chambers

Calibration of miniature fission chambers is a complex but crucial element of uncertainty management in experimental techniques. As fission chambers are mainly used in pulse mode (count rates) in reactor physics applications (i.e. low power research reactors), we will only deal with this type of calibration. In pulse mode, each individual pulse carries information regarding the charge generated by the fission product within the fission ionization chamber. Signals can be processed as a pulse height distribution, called Pulse Height Analysis (PHA) spectrum 2.7-11. Its shape is entirely dependent on the detector characteristics like geometry and gas, and not at all on the electronics. It provides excellent signal-to-noise ratio by allowing discrimination of low amplitude pulses arising from gamma and electron interactions.

Calibration consists in establishing the relation between the measured indication and the physical quantity. Whatever mode is selected, this relation is linear for FC detectors used in saturation regime 2.7-12. Therefore in pulse mode it can be expressed as a calibration factor representing the FC efficiency for a given discrimination threshold applied on the PHA spectrum. This factor has the dimension of a mass (g), so it is conventionally called effective mass, an is noted m_{eff}. It is an arbitrary representation depending only on the discrimination threshold. It takes into account not only fissile mass but also a number of other parameters such as detector geometry; it does not tend to the real mass of the FC deposit. The only hypothesis it requires is the stability of the PHA spectrum for reproducibility of the discrimination, whatever spectrum the FC is used in. For a fission chamber with a pure isotopic fissile deposit, it is written as:

$$m_{eff} = \frac{C(tresh)}{R_m} \quad (1)$$

where:

- $C(tresh)$ is the FC count rate (s^{-1}) at a given threshold,
- R_m stands for the fission rate per mass unit ($s^{-1}.g^{-1}$).

Thus, (1) shows that accuracy of the calibration directly depends on the characterization of the irradiation facility at which it is performed, in terms of neutron spectrum and flux level. This is the first and main constraint which determines the choice of the irradiation facility.

Various facilities, such as the BR1 reactor at SCK-CEN, Belgium 2.7-13 or the (now closed) CALIBAN reactor in CEA Valduc Research Center 2.7-14, offer “reference” neutron fields, both in fast and purely thermal spectra. In BR1, the purely thermal spectrum is obtained into a 1m-large spherical cavity situated into the upper part of the large BR1 graphite reflector (Fig.1). Both reactors are benchmarked in the ICSBEP database 2.7-15.

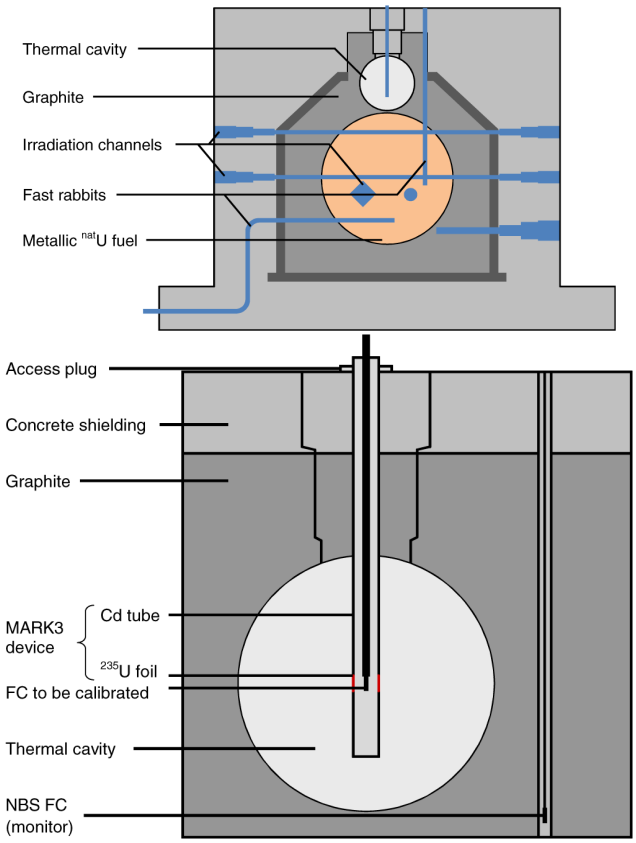

Fig.1 Schematic view of the irradiations channels and thermal column into the BR1 reactor and schematic view of the 1-m diameter BR1 spherical cavity with the MARK-3 device inserted (from 2.7-13)

Fast spectra are obtained using a conversion device called MARK-3 that allows the conversion of thermal neutrons into purely fast fission neutrons. It is made of a ^{235}U sheet surrounded by Cd-filter in order to minimize as much as possible the thermal part of the spectrum at the calibration location. The device is reproduced on Fig.1 right.

1. Details of the Calibration Method

Eq. (1) shows that calibrating a FC in pulse mode only requires one measurement at an irradiation facility where the neutron spectrum is characterized. All the quantities in play for determining this rate—and thereby the effective mass of a FC—are detailed from this equation in the following paragraphs. From this analysis we will then describe the uncertainties which impact the calibration accuracy and how we worked toward reducing them. First, the fission rate depends on the average total neutron flux and the equivalent fission cross section at the measurement location:

$$R_m = \frac{N_A}{M_p}\overline{\sigma_{eq}}\overline{\emptyset} \qquad (2)$$

where:
N_A is the Avogadro number,
M_p is the atomic mass of the main isotope present in the fissile deposit (g.mol^{-1}),

$\overline{\emptyset}$ is the total neutron flux at the measurement location averaged on the FC irradiation (s^{-1}),
$\overline{\sigma_{eq}}$ is the microscopic fission cross section integrated over the neutron spectrum at the measurement location, and taking into account the contributions of all isotopes the fissile material contains (barn):

$$\overline{\sigma_{eq}} = \sum_i \frac{N_i}{N_p} \overline{\sigma_i} \quad (3)$$

where:
i stands for the different isotopes in the deposit,
$\frac{N_i}{N_p}$ is the atomic ratio of each isotope *i* compared to the main one *p*.
FC irradiations are monitored and the neutron flux $\overline{\emptyset}$ is determined *via* the facility calibration factor *K*. It is established through dosimetry measurements:

$$\overline{\emptyset} = K.C_{mon,FC} = \frac{1}{C_{mon,dosi}} \frac{M_{dosi}}{N_A} \frac{R_{dosi}}{\overline{\sigma}_{dosi}} . C_{mon,FC} \quad (4)$$

where:
$C_{mon,irr}$ stands for the facility monitor count rate during an irradiation (*FC* or *dosimetry*, s^{-1}),
M_{dosi} is the atomic mass of the considered reaction isotope within the dosimeter ($g.mol^{-1}$),
R_{dosi} is the measured reaction rate of the dosimeter per mass unit ($s^{-1}.g^{-1}$),
$\overline{\sigma}_{dosi}$ is the integrated cross section of the considered reaction at the measurement location (barn).

From (2), (3) and (4), (1) can be rewritten as:

$$m_{eff} = \frac{C(tresh)}{K.C_{mon,FC} \times \frac{N_A}{M_p} \sum_i \frac{N_i}{N_p} \overline{\sigma_i}} \quad (5)$$

2. Sources of Uncertainty

From (5), it is clear that determining the effective mass m_{eff} of a FC requires a precise knowledge of the neutron flux or spectrum (*i.e.* irradiation location) in which it is measured. The result is **an intrinsic characteristics of the detector**: the quantity is then usable whatever irradiation facility the FC is employed at.

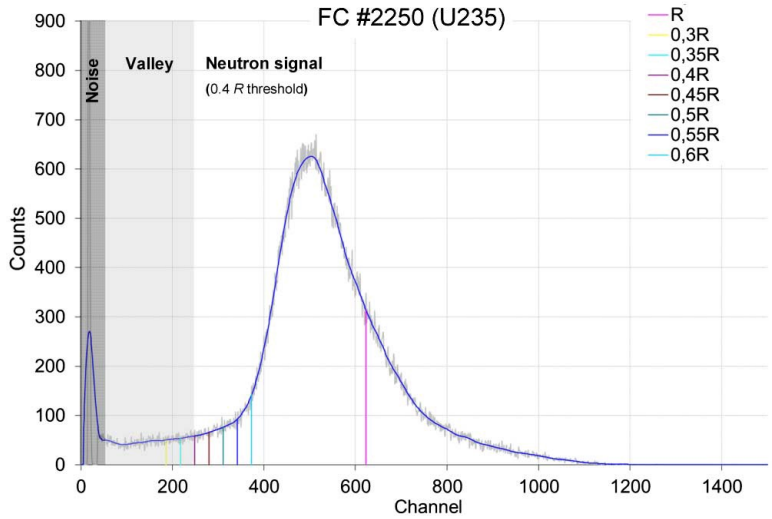

Fig. 4. PHA spectrum of the FC #2250 (235-U fissile deposit) and discrimination thresholds with respect to the reference channel.

2.1. Detectors Count Rates

Statistical uncertainty of detector count rates varies as the square root of the total count numbers, as count rate is considered as being Poisonian. So, $u(C) = \sqrt{C}$, or $u^2(C) = C$.

Reactor power was optimized for maximizing count rates while limiting dead time to less than a few percent. At the observed rates,–from 5 to 5,000 counts/s–pile-up is negligible. Durations of irradiation for each individual FC were adapted depending on the nature and mass of the FC deposit, so as to acquire at least 100,000 cumulated counts. Although some FCs with large fissile quantities would not have required long irradiations it-selves, reduction of irradiation duration was limited by monitor count rates.

The discrimination method enables excellent measurement reproducibility with negligible uncertainty [6]. As presented in Fig. 4, discrimination thresholds are determined on the PHA spectrum with respect to a reference channel, which corresponds to the half maximum of the fission product peak. The second uncertainty on the detector count rates arises from positioning precision, i.e. reproducibility. For this reason, dedicated positioning devices were designed for CEA FC irradiations at both the BR1 and CALIBAN facilities. While the device conceived for Valduc irradiations only allowed static and reproducible positioning, the important flux gradient of the MARK3 device at BR1 required designing a specific system for accurate axial measurements and estimating associated uncertainties.

The axial measurements results for the mm FC are shown in Fig. 5. Standard deviation was estimated to be about 0.5 mm; in this case it corresponds to a 0.2% additional count rate uncertainty. Although the new device solved the axial positioning issue, the results are still suffering from the significant radial uncertainty. It was estimated between 0.5 and 1% depending on the FC type.

Another issue is the size of the FC: the total neutron flux of the facility is characterized at the exact irradiation location while the neutron detector is of finite dimension, averaging flux over a specific volume. In most cases since FCs are miniature, such an effect does not need to be addressed. However in the case of FC irradiations in the MARK3 device, the flux gradient is too significant and has to be

taken into account. Therefore a parametric study was undertaken based on the axial measurements described above. The deviation between accessible and real maximum was estimated for various flux gradient shapes and FWHM in order to evaluate a form factor correction and its related uncertainty. The case of a Gaussian shaped gradient is presented in Fig. 6.

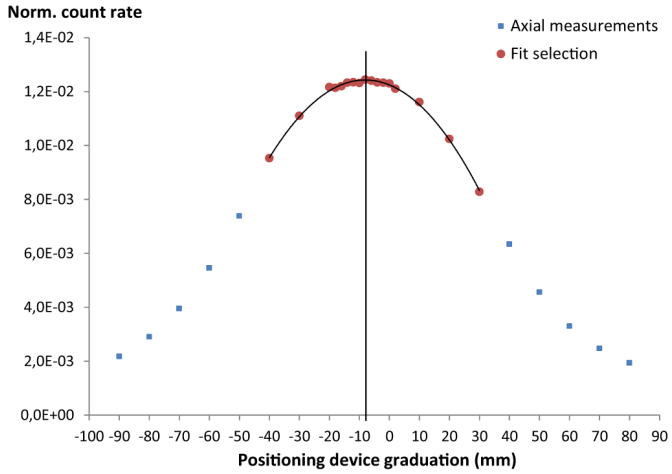

Fig. 5. Measurement of the axial gradient inside the BR1 MARK3 device for determination of the irradiation position during calibration and the associated uncertainties on FC count rates.

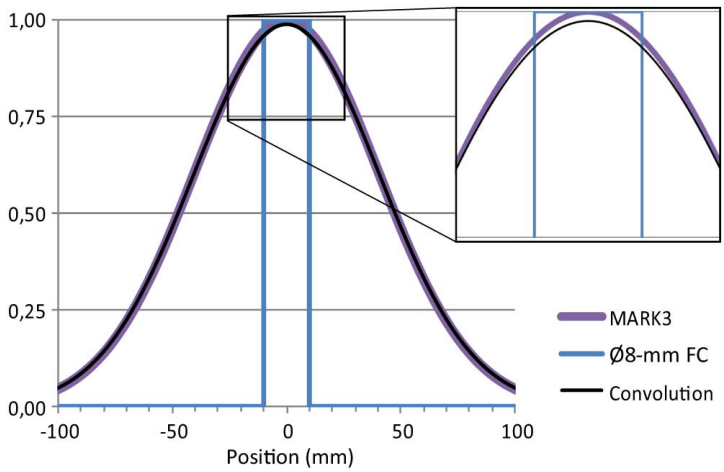

Fig. 6. Convolution of a parametric MARK3 flux gradient (95-mm FWHM Gaussian function) and a simplified Ø - FC representation (deposit is 20-mm wide) for calculation of the axial form factor correction, i.e. deviation between maxima.

2.2. Isotopic Composition of the FC Fissile Deposit

Save for a few exceptions, fissile materials cannot be purely isotopic. Impurities in the deposit contribute to the FC total fission rate depending on the neutron spectrum: impurities contribution goes from negligible (e.g. impurity in a deposit set in a fission spectrum) to major (e.g. same deposit in a thermal spectrum). Therefore uncertainties on their presence influence the final uncertainty of the FC effective mass proportionally: calibration facility has to be selected carefully for limiting their impact. It led to the choice of facilities providing a fission spectrum in which in a deposit has no impact.

2.3. Neutron Spectrum and Cross Sections

All spectra and average cross sections used for the present work were calculated using Monte Carlo codes such as MCNP [7] (BR1) or TRIPOLI [8] (CALIBAN). The results therefore depend on the used databases (JEFF 3.1.2, JEFF 3.1.1 [9], IRDF02, IRDFF [10]) and the evaluations of the associated uncertainties are complex. Because of their designs, both facilities have a spectrum close to a pure fission spectrum: differences come mainly from geometrical effects. Table I presents the spectra of both facilities by dividing them in three energy groups, compared to a standard Watt fission spectrum.

TABLE I - COMPARISON OF SPECTRA DISTRIBUTION

Spectrum	Thermal range (<0.025 eV)	Intermediate energy range	Fission en. range (>0.907 MeV)
CALIBAN	0 %	56 %	44 %
MARK3	0 %	31 %	69 %
Watt spectrum	0 %	27 %	73 %

In addition, the cross sections were calculated for empty irradiation locations: results do not take into account the effect of the materials introduced within the irradiation location for FC measurements. Therefore a sensitivity study was carried out in order to determine the effective fission rate in the FC deposit when all the detection devices are inserted: FC, connector and rod. The MCNP modelling of the Ø mm cylindrical FC is presented in Fig. 7. It became apparent that in the case of a fission spectrum, the material impact increases with the fission threshold of the isotope. In the case of a Ø mm FC (Table II), there is no impact on 235-U and 239-Pu fission rates, approximately 0.5% for fertile isotopes with threshold around 1 MeV (240,242-Pu,237-Np) and more than 1% for 238-U. Although the material impact is low, it constitutes a bias which must be taken into account.

The calculations results were applied as correction factors in the form of ratios between empty and filled irradiation location.

TABLE II - IMPACT OF FC DET. MATERIAL ON CROSS SECTIONS IN A FISSION SPECTRUM

FC type	^{235}U	^{238}U	^{237}Np	^{239}Pu	^{240}Pu	^{242}Pu
Ø4	0.0 %	-1.2 %	-0.5 %	-0.1 %	-0.5 %	-0.5 %
Ø8	0.1 %	-1.1 %	-0.4 %	-0.1 %	-0.4 %	-0.4 %

Therefore the associated uncertainties are considered independent from other contributions, only codes standard deviation uncertainty was taken into account (around 0.2%).

2.4. Facility Calibration Factor

As mentioned above and written out in (4), the determination of the calibration factor is based on simultaneous dosimetry and monitor irradiations. The monitor uncertainty is mainly statistical, whereas the flux determination *via* dosimetry measurements depends on both dosimeter activity measurements and average cross section evaluations as described above. Factor uncertainty sums up the contributions of all the independent parameters. Following the BR1 spectrum and average cross sections characterization, a new evaluation of this calibration factor was done at SCK-CEN. It comprised numerous dosimeters of various materials and energy responses for reducing uncertainties, such as indium, nickel and gold. The calibration factor of the CALIBAN central cavity was established using indium dosimetry during a dedicated irradiation.

2.5. Additional discussion about Uncertainty Sources

The uncertainty sources are not of equal significance, as shown in Table III. Once uncertainties have been reduced by proper experimental setup and realization, the main uncertainty comes from the calibration factor *K* of the irradiation location: it combines uncertainties on dosimetry measurements, cross sections and monitor count rate. The uncertainty on integrated cross sections remains dependent on nuclear databases, even when reduced *via* facility characterization. However, the uncertainty on equivalent cross section is largely reduced by calibrating FCs in a fission spectrum: fissile impurities in a fertile deposit contribute much less to the signal in a fission neutron spectrum. The final uncertainty on both calibrated FCs and monitor count rates is of course greatly reduced by sufficient irradiation duration and flux, and also by accurate positioning.

TABLE III - RESULTS AND COMPARISON OF UNCERTAINTY SOURCES

FC #	Main isotope	$m_{eff}\left(0.4\mathrm{R}^{a}\right)$	$\frac{\Delta C\left(0.4\mathrm{R}^{a}\right)}{C\left(0.4\mathrm{R}^{a}\right)}$	$\Delta K/K$	$\Delta\bar{\sigma}_{eq}/\bar{\sigma}_{eq}$	Total unc.
2135	U 238	255.9 µg	0.4 %	2.0 %	0.6 %	2.3 %
2188	U 235	19.85 µg	0.5 %	2.0 %	0.4 %	2.3 %
2237	Pu 239	20.23 µg	1.1 %	2.0 %	0.6 %	2.3 %
2250	U 235	4.501 µg	1.1 %	2.0 %	0.4 %	2.3 %
2251	U 235	26.13 µg	1.0 %	2.0 %	0.4 %	2.3 %
2266	U 238	91.48 µg	1.0 %	2.0 %	0.6 %	2.3 %
2268	U 235	9.409 µg	1.1 %	2.0 %	0.4 %	2.3 %
2269	Pu 239	8.378 µg	1.1 %	2.0 %	0.6 %	2.3 %
2270	Pu 240	170.0 µg	1.1 %	2.0 %	1.0 %	2.5 %
2271	Pu 242	98.35 µg	1.1 %	2.0 %	1.1 %	2.5 %
2272	U 235	62.11 µg	0.6 %	2.0 %	0.4 %	2.1 %
2273	U 238	104.3 µg	0.5 %	2.0 %	0.6 %	2.1 %
2274	Np237	320.7 µg	0.5 %	2.0 %	1.7 %	2.7 %

0.4R is the discrimination threshold, determined from a reference channel R of the PHA spectrum.

3. Calibration results

Some of the FCs were previously calibrated during a measurement campaign in 2010 at the BR1 facility.

Table IV provides a comparison between the BR1 2012 and 2010 (revised) results. FC #2188 effective masses are consistent throughout calibrations, while discrepancies are observed for the FCs #2135 and #2237. In all cases, the discrepancies directly reflect the revision of the average cross sections within the MARK3 device.

TABLE IV - COMPARISON OF 2012 AND 2010 BR1 CALIBRATION CAMPAIGNS

FC #	Main isotope	BR1 2012 $m_{eff}\left(0.4\mathrm{R}^{a}\right)$	BR1 2010 $m_{eff}\left(0.4\mathrm{R}^{a}\right)$	m_{eff} diff.	Diff. unc.	$\bar{\sigma}$ diff.
2135	U 238	255.9 µg	227.6 µg	11.0 %	3.4 %	10.4 %
2188	U 235	19.85 µg	19.42 µg	2.2 %	3.0 %	3.2 %
2237	Pu 239	20.23 µg	19.10 µg	5.6 %	3.1 %	5.7 %

0.4R is the discrimination threshold, determined from a reference channel R of the PHA spectrum.

In addition to the measurements conducted at the BR1 facility, supplementary calibrations were performed for two FCs with fertile (238-U) and fissile (235-U) deposits at the CALIBAN facility. The aim was to compare the results with those obtained at the BR1 facility and to consequently validate the calibration method. The results are provided in Table V.

TABLE V - COMPARISON OF CALIBRATION RESULTS IN BOTH FACILITIES

FC #	Main isotope	BR1 $m_{eff}(0.4R^{a})$	Unc.	CALIBAN $m_{eff}(0.4R^{a})$	Unc.	Diff.
2135	U 238	255.9 µg	2.3 %	262.8 µg	3.0 %	2.72 %
2188	U 235	19.85 µg	2.3 %	20.02 µg	2.7 %	0.87 %

0.4R is the discrimination threshold, determined from a reference channel R of the PHA spectrum.

Although spectra in the BR1 MARK3 device and in the CALIBAN cavity are different, the results are indeed consistent within the uncertainties. It confirms the effectiveness of the method and the related assumptions which were made.

Another result of the calibration campaign was the constitution of a bench of various FCs the effective masses of which were determined at the same place, i.e. same *K*. One significant application of calibrated FCs in experimental reactor is the measurement of spectral indices [6]. It is the ratio of two integrated cross sections in a local neutron distribution of interest. It is determined by comparing count rates of two calibrated FCs of different and selected isotopes. The spectral index « fission isotope *a* » on « fission isotope *r* » using mass calibrated fission chambers is the followings:

$$S = \frac{\overline{\sigma_a}}{\overline{\sigma_r}} = \frac{m_{eff,r} A_a C_a}{m_{eff,a} A_r C_r} - \sum_{i \neq \{a;r\}} \frac{\overline{\sigma_i} N_i}{\overline{\sigma_r} N_a} \quad (6)$$

where:

m_{eff} is the effective mass (in g) ;

A is the molar mass (in g.mol^{-1}) ;

C is the normalized count rate (ratio of measured count rate in the facility to the count rate in the monitor spectrum)

N is the atom number density ;

$\bar{\sigma}$ is the (spectrum averaged) microscopic cross section (in cm^2).

The index a refers to the measured isotope, whereas the index r refers to the reference isotopes (in the present case ^{235}U).

When the uncertainty on the calibration factor is known and distinct from other contributions, as it is the case here, it can be put aside in the uncertainty budget. In the case of the calibration campaign detailed in the present document, the total uncertainty of spectral indices is then reduced by a factor of three.

Applying it to the previous equation gives, in the case of a *F8/F5* (^{238}U/^{235}U) spectrum index:

$$\frac{F8}{F5} = \frac{\overline{\sigma_{238}}}{\overline{\sigma_{235}}} = \frac{m_{eff,235} A_{238} C_{238} / C_{mon,238}}{m_{eff,238} A_{235} C_{235} / C_{mon,235}} - \frac{\overline{\sigma_{234}} N_{234}}{\overline{\sigma_{235}} N_{238}} - \frac{N_{235}}{N_{238}}$$

Where $C_{mon,i}$ is the monitor fission chamber count rate during the measurement of the fission chamber loaded with isotope i.

Theoretically, the *F8/F5* is also sensitive to the *F4/F5* index (^{234}U/^{235}U), as ^{234}U is naturally present in uranium ores. Practically, one neglects the ^{234}U impurity, due to its very low contribution to the total signal. One can then write:

$$\frac{F8}{F5} = \frac{\overline{\sigma_{238}}}{\overline{\sigma_{235}}} = \frac{m_{eff,235} A_{238} C_{238}/C_{mon,238}}{m_{eff,238} A_{235} C_{235}/C_{mon,235}} - \frac{N_{235}}{N_{238}}$$

Posing:

$$x_5 = \frac{m_{235}}{m_{235} + m_{238}}, \text{ and } x_8 = \frac{m_{238}}{m_{235} + m_{238}} \Rightarrow \frac{N_{235}}{N_{238}} = \frac{x_5}{x_8}\frac{A_{238}}{A_{235}}$$

with m_i the mass of isotope i in the fission chamber. Then:

$$\frac{F8}{F5} = \frac{\overline{\sigma_{238}}}{\overline{\sigma_{235}}} = \frac{A_{238}}{A_{235}}\left(\frac{m_{eff,235}}{m_{eff,238}}\frac{C_{238}/C_{mon,238}}{C_{235}/C_{mon,235}} - \frac{x_5}{x_8}\right)$$

Neglecting all uncertainties on the atomic masses, the relative uncertainty can be expressed as:

$$u_r\left(\frac{F8}{F5}\right) = \frac{\sqrt{u_r^2\left(\frac{m_{eff,235}}{m_{eff,238}}\frac{C_{238}/C_{mon,238}}{C_{235}/C_{mon,235}}\right) \times \left(\frac{m_{eff,235}}{m_{eff,238}}\frac{C_{238}/C_{mon,238}}{C_{235}/C_{mon,235}}\right)^2 + u_r^2\left(\frac{x_5}{x_8}\right) \times \left(\frac{x_5}{x_8}\right)^2}}{\left(\frac{m_{eff,235}}{m_{eff,238}}\frac{C_{238}/C_{mon,238}}{C_{235}/C_{mon,235}} - \frac{x_5}{x_8}\right)}$$

Example: F7/F5

A ^{237}Np fission deposit can be considered as pure. So , the *F7/F5* spectral index can be written as:

$$\frac{F7}{F5} = \frac{\overline{\sigma_{237}}}{\overline{\sigma_{235}}} = \frac{A_{237}}{A_{235}}\frac{m_{eff,235}}{m_{eff,237}}\frac{C_{237}/C_{mon,237}}{C_{235}/C_{mon,235}}$$

Again, neglecting all uncertainties on atomic masses, one gets, for the relative uncertainty:

$$u_r\left(\frac{F7}{F5}\right) = u_r\left(\frac{m_{eff,235}}{m_{eff,237}}\frac{C_{237}/C_{mon,237}}{C_{235}/C_{mon,235}}\right)$$

The uncertainties on the count rates C are equal to , as one considers countings as a poisonian process.

References

[1] G. F. Knoll, Ed., "General properties of radiation detectors," in *Radiation Detection and Measurement*, 4th ed. ed. USA: Wiley, 2010.

[2] S. Chabod, "Saturation current of miniaturized fission chambers,"*Nucl. Instrum. Methods Phys. Res.*, vol. 598, no. 2, pp. 577–590, Jan.2009.

[3] J. Wagemans, G. Vittiglio, E. Malambu, and H. A. Aït, "The BR1 reactor: A versatile irradiation facility for fundamental research and industrial applications," in *Proc. ANIMMA*,Marseille, France, Jun. 7–10, 2009.

[4] N. Authier and B. Mechitoua, "Bare, highly enriched uranium fast burst reactor CALIBAN," NEA/NSC/DOC/(95)03/II vol. II, HEU-MET-FAST-080, 1995.

[5] NEA Nuclear Science Committee, International Criticality Safety Benchmark Experiment Handbook NEA/NSC/DOC(95)03/I-IX Sep. 2012.

[6] N. Blanc de Lanaute *et al.*, "Spectral indices measurements using miniature fission chambers at the MINERVE Zero-Power Reactor at CEA using calibration data obtained at the BR1 Reactor at ," *IEEE Trans. Nucl. Sci.*, vol. 59, no. 4, pp. 1344–1350,Aug. 2012.

[7] X-5 Monte Carlo Team, MCNP—A General Monte Carlo N-Particle Transport Code ver. 5, LA-UR-03–1987, 2005.

[8] E. Brun, E. Dumonteil, F.-X. Hugot, N. Huot, C. Jouanne, Y. K. Lee, F. Malvagi, A. Mazzolo, O. Petit, J.-C. Trama, and A. Zoia, "Overview of TRIPOLI-4 version 7 continuous-energyMonte Carlo transport code," in *Proc. Int. Conf. ICAPP*, Nice, France, 2011.

[9] A. Santamarina *et al.*, The JEFF-3.1.1 nuclear data library, NEA JEFF Report 22, 2009.

[10] E. M. Zsolnay, R. Capote, H. K. Nolthenius, and A. Trkov, Technical report INDC(NDS)-0616, IAEA Vienna, 2012